

Fundamentals of the Planetary Spectrum Generator 2025 Edition

Villanueva, Geronimo Luis
NASA Goddard Space Flight Center
Greenbelt, MD, USA

PSG Team:

Liuzzi, Giuliano
Faggi, Sara
Protopapa, Silvia
Kofman, Vincent
Fauche, Thomas J.
Stone, Shane W.
Mandell, Avi M.

Electronic version publicly available at: <https://psg.gsfc.nasa.gov/help.php>

PSG is funded by NASA's Sellers Exoplanet Environments Collaboration (SEEC), Goddard Fellows Innovation Challenge (GFIC), Goddard's ExoSpec Project, Goddard Center for Astrobiology (GCA) and Fundamental Laboratory Research (FLaRe).



ISBN 978-0-578-36143-7
Library of Congress Control Number: 2022901290
Greenbelt, Maryland, United States of America
Latest revision on March 17, 2025



Table of contents

Chapter 1: Introduction	7
1. About the Planetary Spectrum Generator	8
2. Initializing and running PSG	9
3. Modules and outputs of the PSG architecture.....	10
4. Main sections of the web interface.....	14
Chapter 2: Geometry and orbital modeling	21
1. Geometry modeling	22
2. Orbital modeling of solar system objects.....	22
3. Orbital modeling of exoplanets.....	23
4. Orbital and spectroscopic velocities	25
5. Types of stellar hosts	26
6. Definition of the modeling geometries: angles and sub-sampling.....	26
6.1 Looking up / Looking up to the Sun / Looking to an object / Dome view	26
6.2 Limb / Solar occultation / Stellar occultation	27
6.3 Nadir.....	28
6.4 Observatory	28
7. Description and modeling of the field-of-view (FOV)	29
Chapter 3: Atmospheres, exospheres and comets	31
1. Types of atmospheres.....	32
2. Vertical structure of an atmosphere in hydrostatic equilibrium.....	33
3. Earth atmosphere	34
4. Mars atmosphere	35
5. Gas giants / Dense and hazy atmospheres.....	35
6. Cometary atmospheres.....	36
7. Exoplanet atmospheres	39
8. Three-dimensional characterization (GCM) of the atmosphere and surface	39
Chapter 4: Radiative transfer modeling.....	43
1. Radiative transfer modeling in PSG	44
2. Raytracing in a spherical and refractive atmosphere.....	47

3. Atmospheric opacities.....	49
3.1 Line-by-line modeling	50
3.2 Correlated-k calculations.....	55
3.3 High-temperature linelists: HITEMP and ExoMol	56
3.4 Molecular cross-sections and UV modeling.....	58
3.5 Rayleigh and Raman scattering.....	58
3.6 Collision-Induced-Absorption (CIA) and the Water Continuum (MT_CKD)	60
4. Non-Local Thermodynamical-Equilibrium (non-LTE) modeling.....	62
5. Cometary modeling (CEM module)	64
6. Non-LTE modeling in cometary atmospheres	65
6.1 Coma 3D raytracing and asymmetric outgassing / jets	71
6.2 Modeling of bright optical emissions (OH, CN, C ₂ , CH, NH) in comets.....	72
6.3 Optically thick fluorescence modeling at infrared/optical/UV wavelengths	75
Chapter 5: Multiple Scattering Atmospheric Modeling	77
1. Atmospheric scattering modeling in PSG	78
2. Theory of radiative transfer in a scattering medium	79
2.1 Discretization of the azimuthal intensities, Fourier series and Legendre polynomials	79
2.2 Discretization of the polar angles, Gaussian quadrature angles	82
2.3 Solving the whole system, applying boundary conditions.....	83
2.4 Scattering numerical algorithm.....	84
3. Mie scattering and calculation of the aerosol models	85
4. Selection of the number of stream pairs (NMAX) and Legendre terms (LMAX).....	87
5. Specifics of multiple scattering simulations	92
Chapter 6: Surface Scattering Modeling.....	95
1. Surface modeling in PSG	96
2. Lambert model: isotropic scattering	96
3. Hapke model: parametric surface modeling.....	97
4. Lommel-Seeliger: dark and weakly scattering Lunar/asteroid/comet surfaces.....	101
5. Cox-Munk model: glint and ocean's reflections	104
6. Cometary dust/icy grains.....	105
7. Mixing compositions.....	108

8. Calculation of the single scattering albedo: reflectances, optical constants and albedos	111
9. Disk integrated quantities: albedos and phase integrals.....	113
10. Thermo-physical Modelling (PSGTM)	114
Chapter 7: Mass spectrometry	119
1. Mass spectrometry and its implementation in PSG	120
2. Fragmentation model and an accurate high-resolution mass fragment database	121
3. Simulating mass spectrometry and its noise.....	124
4. Mass spectrometry retrievals and complex organics identification.....	125
Chapter 8: Instruments and Noise Modeling.....	129
1. Principles of noise modeling	130
2. Field-Of-Views (FOVs), diffraction limits and planetary filling factors.....	132
3. Spectral grids, sampling and convolutions	134
4. Radiation and intensity output units	135
5. Zodiacal light, exozodii, telluric and background sources.....	136
6. Coronagraphic modeling	139
7. AOTF and grating modeling.....	141
8. Light Detection and Ranging (LIDAR) spectroscopy	142
Chapter 9: Retrieval Methods	145
1. Retrievals general elements.....	146
2. Optimal Estimation	146
3. Implementation of OE in PSG	149
4. Retrieval of vertical profiles.....	153
5. Nested retrievals: principles	156
6. MultiNest and its implementation: PSGnest	160
Chapter 10: Application Program Interface (API) and Installation.....	163
1. Application Program Interface.....	164
2. Calling the API.....	164
3. Installing a personal version of PSG in your computer	165
4. Types of planetary spectra and special keywords	167
6.1 Structurer of the AWS console and instances.....	172
6.2 Accessing the instances	177

6.2 Configuring AWS on the ssh.....	178
6.2 Cloning an instance.....	178



Planetary Spectrum Generator
National Aeronautics and Space Administration

Chapter 1: **Introduction**

**Villanueva, Faggi and
PSG team**



1. About the Planetary Spectrum Generator

The Planetary Spectrum Generator (PSG, <https://psg.gsfc.nasa.gov>) is a radiative transfer model suite for synthesizing and retrieving planetary spectra (atmospheres and surfaces) for a broad range of wavelengths (50 nm to 100 mm, UV/Vis/near-IR/IR/far-IR/radio) from any observatory (e.g., JWST, ALMA, Keck, SOFIA), any orbiter (e.g., MRO, ExoMars), or any lander. PSG also permits to synthesize/retrieve mass-spectrometry data of orbiters, landers and laboratory instrumentation. This is achieved by combining several state-of-the-art radiative transfer models, spectroscopic databases and planetary databases (i.e., climatological and orbital). The tool first became online in 2015, with a first paper reporting the suite capabilities reported in (Villanueva et al., 2018).

The latest version of PSG has the following general capabilities:

- A 3D (three-dimensional) **orbital calculator** for most bodies in the solar system, and all confirmed exoplanets. Possible observing geometries include observatory, full sky view, nadir, limb, solar/stellar occultation, transit, etc. The orbital calculator provides all possible geometry parameters needed for computing spectroscopic fluxes.
- The program can ingest **billions of spectral lines of almost 1,000 species from several spectroscopic repositories** (e.g., HITRAN, JPL, CDMS, GSFC-Fluor, ExoMol). For mass-spectrometry, PSG operates with a high-resolution (mDa) fragmentation pattern database for +20,000 species calibrated with the NIST public library.
- **Atmospheric models** (e.g., equilibrium chemistry, cometary models), databases (e.g., Mars GCMs, Earth/NASA-MERRA2) and templates (vertical profiles of temperature and abundances) are available for the main atmospheres (Venus, Earth, Mars, Titan, Neptune, Uranus), and general atmospheric and surface parameters are available for the other bodies.
- Radiative transfer analysis can be performed with several models:
 - **Multiple scattering spherical modeling**, PUMAS.
 - Line-by-Line (LTE) **Cometary Model**, CEM.
 - Line-by-Line (non-LTE) **Cometary Fluorescence Model**, CEM.
 - **Generalized Continuum Model**, CONTINUUM.
 - **Mass spectrometry modeling**, MASS.
- The code synthesizes spectra in **any desired radiance unit** (spectral radiance, spectral intensity, spectral flux, radiant energy density, irradiance, spectral irradiance, magnitude, etc.) and transmittance output.
- It includes the possibility to integrate **stellar templates** by adopting the Kurucz 2005 stellar templates (0.15-300 μm), which is complemented at short wavelengths ($<0.4 \mu\text{m}$; X-ray, EUV, FUV) with the MUSCLES Treasury Survey. When considering the Sun and the G-type template, the spectrum is complemented with the SOLAR-HRS and ACE solar spectra (0.4-14 μm) in the infrared and with the LISIRD template ($<0.4 \mu\text{m}$) in the UV.
- It includes a **realistic noise calculator** for a broad range of instruments, including heterodyne instruments in the radio, interferometers, AOTF systems, LIDAR instruments, coronagraphs, orbital cameras. The noise module includes a broad range of background and systematic sources of noise.

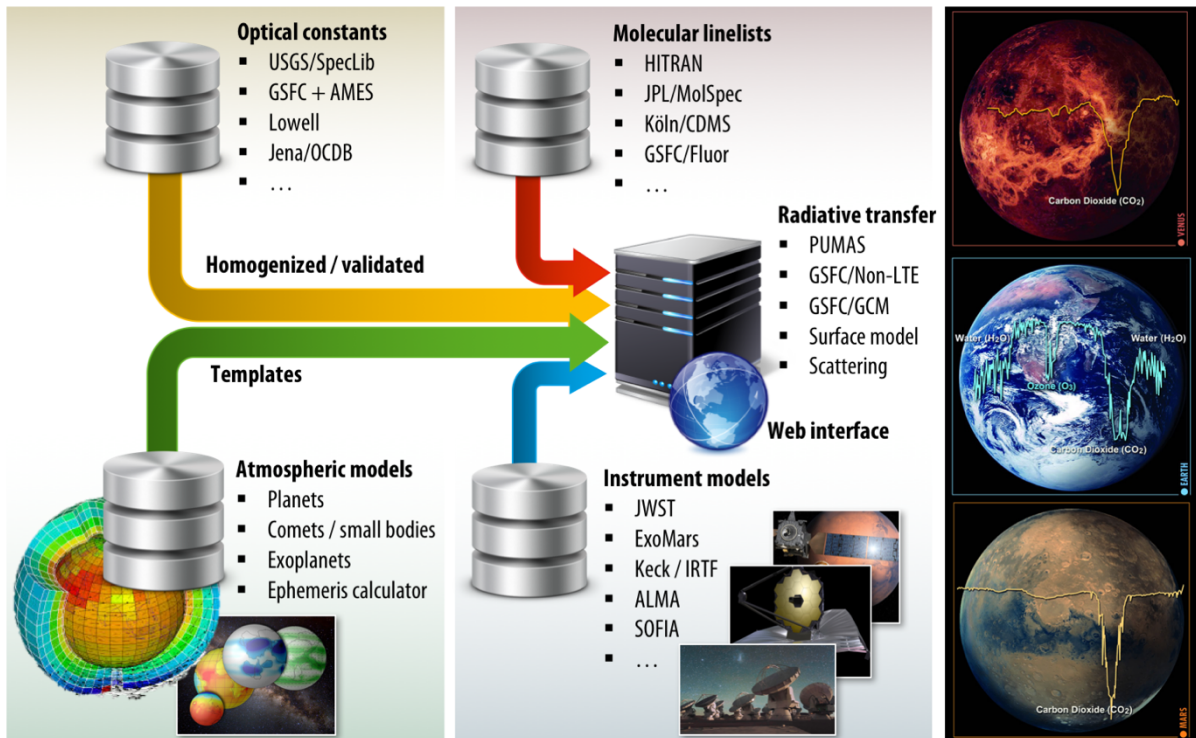


Figure 1: By combining several modern and versatile online radiative transfer models that access state-of-the-art spectroscopic databases, the PSG tool can synthesize a broad range of planetary spectra and regimes, as measured with a broad range of instruments and observatories.

2. Initializing and running PSG

The tool can be operated in several ways: via a web interface (<https://psg.gsfc.nasa.gov>, see Figure 2), via a flexible application program interface (API, <https://psg.gsfc.nasa.gov/api.php>) accessible from any scripting language (e.g., python, MATLAB, IDL), and it can be also operated by an installable suite via the Docker virtualization system. Parameters of PSG are defined for all modules and elements via a single configuration file, typically called “config”, which is formatted in a type of relaxed XML format.

The easiest way to start a simulation is by loading a configuration template file from the website; these templates are pre-saved configuration text files that are read by the radiative transfer modules when requesting an on-demand calculation. The configuration files are listed in the “Select Template” menu below the three main online sections of PSG (see Figure 2). Once a template configuration file is selected, and after clicking the “Load Template” button, all the parameters for the selected simulation are defined. Several templates targeting the main objects in the solar system are available, and any parameter of the run can be modified by clicking on the “Change” buttons, which will redirect into the three PSG modules, and then “Save settings”. The user can also decide to not change any parameter after exploring the module by clicking “Cancel” or clicking “Reset” on the main page.



Figure 2: Home screen of the PSG interface, where the results of the calculations are plotted, and in which the main parameters of the simulation are summarized.

Essentially, the full purpose of the online web-interface GUI is to read/edit/save the configuration file before calling the PSG server requesting for a simulation. This file can also be downloaded and saved in your own computer for future operations by clicking the “Download configuration” button. In the same list-menu that reports the template files, it is possible to select “Upload config-file” option, which allows the user to upload pre-defined/saved files.

Once the configuration of the parameters is ready, one can start the calculation by clicking on “Generate Spectra”. This will first verify the geometric parameters and pre-calculate geometric and atmospheric parameters. These will be fed together with the input configuration file to the radiative transfer modules for analysis. The output of these modules (and most databases accessed by PSG) are easy-to-read text files formatted as multi-column tables with a header defined by the # symbol. These output tables are read by the graphics module to produce the spectral plots.

When accessing the public PSG server (web and API), every user is identified by a cookie and their IP address, and has a unique configuration file associated to this ID. A limit of 100 API calls per day to the public server is defined for every ID, yet the user may obtain a higher limit (up to 100,000 simulations / day) by requesting a personal key (please send us an email). One can forgo any restrictions by installing PSG in any personal machine or computational cluster (e.g., AWS) via the free Docker architecture (see chapter 10).

3. Modules and outputs of the PSG architecture

The generation of spectra is done by following a specific sequence of operations. These are done internally in PSG, in which every module takes a set of input files and produces another set of

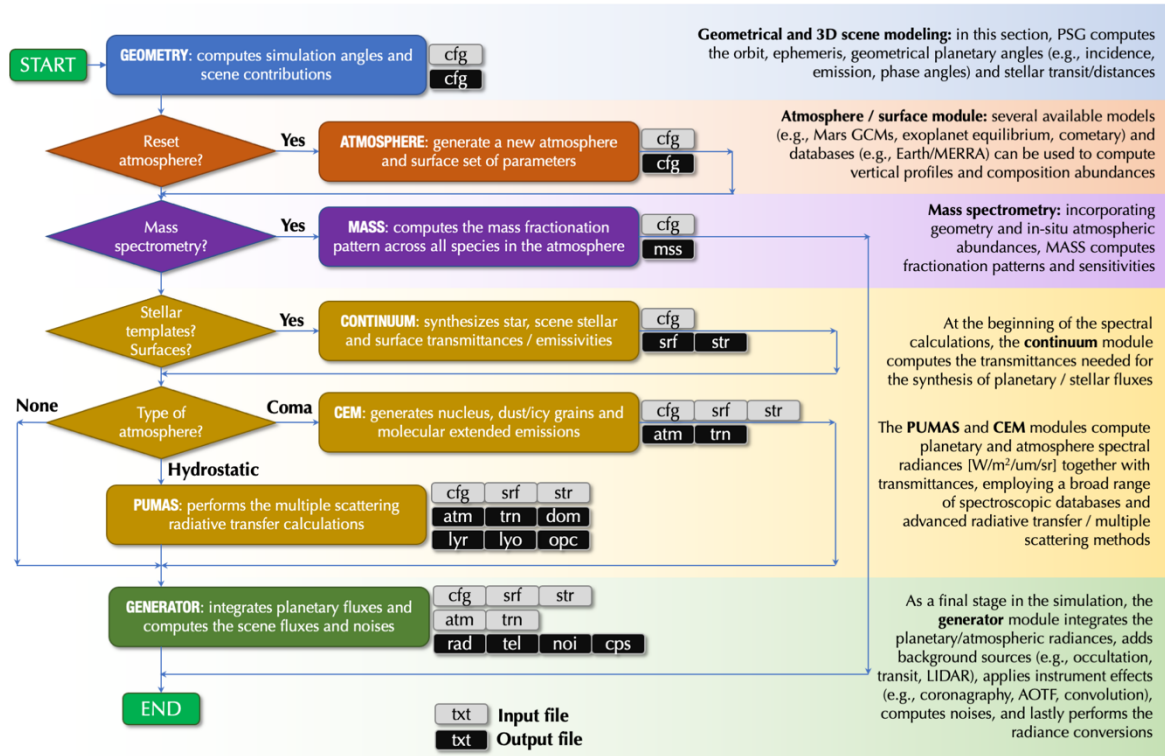


Figure 3: Architecture of the main modules of PSG and their interrelationship. The codes share inputs/outputs by accessing the corresponding output files/parameters from the preceding modules. All the modules are parameterized by the “config” **cfg** file, and the main output of PSG is captured in the **rad** file.

output files. Understanding this sequence is of relevance when scripting and debugging operational issues. In particular, when interfacing with PSG we may want to only to run a specific module and not all of them, as done by the web/API server. For instance, the geometry section of PSG website only calls the “GEOMETRY” module, and similarly the atmosphere section only operates with the “ATMOSPHERE” module. One can choose which module to operate in the API call by establishing the required output and operational modules of the call.

In Figure 3 the sequence of operations performed by PSG is shown, in which the interplay between the different modules (e.g., GEOMETRY, ATMOSPHERE, MASS, CONTINUUM, CEM, PUMAS, GENERATOR) is presented. The retrieval module (see chapter 9) operates above this diagram, and effectively calls PSG as a “wrapper” to compute forward spectra and to determine Jacobians. Similarly, most PSG apps (e.g., GlobES) operate as “wrappers” to this architecture, so once the user understands the core modules of PSG (Figure 3), it is then possible to understand the full structure of the modules operating in the PSG suite.

The input/output files contents are as following:

cfg This is the configuration file that defines the operations of all the modules. A single line is provided for each parameter, in which the parameter name is defined first in the line and given in



brackets as <KEYWORD>. Following '>', the value is provided for that keyword (parameter), which can be a string, a number, or a set of comma separated values. The keywords and their formats (S# defines a string of length #) are listed at <https://psg.gsfc.nasa.gov/helpapi.php#parameters>. Empty lines and strings not starting in '<' are skipped, while if the keyword is provided many times in the file, the latest entry in the file is taken as the desired value. The user can also upload column-formatted data within the “config” file, by bracketing the data in between the following keywords: <DATA>, which define where the data start and </DATA> which define the end- this input is then transferred to the “dat” file (the input file used only by the retrieval module, see Chapter 9). Binary data (e.g., GCM data for GlobES) can be uploaded by bracketing it in between the <BINARY> and </BINARY> keywords - this input is then transferred to the “bin” file. User-defined spectroscopy (e.g., laboratory measurement) can be also provided with the “config” file by adding a line as <SPEC>name_T#_USER (name is the component name and # is the spectroscopic type of the data <https://psg.gsfc.nasa.gov/helpatm.php#profiles>) and then bracketing with </SPEC> - these inputs are then transferred to individual files for each database, and only accessible to that ID/user.

rad This is the main output of PSG, and it is the spectrum used by the retrieval/apps wrappers. This is a text file with headers defined by the # letter with values provided in a multi-column format, organized in rows for each spectral point. The first column of the data is the wavelength/frequency, the following column is the total radiance, then noise (if asked) and then the columns for each sub-component of the radiation. In these files, the line “# Spectral unit:” defines the unit of the first column, while “# Radiance unit:” defines the unit for all the following columns. The line “# Wave/freq ...” defines the name/type of all the columns. If the simulations include a star in the scene (see chapter 2), a column “Stellar” will appear, and/or in LIDAR mode the column “Laser” will appear. For transit observations, the column “Transit” describes the stellar flux lost due to the planetary transit (probably the mostly used column), while “Total” will incorporate this loss but also add the self-emission thermal emission of the planet (i.e., Total = Transit + planet_self_emission).

mss This is the main output of MASS module, and it is the mass spectrometry simulated spectra at the desired mass range and resolution. The natural intensity of the MASS module is [molecules/cm³], yet the MASS module can convert to any desired units (e.g., [counts/second]) by integrating information about the efficiency of the instrument and the sampling strategy considered.

str A key element in any spectral simulation is the properties of the host star impinging spectrum and that of any stellar spectra within the observational scene. In PSG, the stellar fluxes are computed as a multiplication of an underlying blackbody, with an effective temperature and stellar radius, and a stellar “transmittance” (1.0 is as blackbody). In a simulation, two types of stellar sources should be considered, the star from which the planet revolves around and therefore it is the main source of shortwave radiation arriving to the planet – in our solar system, that would be the Sun. The second is any star within the observational scene, as in a stellar occultation or when observing an exoplanet in which the star is within the field (e.g., coronagraphy, transit, see details at <https://psg.gsfc.nasa.gov/help.php#doppler>). Each source can have different relative velocities and may also have different stellar properties (e.g., type, temperature), and as such different transmittances. The “str” file contains three columns, the first is the simulation wavelength, and the



following are star transmittance (star of the planet host) and then stellar transmittance (if any star is within the field).

srf As discussed in chapter 6, the surface properties, independent of scattering model and geometry, are characterized by the single scattering albedo and emissivity. The user can compute reflected/emitted fluxes at a variety of phases and geometries by choosing a model and by knowing these parameters. The CONTINUUM module of PSG computes these two variables and saves them into the “srf” file as a three columns file (wavelength/frequency single_scattering_albedo emissivity). These parameters are integrated into the cometary (CEM), planetary (PUMAS) and radiative integrator (GENERATOR) to compute planetary/cometary fluxes.

atm This file contains the main outputs of the planetary/cometary modules (e.g., PUMAS, CEM), containing spectral radiances [$\text{W}/\text{m}^2/\mu\text{m}/\text{sr}$], which are used to compute scene fluxes by the radiative integrator (GENERATOR). The radiation reported in the atm file specifically pertains to the planet (i.e., reflected, scattered, thermal emissions), surface, atmosphere and to the dust/icy grains for comets, for the selected geometry and coverage of the field-of-view. The GENERATOR module will add these radiances to any background sources to produce the Total observed radiances as reported in the “rad” file – The values in the “rad” file are also converted from [$\text{W}/\text{m}^2/\mu\text{m}/\text{sr}$] in the “atm” file to any desired output unit.

trn This file contains the planetary transmittances (i.e., exponential of the integral of opacities) at the observational emission angle. For transit simulations, this file reports the combined transit transmittances across all layers in transit and for all atmospheric constituents. The file is formatted as a multi-column table, in which the first column is wavelength/frequency and then the total value for all components, followed by columns for each sub-component. This output is only used by GENERATOR module when computing transit and occultation fluxes.

lyr This file reports the input layer information as ingested by the PUMAS module, together with the computed Curtis-Godson effective layer parameters and the corresponding column densities. The header of the file reports additional information pertaining to the radiative transfer simulations, such as the inclusion of CIAs / UV cross sections and the collisional regime assumptions. The upper section of the file reports the parameters at the specific layer points as defined by the <ATMOSPHERE-LAYER-#> keywords in the config file. These boundary values are then taken by the PUMAS module and integrated across the curved path of radiation to define the effective Curtis-Godson P/T/abundances within the layer. Those appear at the bottom part of the file.

lyo When selecting the “Layering” mode in the processes section of the atmosphere (field ATMOSPHERE-CONTINUUM), PUMAS will output the total opacities at each layer as employed by the radiative transfer module. The values are provided as a 2D table (wavelength vs layers) in units of [τ/km]. The per ‘km’ unit refers to the fact that the opacity values are divided by the height of the layer. The altitude of the layers (including TOA) are provided after the “# Wave/freq” keyword in the header.



opc When operating in the “Cell” mode (defined in the geometry section and via OBJECT keyword), the PUMAS module will provide the cell opacities in this file. This mode of operation and output is of relevance when operating PSG to compute opacities at specific P/T conditions.

dom When running full sky 3D simulations, this file contains the spectral radiances at the different azimuth and zenith angles. The output is formatted as a 2D table of $(A \times Z) + 1$ columns: A is the number of azimuth angles, defined in the header by the keyword “# Azimuths”, while Z is the number of zenith angles, defined by the keyword “# Zeniths”. The output radiances are always reported in units of spectral radiance $[W/m^2/\mu m/sr]$.

tel PSG can apply telluric effects (e.g., background atmospheric emission and extinction) to ground-based astronomical simulations by operating with a database of pre-computed telluric transmittances. The database includes telluric transmittances for 5 altitudes and 4 columns of water for each case. The altitudes include that of Maunakea/Hawaii (4200 m), Paranal/Chile (2600 m), SOFIA (14,000 m) and balloon observatories (35,000 m), while the water vapor column was established by scaling the tropical water profile by a factor of 0.1, 0.3 and 0.7 and 1. The “tel” file reports in a 2-column file the extracted telluric transmittances for the selected case.

noi The noise module of GENERATOR can compute sensitivity values for a broad range of instruments and observatories. This file reports the total noise (as reported in the 3rd column of the rad file) and the individual components that led to this noise, which is particularly relevant when exploring the limiting sensitivity factors affecting a simulation. The file reports the components in 6 columns: Wave/freq Total Source Detector Telescope Background.

cps When computing high-contrast coronagraphy simulations, a valuable metric when exploring sensitivities is the count rates, or counts being measured by the detector for the different noise components. These values are collected in the “noi” output, and they can be used to compute and compare sensitivities with other numerical methods.

4. Main sections of the web interface

The configuration file and web interface can be organized into four main blocks or sub-sections. First, we have the definition of the object and the geometry, parameterized via the OBJECT and GEOMETRY fields in the configuration file, and accessed on the website via the “Change Object” button (first block). Second, there are the parameters referring to the atmosphere and surface of the object, defined in the config via the ATMOPHERE and SURFACE fields, and accessed on the website via the “Change Composition” button (second block). Thirdly comes the parameters referring to the instrument/observatory (e.g., wavelength range, resolution), defined via the GENERATOR fields and accessed on the website via the “Change Instrument” button (third block). Lastly, accessed on top of the website via the “Retrievals” button, we have the retrieval interface (fourth block), with its parameters saved on the config via the RETRIEVAL keywords.

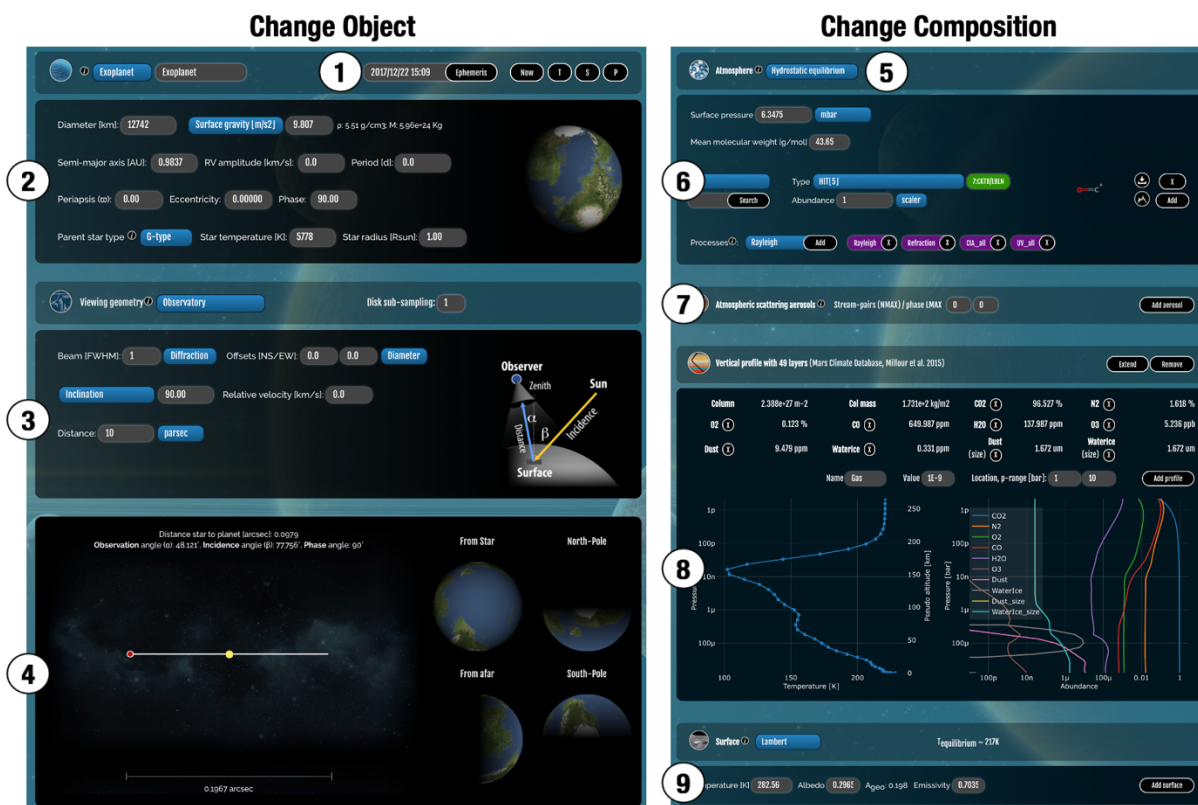


Figure 4: Website graphical user interface (GUI) for the object/geometry and atmosphere/surface sections. The different numbers indicate the main blocks within these interface windows.

The number of parameters (<https://psg.gsfc.nasa.gov/helpapi.php#parameters>) can in principle appear daunting, but PSG will select defaults appropriate for each case, ensuring a simplified parameter entry. Also, there are only 4 interfaces to learn, and once these are understood, the full capabilities of the tool can be accessed and controlled.

Figure 4 shows the interfaces of the “Change Object” and “Change Composition”, in which the main components are:

1. In the upper bar of the geometry section, one can select the type of object (e.g., planet, moon, exoplanet, comet, asteroid, cell), and perform several ephemeris operations. By entering a date (format YYYY/MM/DD HH:MM), and clicking “Ephemeris”, PSG will search the object among its database of solar system objects and exoplanets (extracted from the NASA exoplanet archive every 48 hours) and perform a realistic orbital calculation for that date and viewing geometry. If the solar system object is not in the PSG database, PSG will perform an API request to the JPL/Horizons system. The “Now” button will calculate ephemeris for the current date/time. The next 3 buttons are object dependent. If an exoplanet has been selected, the letters T, S and P will appear, which permit to search for the next primary transit (T), secondary transit (S) and periastron (P). The date will change to the next date when this event occurs, and the planet will be set to this particular orbital phase. If a solar system object has been selected, the symbols < and > will appear, which permit to run ephemeris -1 day (<) and +1 day (>).



2. The upper fields of the geometry section define the properties of the planet (e.g., diameter, gravity) and its relationship to its host star. This includes parameters of the planetary orbit (e.g., periapsis, eccentricity) and importantly the phase/season along this orbit. For exoplanets, the phase of an orbit defines the planet/star location relative to the observer, in which 180 is the planet is in front of the star (primary transit), 0 is secondary eclipse, and 90/270 the planet is at quadrature. For solar system objects, season identifies the angle with respect to equinox, relevant when defining the season/weather on the planet. If performing a theoretical simulation of a solar system object from afar (>0.1 parsec), then season relates to the orbital phase as with exoplanets.
3. The lower fields of the geometry section define how this planetary system is being observed, and specifically the location of the observer with respect to the planet. As discussed in chapter 2, the simulations could be done assuming the observer is within/nearby the planet (e.g., looking from the surface, occultation inside its atmosphere, mass spectrometry, orbital nadir), looking from afar but within the same planetary system (e.g., observatory looking at solar system objects), or looking at the whole planet and star from afar (>0.1 parsec), in which the host star is also included in the simulation (e.g., transit, coronagraphy). In particular, if one wants to calculate transit/coronagraphy simulations, the distance has to be >0.1 parsec in order to properly capture the proper geometry conditions.
4. The bottom panel of the geometry section shows 3D simulations as computed by the GEOMETRY module. The full disk simulations include a realistic treatment of the surface scattering properties (see chapter 6) and showcase the orbital configuration as computed with the orbital model of PSG. PSG also includes a full and interactive 3D model of the solar system, accessible for solar system objects by clicking on the “Show orbit” button.
5. In the upper bar from the atmosphere section, the user can select from several precompiled atmosphere/surface templates and atmospheric models (e.g., equilibrium models, Mars GCMs, Earth NASA/MERRA). In this section, one can also upload user defined spectroscopic databases, such as aerosol scattering models, molecular cross-sections, and surface single scattering albedos. These databases are only accessible to the current user.
6. This is the main section of the atmosphere section. It defines where the surface pressure level (or cometary activity) and the molecules to be considered for the simulation (and for the retrieval). Only the molecules listed here will be considered in the simulation/retrieval, independently of the profiles shown/reported in block 8. The connection between the profiles in section 8 and molecules listed in this section, is done via the “scaler” abundance unit. A scaler of 1 indicates that the values as in the profile shown in 8 will be used, while any other unit (e.g., ppm, ppb) indicates a constant mixing ratio (w.r.t., to the local wet density) with altitude. If a scaler is selected for a constituent for which no profile exists in block 8, PSG will consider a scaler relative to an abundance of 100%. The surface pressure indicates where the atmosphere starts, again independently of the profile pressures shown in block 8. The surface pressure is where the surface starts, and where the diameter and gravity values provided in block 2 relate to in the vertical structure of the planet. Continuum processes and special keywords can be activated by adding them via the “Processes” dropdown list.



7. This block pertains to scattering aerosols and scattering parameters (LMAX/NMAX, see chapter 5). Similarly to block 6, only aerosols listed here will be considered in the simulation, while the scaler unit is the method to relate and scale to the profiles presented in block 8. If NMAX=0, the fast single scattering approximation is employed (see chapter 4), which is only recommended for weakly scattering media.
8. The vertical profile of the atmosphere as provided by the ATMOSPHERE-LAYER keywords is reported in this block. The total column density is the integral of the densities across all the reported layers, while the column mass is that number multiplied by the molar mass. The reported abundances are the average column abundances, so each column density is that reported abundance times the total column density. In this block, the user can also add arbitrary layers of gases/aerosols via the “Add profile” button. The “Extend” button will extend the vertical profiles up to 1 pbar by copying the temperature and mixing ratios of the last layer, which may be useful when exploring weak upper atmosphere signatures, and when performing transit or Solar occultation simulations. The reported profiles are not included in the simulation by default, they are only included when added in blocks 6 and 7.
9. The bottom block permits to provide surface properties (SURFACE keywords) and to alter the composition (areal mixing) by selecting reflectance and optical constants parameters. The user can also choose the method in which the surface is being modelled with (e.g., Hapke).

The main components of the “Change Instrument” and “Retrieval” website graphical user interfaces as presented in Figure 5 are:

1. The upper bar of the instrument section allows to select from a selection of pre-defined instrument templates. These templates are simply text files with the GENERATOR keywords filled to match the properties of these instrument/observatories. The user is free to modify these and to create their own simulation / instrument setup. These instrument models are approximations to the real instruments - they do not account neither for overheads nor subtleties of the instruments/detectors - and the user is advised to work with the official modeling tools of these instruments if available.
2. The main parameters of the simulation are provided in these fields, which include wavelength range, spectral resolution and intensity unit. The resolution defined here refers to the sampling resolution of the output grid. If the “Gaussian” kernel is selected, the sampling resolution is defined to be 10 times the actual resolution, and the spectra is convolved with a Gaussian having a Full-Half-Width-Maximum (FWHM) that of the selected resolution. PSG will internally compute the spectra at the needed spectral resolution to ensure spectral accuracy (see chapter 4), and then bin down to the desired output sampling/convolution resolution. The flag “Include molecular signatures” enable/disable the PUMAS/CEM modules, while a disabled flag “Include continuum fluxes” removes a synthetic model spectrum from the simulated spectra. The flag “Integrate stellar templates” enables/disables the use of stellar templates in the computation of stellar spectra – a disabled flag implies to simply use black-bodies for the stars. If modeling astronomical ground-based observations, one can enable telluric effects with the “Terrestrial transmittance” flags. The flag “Apply” implies that the noise will include telluric transmittances and telluric background sources,

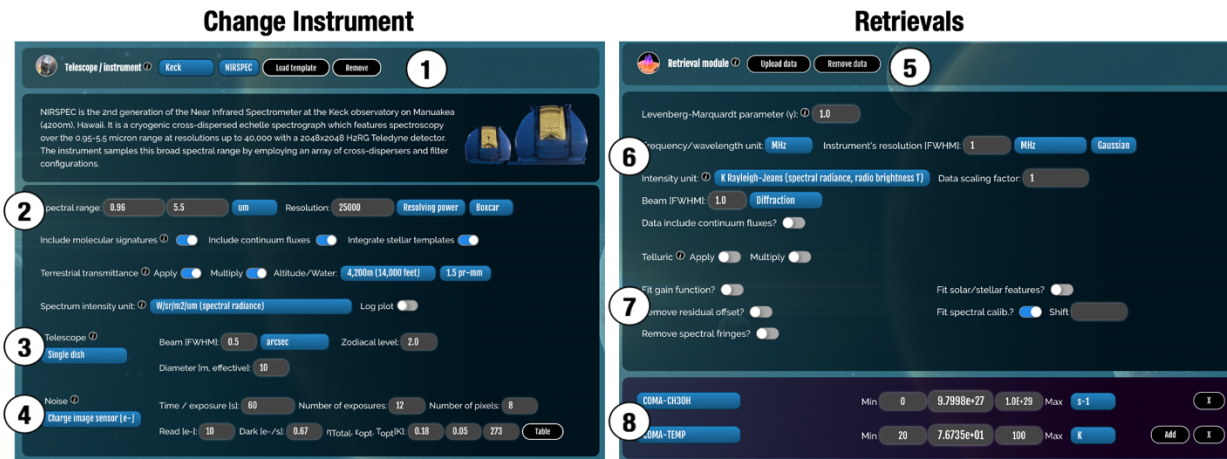


Figure 5: Website graphical user interface (GUI) for the instrument and retrieval sections. The different numbers indicate the main blocks within these interface windows.

but the planetary spectra will not be affected. The flag “**Multiply**” will multiply the simulated spectra by telluric transmittances. As discussed before in the description of the “atm” and “rad” files, the planetary modules compute spectra in spectral radiance [$\text{W/m}^2/\mu\text{m}/\text{sr}$], and the GENERATOR module will convert the fluxes to any unit as selected in this block.

3. Spectra can be simulated for a broad range of instrument types, in which a simple and standard simulation without any complex effect would mean “single dish”. The field-of-view (FOV) setting is important for establishing the amount of planetary flux encompassed by the FOV (see chapter 2), and if and how much stellar background sources should be added to the simulation (e.g., transit, coronagraphy). The telescope diameter is only relevant when computing noise (collecting area) or when defining a diffraction limited simulation.
4. PSG includes a realistic noise calculator, and in this section one can enter the detector parameters. Parameters needed for all simulations include integration time per exposure and number of exposures. The number of pixels refer to how many detector pixels of the instrument are encompassed in each simulation spectral pixels (as selected in block 2). In this block, the user may also provide wavelength dependent detector values as tables via the “**Table**” button. More details regarding the noise parameters can be found in chapter 8.
5. In the upper bar of the retrievals window, the user can upload data. The data should be a 2 or 3 columns file, with the first column is wavelength/frequency (in units as defined in block 6), second column is data (in units as defined in block 6), and noise (this is optional and PSG will assume 5% of the signal if this information is missing). By default, PSG assumes that the wavelength points refer to the center of pixel, with a width as defined by the spacing of the points. If the first column is in the format A:B, then PSG will interpret that the pixel spans from A to B in wavelength. Regarding the second column, if the values are in format C/D, PSG will interpret that the reported values refer to ground-based observations, in which D is the effective transmittance for the signal at C, and the value of TOA for this pixel is C/D.



6. In this block, the user enters the units and general parameters for the retrieval (see chapter 9). The resolution refers to the convolved resolution of the data in the “dat” file, while the scaling factor is a numerical scaler to the provided data.
7. PSG can correct for several typical issues affecting spectroscopic data, and with these flags the user can enable these corrections. Enabling more features adds degeneracy to the retrieval, so a mindful selection of parameters is required. These fitted synthetic effects are later reported in the output “dat” file as additional columns.
8. This is the main block of the retrieval section, in which the retrieval parameters are defined. The initial, minimum and maximum values for each parameter as used when determining the initial covariance matrix and the a-priori background values. They also ensure that the fit remains within physical bounds. More information regarding retrieval variables and their parameterization is presented in chapter 9.



Planetary Spectrum Generator
National Aeronautics and Space Administration

Chapter 2: **Geometry and orbital modeling**

**Villanueva and
PSG team**

1. Geometry modeling

Any spectroscopic simulation of planets requires a precise description of the geometry being considered. For that purpose, PSG is integrated with a three-dimensional (3D) geometry calculator which includes any object in the solar system and all confirmed exoplanets. By setting the appropriate observational geometry, PSG can synthesize spectra for practically any observer and target configuration. In the first step, PSG computes the orbit and orientation of the planet relative to the star in the observer's reference frame. Based on the selected viewing geometry and distance to the planet, PSG then switches between three general geometrical regimes (Figure 1), the first one is the “orbital and in-situ”, for simulations nearby the planet (e.g., nadir, occultation, looking up from the surface, in-situ), and in which the simulated field-of-view samples a finite patch on the planet / sky. On such cases, the observational incidence and emission angles are unique and finite. The other two geometrical regimes are “observatory view” and they are distinguished by the observatory being within 0.1 parsec or beyond 0.1 parsec to the planet. In the first case, PSG does not include the host-star, and the FOV can encompass a broad range of emission and incidence angles on the planet, or even the whole planet. In the second case, at larger distances (>0.1 parsec), PSG considers the location and contribution of the host-star with respect to the planet in the FOV, with the possibility of transit or inclusion of the stellar fluxes in the scene. Transit, eclipse and coronagraphy simulations are therefore only possible when defining distances greater than 0.1 parsec.

2. Orbital modeling of solar system objects

The GEOMETRY module in PSG is the one responsible for computing ephemeris, orbital parameters, and establishing the geometrical angles needed for the radiative transfer simulation. For the main bodies in the solar system (e.g., Mars, Neptune, Europa, etc.), PSG relies on pre-computed ephemeris tables from 1960 to 2050 calculated with the JPL/Horizons ephemerides system (<https://ssd.jpl.nasa.gov/horizons.cgi>) at a cadence of 1 hour, and later interpolated to the observational time, establishing the geometrical location and orientation of the object with respect to the observer. These tables tabulate heliocentric distance, heliocentric velocity, geocentric distance, geocentric velocity, sub-solar latitude, sub-solar longitude, sub-observer latitude and sub-observer longitude. For small bodies (e.g., comets, asteroids) and planetary ephemerides of orbiters, PSG dynamically extracts orbital parameters from the JPL-Horizons ephemerides system by connecting via their API. For small bodies with no sub-solar / sub-observer latitudes and longitudes, PSG defines them based on the ecliptic angles.

A key climatological parameter is the solar longitude, or position of the object across its orbital path (true anomaly) with respect to the northern hemisphere spring equinox (time when the planet's equatorial plane is equal to the orbital plane, $L_s=0$). $L_s=90$ corresponds to northern summer solstice, $L_s=180$ marks the northern autumn equinox and $L_s=270$ indicates northern winter solstice. This parameter is particularly relevant when querying information from general-circulation-models (GCM) or climatological databases of planets, since it is a fundamental factor in describing the structure and dynamics of the atmosphere. From the previously described ephemerides tables, which also include the true anomaly quantity, we determined the $L_s=0$ for each object and used this information to establish the seasonal state and climatology of the planet.

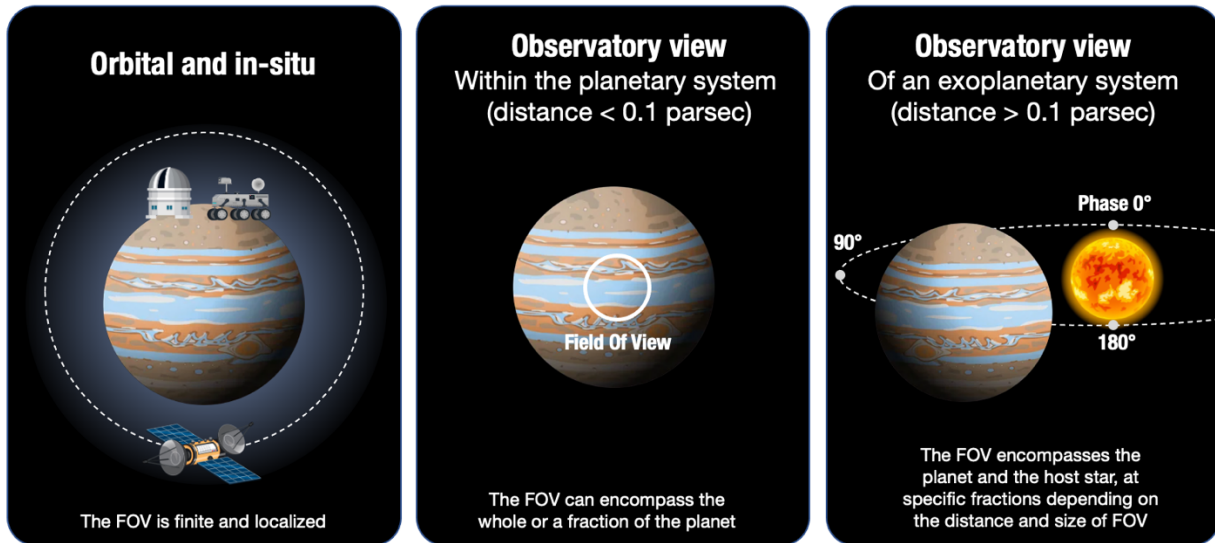


Figure 1: Based on the selected viewing geometry and distance to the planet, PSG switches between three general geometrical regimes: (1) all non-observatory geometries (e.g., nadir, occultation, looking up from the surface, in-situ) are considered to be local to the planet, (2) observatory geometries within 0.1 parsec do not include the host-star, and (3) observatory geometries including host-star are for >0.1 parsec simulations. For exoplanets (or solar system objects simulated beyond 0.1 parsec), the “season” defines the orbital phase, in which 180° is in front of the host-star, 0° behind the star, and 90/270° in quadrature.

When defining the reference point (i.e., location of the observer), PSG typically assumes an Earth-centered position, yet detailed spacecraft information has been integrated into PSG for many orbiters (e.g., MRO, Mars Express, ExoMars/Trace Gas Orbiter, MAVEN, Mars Odyssey, Cassini, Juno) and hundreds of points of interest (e.g., Maunakea, Paranal, Chajnantor, Arecibo, Viking, MSL/Curiosity, MER landers).

3. Orbital modeling of exoplanets

Transit detection and radial velocity characterization of exoplanet orbits provide constraints on the orbital parameters of planets detected around other stars. This information can be used to construct a three-dimensional view of the system and is used by PSG to predict the time of future primary and secondary transits. The NASA Exoplanet Archive (<https://exoplanetarchive.ipac.caltech.edu>) is an excellent repository of the constantly growing database of exoplanet orbital parameters. For exoplanets, PSG does not employ ephemerides tables, but computes the orbital integration of the Keplerian orbit using parameters obtained from the NASA Exoplanet Archive (via their API). This ensures that PSG uses the latest and most accurate orbital parameters, and that newly discovered exoplanets can be properly handled by PSG. Unfortunately, Kepler’s equation that relates the true anomaly (T, position on the elliptical orbital path) and the mean anomaly (M, proportional to time) does not have a closed-form solution (i.e., transcendental equation), and the orbital calculation requires an iterative solver.

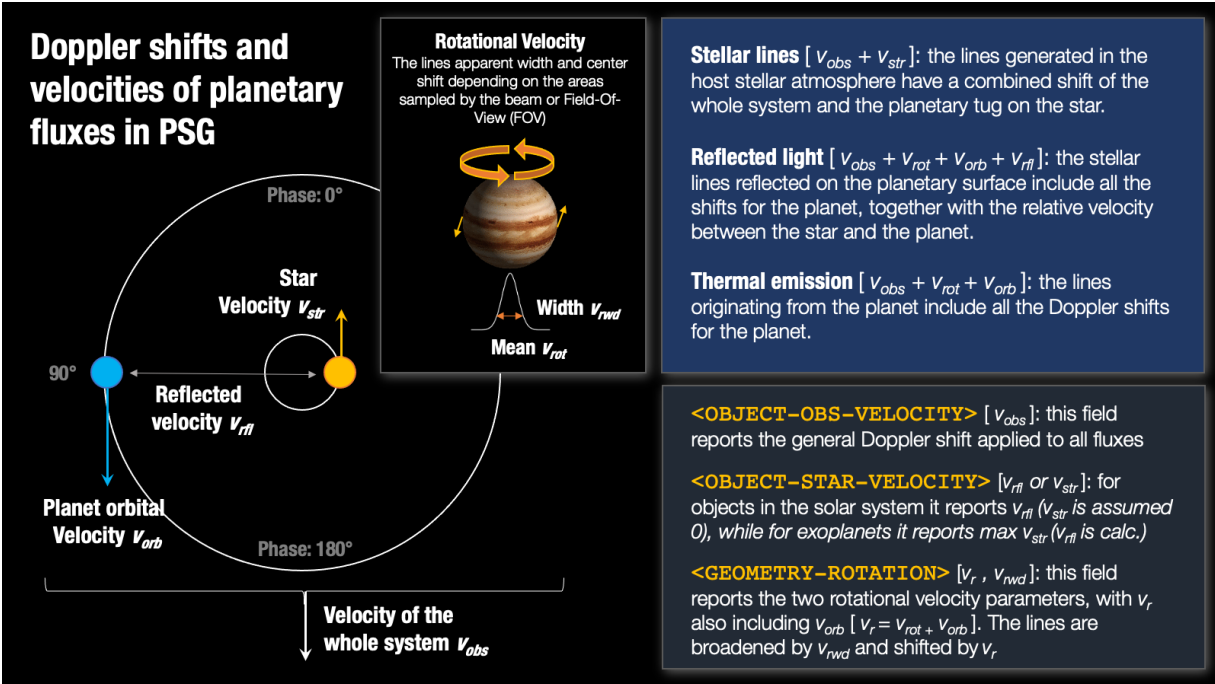


Figure 2: The motion of the planets across their orbit introduces spectroscopic shifts on the planetary and stellar fluxes. This motion also perturbs or "tugs" the host-star, introducing a Doppler shift on the stellar signatures. In PSG, all these effects are taken into account when synthesizing spectra, and are described via three fields: OBJECT-OBS-VELOCITY, OBJECT-STAR-VELOCITY and GEOMETRY-ROTATION. This figure describes how these three fields (calculated by PSG's Geometry module) encode the Doppler information of the motions for the whole system.

PSG employs the iterative Newton–Raphson algorithm to determine the true anomaly (T), constrained to an eccentric anomaly (E) precision of $1e-6$ radians and to a maximum of 30 iterations. This computation employs the longitude of periapsis (w), orbital eccentricity (e) and time of transit (TT) or time of periastron (TP). Even for highly eccentric orbits, such a method is sufficient to accurately determine the location of the exoplanet along its orbit, and this together with knowledge of the orbital inclination, permits PSG to construct an accurate three-dimensional view of the system (within the known certainty of these variables). Determining the actual sub-solar and sub-observer latitudes/longitudes requires knowledge of the rotational period and obliquity of the planet. Such parameters are rarely known for exoplanets, so when computing exoplanet ephemerides PSG assumes that the planets are tidally locked with no obliquity and that the sub-solar latitudes/longitudes are set at the center of the planet. The phase identifies the true anomaly relative to that one of the secondary transit (with a phase of 180 corresponding to the primary transit). Arbitrary or user-defined sub-solar and sub-observer values can be edited manually in the configuration file, or via an API request.

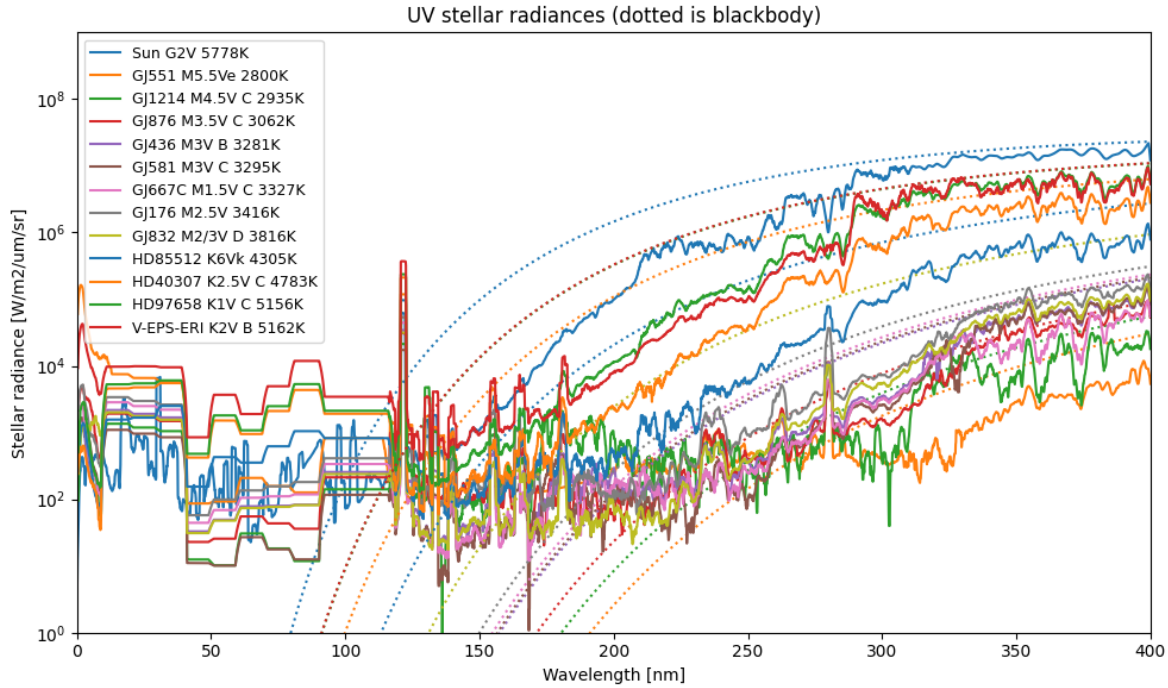


Figure 3: PSG allows to integrate a broad range of stellar templates, with the UV templates shown in this figure. The UV templates ($<0.4 \mu\text{m}$) are based on the MUSCLES Treasury Survey (France et al., 2016), with the UV solar template derived from the LISIRD tool (LASP). The templates at longer wavelengths (i.e., $0.4\text{--}300 \mu\text{m}$, optical, IR and radio) are based on the Kurucz spectral templates, which is complemented with the SOLAR-HRS and ACE solar spectra ($0.4\text{--}14 \mu\text{m}$) for the Sun and G-type stars.

4. Orbital and spectroscopic velocities

When performing high-resolution spectroscopic simulations, a detailed and accurate description of the different velocities is of great importance. In PSG, these parameters are specifically captured via three fields: OBJECT-OBS-VELOCITY, OBJECT-STAR-VELOCITY and GEOMETRY-ROTATION. Each sub-component of the sources sampled by the field-of-view (FOV) will have a particular Doppler shift associated to the object's rotation and orbital parameters. As summarized in Figure 2, the stellar fluxes will have a Doppler shift that integrates the full system velocity and that of the star as being affected by the planet. This "tug" of the star by the orbiting planets is now of the prime methods used to characterize the properties of exoplanets.

The integration of all these Doppler effects is particularly relevant when employing the cross-correlation method in exoplanetary research. This method compares residual planetary spectra at different phases with a synthetic set of templates shifted following the orbital motion of the planet (and all the associated Doppler shifts). This is the prime method to characterize exoplanets using ground-based observatories, since telluric signatures are static spectroscopically, yet the planetary signatures shift by km/s across the planetary orbit. In PSG as shown in Figure 2, the planetary and stellar velocities are computed based on the orbital phase and orbital parameters.

5. Types of stellar hosts

PSG operates with a wide variety of realistic solar and stellar models. For the Sun and G-type stars, PSG utilizes the SOLAR-HRS spectrum (Meftah et al., 2023) in the 0.4-3.6 μm spectral region, the LISIRD UV irradiance spectrum shorter than 0.4 μm , the ACE solar spectrum (Hase et al., 2009) in the 3.6-14 μm infrared region, and the (Kurucz, 2009) Sun template beyond 14 μm .

For other stellar types, PSG utilizes the Kurucz templates, which are complemented at short wavelengths (<0.4 μm ; X-ray, EUV, FUV) with the MUSCLES Treasury Survey (France et al., 2016). PSG picks the template based on the stellar type and temperature, and all fluxes are scaled to the actual effective stellar temperature of the star. The stellar information is used to compute reflected stellar/solar fluxes, and also to compute the total observable exoplanet fluxes, when the (exo)planet and star are within the field-of-view (FOV).

The Kurucz template for the A-type star is based on the Vega model, the K-type is based on the HD189733 model, and the M-type model is based on the M5-3170 model. In the UV, the stellar templates include: Sun (G2V, 5778K), HD85512 (K6Vk, 4305K), HD40307 (K2.5V, 4783K), HD97658 (K1V C, 5156K), V-EPS-ERI (K2V B, 5162K), GJ551 (M5.5V, 2800K), GJ1214 (M4.5V, 2935K), GJ876 (M3.5V, 3062K), GJ436 (M3V B, 3281K), GJ581 (M3V C, 3295K), GJ667C (M1.5V, 3327K), GJ176 (M2.5V, 3416K), GJ832 (M2/3V, 3816K). The fluxes as shown in Figure 3 are in units of spectral radiance in $[\text{W}/\text{m}^2/\mu\text{m}/\text{sr}]$, and in order to compute the actual spectral irradiance $[\text{W}/\text{m}^2/\mu\text{m}]$ received by the planet one needs to multiply by the solid angle encompassed by star as seen from the planet ($\Omega = 6.807\text{e-}5 \cdot (\text{Rstar}/\text{Dstar})^2 [\text{sr}]$), where Rstar is the star size with respect to our Sun [1.0 for Sun], and Dstar is the distance to the star in AU [1.0 for Earth].

6. Definition of the modeling geometries: angles and sub-sampling

The definition of the direction of incidence and emission plays an important role in the calculation of the radiant intensities. As summarized in the equations of chapters 4 to 6, all terms include a direction quantifier (e.g., μ , ϕ), which can be challenging to establish when the observed scene includes many incidence / emission angles, as when we observe a planet from afar. In PSG, the angles are computed by the geometry module, which are then fed to the radiative transfer module. There are several possible geometries (Figure 4), which can be grouped as “Looking up”, “Limb or Stellar/solar Occultation”, “Nadir”, “Observatory”.

6.1 Looking up / Looking up to the Sun / Looking to an object / Dome view

This is the geometry configuration that describes when the observer is located at a specific altitude from the surface, looking up in the sky. The observational zenith angle μ and the solar azimuth angle $\phi - \phi_0$ are user inputs. From here on we will define ϕ to be the solar zenith angle, and therefore ϕ_0 is set to 0. The incidence solar zenith angle μ_0 is calculated from the observer’s longitude (λ) and latitude (φ) as:

$$\mu_0 = \sin \varphi \sin \varphi_0 + \cos \varphi \cos \varphi_0 \cos(\lambda - \lambda_0) \quad (1)$$

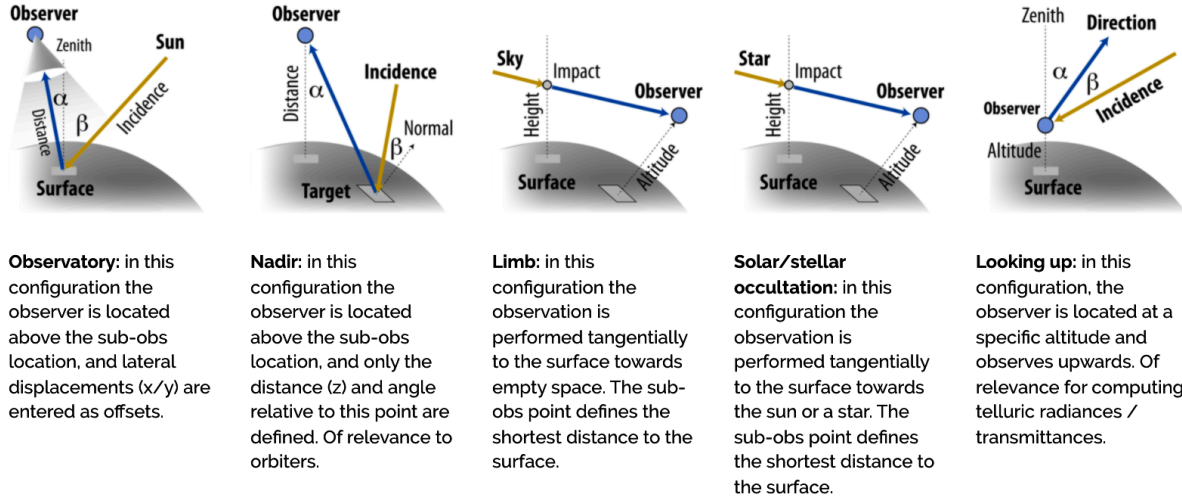


Figure 4: PSG allows for several observational geometries, in which the geometry module computes the zenith, azimuth and phase angles to be employed by the radiative transfer module. α is the observer's zenith angle ($\mu = \cos \alpha$), while β is the incidence solar zenith angle ($\mu_0 = \cos \beta$).

where λ_0 and ϕ_0 are the sub-solar longitude and latitude respectively. On a similar form, the cosine of the phase angle (θ) is calculated as:

$$\cos \theta = \mu \mu_0 + \sin(\cos^{-1} \mu) \sin(\cos^{-1} \mu_0) \cos \phi \quad (2)$$

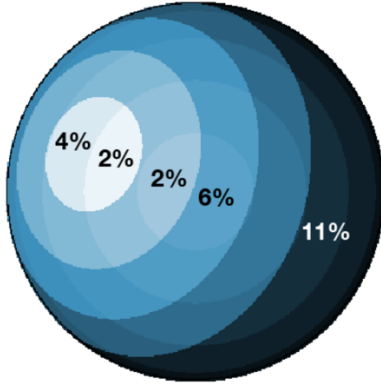
In the “Looking to the Sun” mode the angles are further set to be $\mu_0 = \mu$, $\phi = 0$, $\theta = 0$, and the Sun is the background source, while in “Looking up to an Object” the background source is a point source (a star) of a user defined brightness and temperature / spectral type. In these geometries there is only one set of incidence and emission angles and the path of radiation is computed from TOA to the altitude of the observer. The “Dome” mode is a 360° 3D view of the sky and it is an adaption of the looking up geometry, in which the diffuse radiation field is solved following the discrete ordinates method and intensities are computed at $(2N+1)$ azimuths and $(2N+1)$ zenith angles. If $N=10$, then 441 intensities are computed across the whole sky as: ϕ from 0 to 360° with $\Delta\phi=18^\circ$ and zenith angles α from 0 to 90° with a spacing of 4.5°.

6.2 Limb / Solar occultation / Stellar occultation

These are observation geometries in which the observer is located at a specific altitude in the atmosphere and is observing towards a specific impact height (lowest altitude of the radiation path) of the atmosphere. The possible background source variables ingested by PSG are: **space** for selecting “limb”, **Sun** for “solar occultation” and a **star** of an user defined brightness and temperature / spectral type for “stellar occultation”. By definition, the cosine of the observing zenith angle is $\mu=0$ at the impact height. For limb and stellar occultation modes, μ_0 at the surface is computed following equation 2 (note that the latitude and longitude values entered in PSG refer to those of the impact height, not to the observer), while for the solar occultation configuration, the cosine of the incidence

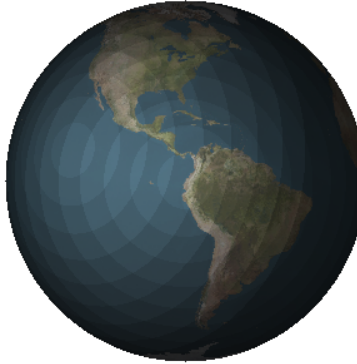
Sub-sampling at phase 40

Sub-sampling N=5
22 distinct regions



Fine sampling at phase 40

Sub-sampling N=10
74 distinct regions



Thermal and phase 0

Sub-sampling N=10
10 distinct regions

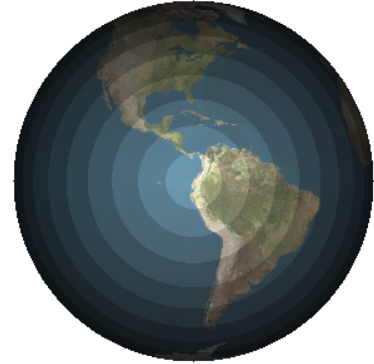


Figure 5: In observatory mode, the sampled region may encompass a broad range of incidence and emission angles, and in PSG a sampling algorithm determines the number of distinct regions and their weights **[Left]**. The sub-sampling N defines how fine to sample the μ_0 and μ terms. A sampling of N=10, indicates $\Delta\mu_0=1/10=0.1$ and $\Delta\mu=0.1$, which leads to a high number of 74 distinct regions. **[Right]** At phase 0 or at thermal wavelengths (where the solar fluxes are negligible), the sampling is solely organized by μ .

angle at the impact height is set to $\mu_0=\mu=0$. The path of radiation travels from TOA to the impact height to the observer.

6.3 Nadir

In this configuration, the observer is at a user-defined altitude looking down to a specific latitude and longitude on the planet. Similarly, to the previously described observing modes, in this configuration there is only one set of incidence and emission angles and those are relative to the observed point on the surface.

6.4 Observatory

In many cases, the observed planetary region by the field-of-view encompasses a broad range of incidence and emission angles, and a single set of angles does not simply fully capture the radiative transfer processes. In PSG, the geometry module will divide the planetary disk into 140×140 regions (19600) regions, each with its own μ_0^i and μ^i and will then compute an “average” incidence and emission angle across the FOV as:

$$\mu_0 = \frac{1}{n} \sum_{i=1}^n \mu_0^i \quad \mu = \frac{1}{n} \sum_{i=1}^n \mu^i \quad (3)$$



where n is the number of pixels encompassed by the FOV. In the case that the FOV encompasses the whole planetary disk, then μ is $2/3$, which corresponds to an average emission angle of 48 degrees. This algorithm will ensure that for a Lambertian surface, the resulting average μ_0 always correspond to the Lambert phase integral (see section 9 of chapter 6). This approach permits to run a single radiative transfer simulation with “average” incidence and emission angles and obtain reasonable results. In cases with strong anisotropic scattering and/or complex absorption processes, such “average” approach may not be accurate enough to capture the diversity of incidence and emissions, and for those cases we have implemented a sub-sampling algorithm that addresses this issue.

The algorithm divides the disk into “bins” of common incidence and emission angles and quantifies how many n pixels correspond to that specific μ and μ_0 bin. For instance, in the case of $N=10$, the disk is organized in bins of $\Delta\mu_0=1/10=0.1$ and $\Delta\mu=0.1$ (all pixels with μ_0 0 to 0.1 and μ 0 to 0.1 will correspond to bin 1, etc.), which depending on the observational phase will lead to less (or more) number of distinct bins (see Figure 5). At phase 0 or at thermal wavelengths ($\lambda > 10 \mu\text{m}$), only N bins are distinct, yet at more orthogonal phases, the number of bins approaches N^2 . Each distinct bin will have an “average” incidence and emission angle computed following equation (3) and a “weight” determined by the projected area of the bin relative to the whole disk (distinct bins are those having a weight greater than 1%).

The benefit of this algorithm, when compared to the other sampling methods (e.g., Cahoy et al., 2010; Horak and Little, 1965) is that it takes advantage of the symmetry in the incidence and emission angles across the disk, and ensures a high fidelity (at thermal and reflected wavelengths) at a low computational cost (Saxena et al., 2021).

7. Description and modeling of the field-of-view (FOV)

When collecting and modeling fluxes across a planet/scene, the spatial region where one has to perform this “collection” or integration of fluxes is defined by the user provided field-of-view (FOV). The simplest form would be a circle with a diameter defined by its Full-Half-Width-Maximum (FWHM) [rad], and then the area can be calculated as $\Omega \text{ [sr]} = \pi(\text{FWHM}/2)^2$. In reality, the integration region may take many shapes and patterns. For instance, if operating with slit instruments, the FOV is rectangular (slit width x slit extract length) and not circular, or when operating with interferometric data (e.g., ALMA), the FOV is a “Gaussian” ellipsoid with a major and a minor axis. As we deviate from a simple circular FOV, then the orientation of the FOV with respect to the N-S axis of the planet also becomes relevant, and a rotation angle needs to be provided (see Figure 6). Furthermore, let us now consider the case of simulations with a smearing “seeing” effect, then the modelled flux is actually a collection of flux across a broader region, and weighted by a “seeing” kernel.

The field <GENERATOR-BEAM> defines the shape and properties of the FOV in PSG. When a single value is provided, PSG would interpret it as the diameter (FWHM_A) of a simple “circular” beam (see example in Figure 6, first frame). By providing a second value (optional) defined as FWHM_B , PSG will assume to have an irregular FOV with a major and a minor axis.

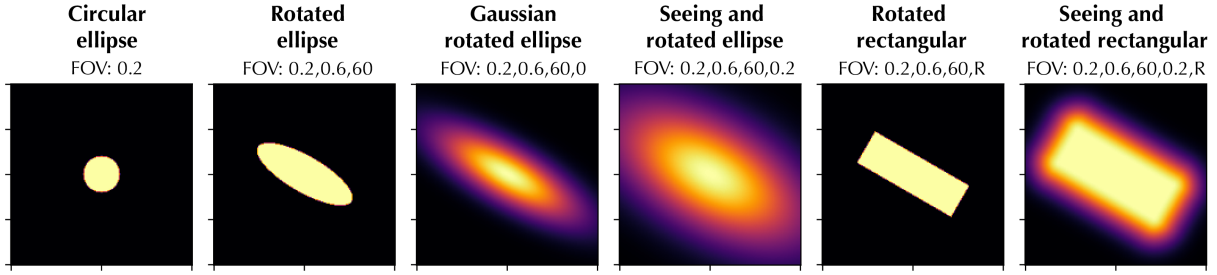


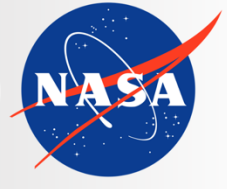
Figure 6: The spatial integration region across the planet/scene can take many shapes and patterns, and in PSG the properties of the field-of-view (FOV) are defined by the keyword GENERATOR-BEAM. Up to five parameters ($FWHM_A$, $FWHM_B$, Rotation, $FWHM_S$, shape) establish the key elements of the response function of the FOV and its orientation with respect to the N-S axis of the planet.

While if a third value (optional) is also provided, PSG will identify this value as the rotational angle [$^\circ$] of the FOV in counter-clockwise direction with respect to the N-S planetary axes (e.g., see Figure 6, second frame). If a fourth number is provided ($FWHM_S$), PSG will switch from a step function to a Gaussian affected kernel with an additional seeing term defined by this value. The transfer function for the FOV would then correspond for an ellipsoid to:

$$\gamma(x, y) = \exp \left(-0.5 \left[\left(\frac{x}{r_A + r_S} \right)^2 + \left(\frac{y}{r_B + r_S} \right)^2 \right] \right) \quad (4)$$

where x and y are the distances from the center of the FOV across the major and minor axis respectively, r_A is sigma across the first axis ($r_A = FWHM_A/2.355$, where $FWHM_A$ is the FWHM across the A-axis and it is the first user provided number), r_B is the sigma across the second axis defined ($r_B = FWHM_B/2.355$), and r_S is the seeing sigma ($r_S = FWHM_S/2.355$). The values x and y are in the rotated FOV frame of reference as defined by the rotational angle of the FOV (see Figure 6, third frame). A keyword “R” at the end of the field will inform PSG that this is a rectangular FOV, not an ellipsoid (see Figure 6, last two frames). For rectangular FOVs, $\gamma=1$ is when x and y are within r_A and r_B axis, and it decays as $\exp(-0.5 \cdot (r/r_S)^2)$ beyond that, where r is the distance from the FOV boundaries.

The area of the field of view is then calculated for an ellipsoid field of view as Ω [sr] = $\pi \cdot FWHM_A \cdot FWHM_B / 4$, and simply as Ω [sr] = $FWHM_A \cdot FWHM_B$ for a rectangular field of view. Information about the weighting function across the FOV as shown in Figure 6 is solely used in the “Observatory” geometry to calculate the effective incidence and emissions (see equation 3) and the effective planetary filling factor.



Planetary Spectrum Generator
National Aeronautics and Space Administration

Chapter 3: **Atmospheres, exospheres and comets**

**Villanueva, Faggi, Fauchez and
PSG team**



1. Types of atmospheres

PSG handles two types of atmospheres: hydrostatic equilibrated atmospheres (typical for planets) and exospheres / expanding comas (i.e., typical of comets and small bodies). Atmospheres are considered in hydrostatic equilibrium when gravity controls their vertical structure and in which the escape velocities are smaller than the kinetic atmospheric velocities. For such planetary atmospheres, gravity, molar mass, pressures, and temperatures define the vertical structure, while for exospheres, where gravity does not play a significant role in controlling the structure, they are defined by the molecular outgassing velocity and photochemical/photodissociation decay.

PSG provides the users with atmospheric templates (vertical profiles of temperature and abundances) available for the main planets of the solar system (e.g., Venus, Earth, Mars, Titan, Neptune, Uranus); and it also permits providing detailed user-defined vertical information of molecular abundances and temperatures. General atmospheric and surface parameters are available for the other bodies. For expanding atmospheres, PSG assumes isotropic outflow, constant expanding velocity and a Haser isotropic 2-steps (i.e., parent and daughter species) photodissociation scheme.

PSG provides access to several atmospheric models (e.g., chemical equilibrium, thermal radiative equilibrium, Mars GCM models, cometary heliocentric models), several databases (e.g., Earth NASA/MERRA2) and numerous templates for defining the atmospheric and surface structure and composition. As mentioned, the user can also provide any arbitrary profile of P/T and of molecular abundances by selecting "**File Template**" in the atmosphere section. The format of this file is a text file with all the entries as in the configuration file for the sections ATMOSPHERE and SURFACE. When providing user-generated profiles, the vertical parameters are provided via the ATMOSPHERE-LAYER keywords. The pressures are provided in [bars], temperatures in [K] and abundances in volume mixing ratio - [molecules / molecules] for gases (e.g., water vapor, methane) and [kg / kg] for hazes (e.g., water ice clouds, methane ice). Particle sizes in [m] are provided by adding the keyword '_size'. The base (molecules or kg) is always wet air (all gases, including water vapor) without hazes. When no vertical profile is provided, the temperature (T) is assumed to be constant across the atmosphere, and the pressure (P) decreases with altitude (z) following the scale-height: $P = P_{\text{surf}} \exp(-zg/RT)$, where g is the gravity (defined in the object section) and R is the gas constant (8.3144598 [J / K / mol]).

It is important to note that only molecules included in the ATMOSPHERE-GAS and ATMOSPHERE-AEROS will be included in the simulation (and/or in the retrieval), independent of the species included in the vertical profiles. Specifically, the vertical profile/structure of the atmosphere is provided by the ATMOSPHERE-LAYER keywords, yet the connection between these profiles to the species listed in the ATMOSPHERE-GAS field is done via the "scaler" abundance unit in the ATMOSPHERE-UNIT keyword (see details in chapter 1 and explore an example config in PSG for further understand this connection). Note: a scaler of 1 indicates that the values as in the profile will be used, while any other unit (e.g., ppm, ppb) indicates a constant mixing ratio with altitude. If a scaler is selected for a constituent for which no profile exists, PSG will consider a scaler relative to an abundance of 100%. The surface pressure indicates where the atmosphere starts,

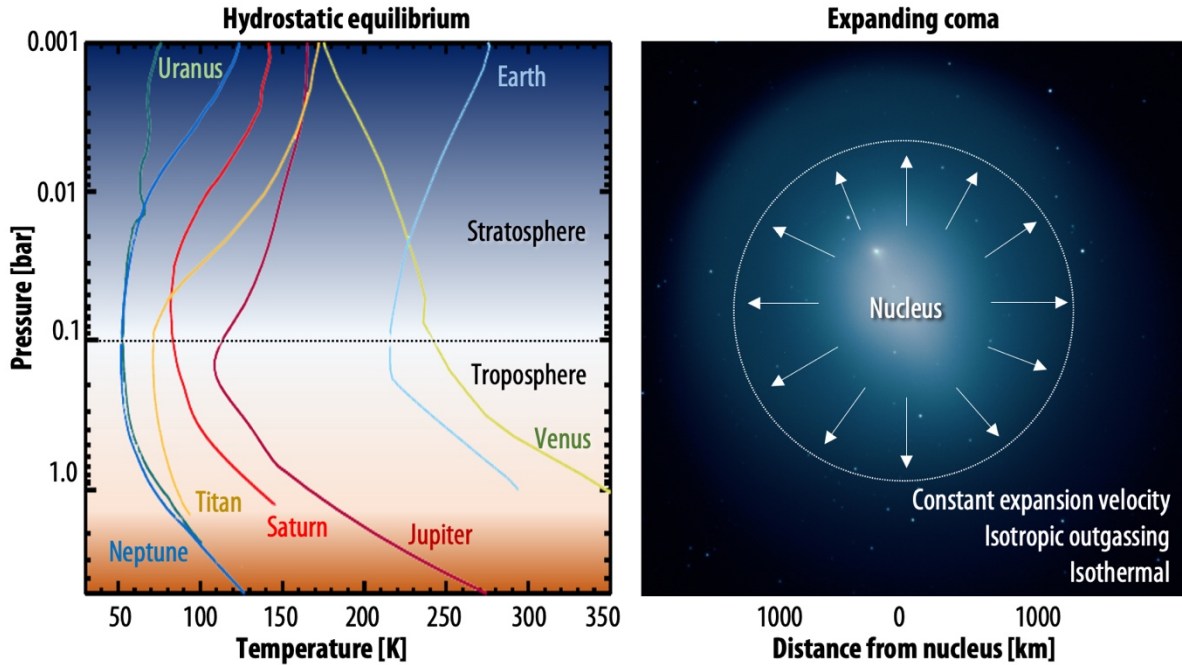


Figure 1: PSG handles two types of atmospheres: (1) the hydrostatic equilibrium atmosphere (typical for planets, profiles adapted from (Robinson and Catling, 2014)) and (2) the expanding coma (i.e., exospheres and typical of comets and small bodies). For the main planets, vertical profiles are available, while the user can also load any arbitrary vertical structure. For expanding atmospheres, PSG assumes isotropic outgassing, a constant temperature across the coma, and an outgassing velocity established by the heliocentric distance.

independently of the provided profile pressures, while the provided planetary diameter and gravity also refer to this pressure/surface point.

2. Vertical structure of an atmosphere in hydrostatic equilibrium

When considering the ideal gas law, the volume of a gas parcel is dependent on its pressure and temperature. If we consider having several parcels of gas on top of each other, all bounded to a planetary surface by the planet's gravity, the structure and "separation" of these parcels will be defined as a balance between the gravity force (trying to squeeze the parcels) and the intrinsic volumes of the parcels (defined by the parcel P/T). The planetary gravity effect on the parcels will depend on the mass of each parcel, with the "local" gravity decaying with distance as $g = g_{\text{surf}} ((h+R_{\text{surf}})/R_{\text{surf}})^2$, in which h is the height of the parcel, R_{surf} is the radius of the planet, and g_{surf} is the gravity at the surface.

When the gravity is too weak to hold the parcels together, then the planetary atmosphere is no longer in hydrostatic equilibrium, and can be considered an exosphere, or as called in the case of comets, a cometary coma (see section 6). A parameter defining the limit between a planetary atmosphere in hydrostatic equilibrium and an exosphere is the escape velocity, with exospheres having outgassing velocities (identified with the variable "Expansion Velocity" in the PSG/GUI)

greater than the escape velocity. For planetary atmosphere, when non-equilibrated atmospheres are modelled the user can select “Expanding coma” in the atmosphere menu in the “Atmosphere and Surface section”, and PSG will report both the outgassing and the escape velocities of the object of interest. For hydrostatic equilibrium atmosphere simulations if the variable “Altitude” is not provided for the vertical profile in the <ATMOSPHERE-LAYERS-MOLECULES> configuration file keyword (see section 1), PSG will compute the layer altitude (h) by employing the hydrostatic equation as:

$$h_{l+1} = h_l + H \ln \left(\frac{p_l}{p_{l+1}} \right) \quad (1)$$

where l is the layer number, p_l is the pressure of the bottom layer, p_{l+1} is the pressure at the top of the layer, and H is the scaleheight. Scaleheight is a key parameter establishing the vertical structure and defines how compact the atmosphere is. It is computed at each layer based on the layer temperature (T [K]), the local molar mass (M_{air} [g/mol]) and the local gravity (g [m/s²]) as $H = (kN_A T)/(M_{\text{air}} g)$, where k is the Boltzmann constant and N_A is Avogadro’s constant. In PSG, we use a constant molecular weight for the whole column defined by the ATMOSPHERE-WEIGHT keyword, yet the user can operate with varying molecular mass atmospheres by providing the “Altitude” values for each layer.

3. Earth atmosphere

For the computation of telluric transmittances and radiances, PSG extracts atmospheric profiles and molecular abundances from the Modern-Era Retrospective Analysis for Research and Applications (MERRA-2) database (Gelaro et al., 2017). MERRA-2 is the latest atmospheric reanalysis of the modern satellite era produced by NASA’s Global Modeling and Assimilation Office, which incorporates information from hundreds of orbiters and ground stations since 1980 and provides a global three-dimensional repository of atmospheric parameters (e.g., temperature, abundance profiles, aerosols). Specifically, PSG works with the M2I3NVASM component, which provides assimilated meteorological fields (pressure, temperature, water vapor, ozone, and water ice clouds) from the surface to ~80 km (72 layers) with a cadence of 180 minutes, and spatial resolution of ~0.5 degrees (576 x 361). The values are further refined temporally and spatially to a resolution of better than 1 km employing the USGS-GTOPO30 topographic maps (Gesch and Larson, 1996) and considering a hydrostatic equilibrated atmosphere within every bin. The MERRA-2 database is constantly being updated, yet it assimilates data with a latency of approximately 2 months. For atmospheric requests before 1980, or newer than present minus 2 months, PSG will extract information for the same season / location / time-of-day but for the nearest year available in the database.

For species not contained in this repository (CO₂, N₂O, CO, CH₄, O₂, NO, SO₂, NO₂, NH₃, HNO₃, OH, HF, HCl, HBr, HI, ClO, OCS, H₂CO, HOCl, N₂, HCN, CH₃Cl, H₂O₂, C₂H₂, C₂H₆, PH₃), PSG will consider standard abundance profiles (Clough et al., 2005). Many of these species have long atmospheric lifetimes (e.g., CO₂, CH₄) and are non-condensable (e.g., CO) so they do not show strong geographical and/or temporal variability, so this assumption should be accurate enough in most cases. Yet other species are known to display strong variability (e.g., H₂CO) and the provided vertical profiles should be considered solely as best-guesses.



4. Mars atmosphere

PSG extracts atmospheric information from the Mars Climate Database (MCD, Millour et al., 2015) and GEM General Circulation Model (Daerden et al., 2019). MCD and GEM are comprehensive repository of meteorological fields derived from General Circulation Model (GCM) numerical simulations and validated using available observational data. The MCD database has a natural spatial resolution of ~ 5 degrees (64×49) and 30 layers up to ~ 90 km, with 12 local times (2-hours resolution) and 12 seasons. PSG operates with the raw information contained in the NetCDF files of both models, which is later refined spatially and temporally to the specific time and latitude / longitude of the PSG calculation. In a similar procedure as done by Millour et al. (Millour et al., 2015) (and in the same way we resample the MERRA-2 database), the 64×49 grid is refined spatially to a much finer scale (11520×5760 , ~ 0.03 degrees) by employing the MOLA topographic data (Smith et al., 2001). Several climatological states are possible (e.g., dust storm, cold scenario) and also for different levels of EUV radiation, with PSG extracting information only considering the typical climatological state (average dust and EUV conditions). Specifically, PSG extracts vertical profiles of pressure, temperature, CO_2 , N_2 , O_2 , CO , H_2O , dust, dust size, water ice and ice particle size from the MCD database, while the surface albedo information is determined from the MGS/TES database (Smith, 2004).

5. Gas giants / Dense and hazy atmospheres

Planets in which their atmospheres are so thick, that the definition of a physical solid “surface” becomes ambiguous (e.g., Jupiter, Saturn, Uranus, Neptune), require a careful and particular parameterization of the radiative transfer. Specifically, the atmospheric layering should be as complete as possible when defining the main species that contribute to the spectroscopic opacities. In giant planets, the main opacity terms that define this optically thick “surface” are hazes (e.g., CH_4 , NH_3 , NH_4SH , H_2S , H_2O hazes) and the effect of collision-induced-absorption by molecular hydrogen and helium. Beyond that, a plethora of hydrocarbon species (e.g., CH_4 , C_2H_2 , C_2H_6) and other trace molecules contribute to the overall atmospheric opacities.

Due to this set of numerous opacity terms, these atmospheres are rarely probed at pressures beyond 10 bars, and in PSG we have provided a basic description of the main hazes and species from 10 bars to ~ 10 nbar. For the giants (i.e., Jupiter, Saturn, Uranus and Neptune), the haze profiles are based on (Sánchez-Lavega and Heimpel, 2017) while for Venus, the temperature profile is based on VIRA and the sulfuric acid haze profile is based on (Knollenberg R. et al., 2012). Molecular abundances are only prescribed for a select set of species based on (Ehrenreich et al., 2012; Lellouch et al., 2010; Marten et al., 2005; Moses et al., 2005), and it is of great importance for the user to update and validate the desired abundance / haze profiles when performing a simulation. Information about molecular line-shapes for non-terrestrial environments (e.g., H_2 , He, CO_2 atmospheres) is still limited, yet with the advent of new laboratory measurements (Devi et al., 2017a, 2017b) and new modeling efforts (Gamache and Renaud, 2017; Villanueva et al., 2012b), many more line-lists are constantly added (see chapter 4).

6. Cometary atmospheres

A cometary atmosphere is characterized by multiple inter-related radiative processes that lead to a complex outgassing halo typically called “coma” (see Figure 2); in PSG many of these processes are included, such as (1) an expanding exosphere, (2) photodissociation processes for parent and daughter species, (3) extended icy-grains structure, 4) thermal, equilibrated and rotational emissions and (5) emissions computed from non-LTE cascade fluorescence models.

In general, cometary outgassing and molecular abundances in comets are highly variable and relatively difficult to estimate or predict. The main parameter that establishes the intensity of spectroscopic fluxes in a cometary coma is the gas production rate, or activity rate, typically identified as Q [molecules/s]. The user can provide this value as an input parameter for any molecule, but in some cases the user may not know it, and PSG will estimate the level of outgassing activity in the comet (i.e., Q) from other observed astronomical quantities (e.g., visual magnitude). Typically, cometary activity is driven by the water outgassing at heliocentric distances (r_h) within 2 au, while the sublimation of more volatile ices tends to dominate cometary activity beyond 2 au, yet this is extremely dependent on composition and structure.

Within 2 au, activity (Q [molecules/s]) is mostly dominated by insolation, with outgassing rates following a r_h^2 relationship ($Q = Q_{au} / R_h^2$, where Q_{au} is the activity at $r_h=1$ au). Outgassing velocities also follow a heliocentric distance dependence, yet much less steep, and in PSG we employ an empirically defined relationship (valid in the collisionless region of the coma, beyond ~ 100 km from the nucleus) to establish the expansion velocities: $v_{exp}=0.8 \cdot R_h^{-0.5}$ [km/s] (Biver et al., 2002; Delsemme, 1982). In a related fashion and employing a sample of 37 comets observed from 1982 to 2004 (234 points), Jorda et al. (Jorda et al., 2008) determined an empirical relationship between visual magnitude (m_v) and gas production rate (Q), $m_v = (30.675 - \log(Q))/0.2453 + 5 \cdot \log(R_g)$. Cometary visual brightness is mainly defined by dust brightness, and such a relationship intrinsically implies a common gas to dust ratio among comets. Even considering this caveat, such a relationship is of great value when estimating cometary activity, and in PSG we use this to estimate the water production rates from visual magnitudes derived from JPL Horizon, yet the user can edit this estimate as needed.

PSG computes three brightness metrics for cometary coma, which are displayed next to the production rate field: the expected visual magnitude (m_v), the infrared Figure-Of-Merit (FOM_{IR}), and the radio Figure-Of-Merit (FOM_{Radio}). These parameters are calculated based on the heliocentric distance (R_h [au]), the geocentric distance (R_g [au]), and the gas production rate (Q [molecules/s]), employing these equations: $m_v = (30.675 - \log(Q))/0.2453 + 5 \cdot \log(R_g)$ (Jorda et al., 2008); $FOM_{IR} = Q \cdot 1E-29 / (R_g \cdot R_h^2)$ (Mumma et al., 2003); $FOM_{Radio} = Q \cdot 1E-28 / R_g$ (Crovisier, 2007). Molecular abundances relative to water tend to vary substantially between comets (Dello Russo et al., 2016; Lippi et al., 2021; Mumma and Charnley, 2011; Villanueva et al., 2006, 2011a), yet a “typical” set of abundance reference ratios, based on decades of observations and statistical analysis, can be assumed, and in PSG we consider as a-priori: $H_2O/CO_2/CO/CH_4/NH_3/H_2CO/C_2H_6/HCN/CH_3OH = 100/15/12/1.5/0.5/0.3/0.6/0.4/2.4$.

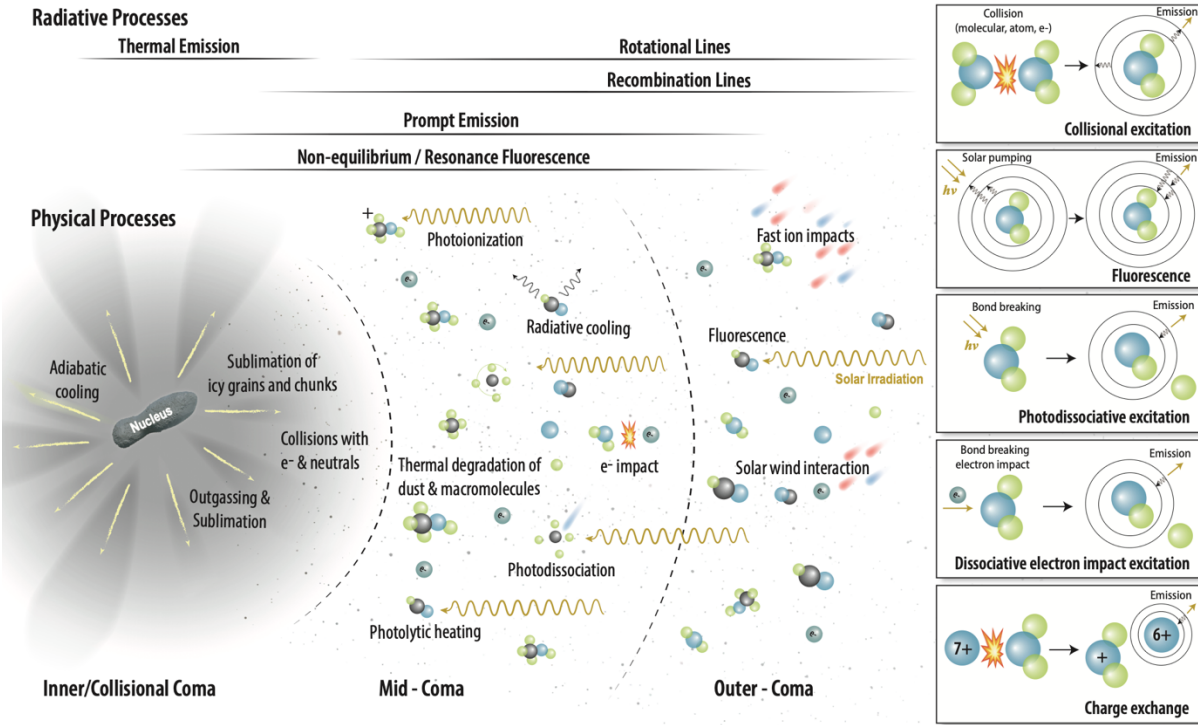


Figure 2: Many non-equilibrated and radiative processes take place in the atmospheres of comets, as summarized in our Comets III review (Bodewits et al., 2022). When computing cometary fluxes, PSG take many of these into account, in particular: a) an expanding and outgassed exosphere atmospheric structure, b) photodissociation processes for parent and daughter species, d) extended icy grains emissions, e) thermal, equilibrated and rotational emissions and f) fluorescence emissions via the pre-computed non-LTE cascade models for many species that include billions of lines (more details in chapter 4).

A key aspect in computing cometary fluxes is determining the number of molecules within the FOV. The total number of molecules in a coma (N [molecules]) can be calculated from the production rate (Q [molecules/second]) as $N = Q\tau$, in where τ is the photo-dissociative lifetime of the molecule. In PSG, reference lifetimes τ_0 can be provided by the user via the ATMOSPHERE-TAU keyword, and these pertain to the lifetimes at 1 heliocentric distance ($R_h=1$ au). These are scaled to the specific heliocentric distance of the comet as $\tau = \tau_0 R_h^2$. PSG will provide recommended values based on (Huebner et al., 1992), which the user can modify at their discretion.

To determine the actual number of molecules encompassed by the FOV (N_{FOV}), one would need a photodissociation model and also detailed information about the shape and location of the FOV with respect to the nucleus of the comet. A metric to quantify how many of the total molecules in the coma are encompassed by the beam is by computing the cometary “filling factor” or usually called $f(x)$, in which 1.0 would mean all total number of molecules are within the FOV, $N_{\text{FOV}} = N f(x)$. There are methods for calculating $f(x)$ for a cylindrical beam centered in a photo-dissociative atmosphere (e.g., analytical, vectorial, Monte Carlo). In PSG, we adapt the analytical methods as presented in Yamamoto (1981), which considers a Haser isotropic expansion coma under a constant

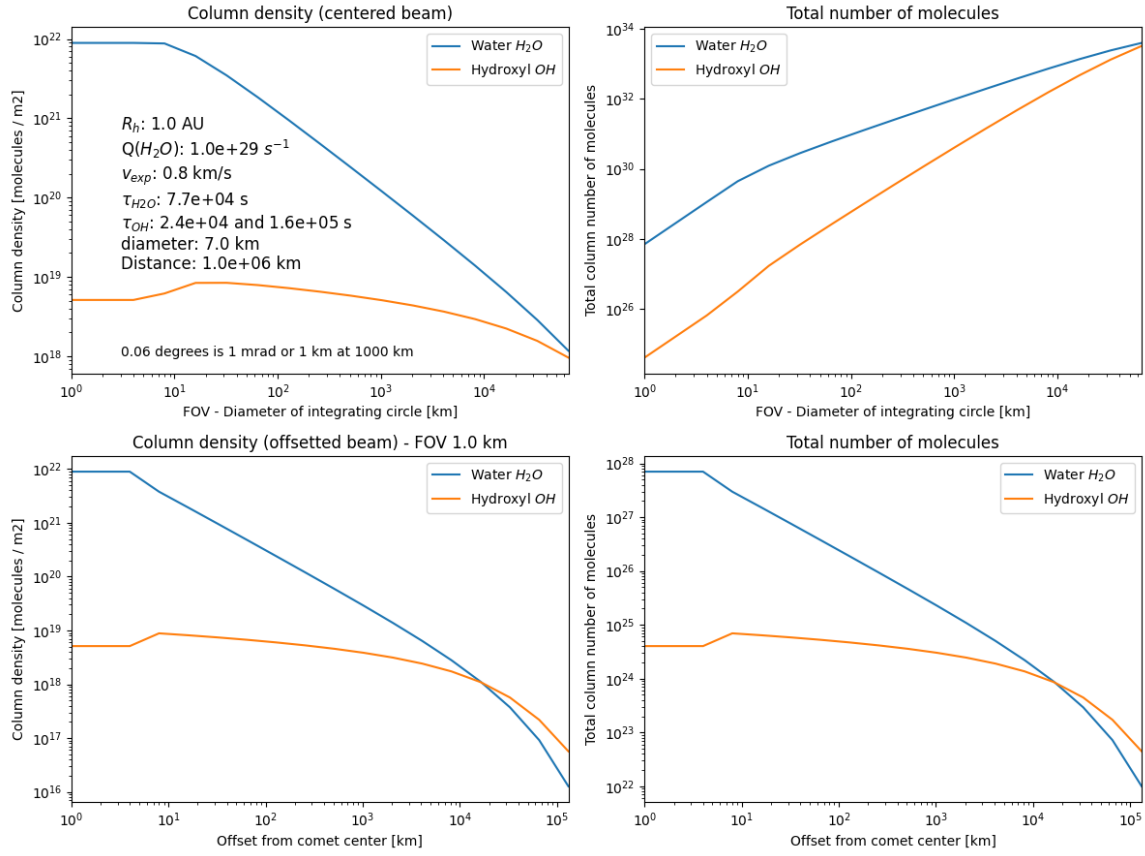


Figure 3: Example of the cometary model for integrating column densities across the line of sight for a centered and offset simulations. These are computed based on Bessel functions to account for photodissociation effects and employ several approximations for non-centered and embedded measurements to included nucleus occultation.

expansion velocity and a multi-step photodissociate decay. Using this method, the cometary filling factor for parent species $f_1(x)$ and daughter fragments $f_2(x)$ contained in a cylindrical centered beam can be calculated as:

$$f_1(x) = xg(x) \quad (2)$$

$$f_2(x) = \frac{\mu_2}{1 - \mu_2} x[g(\mu_2 x) - g(x)] \quad (3)$$

$$g(x) = \frac{1}{x} - K_1(x) + \int_x^\infty K_0(y) dy \quad (4)$$

$$x = \frac{FOV}{2\tau_p v_{exp}} \quad (5)$$

$$\mu_2 = \tau_p / \tau_d \quad (6)$$



where τ_p is the parent lifetime [s], τ_d is the daughter lifetime [s], v_{exp} is the expansion velocity [km/s], FOV is the diameter of the field of the view at the comet [km], $K_0(x)$ is the modified Bessel function of the second kind and of zeroth order, and $K_1(x)$ of the first order. Using this core math, filling factors for square pixels, offset beams (via concentric rings) and embedded probes (via $1/r$ scaling) can be computed. An example of our implementation of these models into PSG is presented in Figure 3 for a parent molecule (H_2O) and a daughter fragment (OH as produced from H_2O). More details about the models and the python code for computing number of molecules in a cometary atmosphere are available online at PSG's GitHub site (<https://github.com/nasapsg/isocoma>). These models were initially developed in support of the ESA/Comet Interceptor mission.

7. Exoplanet atmospheres

The temperature, composition and structure of exoplanets vary substantially, from scorching hot giants to small rocky planets. In an attempt to provide an accurate description of this diversity, in PSG we organize the exoplanets by mass (M in Earth's mass [M_\oplus]) and density (ρ [g/cm^3]) into four categories (in a comparable fashion to the Kepler categorization): Earth-like planets ($M < 2$ and $\rho > 4$), super-Earths ($2 < M < 10$ and $\rho > 4$, bigger than Earth but smaller than Neptune), Neptune-like ($10 < M < 50$, small gas giants, comparable to Neptune and Uranus), and gas-giants ($M > 50$, Saturn-sized and larger). Currently PSG simply assumes a terrestrial structure and composition (MERRA-2) for Earth-like planets, and a Venusian structure and composition (Ehrenreich et al., 2006) for super-Earth like planets. For gas giants, PSG employs the non-grey thermal model by Parmentier & Guillot (2014) to determine the vertical temperature profile of the planet. This analytical model is fast and matches full numerical simulations within 10% over a wide range of effective temperature, internal temperature and gravity and properly predicts the depth of the radiative/convective boundary. The equilibrium temperatures of the atmospheres are assumed to be strongly related to their composition and to the acting greenhouse gases. The model makes reasonable assumptions about composition based on gravity, distance to host star and density, and using two different opacity bands in the thermal frequency range, establishes the dual role of thermal non-grey opacities in defining the temperature profile. Opacities dominated by narrow features enable the upper atmosphere to cool down significantly compared to a grey atmosphere whereas opacities dominated by broad features lead both to a significant cooling of the upper atmosphere and a significant heating of the deep atmosphere (Parmentier and Guillot, 2014). Once the temperature profile of the exoplanet is defined, PSG employs the chemical equilibrium equations-of-state (EOS) derived by Kempton et al. (Kempton et al., 2017) for a wide range of metallicities and primordial states. This implementation provides a-priori vertical profiles for dozens of species: H_2O , CO_2 , O_3 , N_2O , CO , CH_4 , O_2 , NO , SO_2 , NO_2 , NH_3 , HNO_3 , OH , HF , HCl , HBr , HI , ClO , OCS , H_2CO , HOCl , N_2 , HCN , CH_3Cl , H_2O_2 , C_2H_2 , C_2H_6 and PH_3 .

8. Three-dimensional characterization (GCM) of the atmosphere and surface

Realistic modeling of full disk and transit planetary fluxes would require capturing the heterogeneous properties of the atmosphere and the surface across the observable disk and the terminator. PSG allows to ingest General Circulation Model (GCM) 3D data of temperature, pressure, and abundance profiles, together with surface properties, such as albedo, via the GlobES app

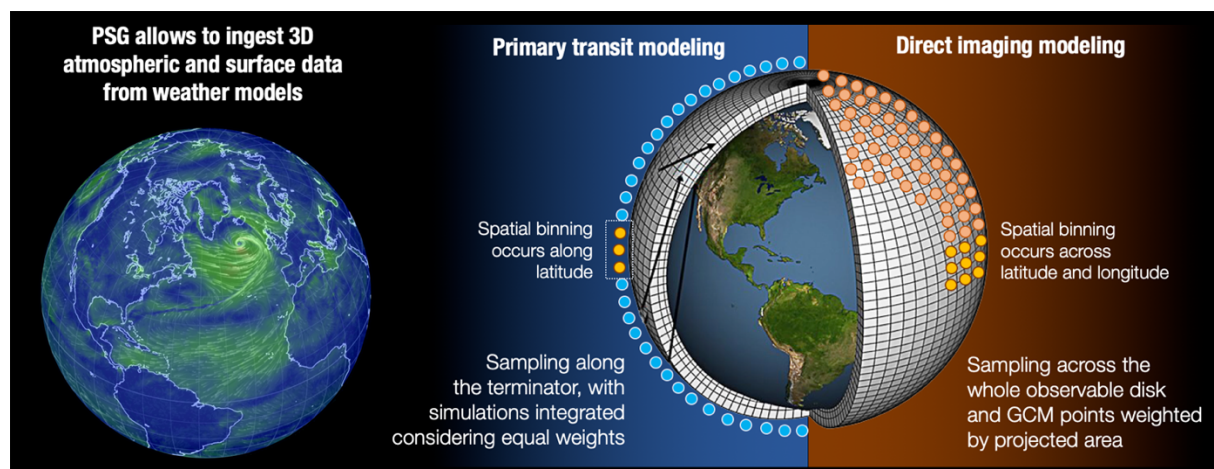


Figure 4: The ingestion of 3D atmospheric data is possible in PSG via the GlobES app, and this allows to accurately capture the heterogeneity of the atmospheric and the surface across the observable disk and terminator. For transit observations, the GlobES app performs radiative transfer simulations across the terminator and integrates the different spectra employing equal weights. For direct imaging and secondary eclipse simulations, the algorithm performs radiative transfer simulations across the whole observable disk, and the individual spectra are integrated considering the projected area of each bin.

(<https://psg.gsfc.nasa.gov/apps/globes.php>). The user can upload atmospheric data from any GCM, after converting the 3D fields (typically in netCDF format) into a PSG GCM binary file. The 3D and temporal atmospheric data are then aggregated and mapped into a 2D projected observationally grid that is fed to the radiative transfer modules. PSG currently provides templates and conversion scripts for several GCM models, including the ROCKE-3D terrestrial model, the Laboratoire de Météorologie Dynamique (LMD) model, the exoplanet Community Atmosphere Model (ExoCAM) model, and the Unified Model (UM). In order to ingest 3D data, these are the steps to follow:

- 1) Run the GCM model in your personal machine, and store the resulting 3D fields and parameters into a GCM formatted file (typically a netCDF file).
- 2) By employing a script (see scripts in PSG's GitHub) convert the GCM netCDF file into a PSG GCM binary file. Several example conversion scripts are available at the GlobES application site, permitting to convert netCDF output files from ROCKE-3D, LMD and ExoCAM. This script should be run at the user's local machine.
- 3) In the GlobES site, upload the PSG GCM file by clicking on "Load GCM data". If the upload process was successful, the site should display graphically the GCM outputs for the different variables.
- 4) Select the observing geometry (e.g., transit, direct imaging) directly on the GlobES site, or at the "Target and Geometry" section of PSG, and verify and update the molecules and aerosols to include in the simulation by visiting the "Atmosphere and Surface" section of PSG.



5) In the GlobES site, click on "Generate 3D spectra". For each position on the planet, the algorithm will update the atmospheric profiles, surface properties and geometry parameters and will run the radiative transfer. These results will be integrated employing the appropriate weights.

To run the GlobES module in script mode via the API, please check the python scripts available in GitHub.

Binning: to speed up the calculations one can horizontally bin/aggregate GCM data to have less PSG radiative-transfer calculations. Higher binning means more aggregation and less PSG radiative-transfer calculations. High "binning" numbers (above 50) should only be used when testing. A "binning" factor of 3 is typically recommended, leading to 3×3 (lat x lon = 9) binning, and a speed up of 9 times while sacrificing a little accuracy.



Planetary Spectrum Generator
National Aeronautics and Space Administration

Chapter 4:

Radiative transfer modeling

**Villanueva, Kofman, Liuzzi, Faggi and
PSG team**

1. Radiative transfer modeling in PSG

In a classical radiative transfer calculation, the photons are being tracked along their path towards the observer. Two main processes occur during this transport, the photons are being absorbed by the prevailing opacity of the medium, and new photons are being generated from the local ambient (see Figure 1). Each wavelength can be treated independently if fluorescence, Raman and other non-LTE (non-Local Thermodynamic Equilibrium, see section 4) effects are ignored. In many cases, the absorbed photons will not be re-emitted and a linear integration of absorptions and thermal emissions along the path can be simply assumed. This is the case for most typical atomic/molecular absorptions, yet when Rayleigh and scattering aerosols are present, one may need to account for the multiple scattering ($N_{MAX} > 0$) of the photons, requiring a specialized treatment (see chapter 5).

Even when scattering elements are active in an atmosphere, if the optical depths are small ($\tau \ll 1$), one can solve the radiative transfer problem via the single-scattering approximation. This is the case because the photon has a high probability of exiting the aerosol before getting scattered a second time. In a highly absorbing environment (small scattering albedo, $w \ll 1$) single scattering is also common since a photon is more likely to get absorbed than to get scattered a second time. In PSG when multiple scattering is disabled ($N_{MAX} = 0$), we employ a combination of the single scattering approximation for diffuse solar light, the Schwarzschild equation for the thermal component and an approximated multiple-scattering term for the reflected diffuse radiances. Such method does not require solving/inverting any matrix, it is computationally fast, and generally accurate for isotropic and weakly scattering regimes. In general, the equation of radiative transfer can be written as (Liou, 2002):

$$\mu \frac{dI(\tau, \mu, \phi)}{d\tau} = I(\tau, \mu, \phi) - J(\tau, \mu, \phi) \quad (1)$$

where $I(\tau, \mu, \phi)$ is the radiance (or intensity) at optical depth τ (proxy to altitude), μ is the cosine of zenith angle (α) and ϕ the azimuth angle. In a plane parallel atmosphere, $\mu = \cos(\alpha)$, with $1/\mu$ is normally referred as the airmass scaler. In PSG, we employ a raytracing algorithm to compute μ across the path of light in a refractive and spherical planet/atmosphere (see section 2). Calculation of the source function is at the core of the radiative transfer, and it can be expressed as:

$$J(\tau, \mu, \phi) = \frac{\omega}{4\pi} \int_0^{2\pi} \int_{-1}^{-1} I(\tau, \mu', \phi') P(\mu, \phi, \mu', \phi') d\mu' d\phi' \quad (2)$$

$$+ \frac{w}{4\pi} F_* P(\mu, \phi, -\mu_0, \phi_0) e^{-\frac{\tau}{\mu_0}} + (1 - \omega) S(\tau)$$

where the first term is the multiple-scattering term (solved explicitly in chapter 5 with $N_{MAX} > 0$), the second term is the single-scattering contribution to the solar diffuse radiance, and last term is the thermal layer source. In LTE, $S(\tau) = B[T(\tau)]$, where B is the Planck function, while in PSG we allow for non-LTE sources via this term (see section 4). Regarding the other coefficients, w is the scattering albedo, F_* is the solar flux at TOA (Top of Atmosphere), $P(\mu, \phi, \mu', \phi')$ is the phase function with incidence μ', ϕ' and emission at μ, ϕ , and μ_0 is the solar Zenith angle (negative in the phase term

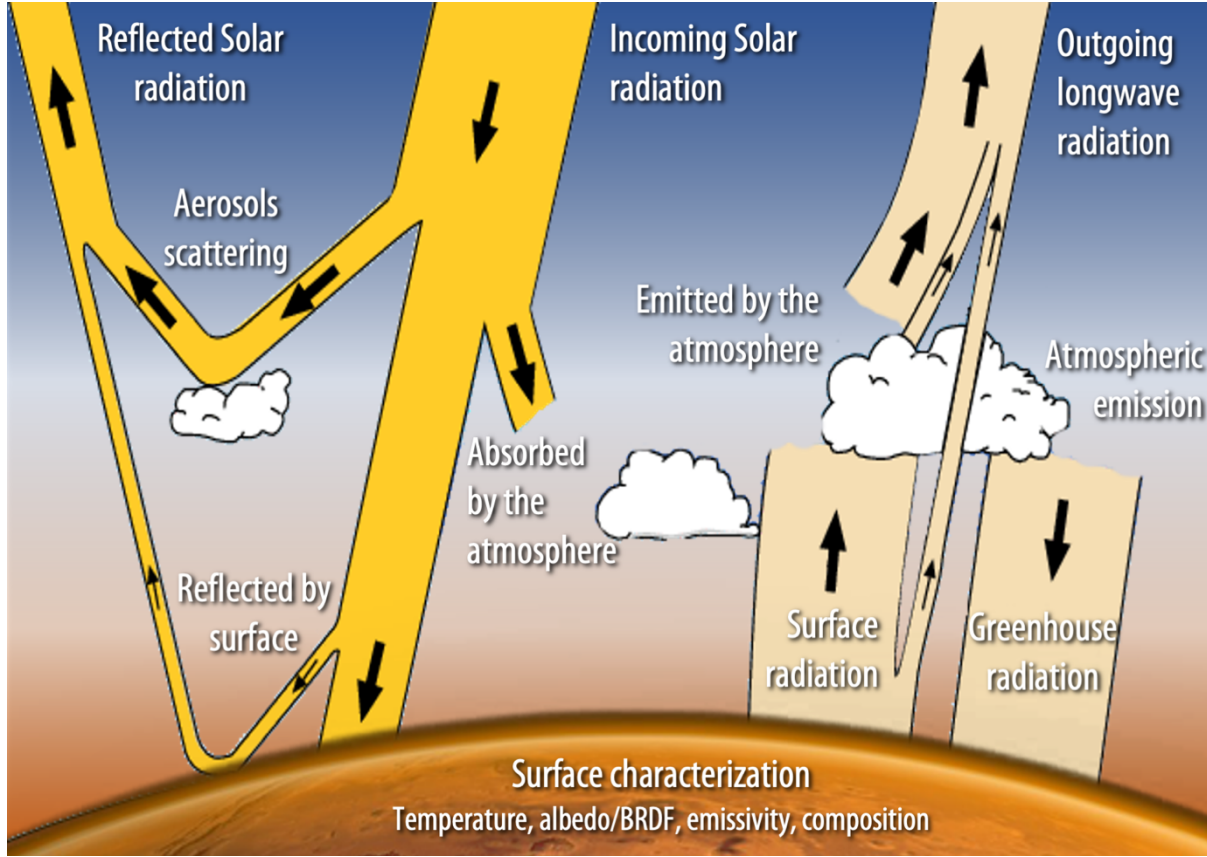


Figure 1: The diagram shows the different processes affecting radiation in a planetary atmosphere. Two main branches can be defined: **(left)** the photons originating from the Sun and their atmospheric scattering and reflection on the surface, **(right)** the thermal radiation. The surface plays an important role in reflecting the downward fluxes towards TOA, while multiple scattering of photons can mean solving for this system quite complex. In PSG, one can perform rapid calculations by assuming single isotropic scattering (NMAX=0), or by employing a discrete ordinate method to solve the systems of equations (NMAX>0, chapter 5).

since it defines incoming fluxes, while positive μ indicates outgoing fluxes). Integrating equation (1) across the path of radiation (τ dimension), one then obtains:

$$I(\tau, \mu, \phi) = I(\tau_0, \mu, \phi) e^{-\frac{\tau-\tau_0}{\mu}} + \int_{\tau_0}^{\tau} J(\tau', \mu, \phi) e^{-\frac{\tau-\tau'}{\mu}} \frac{d\tau'}{\mu} \quad (3)$$

where the first term is the radiance at the bottom of the layer attenuated by the opacity within the layer, and the second term is the integral of the radiance collected across the layer. In the case of LTE [$S=B(T)$] and no scattering ($w=0$), equation 3 gets reduced to the Schwarzschild equation. The integration of equation 3 is done numerically in PSG following the path of the radiation, yet the challenge is in the calculation of the source function $J(\tau, \mu, \phi)$.

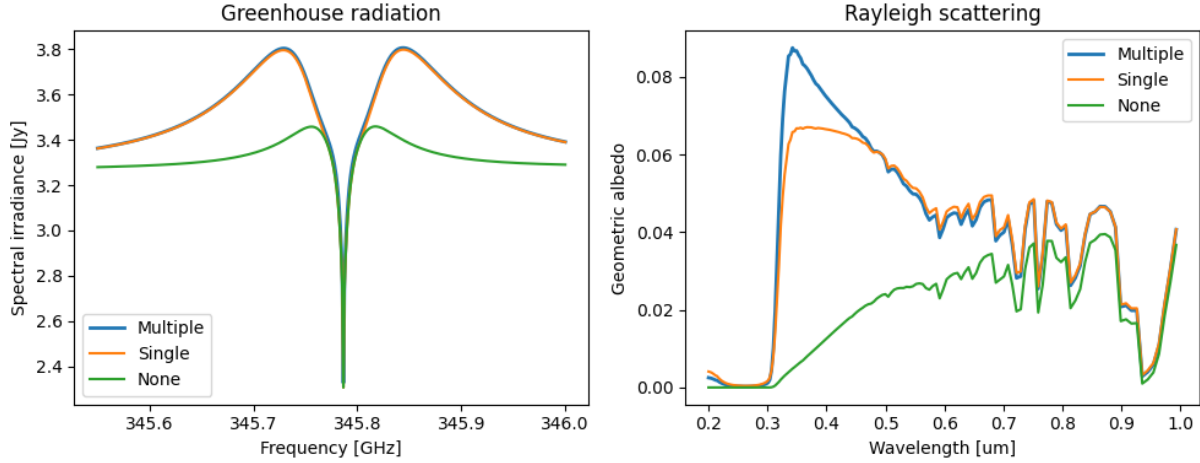


Figure 2: Effects of including multiple/single or no scattering in the calculations. The multiple scattering simulations were performed with NMAX=1 employing PSGDORT (a PSG adaption of DISORT, see chapter 5). **(Left)** Simulation of the CO (J=3-2) line on Mars, in which one can observe that the “scattering” effect is even relevant when operating at thermal wavelengths in a non-scattering atmosphere ($w \approx 0$). The “greenhouse radiation” accounted in equation 7 has a substantial effect on the planetary signature, while the simplified methods described in section 1 reproduce well a full scattering calculation. **(Right)** In a Rayleigh atmosphere, the single scattering assumption is relatively accurate in regions of low scattering opacity, while including only extinction leads to substantial error.

Let us now consider the case of an observer at the surface [$\tau_s = \max(\tau)$] looking up with a cosine of the zenith angle μ and an azimuth angle ϕ . If we neglect multiple-scattering term and assume single scattering, then the diffuse radiance can be calculated as:

$$I^\downarrow(\tau_s, \mu, \phi) = \int_0^{\tau_s} J(\tau', -\mu, \phi) e^{-\frac{\tau_s - \tau'}{\mu}} \frac{d\tau'}{\mu} \quad (4)$$

$$J(\tau, \mu, \phi) = \frac{w}{4\pi} F_* P(\mu, \phi, -\mu_0, \phi_0) e^{-\frac{\tau}{\mu_0}} + (1 - \omega) S(\tau) \quad (5)$$

In the approximation, we can use many Legendre terms in describing P (see eq. 8 in Chapter 5) with a small penalty in computation cost. As presented in Figure 1, the first term of J would be “aerosols scattering” and the second “atmospheric emission / emitted by the atmosphere”. Note the sign of the zenith angle in the source function J of equation 4, indicating downward flux so the phase function is $P(-\mu, \phi, -\mu_0, \phi_0)$. On a similar approach, we can now compute the radiance emanating at TOA as:

$$I^\uparrow(0, \mu, \phi) = I_s^\uparrow(\mu, \phi) e^{-\frac{\tau_s}{\mu}} + \int_0^{\tau_s} J(\tau', \mu, \phi) e^{-\frac{\tau'}{\mu}} \frac{d\tau'}{\mu} \quad (6)$$

where $I_s(\mu, \phi)$ is the surface radiance towards the observer. For a black surface (bi-directional distribution function [BRDF] $r=0$, see chapter 6), the emanating surface radiance is simply $I_s =$



$\varepsilon(\mu, \phi)B(T_s)$, where ε is the surface emissivity towards the observer and T_s is the surface temperature. The issue is that the surface is also reflecting the radiance arriving from all possible μ, ϕ directions, and consequently one would need to solve for multiple scattering across μ, ϕ . If we now consider double Gaussian quadrature ($\mu_q = 0.5$) as a first approximation for the downward direction, the total surface radiance including reflected scattered light is:

$$I_s^\uparrow(\mu, \phi) = \varepsilon(\mu, \phi)B(T_s) + r(\mu, \phi, \mu_0, \phi_0) \left[\frac{\mu_0}{4} F_* + I^\downarrow(\tau_s, \mu_q, \phi) \right] \quad (7)$$

The first term of equation (7) is the thermal surface emission (labelled “surface radiation” in Figure (1), the following term is the reflected direct solar light (“reflected by surface”) and the last term is the reflected diffuse radiation (“greenhouse radiation”). For simplicity the BRDF for the solar flux is assumed to be the same as for the diffuse downward flux in equation (7), which is only valid for Lambert surfaces.

Calculating the radiative transfer solution under these assumptions is therefore straightforward with two numerical integrations (TOA to surface [eq. 4], and surface to observer [eq 6]). This analytical description for NMAX=0 should be only employed when operating with highly isotropic scatterers (e.g., thermal, Rayleigh), and having an optically thin medium (e.g., thin cirrus or dust layers) or a highly absorbing / non-scattering environment (see Figure 2). The user is recommended to use NMAX>0 for other cases (see chapter 5), and PSG would provide recommendations / warnings accordingly.

2. Raytracing in a spherical and refractive atmosphere

The definition of the direction of incidence and emission plays an important role in the calculation of the radiant intensities. As summarized in the equations of the previous section, all terms include a direction quantifier (e.g., μ, ϕ), which can be challenging to establish when the observed scene includes many incidence / emission angles, as when we observe a planet from afar. In PSG, the angles are computed by the geometry module, which are then fed to the radiative transfer module (see details in chapter 2). Beyond those general geometrical considerations, the path of the radiation across a spherical and refractive atmosphere is not a straight line but follows a complex curved path. On the other hand, in a plane parallel atmosphere, the incidence and emission angles across all layers are practically considered constant and simply defined as $\mu = \cos\alpha$, $\mu_0 = \cos\beta$. On such simplified case, the amount of gas interacting across all the layers can be simply scaled to the zenith value by $1/\mu$, which is normally defined as the observational “airmass”. Yet in a spherical refractive atmosphere, each layer would have a distinct set of “entrance” and “exit” angles, and the amount of gas crisscrossed along the layer would not be a straight line but a curved integral.

Chapman functions (e.g., Dahlback and Stamnes, 1991) are analytical functions describing the path lengths at each layer for a spherical atmosphere, yet these solutions do not include or can model the effects of refraction. One can derive approximated curvature effects by refraction for certain incidence angles (e.g., tangential) when assuming isothermal and simple vertical profiles, yet these approximations can be quite inaccurate when modeling realistic atmospheres, since the temperatures

(and thus refractive properties) can change greatly with altitude. Ultimately, the only way to properly model and capture refraction in a spherical inhomogeneous atmosphere is via a numerical raytracing algorithm. As such in PSG, we follow the path of light from the observer all the way through the atmosphere to the surface (or TOA), and we correct the incidence angles at each layer interface by the refractive properties of the layers. The correction also captures the curved nature of the atmosphere, and each layer is divided into 10 sub-layers, permitting a finer and more accurate description of refraction/sphericity within the layers. The sub-layering method is particularly relevant when performing raytracing in limb/occultation/transit geometries.

The refraction coefficient in a medium depends on the local density, the composition, and the wavelength of the radiation. In PSG, the refractive coefficient at each layer (η) is determined based on the molar mass of the atmosphere (a proxy to composition), the layer temperature/pressure (density) and the wavelength λ as:

$$\eta = 1 + \frac{288.15k}{1.01325} \frac{P[bar]}{T[K]} d\eta_0(\lambda) \quad (8)$$

where k is the Boltzmann constant ($1.38064852e-23$ [m²kgs⁻²K⁻¹]) and $d\eta_0$ is the refractive coefficient minus 1 ($d\eta_0 = \eta_0 - 1$) at 288.15 [K] and 1 [atm]. We employ constants and equations as tabulated in <https://refractiveindex.info> to scale $d\eta_0$ to the corresponding simulation wavelengths. These equations are only considered for wavelengths greater than 0.15 μm - the $d\eta_0$ values are maximized at 0.15 μm for shorter wavelengths.

For H₂ rich atmospheres:

$$d\eta_0^{H_2} = \frac{0.148956}{180.7 - \lambda^{-2}} + \frac{0.0049037}{92 - \lambda^{-2}} \quad (9)$$

For He rich atmospheres:

$$d\eta_0^{He} = \frac{0.1470091}{423.98 - \lambda^{-2}} \quad (10)$$

For CO₂ rich atmospheres:

$$d\eta_0^{CO_2} = \frac{6.991 \cdot 10^{-2}}{166.175 - \lambda^{-2}} + \frac{1.4472 \cdot 10^{-3}}{79.609 - \lambda^{-2}} + \frac{6.42941 \cdot 10^{-5}}{56.3064 - \lambda^{-2}} + \frac{5.21306 \cdot 10^{-5}}{46.0196 - \lambda^{-2}} \quad (11)$$

For air (N₂/O₂) rich atmospheres:

$$d\eta_0^{air} = 8.06051 \cdot 10^{-5} + \frac{2.48099 \cdot 10^{-2}}{132.274 - \lambda^{-2}} + \frac{1.74557 \cdot 10^{-4}}{39.32957 - \lambda^{-2}} \quad (12)$$

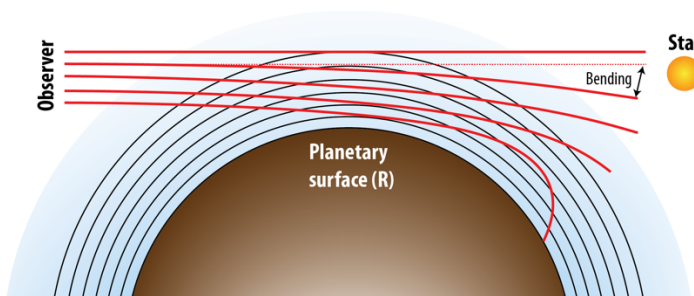


Figure 3: The ray-length and angles across a spherical atmosphere are different for every layer, while refraction “bends” the light across the path. The bending introduced for every ray defines if the observed radiation relates to the surface, to TOA or to the background star (e.g., transit).

At the interface between each sub-layer, the angles across the ray-path are corrected following Snell’s law, $\sin\alpha_1 = (\eta_0/\eta_1)\sin\alpha_0$, while the amount of gas integrated across the sub-layer in a curved path is computed numerically following Simpson’s 1/3 rule integration.

The raytracing algorithm starts at the location of the observer and follows the path of radiation across the atmosphere (see Figure 3). For instance, if the defined geometry is an occultation/limb at impact height H for a planet with radius R , then the starting path angle at H_{TOA} is computed as $\sin\alpha_{\text{TOA}} = [(H+R)/(H_{\text{TOA}}+R)]\sin\alpha_H$. For exoplanet transit observations, one needs to compute the raytracing for every layer, and therefore the raytracing algorithm is repeated for every layer. The algorithm also checks that the path does not curve beyond the size of the star and enters/exits the atmosphere (i.e., it does not crash on the planet surface), which would imply that no stellar light arrives to the observer for that layer.

3. Atmospheric opacities

As discussed in the first section, opacities are a critical component in any radiative transfer calculation. Molecules and atoms absorb light at very specific wavelengths, with the spectral lines shape of the absorption defined by the local temperature (Doppler Gaussian broadening), the ambient pressure (Collisional Lorentzian broadening) and the prevailing kinematic dispersions. One approach is to perform a line-by-line, layer-by-layer treatment, in which every line shape is modelled for every layer for all the lines in the spectral interval of investigation. Generally, the width of a line is normally quite narrow ($<25 \text{ cm}^{-1}$), requiring therefore very high-resolutions ($<0.001 \text{ cm}^{-1}$ in the near-IR) to properly model its line-shapes. Just to capture the complexity of the problem, let us consider a simulation in the 0.2 to $1 \text{ }\mu\text{m}$ ($50,000$ to $10,000 \text{ cm}^{-1}$) spectral range at a resolution of 0.001 cm^{-1} . Some line-lists could contain billions of transitions on such range, so 1 billion lines and 100 layers for that range would require $(50,000-10,000)/0.001 \times 1 \text{ billion} \times 100 = 4 \times 10^{18}$ line-shape calculations, an unachievable and impossible task. As such, several algorithms (e.g., multi grid line-shape modeling) and analytical/numerical methods (e.g., correlated-k analysis) exist, permitting to accurately calculate atmospheric opacities in practical amounts of times. In this section, we describe the methods and techniques integrated into PSG for the calculation of molecular and atomic opacities. PSG will automatically switch between the different methods and internally synthesize at the needed spectral resolutions depending on the selected spectral database and the availability of pre-computed correlate-k tables.

3.1 Line-by-line modeling

Line-by-line calculations are required for all calculations with resolving powers greater than 5000 ($\lambda/\delta\lambda > 5000$), or when the user selects databases that PSG does not have pre-computed correlated-k tables (e.g., JPL-MolSpec, CDMS, Kurucz, GEISA). PSG will perform these calculations using an internal grid with the fine resolution needed to properly capture the shape of the lines. As such, an apparently simple calculation could mean a large internal calculation, yet PSG will take care of internally expanding / binning the spectra to ensure accurate modeling of the line-shapes. At the core of any line-by-line calculation are line-lists that tabulate the line parameters, which include: a) the line center wavelength/frequency [ν_0], b) the line intensity [$S(T_{ref})$], c) the transition lower state energy [E], and d) the line-shape parameters [w_{CO} , ew_P , dv_P , ev_P] for the different collision regimes (e.g., air, CO₂, H₂, He atmospheres). Line lists like JPL-MolSpec or CDMS do not provide line-shapes information, so the user needs to provide this information, while other line-lists only provide line-shape parameters for certain collisional regimes (e.g., air for GEISA) and would therefore be non-applicable to other environments (e.g., a CO₂ atmosphere). HITRAN and GEISA tabulate line intensities $S(T_{ref})$ at $T_{ref}=296$ K, while JPL-MolSpec and CDMS at $T_{ref}=300$ K. These can be scaled for every layer considering the effective Curtis-Godson ray-trace temperature (T) at the layer as:

$$S(T) = S(T_{ref}) \frac{Q(T_{ref})}{Q(T)} \frac{\exp(-hcE/kT)}{\exp(-hcE/kT_{ref})} \frac{1 - \exp(-hcv/kT)}{1 - \exp(-hcv/kT_{ref})} \quad (13)$$

where $Q(T)$ is the partition function at temperature T (PSG contains tables for all isotopologues from 1 to 3000K), E is the lower state energy of the transition and ν is the frequency of the transition. The Kurucz atomic database reports intensities “log gf ”, a representation of the spontaneous Einstein emission coefficient A_{ul} . Converting from “log gf ” to $S(T_{ref})$ is done following:

$$A_{ul} = \frac{10^{\log gf}}{1.499 \cdot 10^{-14} g_u \lambda [\text{nm}]^2} \quad (14)$$

$$S(T_{ref}) = A_{ul} \frac{10^{\log hf} 10^{\log iso}}{8 \cdot \pi c \cdot 100 \cdot Q(T_{ref}) \nu^2} \left[g_u \exp\left(-\frac{hcE}{kT_{ref}}\right) - \exp\left(-\frac{hc(E + \nu)}{kT_{ref}}\right) \right] \quad (15)$$

where “log hf ” is the hyperfine component log fractional strength, “log iso ” is the log isotopic abundance fraction and g_u the upper-state statistical weight.

The anatomy of a line-shape can be divided into three regions with two transition regions (see Figures 4 and 5): 1) a Doppler Gaussian core, 2) extended Lorentz wings, and 3) far quasi-static and exponential wings. The first two components are described via the Voigt equation, which is a convolution of a Gaussian function and a Lorentz function. There is no closed form analytical form of the Voigt equation, yet several numerical algorithms exist that achieve great accuracy. In PSG, we employ the Fadeeva function as originally implemented by (Humlíček, 1982) with the improvements suggested by (Wells, 1999).



Water (H ₂ O) ID:1									
ISO	Self	Air		CO ₂		H ₂		He	
1	0.3445	0.0683	0.5826	0.0880	0.6707				
2	0.3535	0.0698	0.5971	0.1005	0.6784				
3	0.3582	0.0708	0.6054	0.1060	0.7016				
4	0.3779	0.0713	0.7783	0.0799	0.7437				
5	0.3847	0.0750	0.7824	0.0793	0.7687				
6	0.3887	0.0764	0.7840	0.0791	0.7793				
7	0.3929	0.0792	0.6200	0.1328	0.5912				
Ozone (O ₃) ID:3									
1	0.0905	0.0732	0.7703						
2	0.0937	0.0751	0.7699						
3	0.0911	0.0736	0.7763						
4	0.0893	0.0732	0.7847						
5	0.0894	0.0732	0.7858						
Carbon Monoxide (CO) ID:5									
1	0.0545	0.0511	0.7065	0.0614	0.6609	0.0686	0.5811	0.0461	0.5388
2	0.0554	0.0516	0.7046	0.0621	0.6614	0.0687	0.5840	0.0462	0.5394
3	0.0553	0.0515	0.7050	0.0620	0.6614	0.0687	0.5835	0.0462	0.5392
4	0.0555	0.0517	0.7028	0.0621	0.6620	0.0687	0.5848	0.0462	0.5396
5	0.0547	0.0510	0.7010	0.0611	0.6598	0.0686	0.5795	0.0461	0.5387
6	0.0552	0.0514	0.7021	0.0619	0.6611	0.0687	0.5829	0.0462	0.5392
Oxygen (O ₂) ID:7									
1	0.2109	0.0401	0.1365						
2	0.2166	0.0404	0.2460						
3	0.0379	0.0382	0.7228						
Sulfur Dioxide (SO ₂) ID:9									
1	0.3925	0.0969	0.7500	0.1536	0.5879	0.1442	0.7500	0.0704	0.6400
2	0.3871	0.0986	0.7500	0.1586	0.5937	0.1449	0.7500	0.0715	0.6400
3	0.3848	0.0985	0.7500	0.1570	0.5866	0.1450	0.7500	0.0717	0.6400
4	0.3902	0.0994	0.7500	0.1610	0.5949	0.1453	0.7500	0.0720	0.6400
Ammonia (NH ₃) ID:11									
1	0.4794	0.0798	0.7382	0.1435	0.7730	0.0776	0.5971	0.0282	0.3700
2	0.4742	0.0855	0.7945	0.1431	0.7730	0.0768	0.6055	0.0282	0.3700
Hydroxyl (OH) ID:13									
1	0.3000	0.0481	0.6600			0.0497	0.8600	0.0093	0.4200
2	0.3000	0.0570	0.6600			0.0589	0.8600	0.0110	0.4200
3	0.3000	0.0512	0.6600			0.0529	0.8600	0.0099	0.4200
Hydrogen Chloride (HCl) ID:15									
1	0.0932	0.0213	0.4924	0.0483	0.7500	0.0308	-0.4113	0.0124	0.7500
2	0.0931	0.0212	0.4924	0.0479	0.7500	0.0308	-0.4113	0.0124	0.7500
3	0.0891	0.0260	0.4948	0.0525	0.7500	0.0298	-0.4108	0.0110	0.7500
4	0.0892	0.0261	0.4947	0.0522	0.7500	0.0298	-0.4108	0.0110	0.7500
Hydrogen Iodide (HI) ID:17									
1	0.0445	0.0302	0.5000						
2	0.0420	0.0296	0.5000						
Carbonyl Sulfide (OCS) ID:19									
1	0.1455	0.0896	0.6038	0.1143	0.7482	0.0996	0.7500	0.0782	0.7500
2	0.1495	0.0903	0.6344	0.1153	0.7613	0.1004	0.7500	0.0785	0.7500
3	0.1485	0.0903	0.6269	0.1152	0.7588	0.1005	0.7500	0.0785	0.7500
4	0.1470	0.0901	0.6139	0.1150	0.7541	0.1003	0.7500	0.0784	0.7500
5	0.1484	0.0901	0.6258	0.1148	0.7565	0.0999	0.7500	0.0784	0.7500
6	0.1279	0.0857	0.4935	0.1075	0.6941	0.0936	0.7500	0.0761	0.7500
Hypochlorous Acid (HOCl) ID: 21									
1	0.1500	0.1000	0.7000						
2	0.1500	0.1000	0.7000						
Hydrogen Cyanide (HCN) ID:23									
1	0.6643	0.0980	0.7981			0.1127	0.9000	0.0428	0.7100
2	0.7593	0.1042	0.7989			0.1174	0.9000	0.0431	0.7100
3	0.4790	0.0869	0.7937			0.1037	0.9000	0.0425	0.7100
Hydrogen Peroxide (H ₂ O ₂) ID:25									
1	0.3000	0.1000	0.7500						

Carbon dioxide (CO ₂) ID:2									
ISO	Self	Air		CO ₂		H ₂		He	
1	0.0880	0.0700	0.7127	0.0880	0.6346				
2	0.0890	0.0705	0.7137	0.0890	0.6383				
3	0.0897	0.0708	0.7134	0.0897	0.6410				
4	0.0904	0.0711	0.7135	0.0904	0.6435				
5	0.0911	0.0715	0.7134	0.0911	0.6467				
6	0.0917	0.0717	0.7135	0.0917	0.6489				
7	0.0903	0.0711	0.7137	0.0903	0.6430				
8	0.0919	0.0718	0.7139	0.0919	0.6496				
9	0.0921	0.0720	0.7138	0.0921	0.6501				
10	0.0927	0.0721	0.7135	0.0927	0.6522				
11	0.0931	0.0723	0.7133	0.0931	0.6552				
12	0.0963	0.0736	0.7124	0.0963	0.6669				
Nitrogen Oxide (N ₂ O) ID:4									
1	0.0920	0.0750	0.7449						
2	0.0933	0.0757	0.7458						
3	0.0930	0.0756	0.7466						
4	0.0933	0.0745	0.7500						
5	0.0937	0.0760	0.7459						
Methane (CH ₄) ID:6									
1	0.0679	0.0519	0.6663						
2	0.0674	0.0502	0.6430						
3	0.0689	0.0512	0.7407						
4	0.0717	0.0529	0.6619						
Nitric Oxide (NO) ID:8									
1	0.0497	0.0394	0.6559						
2	0.0500	0.0395	0.6544						
3	0.0502	0.0397	0.6544						
Nitrogen Dioxide (NO ₂) ID:10									
1	0.0928	0.0727	0.7046						
2	0.0950	0.0729	0.7095						
Nitric Acid (HNO ₃) ID:12									
1	0.8057	0.1025	0.7647						
2	0.8070	0.1084	0.7500						
Hydrogen Fluoride (HF) ID:14									
1	0.1394	0.0283	0.5019	0.1135	0.5000	0.0419	0.7500	0.0077	0.5000
2	0.1136	0.0255	0.5000	0.0954	0.5000	0.0406	0.7500	0.0040	0.5000
Hydrogen Bromide (HBr) ID:16									
1	0.0693	0.0304	0.5000						
2	0.0694	0.0305	0.5000						
3	0.0669	0.0288	0.5000						
4	0.0669	0.0288	0.5000						
Chlorine Monoxide (ClO) ID:18									
1	0.1000	0.0768	0.6414						
2	0.1000	0.0768	0.6410						
Formaldehyde (H ₂ CO) ID:20									
1	0.3386	0.0986	0.6275	0.1821	0.6275	0.1256	0.7500	0.0343	0.7500
2	0.2984	0.0992	0.5763	0.1832	0.5763	0.1256	0.7500	0.0285	0.7500
3	0.3320	0.0994	0.6306	0.1838	0.6306	0.1262	0.7500	0.0332	0.7500
Nitrogen (N ₂) ID:22									
1	0.0347	0.0349	0.4009						
2	0.0348	0.0349	0.3957						
Methyl Chloride (CH ₃ Cl) ID:24									
1	0.3748	0.0973	0.7181						
2	0.3743	0.0969	0.7169						
Acetylene (C ₂ H ₂) ID:26									
1	0.1286	0.0693	0.7500	0.0904	0.5000	0.0872	0.5880	0.0434	0.4400
2	0.1460	0.0783	0.7500	0.1030	0.5000	0.0907	0.5880	0.0444	0.4400
3	0.1236	0.0667	0.7500	0.0872	0.5000	0.0864	0.5880	0.0432	0.4400
Phosphine (PH ₃) ID:28									



Ethane (C ₂ H ₆) ID:27									
1	0.1344	0.0788	0.9022						
2	0.1292	0.0760	0.8576						
Carbonyl Fluoride (COF ₂) ID:29									
1	0.1750	0.0845	0.9400						
2	0.1750	0.0845	0.9400						
Hydrogen Sulfide (H ₂ S) ID:31									
1	0.1451	0.0581	0.7500		0.0592	0.7000	0.0353	0.4600	
2	0.1480	0.0604	0.7500		0.0611	0.7000	0.0387	0.4600	
3	0.1467	0.0593	0.7500		0.0607	0.7000	0.0386	0.4600	
Hydroperoxil (HO ₂) ID:33									
1	0.3000	0.1005	0.6371						
Chlorine Nitrate (ClONO ₂) ID:35									
1	0.8000	0.1400	0.5000						
2	0.8000	0.1400	0.5000						
Hypobromous Acid (HOBr) ID:37									
1	0.1500	0.0600	0.6700						
2	0.1500	0.0600	0.6700						
Methanol (CH ₃ OH) ID:39									
1	0.4000	0.1000	0.7500						
Acetonitrile (CH ₃ CN) ID:41									
1	1.4839	0.1353	0.7200						
Diacetylene (C ₄ H ₂) ID:43									
1	0.2000	0.1000	0.7500						
Hydrogen (H ₂) ID:45									
1	0.0500	0.0500	0.7500		0.0500				
2	0.0500	0.0500	0.7500		0.0500				
Sulfur trioxide (SO ₃) ID:47									
1	0.1000	0.0700	0.7000						
Phosgene (COCl ₂) ID:49									
1	0.3000	0.0800	0.7500						
2	0.3000	0.0800	0.7500						
Methyl fluoride (CH ₃ F) ID:51									
1	0.3898	0.0802	0.7500						
Carbon disulfide (CS ₂) ID:53									
1	0.1081	0.0862	0.7167						
2	0.1067	0.0851	0.7188						
3	0.1074	0.0856	0.7183						
4	0.1083	0.0863	0.7180						
Nitrogen trifluoride (NF ₃) ID:55									
1	0.5000	0.1000	0.5500						
1	0.0927	0.0566	0.5753		0.0916	0.6255	0.0476	0.3030	
Sulfur Hexafluoride (SF ₆) ID:30									
1	0.0420	0.0500	0.6500						
Formic Acid (HCOOH) ID:32									
1	0.3229	0.1010	0.7500						
Oxygen atom (O) ID:34									
1	0.0500	0.0500	1.0000						
Nitric Acid Cation (NO ⁺) ID:36									
1	0.0500	0.0600	0.5000						
Ethylene (C ₂ H ₄) ID:38									
1	0.1138	0.0838	0.7669						
2	0.1235	0.0844	0.7609						
Methyl Bromide (CH ₃ Br) ID:40									
1	0.2874	0.0939	0.7978						
2	0.2890	0.0939	0.7972						
PFC-14 (CF ₄) ID:42									
1	0.0800	0.0780	0.6600						
Cyanoacetylene (HC ₃ N) ID:44									
1	0.1000	0.1000	0.7500						
Carbon Monosulfide (CS) ID:46									
1	0.0659	0.0731	0.7500						
2	0.0659	0.0731	0.7500						
3	0.0659	0.0731	0.7500						
4	0.0659	0.0731	0.7500						
Cyanogen (C ₂ N ₂) ID:48									
1	0.1000	0.1066	0.7500						
Sulfur monoxide (SO) ID:50									
1	0.0311	0.0312	0.7100						
2	0.0285	0.0293	0.7100						
3	0.0284	0.0292	0.7100						
Germane (GeH ₄) ID:52									
1	0.0693	0.0600	0.7500		0.1290	0.7900			
2	0.0693	0.0600	0.7500		0.1290	0.7900			
3	0.0693	0.0600	0.7500		0.1290	0.7900			
4	0.0694	0.0600	0.7500		0.1290	0.7900			
5	0.0693	0.0600	0.7500		0.1290	0.7900			
Methyl iodide (CH ₃ I) ID:54									
1	0.2992	0.1041	0.7500						

Table 1: Typical line-shape information for the main isotopologues in different collisional regimes. The tabulated values are: self w_{CO} , air w_{CO} , air ew_P , CO₂ w_{CO} , CO₂ ew_P , H₂ w_{CO} , H₂ ew_P , He w_{CO} , He ew_P , which were derived by averaging the parameters in HITRAN2020 for that isotopologue (Gordon et al., 2022), supplemented with H₂O in CO₂ parameters by (Devi et al., 2017; Régalia et al., 2019, compiled by Séverine Robert). The w_{CO} values are in [cm⁻¹/atm]. The line parameters are weighted layer-by-layer based on the ambient collisional regime and are supplemented with the air parameters when missing. Molecules with correlated-k tables are marked in yellow (see Section 3.2), and molecules with green headers have also high-energy (HITEMP and ExoMol) correlated-k tables (see Section 3.3).

The extended wings (beyond 25 cm⁻¹ from the line center) are only considered for atomic species, and are implemented in PSG following the quasi-static approximation (Burrows et al., 2000; Iro et al., 2003; Nefedov et al., 1999). The line center at each layer is calculated as:

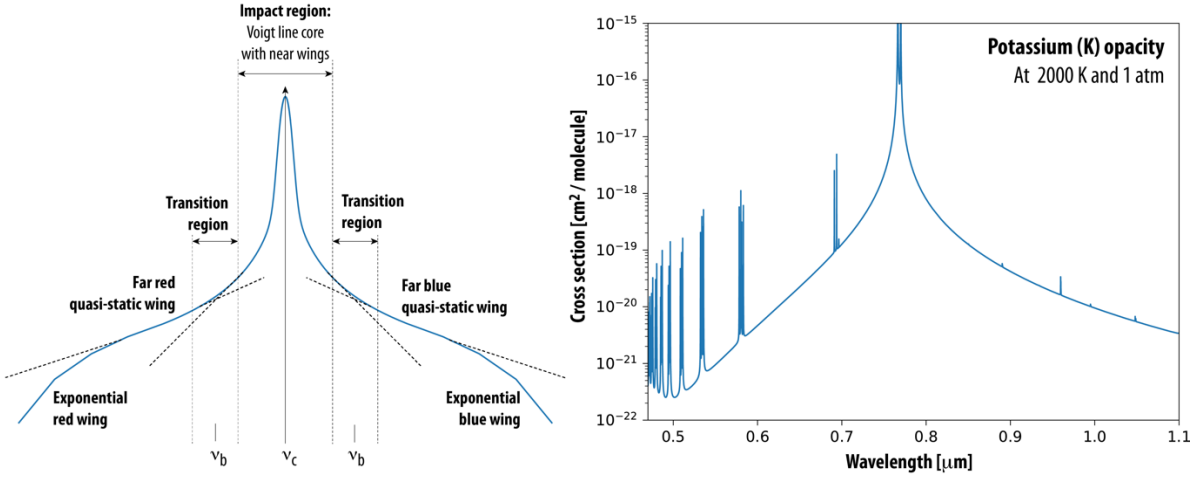


Figure 4: Anatomy of a spectroscopic line. **(Left)** Several regions dominate the shape of the line, in which the impact region captures the Voigt profile with Gaussian core and Lorentzian wings for molecules, while for atoms the line-shape extends greatly in frequency/wavelength into the quasi-static regime. The transition from the classical Lorentzian wing into the quasi-static region is defined by the detuning frequency (ν_b , eq. 24), in which the extended line-shape is affected by an exponential decay term (eq. 23). The vertical scale is logarithmic. **(Right)** Example of a simulation of the opacity for Potassium (K) at 2000 [K] and at a pressure of 1 [atm] (to be compared with Figure 5 in Burrows et al., 2000), in which one can see the linear $(\nu'-\nu)^{-3/2}$ decay of the lineshape following the quasi-static formalism (eq. 23).

$$\nu_c = \left[\nu_0 + P \, dv_P \left(\frac{T_{ref}}{T} \right)^{ev_P} \right] \left[1 - \frac{v_l}{c} \right] \quad (16)$$

where ν_0 is the line rest frequency at 1 [atm], P is the layer pressure [atm], dv_P is the pressure shift of the line, ev_P is the temperature dependence of the pressure shift and v_l is the Doppler velocity towards the observer at the layer. The linewidth (w_D) of the Gaussian Doppler core is a combination of the thermal kinetic broadening (w_T) and the apparent velocity broadening (w_R) introduced by the rotation of the planet:

$$w_D = \sqrt{w_T^2 + w_R^2} \quad w_T = v_c \sqrt{\frac{k_D T}{m}} \quad w_R = v_c \frac{v_R}{c} \quad (17)$$

where m is the molar mass [g/mol] of the isotopologue, k_D is the Doppler width parameter ($9.25108423 \times 10^{-14}$ [g/mol/K]) and v_R is the apparent velocity dispersion across the FOV. The Lorentzian component (w_L) is defined by the collisional environment (w_C) and the natural width (w_N) of the line as:

$$w_L = w_C + w_N \quad w_C = P \, w_{C0} \left(\frac{T_{ref}}{T} \right)^{ew_P} \quad (18)$$

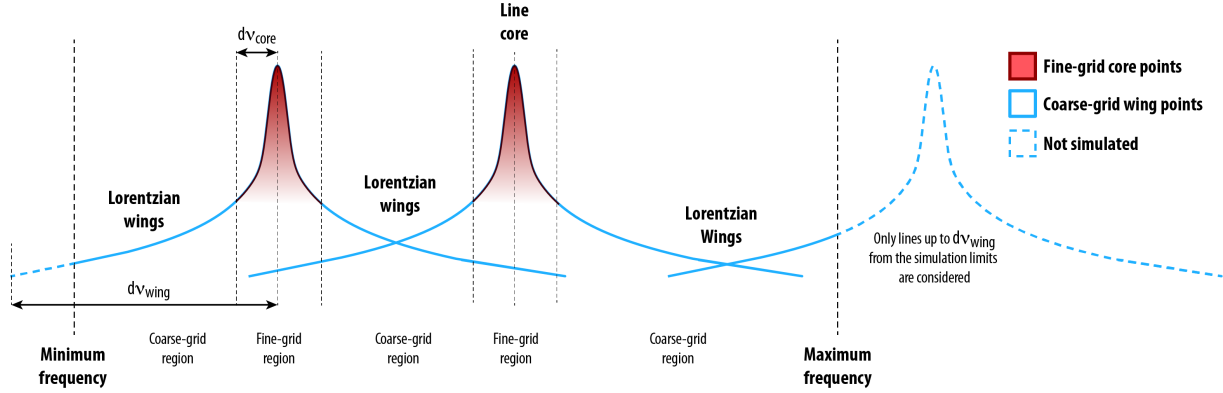


Figure 5: PSG employs a multi-grid scheme to simulate the line-shapes. The line cores (within dv_{core}) are synthesized at a fine resolution (at least dv_{min}) ensuring a proper handling of the Gaussian and Lorentzian components, while the Lorentzian wings (beyond dv_{core} and within dv_{wing}) are synthesized at a coarser resolution (dv_{core}) and later interpolated to the fine resolution grid. The interpolation from coarse to fine is only done once all the line shapes have been computed and PSG employs a 3-point spline interpolation scheme. Line shapes are shown on a logarithmic vertical scale.

where w_{C0} is the linewidth at 1 [atm] and ew_P is the temperature dependence of the linewidth (see mean values for many isotopologues in Table 1). For molecular species, w_N is negligible and assumed to be zero, while w_N is calculated from the atomic radiative damping constant (γ_{RAD} [s^{-1}]) as $w_N = \gamma_{RAD} / (4\pi c)$. Similarly, the collisional halfwidth of atoms can be derived from the Van der Waals damping constant (γ_6 [s^{-1}]) as $w_{C0} = \gamma_6 \cdot 8.62489e18 / (4\pi c)$, with $T_{ref}=296$ [K] and $ew_P=0.7$. Within the impact region or main region of the line (<25 cm^{-1}), the line profile at frequency ν for a line centered at ν_C is a Voigt function (modelled internally in PSG via the Fadeeva function) as:

$$k(\nu) = \int_{-\infty}^{\infty} \left[\frac{\exp(-(v' - \nu_C)^2 / 2w_D^2)}{w_D \sqrt{2\pi}} \right] \left[\frac{w_L}{\pi((v' - \nu_C)^2 + w_L^2)} \right] dv' \quad (19)$$

For molecules, the lines shapes are assumed to extend up to 25 cm^{-1} , while for atoms the far wings beyond the detuning frequency (ν_b) are further extended employing the basic form of the quasi-static approximation (see Figure 4) assuming $q=1$ as:

$$k(\nu) = (\nu - \nu_C)^{-3/2} \exp\left(-\frac{h(\nu - \nu_C)}{kT}\right) \quad (20)$$

The detuning frequency primarily depends on the collisional regime/partner and the ambient temperature. Considering the values of sodium and potassium in several collisional regimes (Nefedov et al., 1999), the ν_b for atoms can be approximated based on the ambient temperature (T) and atmospheric molar weight (m_{atm}) as:

$$\nu_b [cm^{-1}] = 25 \sqrt{\frac{T[K]}{250 \cdot m_{atm}[g/mol]}} \quad (21)$$



Once the line parameters are defined for all lines across all layers, it is critical to employ a spectral grid with a sufficiently high enough resolution that properly captures the shape across all species, lines, and layers. For instance, if the core of the line has a width of 0.001 cm^{-1} , the simulation would need up to ~ 5 points across the line and a synthesis grid resolution of $0.001/5 \text{ [cm}^{-1}\text{]}$ to properly capture the opacity across the line. All lines have a Gaussian core with a width defined by equation 20, which slowly transitions to a Lorentzian shape. The user may desire a simulation at a resolution of $dv_{\text{user}} \text{ cm}^{-1}$, but PSG will internally oversample the radiative transfer spectral grid by $dv_{\text{user}}/dv_{\text{min}}$ in order to ensure accurate line-shapes, in which dv_{min} is the minimum needed resolution to ensure up to ~ 5 spectral points per line core. Employing equation 20, dv_{min} can be defined as:

$$dv_{\text{min}}[\text{cm}^{-1}] = v_{\text{min}}/2 \sqrt{\frac{k_D T_{\text{min}}}{m_{\text{max}}}} \quad (22)$$

where v_{min} is the minimum frequency $[\text{cm}^{-1}]$ of the simulation, T_{min} is the minimum temperature across the atmosphere and m_{max} is the maximum molecular weight to be modelled. Far from the Gaussian core ($>1000dv_{\text{max}}$), the Lorentzian wings dominate and the line-shape follows a relatively monotonic $1/(v-v_c)^2$ dependence. As such one can employ a fine resolution grid for the line cores (within $dv_{\text{core}} = 1000dv_{\text{max}}$ of the line core), and a coarser grid beyond this limit all the way to the 25 cm^{-1} wing limit (dv_{wing}), see Figure 5. Once all the lines have been computed, PSG then performs a single interpolation from the coarse to the fine grid, permitting dramatic improvements in performance for line-by-line calculations with very low penalties in accuracy. Such a multi-grid scheme for modeling line-shapes was originally devised in the 80s (e.g., LINEPAK) and later integrated in many other radiative transfer codes (e.g., GENLN2, Edwards, 1992). In PSG, we have greatly improved the accuracy (typically better than $1e-5$) of the coarser-fine interpolation from the original methods by performing a 3-points spline interpolation.

3.2 Correlated-k calculations

When considering large frequency ranges, simulating millions of lines at high-resolution can become an unattainable task. An effective approach to address this issue is to pre-compute opacities at a broad range of temperatures, pressures and collisional regimes. To do this, a first approximation to the problem is to compute cross-sections at high-resolution, but such would require billions/trillions of spectral points in order to properly capture the line-shapes (dv_{min} , eq. 25) across the full 0.2 to $100,000 \text{ }\mu\text{m}$ wavelength range. One could store “binned” cross-sections with “average” cross-sections across spectral ranges, but that can lead to large errors when performing radiative transfer calculations. An alternative and very effective approach is the correlated-k method, in which instead of storing the “average” opacities across the spectral range, one stores the histogram or frequency of opacities across that range. For instance, in a 20-points correlated-k database, the tables would contain the probability of opacities across 20 histogram bins for every spectral range. In order to compute correlated-k tables, one first need to compute spectra at high-resolution ($<dv_{\text{min}}$) for a wide range of environments, and then compute histograms across the desired database spectral grid. A challenge with correlated-k tables is that they cannot be simply transformed to any spectral grid, in contrast to cross-section tables that a simple interpolation in frequency is possible. Typically,

radiative transfer models have pre-computed correlated-k tables for specific instrument resolutions, an approach not possible in PSG, due to the generic nature of our model. When using correlated-k tables to calculate opacities, the radiative transfer has to be computed for each correlated-k bin and the radiances then added weighting by the frequency of that opacity bin. Therefore a 20 points correlated-k table, requires 20 radiative transfer calculations per spectral point.

In PSG, we have pre-computed correlated-k tables in the 0.2 to 100,000 μm wavelength range with 20 opacity bins per spectral point for spectral resolving powers of $\text{RP}=500$ and $\text{RP}=5000$. All simulations in PSG requiring resolving powers higher than 5000, are computed employing the line-by-line method, while simulations with a maximum resolving power between >500 and 5000 are computed using the $\text{RP}=5000$ tables, and using the $\text{RP}=500$ for resolving powers lower than 500. The correlated-k tables are computed for 21 molecules (see Table 1) at a broad range of temperatures (20 cases from 40 to 2000K), pressures (17 cases, $1\text{E}-6$ to 100 bar) and collisional regimes (e.g., air, CO_2 , H_2 and He). These opacity correlated-k tables are two-dimensionally interpolated in P and T layer by layer by performing a bilinear interpolation in logarithmic scale. The opacities are converted from the natural $\text{RP}=500/5000$ spectral grids to the simulation spectral grid by performing a transformation in the cumulative density function (CDF, g -distribution) of the opacities within the bands encompassed by each simulation grid points. The method was nicely mathematically demonstrated and validated by (Leconte, 2021), and in PSG we employ an histogram oversampling of 5 when performing the g -distribution transformation.

3.3 High-temperature linelists: HITEMP and ExoMol

Linelists and their completeness play a fundamental role in the accuracy and precision of synthetic planetary spectra. The historical main driver of popular community databases (e.g., HITRAN, GEISA) has been the precise characterization of our own atmosphere, which rarely exceeds a temperature of 300K. These databases therefore omit information related to high energy transitions, which are only populated significantly at high temperatures. In the last decades and thanks to developments in molecular variational techniques for solving the nuclear motion problem, a revolution took place in the field of modeling high energy linelists. These methods are capable of generating accurate spectral parameters for millions/billions of lines when considering a precise potential energy surface (PES) and dipole moment surface (DMS). The ExoMol repository (Tennyson and Yurchenko, 2012) is now the leading repository for high-energy molecular linelists, containing billions of transitions, energy levels and partition functions for dozens of molecules/atoms and their isotopologues. A challenge with these databases is the sheer size of the linelists, in many cases containing billions of transitions for a single isotopologue, which can be particularly challenging to integrate into a radiative-transfer calculation. In addition, lineshape information is not readily available for each transition, so certain assumptions about lineshapes and collision regimes have to be assumed when operating with such databases.

As a bridge to capture the advances of high-energy linelists into classical databases, the HITRAN team developed HITEMP (Rothman et al., 2010), that preserves the format and structure of HITRAN, but integrates lines and/or pseudo-lines that capture the opacity effects of the billions of transitions into a more manageable linelist size. HITEMP also adds lineshape information based on



rotational quantum number progressions and laboratory studies. In PSG, we have integrated the spectroscopy of both databases, HITEMP and ExoMol, for the best characterized species at high-temperatures, and the ones that typically dominate the spectra of high-energy planets (i.e., H₂O, CO₂, CO and CH₄).

The computation of the correlated-k tables is done in PSG as reported in section 3.2, yet for the high-energy linelists we handle the modeling of lineshapes in an alternative manner. We first compute a high-resolution stick spectrum (no lineshape) for the billions of lines contained in these repositories for the 20 temperatures cases (40 to 2000K). For HITEMP, we integrate all lines, and for ExoMol, we integrate only the lines from the main isotopologue and complement it with isotopic lines of the rarer isotopes as reported in HITRAN. This is a valid assumption, since isotopic lines typically only complement opacity at spectral regions dominated by their fundamental bands, which are already well captured by HITRAN. The ExoMol line intensities are then scaled and integrated assuming telluric isotopic abundances, while HITEMP already integrates this scaling of the high-energy spectroscopic information. Since ab-initio high-energy calculations do not intrinsically provide lineshape information, we take the average lineshape information for each molecule as reported in Table 1, and we convolve the stick spectrum with a spectrally varying lineshape kernel. This dramatically accelerates the computation of high-energy opacities, and instead of computing billions of lineshapes, only 1-3 million lineshapes are computed per molecule. The lineshape kernel is varied across pressure, temperature and frequency following equations 17 and 18.

ID	Reference	Size	Regime
H₂O EXO[1]	ExoMol POKAZATEL Polyansky et al., 2018	Lines: 5,722,457,245 Levels: 810,269 Iso: 166,371 [HITRAN]	Air, CO ₂
CO₂ EXO[2]	ExoMol UCL-4000 Yurchenko et al., 2020	Lines: 2,557,549,930 Levels: 3,562,798 Iso: 370,638 [HITRAN]	Air, CO ₂
CO EXO[5]	ExoMol Li et al., 2015	Lines: 125,495 Levels: 6,383 Iso: 4,037 [HITRAN]	Air, CO ₂ , H ₂ , He
CH₄ EXO[6]	ExoMol MM database Yurchenko et al., 2024	Lines: 50,395,644,806 Levels: 9,155,208 Iso: 135,886 [HITRAN]	Air
H₂O HOT[1]	HITEMP Rothman et al., 2010	Lines: 114,241,164	Air, CO ₂
CO₂ HOT[2]		Lines: 11,193,608	Air, CO ₂
CO HOT[5]		Lines: 752,976	Air, CO ₂ , H ₂ , He
CH₄ HOT[6]	HITEMP Hargreaves et al., 2020	Lines: 31,880,412	Air

Table 2: List of high-energy databases available in PSG and the available operational collisional regimes.

3.4 Molecular cross-sections and UV modeling

For many species there are no available accurate Hamiltonians, and therefore linelists are not available, not permitting to perform line-by-line, nor correlated-k, computations. In addition, at high energies/frequencies (e.g., UV, optical), the energy structure of the molecules become increasingly non-quantized into a broad swath of energy levels. As such, classical linelists do not accurately characterize these high-frequency spectral regions, and laboratory measurements of molecular cross-sections are needed.

Similarly to correlated-k tables, cross-sections are needed at temperatures, pressures and collisional regimes similar to the simulation layer-by-layer parameters. This requirement is somewhat mitigated at UV wavelengths, since the effect of line-shapes and excitation properties are typically masked by the coarse frequency sampling at these very large frequencies. In PSG, we complement the classical line-by-line and correlated-k simulations in the UV/optical range, by ingesting UV/optical cross-sections for 44 species collected from a range of spectral databases. Most of these cross-sections originate from the MPI-Mainz Spectral Atlas (Keller-Rudek et al., 2013), which have been parsed, combined and formatted to provide a comprehensive and cohesive set of cross-sections per molecule across the 0.01 to 1 μm wavelength range. Additional UV cross-sections include those of O_3 by (Serdyuchenko et al., 2014), CO_2 by (Venot et al., 2018), the Herzberg O_2 continuum bands as well as the O_2 – O_2 absorption bands (Wulf bands, 0.24 and 0.3 μm) by (Fally et al., 2000), and the Herzberg O_2 band system (Jenouvrier et al., 1999; Mérienne et al., 2001, 2000). In PSG, we also integrate all HITRAN molecular cross-sections for trace species (Gordon et al., 2022).

3.5 Rayleigh and Raman scattering

At wavelengths approaching the size of the molecules, the oscillating electric field of a light wave acts on the charges within a particle, leading the molecule to become a radiating dipole. Rayleigh scattering results from the electric polarizability of the particles, and the elastically scattered radiation is at the same wavelength of the incoming radiation. Among those scattered photons, a small fraction is scattered inelastically, with the scattered photons having an energy different (usually lower) from those of the incident photons - these are Raman scattered photons. Modeling these processes can be particularly difficult, considering the wide range of possible interacting levels, the non-isotropic nature of these scattering processes, and the fact that radiation is absorbed at one wavelength and radiated at another wavelength. Furthermore, these processes depend on the molecular aggregate and environment, and numerically solving for these for a diverse set of the atmosphere compositions can be challenging.

Rayleigh cross-sections [$\text{m}^2/\text{molecule}$] are computed as a summation of the individual molecular cross-sections (Sneep and Ubachs, 2005), which are computed at wavelength λ [μm] based on the polarizability α_{pol} [\AA^3] of the encompassing molecules as:

$$\sigma_{\text{Rayleigh}}(\lambda) = \frac{\pi \cdot 8 \cdot 10^{-36}}{3} (\alpha_{\text{pol}} f_{\text{pol}})^2 \left(\frac{2\pi}{\lambda}\right)^4 \quad (23)$$

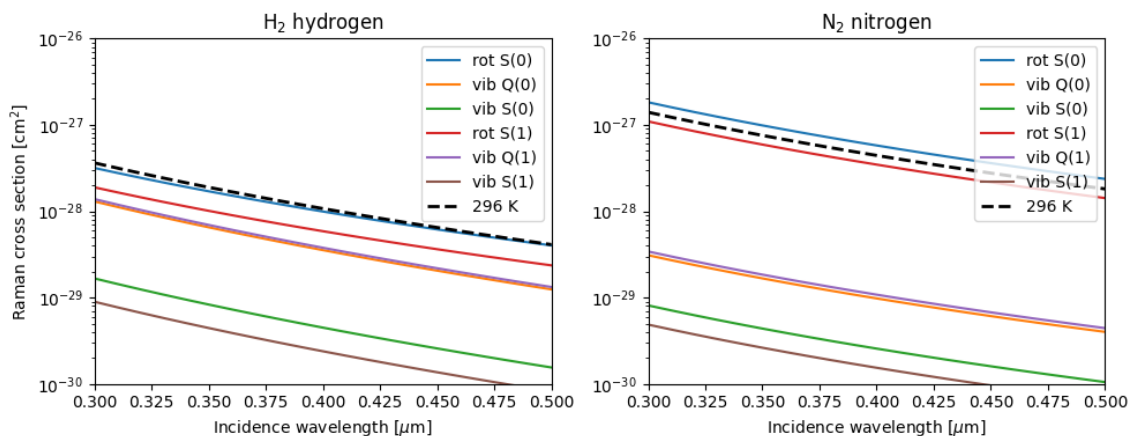


Figure 6: Raman cross sections for the first transitions of H_2 (left) and N_2 (right). The equivalent value at 296 [K] is computed by properly weighting the contribution from each line based on the level population at that temperature. The designation ‘vib’ refers to vibrational transitions in which the vibrational quantum number of the molecule changes from 0 to 1 (ground to first excited state), while ‘rot’ describes pure rotational transitions in which the vibrational quantum number does not change. S(i) denotes transitions in which the rotational quantum number increases by 2 (from i to i + 2), for Q(i) the rotational quantum number does not change, and for O(i) the rotational quantum number decreases by 2. These cross-sections have been computed following the methods in (Oklopčić et al., 2017), and are to be compared with the values presented in figure 14 of that paper.

In PSG, we employ polarizability values (α_{pol}) as compiled on the Computational Chemistry Comparison and Benchmark DataBase at NIST (<https://cccbdb.nist.gov/pollistx.asp>). Based on empirical measurements of the Rayleigh cross-sections of several molecules (Sneep and Ubachs, 2005), we adopt the following correction factors (f_{pol}): 1.0344 for N_2 , 0.9978 for CO, 1.1001 for CO_2 , 1.1298 for CH_4 , 1.0637 for O_2 , 1.0418 for N_2O , 0.9914 for SF_6 , 1.0724 for H_2 , and 1.0954 for H_2O . The scattering parameters are defined as $\omega=1$, $g_0=1.0$ and $g_2=0.1$ (see Chapter 5).

The effects of Raman scattering on planetary spectra are more subtle (typically a few percent), yet because the scattered radiation occurs at a different wavelength as the incidence flux, Raman scattering leads to observable spectral features in the I/F signal, which can be notably prominent at moderate/high resolutions. This also means that the scattering simulation has to be done for each specific Raman line individually, since the scattering delta-wavelength is different for each transition. Several numerical approximate methods exist to perform these calculations, yet in many cases they can be extremely computationally expensive. In PSG, we adopt a similar approach as implemented in PICASO (Batalha et al., 2019), in which the original method developed by (Pollack et al., 1986) is adapted to include the Raman cross sections for H_2 and N_2 computed by (Oklopčić et al., 2017). At the core of this method is the scaling of the “apparent” Raman scattering albedo at the emission wavelength by the ratio of the incoming/emitting solar fluxes. Since the scattering albedo can never exceed unity in PSGDORT, such method is only valid when other non-scattering opacity sources (e.g., CH_4 , H_2O , O_2 , O_3 , H_2 UV/optical absorptions) are also present in the atmosphere at these

wavelengths or when the difference between the impinging incidence/scattered stellar flux is small. The Raman extinction cross section (see Figure 6) is computed for each line of N₂ and H₂ as:

$$\sigma_{Raman}(\lambda) = \frac{C}{\lambda' \lambda^3} \quad (24)$$

where C is the cross-section factor calculated as presented in (Oklopčić et al., 2017), λ' is the incidence wavelength and λ^3 is the emission/scattering wavelength. The incident (λ') and scattered (λ) wavelengths are related by $1/\lambda'^{-1} = 1/\lambda + \Delta\nu$, where $\Delta\nu$ is the Raman shift of the transition. In PSG, we internally recreate the Hamiltonians for H₂ and N₂ and compute Raman opacities layer-by-layer considering the appropriate partition functions and energy populations. The total scattering albedo including Raman is approximated to be:

$$\omega(\lambda') = \frac{\sigma_{Rayleigh}(\lambda') + \sigma_{Raman}(\lambda') \left(\frac{F_*(\lambda')}{F_*(\lambda)} \right) + \sigma_{scatt}}{\sigma_{Rayleigh}(\lambda') + \sigma_{Raman}(\lambda') + \sigma_{absorb}} \quad (25)$$

where σ_{scatt} is the scattering fractional opacity due to aerosols, σ_{absorb} is the non-scattering absorbing opacity due to aerosols and molecules (e.g., UV molecular cross-sections), and $F_*(\lambda')/F_*(\lambda)$ is the ratio of the impinging incident to scattered solar/stellar fluxes.

3.6 Collision-Induced-Absorption (CIA) and the Water Continuum (MT_CKD)

Collision-induced absorption and emission are generated by inelastic collisions of molecules in a gas. Such inelastic collisions (along with the absorption or emission of photons) may induce quantum transitions in the molecules, or the molecules may form transient supramolecular complexes with spectral features different from the underlying molecules. Collision-induced absorption and emission is particularly important in dense gases, such as hydrogen and helium clouds found in astronomical systems. Different to regular molecular absorptions which are dependent linearly on the molecular column density, CIAs depend quadratically on the X-Y pair column densities. In that sense, such processes are particularly relevant in deep and high-density atmospheres but can also be quite relevant even at moderate fractional atmosphere pressures. In PSG, we integrate all CIAs available in HITRAN (Gordon et al., 2022), which are complemented with several other specifically defined CIAs, including several O₂-X pairs (Fauchez et al., 2020) in the infrared, the Wulf O₂-O₂ CIAs in the UV (Fally et al., 2000), and of several CO₂-X pairs (Turbet et al., 2020).

Another spectroscopic process associated molecular pairs with quite prominent and strong signatures is the water continuum, which have been historically modelled empirically employing a set for Fortran routines that form the MT_CKD model (Mlawer–Tobin–Clough–Kneizys–Davies, Clough et al., 2005). Although the physical process underlying the water continuum as described by the MT_CKD continuum is still under debate (Baranov and Lafferty, 2012; Shine et al., 2012), whether it is due to water dimers or collision induced absorption, both processes follow the same quadratic dependence on the water density. In PSG, we parameterize the temperature dependent MT_CKD continuum in terms of collision induced absorption (CIA) coefficients, following the methodology presented in (Kofman and Villanueva, 2021). The MT_CKD scripts outputs the water continuum

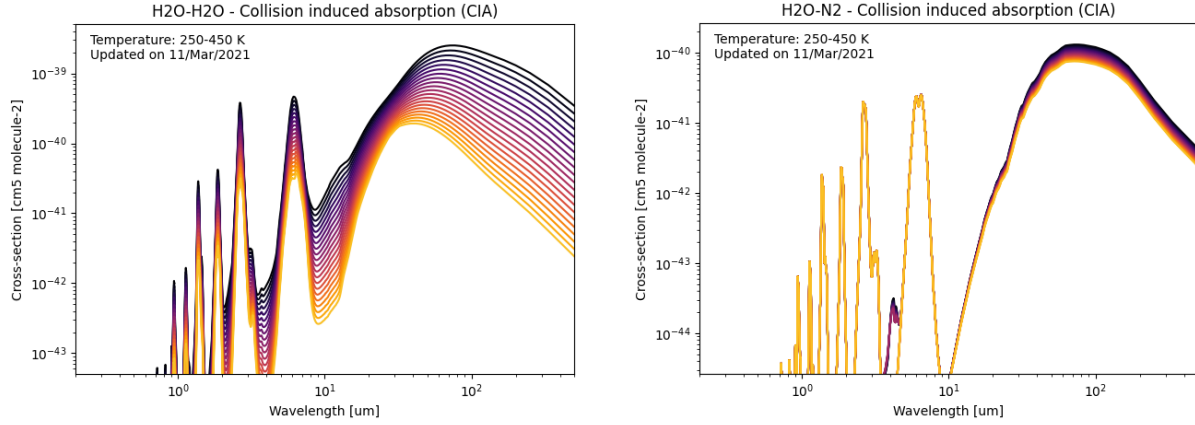


Figure 7: Water continuum (left: self, right: foreign) modelled as a Collision-Induced-Absorption (CIA) following the methods in (Kofman and Villanueva, 2021). The foreign values also include a known H₂O-N₂ CIA near 4 μm (appearing in dark blue/red on the left panel).

absorbance continuum coefficient, $C_s(\nu, T)$, which can be expressed in unit of $[\text{cm}^2 \text{ molecule atm}^{-1}]$, $C_s^*(\nu, T)$ or in units of $[\text{cm}^2 \text{ molecule cm}]$, $C_s(\nu, T)$. The former used most often in the literature, but the MT_CKD work reports the units in the latter, which will be used here. Conversion between both definitions are done using (Paynter et al., 2009; Shine et al., 2016):

$$C_s(\nu, T) = C_s^*(\nu, T) \frac{T}{296} \quad (26)$$

Opacity from the water continuum coefficient is calculated as following:

$$\tau(\nu, T) = l \rho_s R(\nu, T) \left[\frac{\rho_s}{\rho_0} C_s(\nu, T) + \frac{\rho_f}{\rho_0} C_f(\nu, T) \right] \quad (27)$$

Where $R(\nu, T) = \nu \tanh\left(\frac{h\nu}{2k_b T}\right)$ and is the radiative term (Clough et al., 1989), with h Planck's constant, c the speed of light, and k_b Boltzmann's constant (which is $1.36 \times 10^{-22} [\text{atm molecule}^{-1} \text{cm}^3 \text{K}^{-1}]$ for these calculations). Equations (1) and (3) can be combined to convert $C_s(\nu, T)$ to $k_s(\nu, T)$:

$$l k_s(\nu, T) \rho_s^2 = l \rho_s R(\nu, T) \frac{\rho_s}{\rho_0} C_s(\nu, T) \quad (28)$$

$$k_s(\nu, T) \rho_s = R(\nu, T) \frac{\rho_s}{\rho_0} C_s(\nu, T) \quad (29)$$

$$k_s(\nu, T) = \frac{1}{\rho_0} R(\nu, T) C_s(\nu, T) \quad (30)$$

The obtained values for $k_s(\nu, T)$ and $k_f(\nu, T)$ are shown in Figure 7, which have been also combined with the other known H₂O-N₂ CIAs. These are derived from the MT_CKD $C_s(\nu, T)$ values and include the radiative term. Note that k_f shows little temperature dependance, and mostly below 500 cm^{-1} k_s decreases as a function of temperature.

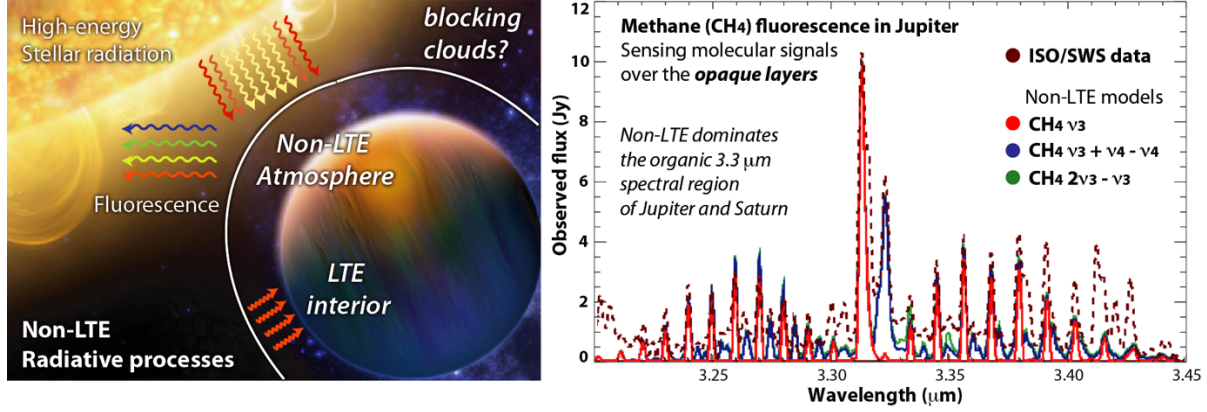


Figure 8: As the atmospheres are bombarded by high-energy photons from their partner stars, the upper layers efficiently emit via non-LTE processes. This disequilibrium has been observed in many planets of our solar system (shown is the detection of non-LTE methane in Jupiter, Encrenaz et al., 1996), and it is certainly active in many exoplanets' atmospheres.

4. Non-Local Thermodynamical-Equilibrium (non-LTE) modeling

When collisions are infrequent enough to equilibrate the radiative populations of the molecules, an atmosphere is considered to be in non-local thermodynamical equilibrium (non-LTE). Then, the classical Boltzmann distribution equation describing the population of the molecular energy levels and the Planck's function assumed to describe the source radiation terms are no longer valid. This primarily occurs in the tenuous regions of the atmosphere, where collisions are infrequent and solar radiation is strong and unattenuated, leading to strong emissions as the molecules cascade back to their ground state. The radiative equilibrium equation for a two-level system can be written as:

$$\frac{n_u}{n_l} = \frac{g_u}{g_l} \exp(-h\nu/KT) \left[\frac{1 + \rho B_{lu}/C_{lu}}{1 + A_{ul}/C_{ul}} \right] \quad (31)$$

where n are the populations of the upper (u) and lower (l) levels, g the statistical weights, T is the local kinetic temperature, C_{lu} and C_{ul} the collisional excitation and relaxation rates respectively, B_{lu} and A_{ul} are the Einstein coefficients for absorption and spontaneous emission, and ρ is the impinging excitation flux.

The Einstein coefficients are radiative properties of the levels in question, while the collision rates are dependent on the local temperature ($\propto \sqrt{T}$) and density. At high pressures, collisions dominate the radiative processes ($C \gg A_{ul}$ or $C \gg B_{lu}$), and the relative populations of the levels can be simply described by Maxwell-Boltzmann statistics (LTE) dependent on the local kinetic temperature. In regions with strong external radiative fields (ρ), and more infrequent collisions ($C \ll A_{ul}$ or $C \ll B_{lu}$), the radiative parameters start to define the energy balance of the molecule and its emitting spectrum (non-LTE).

As nicely summarized by (Appleby, 1990), non-LTE starts to become relevant for methane in the mesosphere of the giant planets (e.g., Jupiter, Saturn, Uranus, Neptune, see Figure 8) at pressures

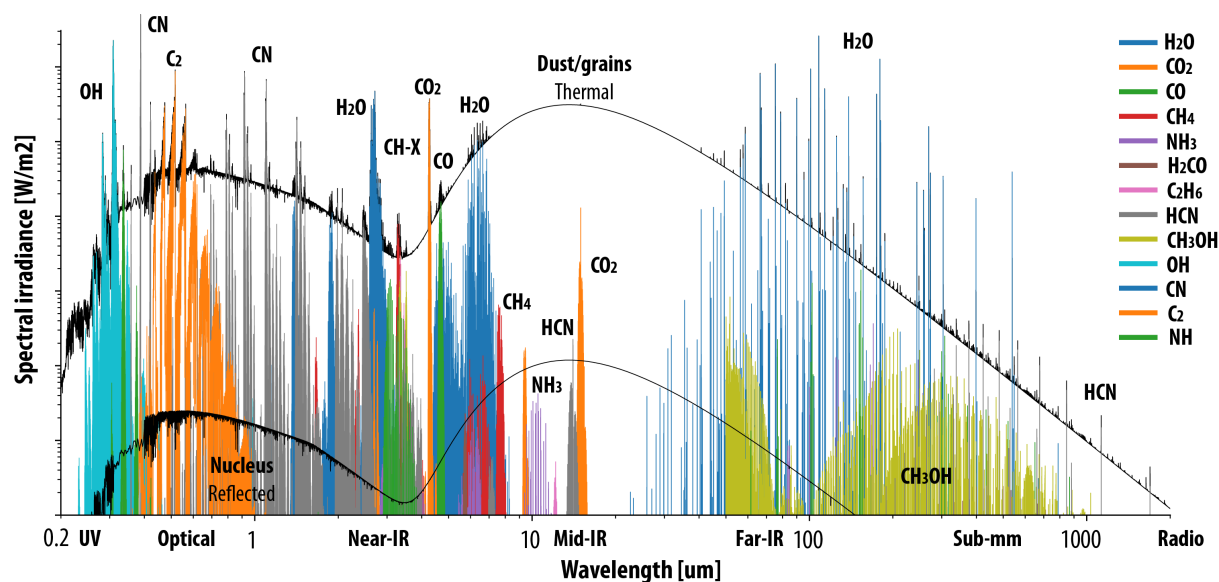


Figure 9: Simulated components of a cometary spectrum (the nucleus and dust coma are shown in black, while each molecular gas emission is identified with different colors) across most of the electromagnetic spectral range using PSG (see further details in our review about radiative processes in Comets III, Bodewits et al., 2022). The model includes nucleus and dust/grains emission (see chapter 6), non-LTE fluorescence emissions dominating the UV/Optical/near-IR, and thermal emissions dominating the longer wavelengths beyond the near-IR.

less than 0.1 [mbar]. In CO₂ rich atmospheres (e.g., Mars, Venus), the efficient collisional rates for this molecule, keeps LTE up to much lower densities (>1 [μ bar], Lopez-Puertas and López-Valverde, 1995). In the atmospheres of hot-giants, stronger radiation fields will bring this limit deeper into the atmosphere, while higher kinetic temperatures will push LTE further up in the atmosphere. Chemical reactions also lead molecules into highly excited non-equilibrium states, from which diagnostic photons are released, as it is the case for the dayglow O₂(1 Δ) emission tracking the photo-destruction of O₃ in terrestrial atmospheres.

Non-LTE affects two key parameters in a radiative transfer simulation, the opacity terms and the source function. Specifically, the intensity of the line no longer follows a simple LTE relationship (eq. 13), but it is computed from a non-equilibrated population. Similarly, the source function $S(\tau)$, typically considered to be a blackbody in equation 2, is now computed based on the specific radiative equilibrium constants for that level/wavelength.

In PSG, we have implemented a method in which the user can provide non-equilibrated populations, and the radiative transfer will compute non-LTE populations and source functions accordingly. The user must provide vertical profiles of vibrational temperatures [K] (computed relative to the ground-state) for every isotopologue and vibrational band, in the form of "Tvib[MOL:ISO:IDvib]" (MOL:HITRAN molecular ID, ISO:Isotopologue ID, IDvib: vibrational band ID as defined for the isotopologue [see vibrational bands in the line-list help]). For instance "Tvib[6:1:7]" would correspond to the $v_3=1$ level of the main isotope of CH₄.

5. Cometary modeling (CEM module)

In comets, non-equilibrated atmospheres are particularly prevalent due to the typical low densities across most of their coma. The structure and composition are defined as presented in chapter 3, while the emitted fluxes are computed by the PSG Cometary Emission Model (CEM).

The spectra of a comet can be divided into three main components (see Figure 9): the nucleus (reflected, emitted and absorbed radiation), coma grains or dust (reflected, emitted and absorbed radiation), and the coma gas emissions (e.g., LTE, non-LTE). The Cometary Emission Model (CEM) employs the PSG surface models, as described in chapter 6, to simulate the nucleus and the grains components, while the gas emissions are calculated by employing radiative transfer methods considering non-LTE and/or LTE excitation processes. The nucleus is assumed to be a spherical emitting surface, while the dust in the coma is calculated as a diffuse and extended emitting component. The outgassing of dust-grains and parent molecular species is assumed to be isotropic and at constant expansion velocity, with photo-dissociation defining the lifetime and spatial extent of molecular species. Using these assumptions, the integrated number of molecules (N [molecules]) within the FOV is defined as $N_{\text{gas}} = Q \cdot \tau \cdot f(x)$, where τ is the molecular lifetime [s], $f(x)$ is the filling-factor of the FOV with respect to the total coma, and Q is the molecular production rate [molecules/s]. The definition and calculation of $f(x)$ is complex, and we employ a combination of analytical methods that make use of Bessel functions (see chapter 3). Two possible excitation regimes are considered in PSG for the molecules: non-LTE fluorescence (typically dominating the flux in the UV-Optical-IR range) and LTE excitation (modelled using the methods as previously described in this section). In PSG, we model cometary non-LTE by ingesting fluorescence efficiencies (g-factors) which are pre-computed for a particular rotational temperature and solar radiation flux (e.g., Villanueva et al., 2013, 2012b, 2012a, 2011). These line lists can be applied to other similar exospheres of comparable low-collisional rate and high-insolation rate (see simulation example in Figure 9). For the dense inner regions of the coma, the fluorescence pumps can become optically thick, and an approximate treatment for opacity is discussed in section 6.3, while a full non-LTE solver and multi-shells radiative transfer algorithm can be employed for pure rotational lines (see section 6).

These assumptions are generally accurate enough (and widely employed by the community) to determine integrated column densities and molecular fluxes across the coma, yet the lifetime and velocity of the dust-grains can be mass/size/composition dependent and may differ from the surrounding gas environment. On the other hand, the strong relationship between visual magnitude (mainly defined by dust) and water production for 37 comets (Jorda et al., 2008) indicates that a common dust and gas outgassing scheme should be accurate enough for most cases, and in PSG we employ a relationship between dust radiation and gas production rate, that the user can scale as needed ($\langle \text{SURFACE-GAS-RATIO} \rangle$ of 1.0 is assumed to be typical, yet it is an adjustable parameter in CEM). The dust intensity is corrected by opacity following $A_{\text{em}} = A_{\text{beam}} \cdot (1.0 - \exp(-O_{\text{dust}}))$, with the dust opacity calculated as $O_{\text{dust}} = N_{\text{dust}} \cdot (A_{\text{dust}}/A_{\text{beam}})$, where A_{beam} is the area of the FOV at the comet. Further details on the nucleus and grain modeling are summarized in chapter 6.



6. Non-LTE modeling in cometary atmospheres

When modeling cometary atmospheres, the radiative transfer can become relatively complex, since the low densities, highly radiated environment and chemically rich coma leads to a plethora of excitation processes (see Figure 2 in chapter 3). As we summarized in the previous section, one can model infrared fluorescence effectively by employing pre-computed g-factor efficiencies. This is mainly possible because of three reasons: a) at infrared wavelengths, the FOVs are typically small with fluxes dominated by emissions originating in the inner coma, in which rotational levels are normally equilibrated, b) non-LTE fluorescence emissions are typically quite fast, and do not affect the overall populations of the molecules, and c) infrared fluorescence emissions are typically optically thin, and emission fluxes can be derived by analytical coma integrations and tabulated fluorescence efficiencies. At longer wavelengths ($>10 \mu\text{m}$) and when sampling ground rotational levels, the situation becomes more complex, since the FOVs at these wavelengths tend to be much larger, the lines are optically thicker, and the level populations are ultimately defined by a complex balance between emissions, solar pumping and collisions.

In the eighties, the pioneering work by (Bockelée-Morvan, 1987; Chin and Weaver, 1984; Crovisier and Encrenaz, 1983; Weaver and Mumma, 1984) set the foundation of most modern models for the interpretation of cometary spectra. These models were later advanced to include the effects of collisions with electrons (Biver, 1997; Xie and Mumma, 1992), and benchmarked with modern Montecarlo models (Bensch and Bergin, 2004; Zakharov et al., 2007), among other advancements. In PSG, we build on these works and expand to include the latest fluorescence models (Villanueva et al., 2013, 2012b, 2012a, 2011) and spectroscopy (e.g., Gordon et al., 2022). Specifically, we focus here on the time-dependent solution of rotational levels, in which the molecules are followed upon their release from the nucleus, and a careful balance across the levels is determined by integrating emission, absorption and collisions rates into a set of differential equations. In this problem, the “knowns” are the underlying molecular and electron abundances across the coma, and the emission/rates/absorption rates per molecule and level; while the “unknowns” are the individual level populations at each location of the coma. At each location of the coma, or spherical “shell”, the rates are determined from spectroscopic databases, and lead to a matrix of input/output for each level. A numerical solver of “stiff” differential equations is then used to solve the N system of equations, where N is the number of levels. We employ LSODA (Livermore Solver for Ordinary Differential equations with Automatic stiff mode, Hindmarsh, 1983; Petzold, 1983) to solve this problem.

At first, we need to establish the foundational properties of the coma across a broad range of distances (e.g., 10 to 1 million kms from the nucleus). This includes the density [m^{-3}] of the underlying main collisional constituent (typically H_2O within $R_h=1\text{AU}$), the density [m^{-3}] of the molecule investigated, the kinetic temperature [K], the electron density [m^{-3}], the electron temperature [K], and the expansion velocity [m/s]. These properties can be defined based on known properties of the comet, and also from typical profiles observed in comets. The atmosphere density [m^{-3}] is defined as:

$$n_{\text{atm}}(r) = \frac{Q_{\text{atm}}}{4\pi r^2 v_{\text{exp}}} \exp\left(-r \frac{\beta_{\text{atm}}}{v_{\text{exp}}}\right) \quad (32)$$

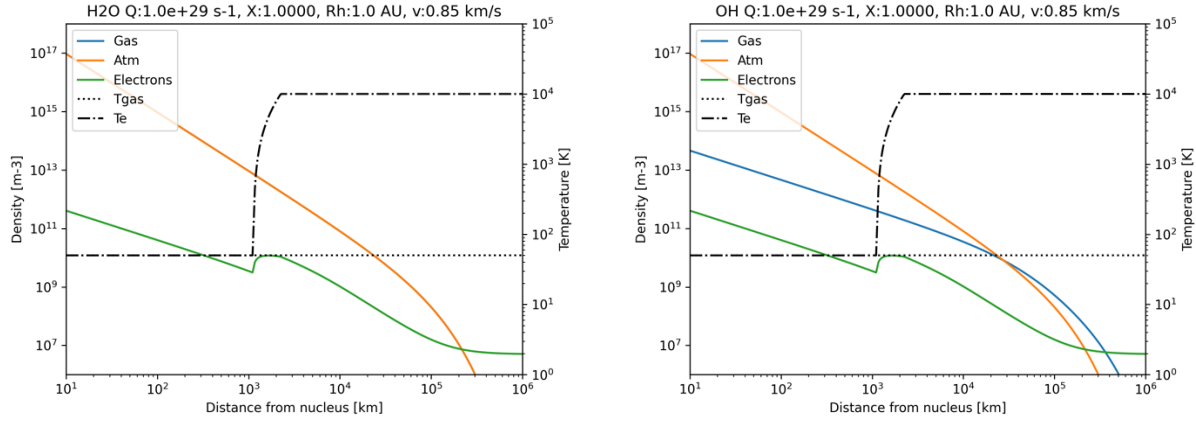


Figure 10: Structure of a cometary atmosphere for a water production rate of $1e29$ molecules per second, and expansion velocity of 0.85 km/s and at $R_h=1$ AU. The left panel shows the profile for water as the ambient and modelled gas, and the right panel the spatial profile of the daughter OH molecule. Electron densities and temperatures are computed following the methods described in this section, and match very well to those presented in (Bensch and Bergin, 2004; Zakharov et al., 2007) for the same conditions.

where r is the distance from the nucleus [m], v_{exp} the expansion velocity [m/s], Q_{atm} is the ambient production rate [molecules/s] and β_{atm} is the photodissociation rate [s^{-1}] of the ambient molecule. The photodissociation rates can be scaled from the tabulated values at $R_h=1$ AU by scaling them by R_h^{-2} . For the modelled molecule, one could have a parent (e.g., H_2O) of a daughter fragment (e.g., OH), and could employ equation 32 for the former, and the following equation for the latter:

$$n_{mol}(r) = \frac{Q_{mol}}{4\pi r^2 v_{exp}} \frac{\beta_1^{-1}}{(\beta_0^{-1} - \beta_1^{-1})} \left[\exp\left(-r \frac{\beta_0}{v_{exp}}\right) - \exp\left(-r \frac{\beta_1}{v_{exp}}\right) \right] \quad (33)$$

where β_0 is the photodissociation rate [s^{-1}] of the parent molecule, and β_1 is the photodissociation rate [s^{-1}] off the daughter fragment. For simplicity in our model, we assume isotropic outflow with constant expansion velocity and a constant kinetic temperature [T_{kin}] across the coma.

For the electron properties, we employ the prescription as summarized in (Biver, 1997; Xie and Mumma, 1992), which are based on measurements in the coma of 1P/Halley by *Giotto* mass spectrometers and include physically justified scaling laws to account for their dependency with the water production rate and heliocentric distance of the comet. The electron density [m^{-3}] is defined as:

$$n_e(r) = x_{ne} \left(\frac{Q_{atm} k_{ion}}{v_{exp} k_{rec} r_h^2} \right)^{0.5} \left(\frac{T_e}{300} \right)^{0.15} \left(\frac{R_{rec}}{r^2} \right) \left[1 - \exp\left(-\frac{r}{R_{rec}}\right) \right] + \frac{5e6}{r_h^2} \quad (34)$$



where $k_{\text{ion}} [4.1\text{e-}7 \text{ s}^{-1}]$ is the water photoionization rate at $r=1\text{AU}$ and k_{rec} is recombination rate $[\text{m}^3\text{s}^{-1}]$ for electrons with H_3O^+ ions at electron temperature T_e [K], calculated as $k_{\text{rec}}=7\text{e-}13(300/T_e)^{1/2}$. $R_{\text{rec}} = 3.2\text{e}6 \ x_{\text{re}} (Q_{\text{atm}}/1\text{e}29)^{1/2} [\text{m}]$ is the recombination surface defining the active region for electron recombination, and x_{ne} and x_{re} are scaling factors relative to *Giotto* (Xie and Mumma, 1992), both assumed to be 1 here. The electron temperature varies greatly (from T_{kin} to $T_e^{\text{MAX}}=1\text{e}4$ [K]) with distance and it is prescribed relative to the contact surface ($R_{\text{CS}} = 1.125\text{e}6 \ x_{\text{re}} (Q_{\text{atm}}/1\text{e}29)^{3/4} [\text{m}]$) as:

$$T_e(r) = \begin{cases} T_{\text{kin}} & r < R_{\text{CS}} \\ T_{\text{kin}} + (T_e^{\text{MAX}} - T_{\text{kin}}) \left(\frac{r}{R_{\text{CS}}} - 1 \right) & R_{\text{CS}} \leq r \leq 2R_{\text{CS}} \\ T_e^{\text{MAX}} & r > 2R_{\text{CS}} \end{cases} \quad (35)$$

Five terms describe the main parameters at each r location, with the first set of rates describing the gas collisional rates $C^{\text{gr}} [\text{s}^{-1}]$, the rates induced by collisions with electrons $C^{\text{er}} [\text{s}^{-1}]$, and then the radiative terms, with $A^{\text{r}} [\text{s}^{-1}]$ as the Einstein A coefficients for spontaneous emission, $B [\text{J}^{-1} \text{s}^{-2} \text{cm}^3]$ as the Einstein B coefficients for absorption (with J_v as the impinging rotational flux $[\text{J s cm}^{-3}]$), and G as the fluorescence pumping rates $[\text{s}^{-1}]$.

If we assume an optical thin case, the last three matrix terms are constant and common across the coma, but as we discuss later, we can affect the A terms by opacity considering the escape probability principle. The collisional terms (C^{gr} and C^{er}) are by de-facto dependent on the local density which drops greatly with distance ($\sim 1/r^2$), and this together with the large changes in T_e (affecting C^{er}) across the coma leads to large variations of the rates with distance, ultimately requiring an “stiff” solver of differential equations for this problem.

$$\frac{d}{dt} \begin{bmatrix} n_1 \\ \vdots \\ n_N \end{bmatrix} = \left\{ \begin{pmatrix} C_{11}^{\text{gr}} & \cdots & C_{1N}^{\text{gr}} \\ \vdots & \ddots & \vdots \\ C_{N1}^{\text{gr}} & \cdots & C_{NN}^{\text{gr}} \end{pmatrix} + \begin{pmatrix} C_{11}^{\text{er}} & \cdots & C_{1N}^{\text{er}} \\ \vdots & \ddots & \vdots \\ C_{N1}^{\text{er}} & \cdots & C_{NN}^{\text{er}} \end{pmatrix} \right. \\ + \begin{pmatrix} A_{11}^{\text{r}} & \cdots & A_{1N}^{\text{r}} \\ \vdots & \ddots & \vdots \\ A_{N1}^{\text{r}} & \cdots & A_{NN}^{\text{r}} \end{pmatrix} + \begin{pmatrix} B_{11} & \cdots & B_{1N} \\ \vdots & \ddots & \vdots \\ B_{N1} & \cdots & B_{NN} \end{pmatrix} J_v \\ \left. + \begin{pmatrix} G_{11} & \cdots & G_{1N} \\ \vdots & \ddots & \vdots \\ G_{N1} & \cdots & G_{NN} \end{pmatrix} \right\} \begin{bmatrix} n_1 \\ \vdots \\ n_N \end{bmatrix} \quad (36)$$

If we organize the levels in ascending order of energy, then the A^{r} matrix would only have values in the lower-left part, since emissions only occur from upper-to-lower levels, while the B matrix will only have values in the upper-right corner, since absorptions only occur from lower-to-upper. These two matrixes will also be sparsely populated and defined by the line selection rules of the molecule. All these matrixes share a common property, the diagonal terms are negative and act as “balancers” of the equations in order to ensure mass/population conservation (i.e., rates from x to y , imply a gain to y and a loss to x). In that case, each column in this matrix should add to 0.

If a molecule collides with an ambient molecule at T_{kin} , it can get excited (lower→upper) and also de-excited (upper→lower). De-excitation collisional rates (C_{ul}^g) are typically tabulated for different molecules-pairs and temperatures in units of $[cm^3 s^{-1}]$, which are scaled to each coma distance by multiplying by the ambient density $[cm^{-3}]$ at r , leading to $C_{ul}^{gr} [s^{-1}]$. In PSG, we integrate the collisional de-excitation rates for many molecules with H_2 at different temperatures as compiled in the Leiden Atomic and Molecular Database (LAMDA, Schöier et al., 2005). The user can scale these arbitrarily with C_{sc1} , for instance we found $C_{sc1}=m_{atm}/m_{H2}=9$ to be effective when matching to the H_2O - H_2O rates as reported in (Buffa et al., 2000). Excitation rates (C_{lu}^{gr}) are computed from C_{ul}^{gr} by employing the balance equation:

$$C_{lu}^{gr} = C_{ul}^{gr} \frac{w_u}{w_l} \exp(-[E_u - E_l]c_2/T_{kin}) \quad (37)$$

where c_2 is the second radiation constant ($1.43877736 [K/cm^{-1}]$), w is the statistical weight of the level, and E its energy $[cm^{-1}]$. For molecules without collisional rates, we assume an average cross-section of $\sigma_c = 5e-18 m^2$ across all levels. Such assumption ultimately implies that after a collision, the molecule is redistributed among the rotational levels according to the Boltzmann distribution at T_{kin} (Crovisier, 1987), and therefore $C_{lu}^g = C^g n_u^{th}$ (with the exception of $u=l$ values, which is the diagonal term and balances that matrix, see also Biver 1997). The collisional cross-section $\sigma_c [m^2]$ is transformed into a collisional rate $C^g [m^3 s^{-1}]$ by multiplying by the average collisional kinetic velocity $v_{kin} [m s^{-1}]$, with $C^g [m^3 s^{-1}] = \sigma_c v_{kin}$ and:

$$v_{kin} = \sqrt{\frac{N_A 8e3kT_{kin}}{\pi} \left[\frac{1}{m_{atm}} + \frac{1}{m_{mol}} \right]} \quad (38)$$

in which $m_{atm} [g/mol]$ is the molar mass of the atmosphere, $m_{mol} [g/mol]$ is the molar mass of the modelled molecule, N_A is Avogadro's constant ($6.022140857e23 [molecules/mol]$), and k is the Boltzmann's constant ($1.3806505e-23 [m^2 kg / (s^2 K)]$).

The electron collisional de-excitation (C_{ul}^{er}) and excitation rates (C_{lu}^{er}) can be computed from the spectroscopic Einstein coefficients (A_{ul}) following the methodology described in (Biver, 1997; Xie and Mumma, 1992). Specifically and if we assume that the kinetic velocity of the electrons dominate the excitation process, the rates are computed as:

$$C_{ul}^{er} = n_e(r) v_e(r) \sigma_{ul}^e 2a_{ul} \exp(a_{ul}) K_0(a_{ul}) \quad (39)$$

$$C_{lu}^{er} = n_e(r) v_e(r) \frac{w_u}{w_l} \sigma_{ul}^e 2a_{ul} \exp(-a_{ul}) K_0(a_{ul}) \quad (40)$$

where $v_e [m/s]$ is the average thermal speed of the electrons $[8kT_e/(\pi m_e)]^{1/2}$, m_e is the electron mass ($9.10938e-31 kg$), and K_0 is the modified Bessel functions of the second kind. The coefficient a_{ul} relates to the electron temperature as $a_{ul} = (E_u - E_l)c_2/2T_e$, while the collisional cross-section $[m^2]$ are derived from the transition Einstein $A_{ul} [s^{-1}]$ following (Itikawa, 1972):

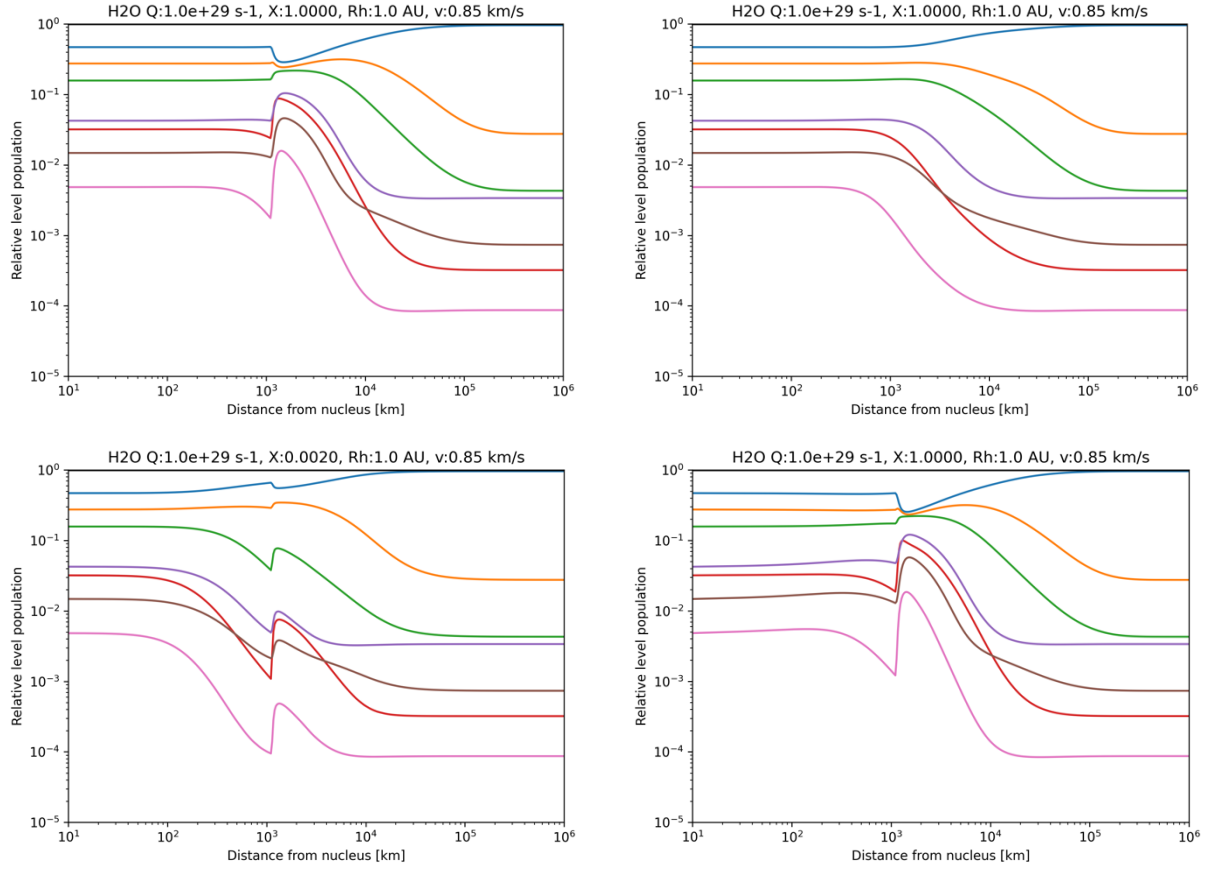


Figure 11: Level populations of water as computed with the methods described here, for difference abundance ratios and collisional regimes. **Top-left:** for $Q_{\text{atm}}=Q_{\text{gas}}=1\text{e}29\text{ s}^{-1}$ at $R_h=1\text{AU}$, $v_{\text{exp}}=0.85\text{ km/s}$; **top-right:** same as top-left but without electron collisions; **bottom-left:** assuming a gas abundance of 0.002 (e.g., H_2^{18}O); **bottom-right:** same as top-left but without considering neutral collisions. These results match very well to those presented in (Bensch and Bergin, 2004; Zakharov et al., 2007) for similar conditions, even though we use scaled collisional rates (scaled from $\text{H}_2\text{O}-\text{H}_2$), employ our own computed G rates, and employ updated spectroscopy considering the latest ExoMol and HITRAN2020 databases.

$$\sigma_{ul}^e = A_{ul} \frac{m_e q_e^2}{16\pi^2 c \epsilon_0 h^2 v_{ul}^4} \quad (41)$$

where q_e is the elementary charge ($1.602176634\text{e-}19\text{ [C]}$), c is the speed of light ($2.99792458\text{e}8\text{ [m/s]}$), ϵ_0 is vacuum's permittivity ($8.854187812\text{e-}12\text{ [F/m]}$), h is Planck's constant ($6.62606896\text{e-}34\text{ [J s]}$), and v_{ul} is the line frequency [cm^{-1}].

As we now explore the radiative terms, the absorption coefficients $B\text{ [J}^{-1}\text{ s}^{-2}\text{ cm}^3]$ can be calculated from the Einstein A coefficients as:

$$B_{lu} = A_{ul} \frac{w_u}{w_l} \frac{1}{8\pi h v_{ul}^3} \quad (42)$$

The set of equations listed in equation 36 pertain only to the rotational levels, yet in reality the molecule absorbs (B) and emits (A) radiation across all wavelengths and all the way to infrared/optical/UV. For instance, a recent linelist of water (Villanueva et al., 2012b and refs. therein), contains 500 million lines and 29,000 levels, which would require a differential system of equations with $N=29,000$, an impractical task. Considering that the higher energy transitions are much more transient and less strong than the pure rotational lines, one can separate the problem into the pure rotational terms (equation 36) and the higher-energy pumps/emissions/cascades (G rates). Therefore, the B matrix in equation 36 refers only to absorptions at radio/rotational wavelengths, in which J_v is mostly dominated by the CMB (Cosmic Microwave Background). Thermal dust emission, nucleus emission and solar radiation at these wavelengths are also relevant, yet of typically lower intensity (Biver, 1997; Crovisier and Encrenaz, 1983), and therefore neglected for simplicity here. The CMB flux [J s cm^{-3}] for $T_{\text{CMB}}=2.725$ [K] is computed as:

$$J_v = \frac{2h\nu_{ul}^3}{\exp(\nu_{ul}c_2/T_{\text{CMB}}) - 1} \quad (43)$$

The two main radiative terms are defined by A and G rates, which dominate equation 36 in the outer regions of the coma when collisions are infrequent. The challenge is that at large opacities, the emissions can be quickly re-absorbed, and the effective impact of these decay rates gets reduced. An approach to treat this problem in comets was initially formulated for water by Bockelée-Morvan (1987), which is called “escape probability” (Sobolev’s method), in which the opacity effects are treated for the “average” photon at the systemic velocity. At the core of this method, there is the β parameter, which effectively behaves as an emission A_{ul} scaler, and therefore $A_{ul}^r = A_{ul} \beta_{ul}^r$. This parameter is dependent on the prevailing opacity τ , which is computed as:

$$\tau = B_{lu}h \frac{n_{mol}(r)r}{v_{exp}} \left(\frac{w_l}{w_u} n_u - n_l \right) \quad (44)$$

Depending on the local line opacity, three regimes are then possible 1) for low opacities ($0 \leq \tau \leq 1e-4$), we would be in an optically thin case and therefore $\beta_{ul}^r=1$; 2) for maser conditions in which τ is negative, β would then correspond to a maser amplification factor that can be approximated as $\beta_{ul}^r = (1-\exp(-\tau))/\tau$ (Bockelée-Morvan, 1987); 3) for $\tau > 1e-4$, the β parameter operates as a moderator of the A rates based on the prevailing local opacity τ , which operating under the principles of “escape probability” for a spherical expanding atmosphere, β is approximated as (Biver, 1997):

$$\beta_{ul}^r = \frac{2}{3\tau} - \frac{\exp(-\tau/2)}{3} \left\{ K_1\left(\frac{\tau}{2}\right) + \tau \left[K_0\left(\frac{\tau}{2}\right) - K_1\left(\frac{\tau}{2}\right) \right] \right\} \quad (45)$$

where K_0 and K_1 are the modified Bessel functions of the second kind.

The last term in equation 36 is the one referring to the pumping G rates, which capture the pumping from rotational levels and the sub-sequent cascades back into other rotational levels. Figure 3 in (Bensch and Bergin, 2004) nicely captures the principle behind these rates, in which the water



molecule is pumped in the infrared from the rotational ground level 1_{01} into the $v_2\ 2_{12}$ level, and then quickly cascades back to several rotational ground levels (3_{21} , 3_{03} , 2_{21} , 1_{01}). For the purpose of the calculations described by equation 36, the G rates are then only between pure rotational levels, yet they have to be calculated by including all possible vibrational/electronic levels. In PSG, the G rates are calculated by employing a full multi-cascade fluorescence model (Villanueva et al., 2012b), and considering high energy spectroscopic databases (e.g., ExoMol, HITEMP, Villanueva et al. 2012/2013), in order to properly capture the high-energy pumps introduced by the Sun with an effective temperature of 5778 K. For the pumping rates, we considered a realistic solar spectrum at $R_h=1\text{AU}$ and a heliocentric velocity of +10 km/s. Detailed spectroscopic and collisional coefficients (energies, statistical weights, Einstein A coefficients, collisional rates and pumping rates), together with the model non-LTE source code, are provided in the PSG site at <https://psg.gsfc.nasa.gov/helpatm.php#linelists>.

6.1 Coma 3D raytracing and asymmetric outgassing / jets

The user can provide information about jets and calculate non-LTE populations in PSG by selecting the “Atmospheric template” and “Cometary non-LTE model” in the Atmosphere/Surface section of the web GUI. Ingesting these non-LTE populations and computing high-resolution spectra in an optically thick medium is not trivial, requiring a detailed layer-by-layer non-LTE modeling in a 3D geometry. As discussed in the previous section, the non-LTE populations are solved at shells with distances increasing exponentially from the nucleus. Our current implementation in PSG considers 200 shells spanning up to 1 million kilometers from the nucleus. Using these shells, we then create a 3D representation of the coma in spherical coordinates (distance, inclination and azimuth). When considering isotropic outflow, one can assume radial symmetry, and effectively the radiative transfer can be solved in 2D (distance and inclination). Transformation from spherical to cartesian geometry for numerical solving is done employing a ray-tracing algorithm as described in section 2, and similarly to what is done when performing exoplanetary transit observations. Effectively, this means performing a raytracing at each shell height, and computing the radiative transfer across the crisscrossed spherical paths.

The modeling of molecular emissions in a non-isotropic coma (i.e., isotropic and jets) is specifically done in two steps: 1) PSG computes non-LTE populations within each jet outgassing cone; 2) these populations and excitation properties are assigned to each spherical sub-cell (distance, inclination, azimuth) discretized across the 200 shell distances, and considering 20 radial subdivisions (regions of ± 9 degrees). PSG permits to have 2 distinct jets beyond the underlying isotropic outflow, with each jet defined by its outgassing source location, cone width, outgassing velocity and relative contribution to the total outgassing. Within each outgassing region, PSG then assumes the density to drop following a 1D photodissociation decay and scaled by the steradian of each cone, while the populations are solved for each cone using the time dependent model as previously explained. A challenge in this implementation is that the “escape probability” approximation is no longer fully representative of the situation, since this is now breaking the isotropic nature of the outgassing, with the directionality of the coma and the sun orientation becoming relevant to the non-LTE solution. Therefore, the solutions for non-isotropic outgassing should be considered as a first approximation.

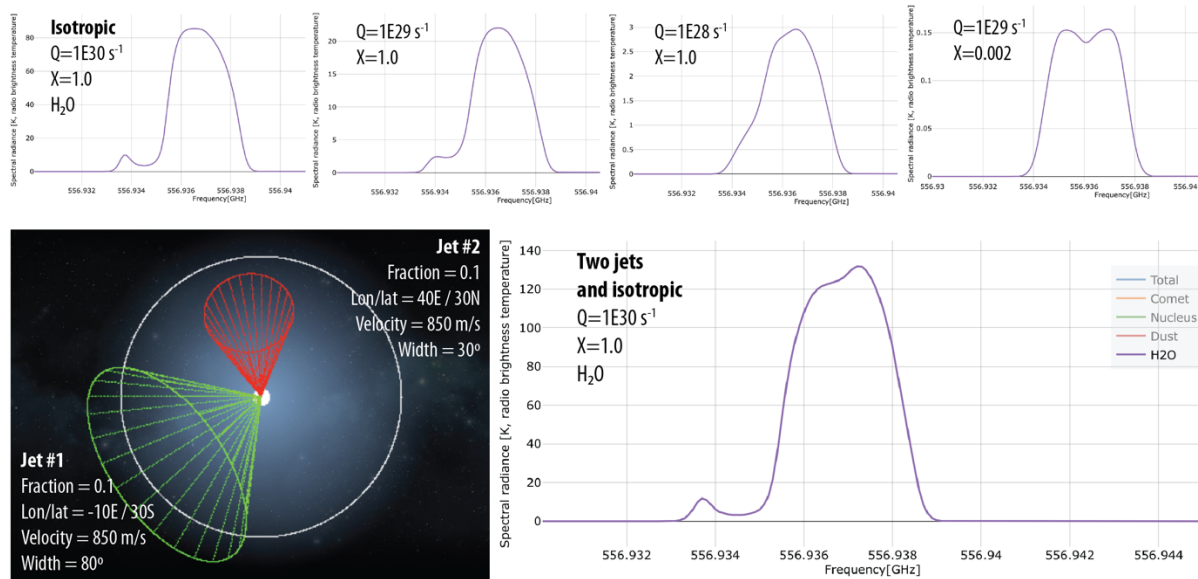


Figure 12: Synthetic spectra for the $1_{10}-1_{01}$ water line as measured with Herschel at a geocentric distance of 1 AU. **The upper panels** are simulations for an isotropic outgassing of water at different levels of activity and abundance. These results match very well to those presented in (Bensch and Bergin, 2004; Zakharov et al., 2007) for similar conditions, even though we use scaled collisional rates (scaled from $\text{H}_2\text{O}-\text{H}_2$), employ our own computed G rates, and employ updated spectroscopy considering the latest ExoMol and HITRAN2020 databases. **The lower panels** show a PSG cometary simulation, and its corresponding 3D rendering, considering two jets and an ambient isotropic outgassing of 80%.

Once the different jets population profiles are computed (i.e., 3 x 1D simulations), the radiative-transfer is ultimately computed in 3D. PSG defines a 3D grid organized in rings, shells and cells, and then fills each cell with the populations of the cone associated for that cell. PSG then performs many ray-tracing integrations across the 3D field and integrate them to create a total integrated spectrum. In this numerical integration, PSG allows for irregular FOVs (e.g., circular, rectangular, seeing; see more in chapter 2), and allows for complex limb/offset beam locations. The full 3D integration and radiative-transfer (e.g., line-shapes, source-functions) has been greatly optimized for performance and is ultimately notably fast, taking only ~ 0.1 second on a standard computer for a regular high-resolution simulation. We have benchmarked our simulations to those reported in (Zakharov et al., 2007), who employ similar methods as those presented here, and to detailed Monte Carlo simulations as presented in (Bensch and Bergin, 2004), obtaining relatively good agreement (see Figure 12), in particular considering that we are using updated spectroscopic parameters.

6.2 Modeling of bright optical emissions (OH, CN, C_2 , CH, NH) in comets

As shown in Figure 9, the optical spectrum of comets is dominated by molecular emission from diatomic species (e.g., OH, CN, C_2 , CH, NH) that have strong fluorescence efficiencies at these wavelengths. These molecules are in most cases daughter species, meaning that they originate in the coma from the photodissociation of parent molecules emitted from the cometary surface. Therefore, these emissions are related to a complex interplay between highly non-equilibrated prompt emission,

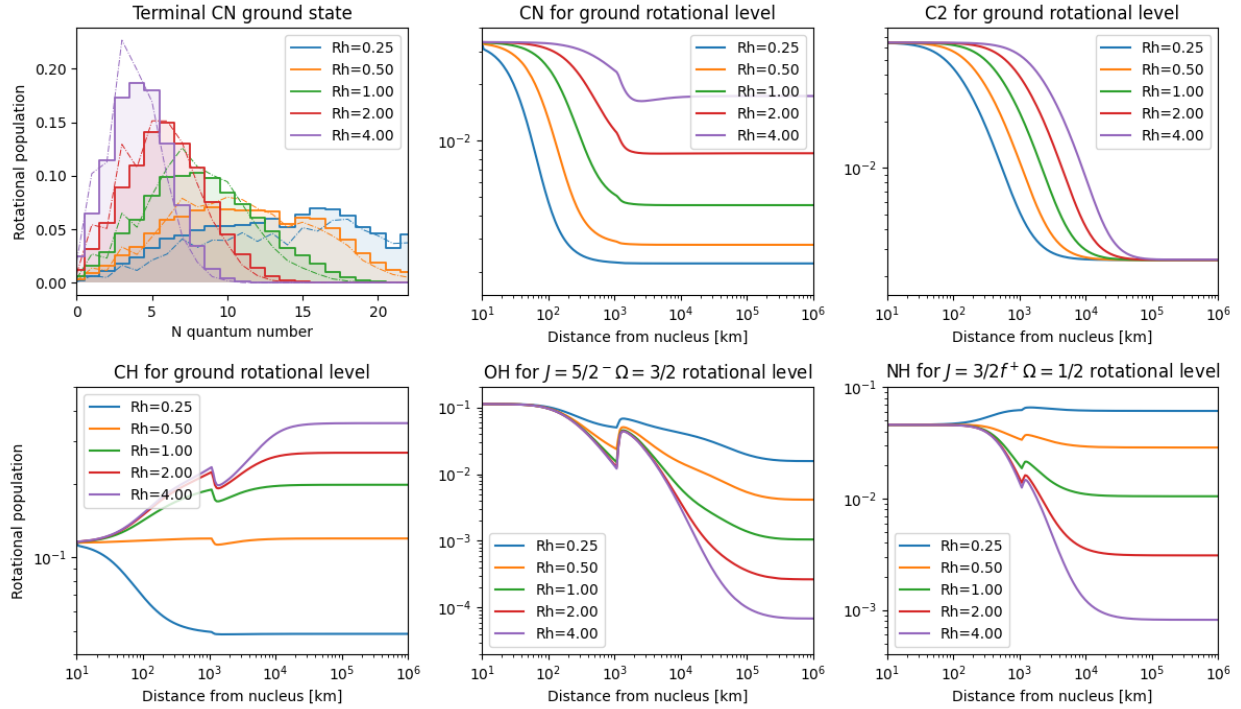


Figure 13: Relative rotational populations for diatomic molecules at different heliocentric distances (rh). **The upper-left panel** shows the evolution of the CN rotational population with rh, computed for a zero heliocentric velocity and compared to (Schleicher, 2010) (dot-dashed). The two models agree relatively well, even though we employ different solar reference spectra, different databases and solving schemes. **The other panels** show the evolution of one rotational level across the coma, highlighting the complex excitation schemes, and where fluorescence equilibrium (the state at 1 million km) is rarely prevalent in many cases.

non-LTE fluorescence equilibrated populations and collisionally thermalized regimes. The fact that these molecules have strong fluorescence emissions in the optical (at the peak of the solar spectrum) also means that they strongly absorb light at these wavelengths, effectively pumping their populations to non-LTE fluorescence equilibrated populations. Consequently, emissions of these species have historically been primarily modeled considering fluorescence equilibrium (e.g., Schleicher, 2010; Schleicher and A'Hearn, 1988, 1982). In addition, these emissions are so strong that they allow to probe and image the extended regions of coma at extremely large distances from the nucleus, further validating the consideration of fluorescence equilibrium for these emissions, since collisions are infrequent at these distances. Nevertheless, astronomers should be aware that when employing narrow slit spectrometers targeting the inner regions of the coma this assumption may not be valid, and we provide here some guidelines to assist with the characterization and treatment of this issue (see Figure 13).

The accuracy of the simulations is determined by three main components: 1) the completeness and accuracy of the line lists; 2) the intensity, fine-resolution and granularity of the solar spectrum, in particular at short wavelengths (e.g., UV, optical); and 3) the numerical methods and techniques employed to determine populations and fluorescence emissions/branching-ratios. Let us explore first

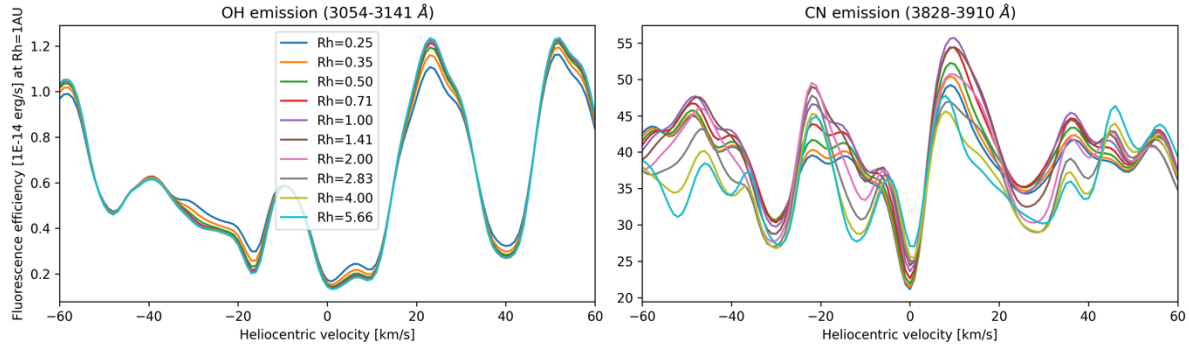


Figure 14: Integrated fluorescence emissions for OH and CN at different heliocentric velocities and distances. At different heliocentric distances, the molecule reaches a different terminal fluorescence equilibrium state, while the total band emissions are affected by the pumpings at each ro-vibrational line affected by Fraunhofer solar lines. Our band emissions are comparable to those presented in Schleicher and A’Hearn (1988) for OH (left-panel), and for CN (right-panel) as reported in (Schleicher, 2010), yet some differences remain and could be related to subtle differences between the assumed solar reference spectrum.

item 3, related to the model. Certain molecular bands tend to dominate these emissions, and therefore, the modeling of the optical fluxes has been normally approached band-by-band separately, with a selected number of rotational levels and only considering the associated two/three electronic-vibrational levels. We alternatively approach the modeling of these emissions by integrating all possible bands and transitions together and self-consistently, as we do for water and other species (e.g., Villanueva et al., 2012b). Yet for these diatomic species, we perform detailed time-dependent non-LTE populations at different heliocentric distances and determine the rotational state of the molecules at different regions of the coma. We then take the “terminal” (final) fluorescence equilibrated populations from these simulations as our starting point when computing multi-cascade fluorescence efficiencies.

This two-steps approach allows us to integrate the full range of the most modern databases via the G rotational coefficients, and to compute spectrally complete fluorescence efficiencies across all wavelengths by incorporating branching ratios and multi-cascade accurately by considering all lines/bands simultaneously. Regarding the linelists, there have been great advancements lately in the modeling of these diatomic molecules (OH/CH/NH: Bernath, 2020, CN: Syme and McKemmish, 2021, C₂: McKemmish et al., 2020), which permit to accurately capture the full range wavelength of emission for these species. Regarding the pumping fluxes, we make use of PSG’s database of stellar templates, which for our Sun is based on the SOLAR-HRS spectrum (Meftah et al., 2023) in the 0.4-3.6 μm spectral region, the LISIRD UV irradiance spectrum shorter than 0.4 μm , the ACE solar spectrum (Hase et al., 2009) in the 3.6-14 μm infrared region, and the (Kurucz, 2009) Sun template beyond 14 μm .

In Figure 14, we show integrated fluorescence emissions as calculated with our simulation approach, showing a strong variability with heliocentric distance and velocity. Yet, the challenge of interpreting cometary emissions with fluorescence equilibrium models is presented in figure 13. In the inner



regions of the coma (typically within 10,000 km), the molecules are not yet in fluorescence equilibrium, and collisions with electrons and the ambient gas still play a significant role. These simulations were done considering a fixed production of $1e29$ molecules/s, a kinetic temperature of 80K, and considering typical molecular abundances (OH:1.0, NH:6e-3, CN:3e-3, C₂:3-e3, CH:6e-3). Therefore, the users should take this into consideration when interpreting cometary spectra with fluorescence equilibrium models, in particular in the inner coma, or when the comet is particularly active and/or quite close to the Sun.

6.3 Optically thick fluorescence modeling at infrared/optical/UV wavelengths

As previously presented in this chapter, fluorescence emissions originate from a myriad of pump and cascade processes. Considering the high-energy of the Sun pumping flux, comprehensive high-energy pump linelists including billions of transitions are required. Treatment of opacity and full radiative transfer employing such large databases, in particular for non-resonance fluorescence, can be therefore extremely challenging. In PSG, we have developed an approximate approach to estimate the opacity the pump and correct for it. For every g-factor, we keep track of the associated line intensities that led to that specific emission. We then compute a weighted “representative” line intensity S_p [$\text{cm}^{-1} / (\text{molecule cm}^{-2})$], and document for each g-factor its weighted pump line intensity. The weight is defined based on the pump intensity (glu) divided by the pump line frequency [cm^{-1}]. The inclusion of the frequency in the weight originates from the fact that the calculation of the opacity is done employing the emission frequency, not the pump frequency (see below). In the case of a non-resonant emission for $v=1 \rightarrow 0$ originating from a pump of $v=0 \rightarrow 2$ (cascaded later to $v=1$), the line width at the pump is twice as big in [cm^{-1}], and the opacity lower by 2 for the same line intensity. For instance, for the ro-vibrational line P2 ($J=1$ to $J=2$) of CO, the pumps to $J=1$ originate from the lines R0 ($J=0$ to $J=1$) and P2 ($J=2$ to $J=1$), while the effective line intensity is calculated as $S_p = \text{ful}_{P2} \cdot (glu_{R0} \cdot \text{Slu}_{R0} / \text{flu}_{R0} + glu_{P2} \cdot \text{Slu}_{P2} / \text{flu}_{P2}) / (glu_{R0} + glu_{P2})$, where glu is the pump g-factor [s^{-1}], flu is the frequency of line [cm^{-1}] at the pump, ful is the emission frequency [cm^{-1}], Slu is the line intensity [$\text{cm}^{-1} / (\text{molecule cm}^{-2})$] at the specific rotational temperature, population state and heliocentric velocity. This is generalized in the fluorescence model to allow for complex non-resonant cascades, by computing S_p following branching ratios and weights as done for the emission g-factor.

For low Sun-Target-Observer phases, the integrated column density as measured by the observer also describes the column density of the incident solar flux. The average linewidth of the pump can be computed as $w_p [\text{cm}^{-1}] = 2 \cdot v_p \cdot \text{ful} / \text{CS}$, where v_p [m/s] is the expansion velocity, ful is the emission frequency [cm^{-1}] and CS is the speed of light [299792458 m/s]. The integrated opacity across the pump can be calculated as $\tau_p = N_{\text{col}} \cdot S_p / v_p$, where N_{col} is the integrated column density [molecules cm^{-2}] across the line of sight. The transmittance at the end of column is $\exp(-\tau_p)$ at the frequency the pump. For low opacities, there are not enough molecules attenuating the solar light at the pump frequency and the pumps are optically thin. As the opacity increases across the column for the solar pump, we only receive radiation for the molecules up to $\tau_p < 1$, and therefore the expected fluorescence efficiency can be approximated to $g_{\text{thick}} = g_{\text{thin}} \cdot [1 - \exp(-\tau_p)] / \tau_p$. This is certainly a first order correction to a complex problem and is only valid for low solar phases. Importantly, by



documenting the level of opacity at the pump, PSG provides a guidance to the user on the level of opacity that the simulation is taking place.



Planetary Spectrum Generator
National Aeronautics and Space Administration

Chapter 5: **Multiple Scattering Atmospheric Modeling**

**Villanueva, Liuzzi and
PSG team**

1. Atmospheric scattering modeling in PSG

As light travels across an atmosphere, it is absorbed (then transformed into heat and thermally emitted) and it is also scattered into many directions. Scattering in this sense, refers to the reflection and deflection of photons in a 3D manner across an atmosphere. When this process is active in an atmosphere, it leads to an “ambient” of diffuse shine and to a peculiar light pattern when looking close to the Sun. For instance, when no scattering is active (only absorption), we would have black skies with only a disk of light at the location of the Sun. Molecular Rayleigh scattering is the reason we have blue skies, in which molecules “scatter” the photons in many directions with a specific wavelength dependance, and in which photons are scattered towards the observer even when the Sun is quite far from the observed patch of the sky. As can be quickly inferred, computing scattering is therefore a 3D problem, which can be numerically extremely difficult to solve since photons need to be tracked across the full three-dimensions (azimuth angle, polar angle, depth/altitude). In a non-scattering medium, the solution of the radiative transfer equation is straightforward, with only needing to track the photons as they go through the incidence and emission paths. For such case, PSG can solve this integral-differential equation readily and efficiently without needing to solve any multiple scattering 3D problem.

Ultimately, solving a full 3D integral-differential scattering problem for the myriad of possible incidence and emission angles would appear in principle unattainable. Several methods do exist, and these include the *doubling-adding method*, the *successive orders of scattering method*, *Gauss-Seidel iteration method*, and the *Monte Carlo approach*, among others. In particular, Chandrasekhar introduced in 1940 a pioneering method for solving radiative transfer in a scattering medium, the *discrete ordinate method*. The primary merit of this method is that it reduces the integral-differential equation to a system of ordinary differential equations, and it divides the scattering directions into numerical series. The foundation math and the proposed numerical implementation are still at the core of the most popular modern scattering methods, yet the original implementation suffered from many numerical and stability issues, and basically doomed Chandrasekhar’s analytic approach for any but the isotropic and Rayleigh scattering problems. In the 1970s, the discrete ordinate method was further improved and many numerical enhancements were developed to improve its accuracy (e.g., Liou, 1973; Wiscombe, 1977). Despite their improved accuracies and enhanced numerical methods, these codes still had instabilities and issues at high opacities, requiring a very high number of computational layers and scattering polar angles. For instance, in the popular delta-Eddington method, the high opacity instability was sidestepped by subdividing layers until each sub-layer was optically thin, which was extremely computationally expensive and probably impractical for many problems.

In the 1980s, the foundational work by Stamnes and others, led to the now widely used DISORT package (Stamnes et al., 2000, 1988), which captures the pioneering discrete ordinate math by Chandrasekhar, the improvements done in the 1970s and finally solved the many issues affecting this method (e.g., stable for high opacities, accurate for low number of polar angles). Since its inception, DISORT has been constantly updated and improved, and the core foundational concepts have not substantially changed since then. In PSG, we employ the core methods of DISORT 2.1 written in C by Dowling and colleagues (Buras et al., 2011) which we adapted for non-LTE and optimized to operate with a variety of spectral grids (e.g., line-by-line, correlated-k, surface scattering



grids) as employed by the PSG radiative transfer algorithm. The model also includes correction for pseudo-spherical geometry as described by (Dahlback and Stamnes, 1991).

2. Theory of radiative transfer in a scattering medium

Solving the scattering problem requires of balancing out the fluxes and radiation across the layers in order to preserve energy conservation and the pre-defined scattering properties of the medium. For this report, we will only present a summarized set of equations as those presented in Stamnes et al. (2000). Please refer to that document for a more complete and detailed mathematical description of the scattering methods. The fundamental core equation used in PSG is the following, which defines how flux is gained and lost at every layer:

$$\mu \frac{dI(\tau, \mu, \phi)}{d\tau} = I(\tau, \mu, \phi) - J(\tau, \mu, \phi) \quad (1)$$

where I is the intensity at the layer, τ is the layer opacity (a metric for depth/altitude), μ is the cosine of the polar angle, ϕ is the azimuth angle and J is the source function. The source function includes two main terms:

$$J(\tau, \mu, \phi) = \frac{w(\tau)}{4\pi} \int_0^{2\pi} \int_{-1}^1 I(\tau, \mu', \phi') P(\tau, \mu, \phi; \mu', \phi') d\mu' d\phi' + Q(\tau, \mu, \phi) \quad (2)$$

where the first term captures the radiation being scattered into this layer from other polar (μ') and azimuth (ϕ') angles via the phase function P , and where w is the single scattering albedo of the medium. The second term is described by Q which refers to the direct beam radiation coming from the Sun, and the isotropic thermal emission emanating from this source:

$$Q(\tau, \mu, \phi) = Q^{thermal}(\tau) + Q^{beam}(\tau, \mu, \phi) \quad (3)$$

$$Q^{thermal}(\tau) = [1 - w(\tau)]S(\tau) \quad (4)$$

$$Q^{beam}(\tau, \mu, \phi) = \frac{w(\tau)}{4\pi} F_* P(\tau, \mu, \phi; -\mu_0, \phi_0) e^{-\tau/\mu_0} \quad (5)$$

where $S(\tau)$ is simply the Planck function $B[T(\tau)]$ in a LTE regime, yet in PSG we allow for non-LTE sources by incorporating their contribution to this term (see details in chapter 4). F_* is the solar flux at the top of the atmosphere and μ_0 and azimuth ϕ_0 are the polar and azimuth angles of the Sun.

2.1 Discretization of the azimuthal intensities, Fourier series and Legendre polynomials

Solving for I from equation (1) across all layers (L) would involve sets of differential equations across three dimensions (see Figure 1), which are not directly solvable, so some transformations and discretizations will be required to determine the layer-by-layer intensities. Foremost, let us consider that the phase function P depends only on the angle θ between the incident and scattered beams.

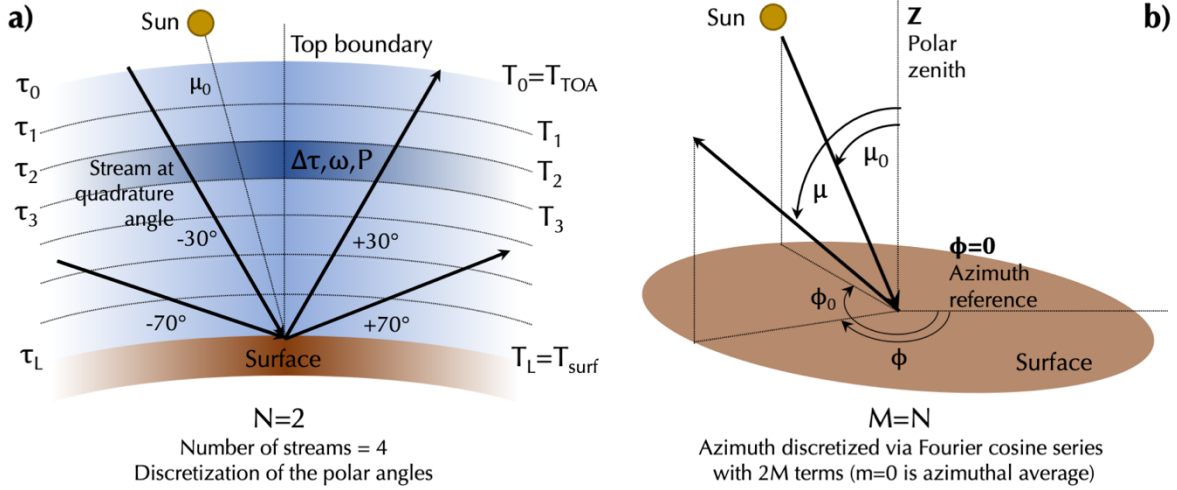


Figure 1: Discretization of the 3D pseudo-spherical scattering geometry. The vertical dimension is discretized in layers with specific opacities ($\Delta\tau$), single scattering albedo (ω), phase function (P) and temperature (T). **a)** The number of streams ($2N$) allows to sample the medium via a set of polar angles, which for this example of $N=2$, would correspond with Gaussian quadrature streams at ± 30 and ± 70 degrees. **b)** The azimuthal dependence is modeled by separating the flux in Fourier cosine series with $m < (2M=2N)$ and the phase function in Legendre polynomials of order M .

This fact can be utilized to factor out the ϕ -dependence in the equations. Let us then set that the intensity can be divided in independent terms of a Fourier cosine series as:

$$I(\tau, \mu, \phi) = \sum_{m=0}^{2M-1} I^m(\tau, \mu) \cos m(\phi_0 - \phi) \quad (6)$$

where $2M$ is the number of azimuth components, and m the index among the series (ϕ is azimuth, and ϕ_0 is solar azimuth angle), with $m=0$ defining the azimuthally average intensity. In a similar fashion, we can expand the phase function (Θ is phase) in a series of $2M$ Legendre polynomials P_ℓ as:

$$P(\tau, \mu, \phi; \mu', \phi') = P(\tau, \cos \Theta) \quad (7)$$

$$P(\tau, \cos \Theta) = \sum_{\ell=0}^{2M-1} (2\ell + 1) g_\ell(\tau) P_\ell(\cos \Theta) \quad (8)$$

$$\cos \Theta = \mu\mu' + \sqrt{(1 - \mu^2)(1 - \mu'^2)} \cos(\phi - \phi') \quad (9)$$



$$P(\tau, \cos \Theta) = \sum_{\ell=0}^{2M-1} (2\ell + 1) g_{\ell}(\tau) \left\{ P_{\ell}(\mu) P_{\ell}(\mu') + 2 \sum_{m=1}^{\ell} \Lambda_{\ell}^m(\mu) \Lambda_{\ell}^m(\mu') \cos m(\phi - \phi') \right\} \quad (10)$$

where g_{ℓ} are the Legendre coefficients of the phase function, and Λ the normalized associated Legendre polynomial, which are defined as:

$$\Lambda_{\ell}^m(\mu) = \sqrt{\frac{(\ell - m)!}{(\ell + m)!}} P_{\ell}^m(\mu) \quad (11)$$

These transformations allow us to remove the azimuth term from the system of equations, and the scattering problem can be then decoupled in independent Fourier azimuth components as:

$$\mu \frac{dI^m(\tau, \mu)}{d\tau} = I^m(\tau, \mu) - J^m(\tau, \mu) \quad m = 0, 1, \dots, 2M - 1 \quad (12)$$

where the source function is given by the integral across polar angles of:

$$J^m(\tau, \mu) = \int_{-1}^1 D^m(\tau, \mu, \mu') I^m(\tau, \mu') d\mu' + Q^m(\tau, \mu) \quad (13)$$

and the scattering terms and direct sources are defined as:

$$D^m(\tau, \mu, \mu') = \frac{\omega(\tau)}{2} \sum_{\ell=m}^{2M-1} (2\ell + 1) g_{\ell}(\tau) \Lambda_{\ell}^m(\mu) \Lambda_{\ell}^m(\mu') \quad (14)$$

$$Q^m(\tau, \mu) = X_0^m(\tau, \mu) e^{-\frac{\tau}{\mu_0}} + \delta_{m0} Q^{thermal}(\mu) \quad (15)$$

$$X_0^m(\tau, \mu) = I_0 \frac{\omega(\tau)}{4\pi} (2 - \delta_{m0}) \sum_{\ell=m}^{2M-1} (-1)^{\ell+m} (2\ell + 1) g_{\ell}(\tau) \Lambda_{\ell}^m(\mu) \Lambda_{\ell}^m(\mu_0) \quad (16)$$

where δ_{m0} defines if this term relevant for $m=0$ ($\delta_{m0}=1$ for $m=0$, otherwise $\delta_{m0}=0$). This set of transformations removes the azimuth (ϕ) dependence and it also decouples the different Fourier component of intensity.

2.2 Discretization of the polar angles, Gaussian quadrature angles

In the previous section, a method to treat one of the dimensions has been identified. The next stage is addressing the polar angle integral, as presented in equation 13. This can be done by employing Gaussian quadrature angles, since it makes phase function renormalization unnecessary, implying that energy is conserved in the computation (Wiscombe, 1977). The reason for this is simply that the Gaussian rule is based on the zeros of the Legendre polynomials which are also used for expanding the phase function. Following this concept, equations 12 and 13 can be defined for a discretized polar angle scheme as:

$$\mu_i \frac{dI^m(\tau, \mu_i)}{d\tau} = I^m(\tau, \mu_i) - J^m(\tau, \mu_i) \quad m = 0, 1, \dots, 2M - 1 \quad i = \pm 1, \dots, \pm N \quad (17)$$

$$J^m(\tau, \mu_i) = \sum_{\substack{j=-N \\ j \neq 0}}^N w_j D^m(\tau, \mu_i, \mu_j) I^m(\tau, \mu_j) + Q^m(\tau, \mu_i) \quad (18)$$

where μ_i is called a “stream”, in which this is a $2N$ -stream solution (N is labeled NMAX in PSG). When only a limited number of streams is considered (2: NMAX=1, 4: NMAX=2), there exist analytical solutions to the systems of equations summarized above (Kylling et al., 1995; Toon et al., 1989), which are popularly employed by the planetary community. The analytical solution for NMAX=1 is effective for calculating fluxes and in energy balance calculations, but it can lead to substantial errors when computing intensities/radiances at a specific direction due to the coarse sampling of the polar angles and phase function (see section 4). We have compared the solutions obtained with NMAX=1 in PSG to the analytical method as presented in (Kylling et al., 1995; Toon et al., 1989), and obtained very good agreement when selecting the same quadrature angles.

At this stage, it is important to make a note regarding the required number of azimuthal components ($2M$). As summarized above, it is related to the number of Legendre polynomials of the phase function which can be hundreds or even thousands of terms long. In practice, however, the intensity expansion is much shorter, and what practically limits the length is the number of quadrature angles. Following Chandrasekhar and DISORT, it has been customary not to extend these expansions beyond the number of quadrature angles, so for a $2N$ calculation, we define the maximum number of terms to be $2M=2N$.

Following these transformations, equations 17 and 18 become a linear combination of I^m (independent for each m component) and at all quadrature angles μ_i . At each layer, this system of differential equations can be reorganized in matrix form, and presented as for the upwelling (+) and downwelling streams (-):

$$\frac{d}{d\tau} \begin{bmatrix} I^+ \\ I^- \end{bmatrix} = \begin{bmatrix} -\alpha & -\beta \\ \beta & \alpha \end{bmatrix} \begin{bmatrix} I^+ \\ I^- \end{bmatrix} - \begin{bmatrix} Q'^+ \\ Q'^- \end{bmatrix} \quad (19)$$



where α and β may be interpreted as layer transmission and reflection operators, respectively, and are $(N \times N)$ matrixes. The problem then becomes of set of $2N \times 2N$ differential equations at each layer. In solving this set of linear ordinary differential equations (ODEs), one can break the solution into two parts, the homogeneous and particular solution. The homogeneous solution satisfies the ODEs with no source term ($Q^\pm = 0$), and does not have to satisfy the boundary conditions. While, the particular solution is a solution with the source terms included, it is not yet required to satisfy the boundary conditions. By reorganizing equation 19, one can solve the homogenous solution of this equation by defining k as the eigenvalues and G^\pm as the eigenvectors, which is customary to be expressed in the form $G^\pm = I^\pm e^{k\tau}$, yielding:

$$\begin{bmatrix} \alpha & \beta \\ -\beta & -\alpha \end{bmatrix} \begin{bmatrix} G^+ \\ G^- \end{bmatrix} = k \begin{bmatrix} G^+ \\ G^- \end{bmatrix} \quad (20)$$

This numerical solving of the homogenous system of equations is done by employing the DISORT AYMTX function, which is a version of EISPACK solver using real arithmetic. Particular solutions are then computed employing linear algebraic system of equations for every layer for solar pseudo-sources and for thermal emission allowing for linear-in-optical-depth variation of the Planck function within each layer.

2.3 Solving the whole system, applying boundary conditions

We have now identified the eigenvalues and eigenvectors that satisfy the differential equations at each layer, but we need to apply realistic boundary conditions to the whole system to determine the layer-by-layer intensity field. Integrating the eigenvalues and eigenvectors previously determined and re-organized the system of equations, one can establish that intensity at each layer can be described by a particular linear form in the optical depth τ :

$$I(\tau, \mu_i) = \sum_{j=-N}^N C_j G_j(\mu_i) e^{-k_j \tau} + \delta_{m0} [Y_0(\mu_i) + Y_1(\mu_i) \tau] \quad (21)$$

where the C_j scaling coefficients for each stream are unknown. By setting this as a set of linear equations across layer (τ) and polar angle (μ_i), one can define solution boundaries and then calculate a solution to the system of linear equations. For instance, the fluxes at the top of the atmosphere ($\tau=0$) are known, while the reflecting/emitting properties of the surface ($\tau=\max$) are also defined. Solving C across the whole atmosphere, then constitutes a $(2N \times L) \times (2N \times L)$ system of linear algebraic equations from which the $2N \times L$ unknown coefficients C_{jp} ($j=\pm 1, \dots, \pm N$; $p=1, \dots, L$) must be determined.

This set of equations is ill-conditioned for large optical thicknesses, so a scaling transformation is applied following the methods presented in (Stamnes and Conklin, 1984), which entirely eliminates this problem at its source. Numerically, the solution to this banded matrix inversion is done with the LINPACK SGBSL algorithm.

2.4 Scattering numerical algorithm

The algorithm for determining the layer-by-layer scattering intensities can be organized into a sequence of nested loops (see Figure 2). Initially, the code will allocate the matrix memories, and then compute the Legendre polynomial coefficients (see equation 11) and Gauss quadrature angles / weights which are common to all calculations and wavelengths. At the center of the algorithm, the code will determine the eigenvalues and eigenvectors (layer-by-layer), which are then used for each Fourier term component to determine specific intensities for that m^{th} term. At each m iteration, the code will test for convergence by analyzing the intensity of the Fourier term with respect to the total intensity, and will stop when the required accuracy is achieved or when the maximum number of terms is reached ($m < 2M = 2N$). Finally, the intensities are computed for the desired azimuth angle and corrected for delta-M (Wiscombe, 1977) and for N-stream truncation employing the IMS method (Nakajima and Tanaka, 1988). The parameter LMAX in PSG defines the number of Legendre polynomials in the description of the phase function (equation 8). As explained before, the code computes the scattering solution only using $2M = 2N$ Legendre terms, yet by employing the IMS method, the model can add information for terms beyond $2M$ up to the desired LMAX number of terms. In PSG, LMAX is always at least $2 \times N_{\text{MAX}}$.

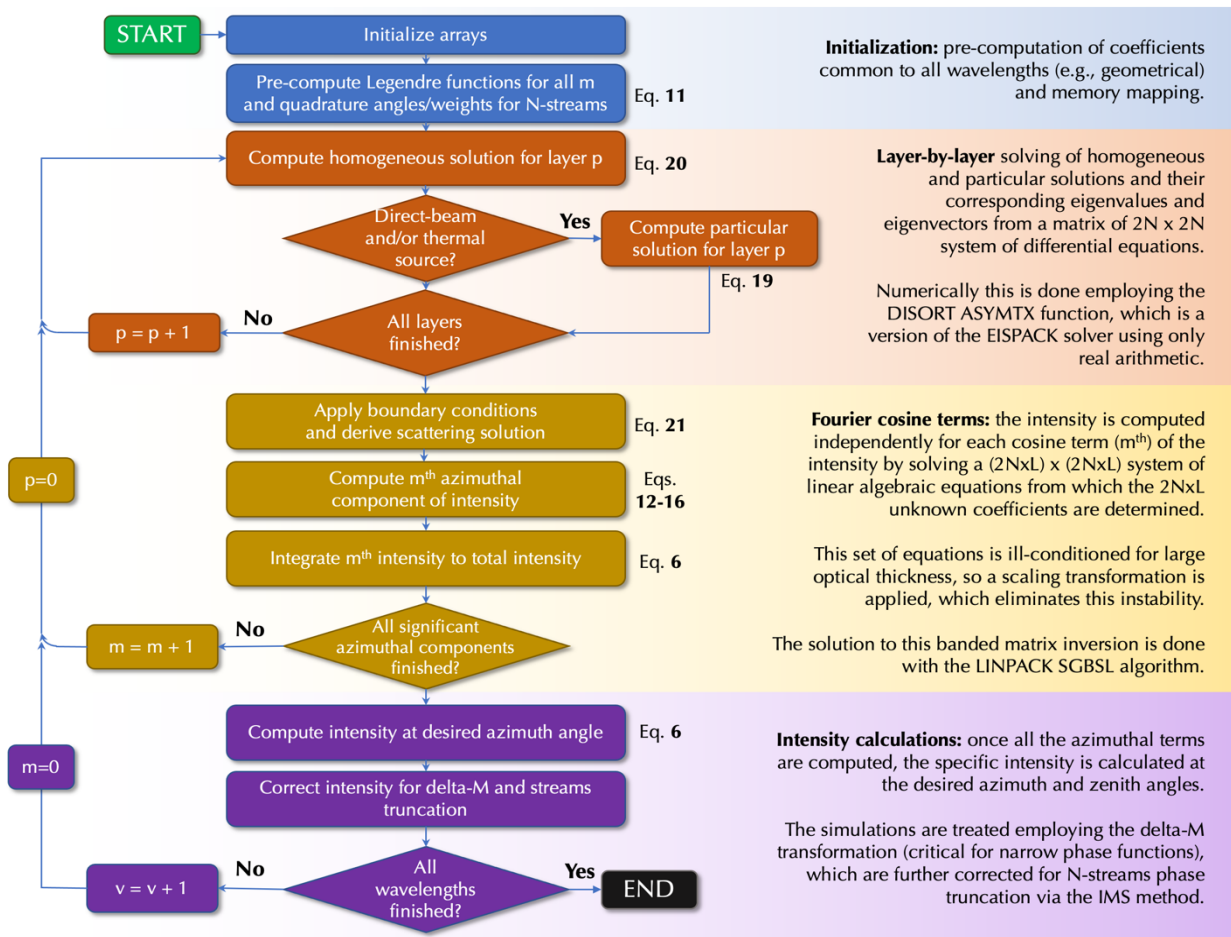


Figure 2: Overview of the operations performed by the scattering module. Flow chart adapted from (Stamnes et al., 2000).



3. Mie scattering and calculation of the aerosol models

The three key input parameters for a multiple scattering calculation are opacity (τ , see equations 2-5), single scattering albedo (w , see equations 2-5) and the Legendre coefficients of the phase function (g , see equation 10). The opacity of an aerosol is determined by the extinction coefficient [m^2/kg] and the mass column density [kg/m^2] of the aerosol in the layer. For molecular Rayleigh scattering, τ is determined from the polarizability of the molecule (Sneep and Ubachs, 2005), with $\omega=1$, $g_0=1.0$ and $g_2=0.1$.

The extinction coefficient, scattering albedo and Legendre coefficients are dependent on the wavelength, composition, and size/shape of the scattering particles. In PSG, scattering models for a variety of aerosols are available, which are prescribed in two forms. One form is that of wavelength [μm], extinction coefficient [m^2/kg], scattering albedo for each Legendre term, which allow for arbitrary scattering models to be used. Such models include T-matrix scattering models, which are computed for a specific particle size distribution and composition (Wolff et al., 2009). In addition, PSG has pre-computed Mie scattering models for a large variety of species and particle radius distributions. These models contain the wavelength [μm], extinction coefficient [m^2/kg], scattering albedo [ω , 0 to 1], and Henyey-Greenstein asymmetry factor [HG, -1 to 1]. The Henyey-Greenstein phase function is defined as:

$$P(\theta) = \frac{1 - HG^2}{(1 - 2HG \cos \theta + HG^2)^{3/2}} \quad (22)$$

The Mie implementation for these models is based on (Bohren and Huffman, 1983), and considers 20 angles of scattering with 200 size bins having $\sigma_{\text{peak}} : r_{\text{eff}}/1.50833$. The models are computed for size distributions centered at different mean size distributions (0.01, 0.05, 0.1, 0.5, 1.0, 5.0, 10.0, 50.0, 100.0 μm) and considering different compositions. The underlying indices of refraction of the particles is dependent on the composition of the aerosol, and in PSG we mostly employ the optical constants in the HRI database (HITRAN Refractory Index, Massie and Hervig 2013). We also complement this database with optical constants from other laboratory sources.

When modeling the properties of scattering in a medium, one normally does not deal with a fully homogenous medium with a common set of properties for all particles, but with a distribution of properties. A practical approach is to assume a statistical distribution description of the particle properties, in particular its size distribution. A particle size distribution is described as a histogram of the number of particles per unit volume within a defined size bin. In a distribution, several statistical quantities describe its organization and structure: mean (arithmetic average), geometric mean, mode (size corresponding to the maximum of the distribution), median (statistical middle of the distribution), variance (σ_0^2), standard deviation (σ_0), and geometric standard deviation. When a user picks a “size”, one needs to first understand what actual parameter of the distribution the user is referring to. Differences in assumptions of what “size” means could mean different distributions and therefore scattering properties. It is therefore of great importance to define these quantities in this chapter to ensure proper integration of these parameters in the radiative transfer calculations.

A popular size distribution is the log-normal, in which the densities are organized in a Gaussian distribution considering a logarithmic size scale:

$$n(r) = \frac{N_0}{\sqrt{2\pi}} \frac{1}{\ln(S)} \frac{1}{r} \exp \left[-\frac{(\ln r - \ln r_m)^2}{2 \ln^2(S)} \right] \quad (23)$$

$$N_0 = \int_0^\infty n(r) dr \quad (24)$$

$$\ln(S) = \sigma \quad (25)$$

where N_0 is the number of particles per unit volume [particles/m³], r_m [m] is the modal center of the distribution, S is the geometric standard deviation, and σ is the standard deviation. By definition, S must be greater or equal to one, and when S is one the distribution is monodisperse. Typical aerosol distributions have S values in the range 1.2 – 2.0. The statistical properties of this distribution are:

$$A_v = \pi r_m^2 \exp(2\ln^2 S) = \pi r_e^2 \exp(-3\ln^2 S) = A_e \exp(-3\ln^2 S) \quad (26)$$

$$V_v = \frac{4}{3} \pi r_m^3 \exp\left(\frac{9}{2} \ln^2 S\right) = \frac{4}{3} \pi r_e^3 \exp(-3\ln^2 S) = V_e \exp(-3\ln^2 S) \quad (27)$$

$$r_{\mu 0} = r_m \exp\left(\frac{1}{2} \ln^2 S\right) \quad \ln r_M = \ln r_m - \ln^2 S \quad (28)$$

$$\sigma_0^2 = r_m^2 \exp\left(\frac{1}{2} \ln^2 S\right) [\exp(-\ln^2 S) - 1] \quad (29)$$

$$r_e = r_m \exp\left(\frac{5}{2} \ln^2 S\right) \quad v_e = \exp(\ln^2 S) - 1 \quad A_e = \pi r_e^2 \quad V_e = \frac{4}{3} \pi r_e^3 \quad (30)$$

where r_e is the effective radius, v_e is the effective variance, A_e is the area of the particle considering r_e , V_e is the volume of the particle considering r_e , A_v is the representative average area of the particles in the distribution, V_v is the representative average volume of the particles, $r_{\mu 0}$ is the mean radius, r_M is the median radius, and σ_0^2 is the variance. The most common way to define the size of a distribution is via its effective radius (r_e), and it is the value entered in the PSG fields. Specifically, PSG employs scattering models pre-computed with a size distribution around r_e and using a S value of 1.5, yet the user can upload scattering models computed with any size distribution and scattering properties.

The collective scattering properties (β^{abs} [m⁻¹]: volume absorption coefficient, β^{sca} [m⁻¹]: volume scattering coefficient, β^{ext} [m⁻¹]: volume extinction coefficient) of the distribution are described as the area weighted sum of the scattering properties (i.e., efficiency factors Q):

$$\beta(\lambda) = \bar{\sigma}(\lambda) N_0 = \int_0^\infty \pi r^2 Q(\lambda, r) n(r) dr \quad (30)$$



where $\bar{\sigma}$ [m²] is the mean cross section. The optical depth is related as $\tau = \beta^{\text{ext}} Z = \bar{\sigma}^{\text{ext}} N_0 Z$, where Z [m] is the path length. A typical way to provide these parameters in a radiative transfer model is by providing profiles of $N_0(z)$ [particle/m³] and $\bar{\sigma}(\lambda, z)$ [m²], where $\bar{\sigma}$ is calculated at each height considering the local size distribution. Alternatively, as in PSG, the aerosols profiles are provided in f_M [kg/kg] relative to the air density [kg/m³], and the extinction cross section is provided per unit of mass, $X_e(\lambda, z)$ [m²/kg], for an effective radius size of r_e [m]. To determine f_M for PSG based on a profile of $N_0(z)$ with r_e , please use the following conversion equations considering typical used units:

$$f_M \left[\frac{kg}{kg} \right] = N_0 \left[\frac{particle}{cm^3} \right] m_{aero} \left[\frac{g}{particle} \right] \frac{N_A \left[6.022140857 \cdot 10^{23} \frac{molecule}{mol} \right]}{\rho_{atm} \left[\frac{molecule}{cm^3} \right] m_{atm} \left[\frac{g}{mol} \right]} \quad (31)$$

$$m_{aero} \left[\frac{g}{particle} \right] = \frac{4}{3} \pi r_e^3 \left[\frac{um^3}{particle} \right] \rho_{aero} \left[\frac{g}{cm^3} \right] \exp(-3 \ln^2 S) 10^{-12} \quad (32)$$

$$\rho_{atm} \left[\frac{molecule}{cm^3} \right] = \frac{P[bar]}{k_B [1.38064852 \cdot 10^{-23}] T[K]} 10^{-1} \quad (33)$$

where m_{aero} is the mass of an aerosol particle, m_{atm} is the molar mass of the atmosphere, N_A is the Avogadro constant, ρ_{aero} is the density of the particles, S is the geometric standard deviation of the log-normal distribution ($\exp[-3 \ln^2 S] = 0.6107$ if using the PSG scattering models), ρ_{atm} is the density of the atmosphere, P is the ambient pressure, T is the temperature and k_B is the Boltzmann constant.

4. Selection of the number of stream pairs (NMAX) and Legendre terms (LMAX)

As we summarized in the previous sections, solving for the multiple scattering in a multi-layer atmosphere involves the discretization and separation of the problem into three dimensions: depth/ τ (L or number layers), number of stream pairs (2N) and number of azimuthal terms (2M). In PSG as in other multiple scattering solvers, we assume $2N = 2M = 2NMAX$. We can use information of Legendre terms beyond 2M up to a desired LMAX by employing the delta-M (Wiscombe, 1977) and IMS methods (Nakajima and Tanaka, 1988).

The calculation requirement scales linearly with L, yet it grows immensely with NMAX, in the order of NMAX to the power of 3. This means that 10 times more streams would lead to factor of 1,000 longer computation time. Higher values of NMAX, LMAX and L would lead to greater accuracy but require much larger number of calculations, with perhaps minimum improvement in accuracy. In that sense, a careful definition of these parameters is critical. Importantly, the a-posteriori IMS correction has been demonstrated to be quite accurate (Kokhanovsky et al., 2010) in compensating for the truncation of the Legendre terms with the delta-M method, and it is relatively inexpensive. For instance, a large increase in the number of LMAX terms (beyond 2M) would only lead to marginal (10-20%) greater computational times.

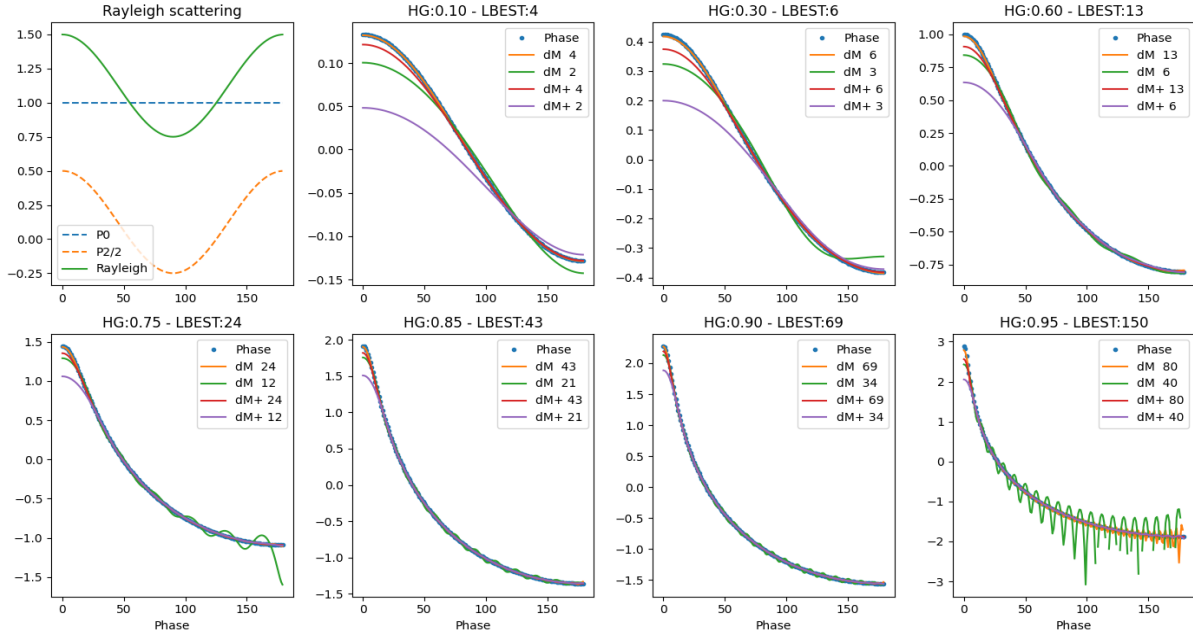


Figure 3: Comparison of different methods for modeling Rayleigh and Henyey-Greenstein phase functions with Legendre polynomials. LBEST is the optimum value of terms as defined in (Nakajima and Tanaka, 1988) with an accuracy of 0.5%. The y-values of the HG-plots are in \log_{10} of the intensity. The plots show how the delta-M and new delta-M+ methods perform for different values LMAX and when considering the optimum LBEST value. We have capped LMAX to be 80. In general, the delta-M correction produces reasonable results even at half LMAX, while the delta-M+ solution removes the strong ringing, yet it struggles at low phase angles.

Recently, an improved phase truncation method for modeling the forward scattering peak with a Dirac delta function has been developed, the delta-M+ method (Lin et al., 2018). Compared with the original delta-M method (Wiscombe, 1977), the delta-M+ model has the same computational efficiency, but for radiance computations, its accuracy and stability are estimated to increase greatly. This new method provides generally very good results with low number of LMAX for highly asymmetrical scatterers, yet it introduces higher errors at lower phase angles. Perhaps, the IMS correction could be adapted to this new method, but this has not been demonstrated nor fully tested yet. For that reason, in PSG, we maintained the classical delta-M and IMS method, yet we will be exploring this new method more closely for a potential integration in the near future.

To showcase the effects of LMAX on the description of the phase function, we have computed phase functions for a selection of scatterers, from highly symmetrical with HG: 0.1 to highly forward peaked scatterers with HG: 0.95. For numerical reasons, and also for physical reasons, the maximum value of HG is capped to 0.95 (Andrews et al., 2006; Fu, 2007; Granate et al., 2016). We tested the delta-M and delta-M+ methods with a selection of different terms. It has been shown that errors lower than 0.5% can be achieved with $LMAX = 3.77P(0)^{0.553}$ (Nakajima and Tanaka, 1988), where $P(0)$ is the intensity of the phase function at phase=0. We define this metric to be LBEST, yet such number of terms can reach several hundred for highly asymmetric functions ($HG > 0.95$). Importantly, errors in the phase-function do not directly propagate to radiance errors. They are smoothed due to the intrinsic nature of collecting scattered light originating from many directions.

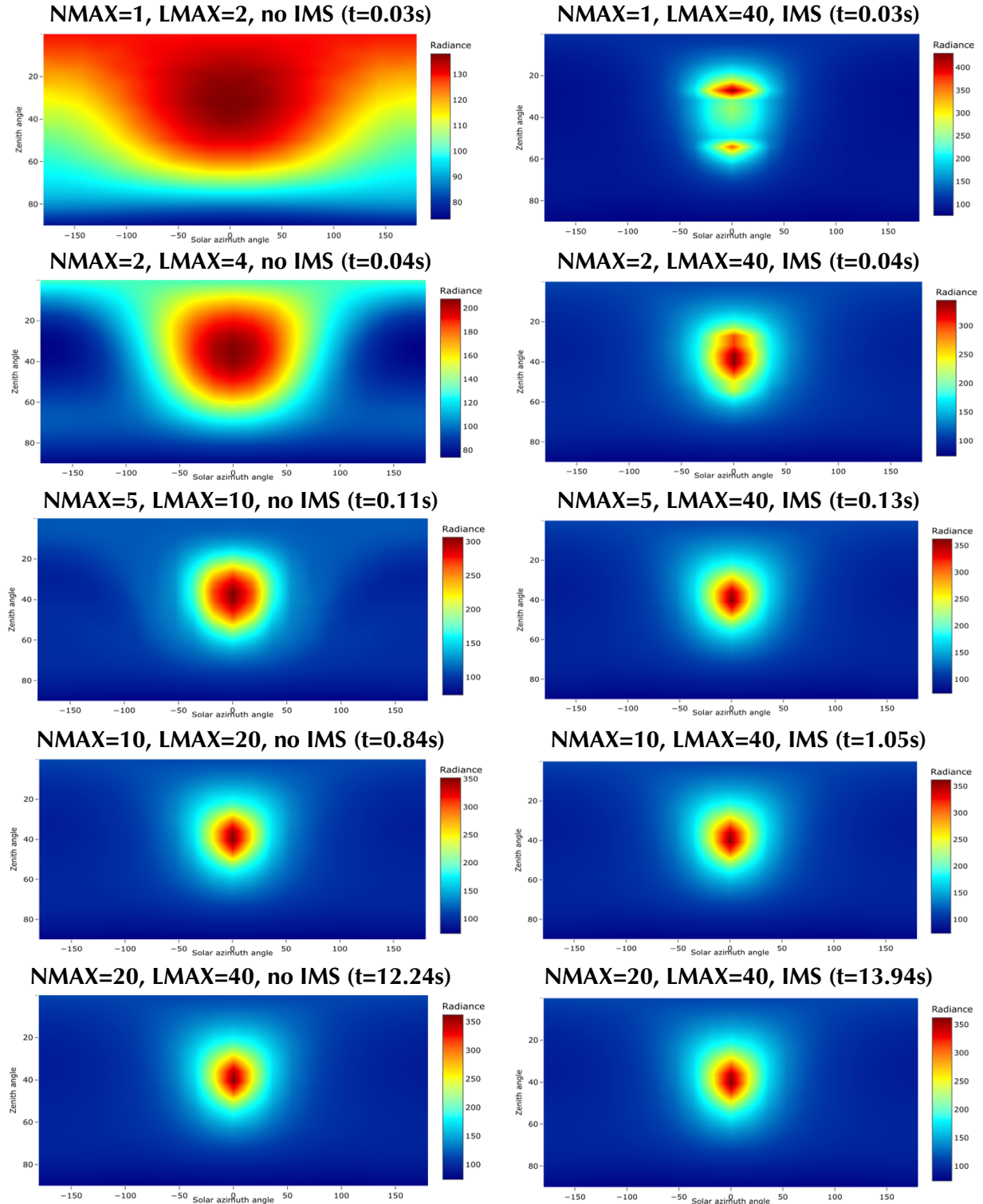


Figure 4: Comparison of full-sky scattering simulations (441 sky points x 100 wavelengths) for water-ice (HG: 0.85) and Rayleigh for different values of NMAX, LMAX and with/without IMS. The default in PSG is with IMS. In brackets, the required computational time is presented, which grows greatly with NMAX and modestly with LMAX (compare IMS and no IMS). As shown in Figure, LBEST is 43 for HG: 0.85, so at LMAX=43 we should have convergence in the solution.

Considering that the cost of including higher LMAX values is relatively low when employing the IMS correction, one could select a relatively high number conservatively. Yet, it is always important to test the selection of NMAX and LMAX at higher values and determine when the synthesized radiances converge to the needed accuracy. One can use Figure 3 as a first guide in determining the number of LMAX as a function on the HG value of the considered aerosols. PSG will also perform recommendations / warnings on the needed LMAX based on the here presented simulations.

Determining NMAX is somewhat more critical considering the high computational penalty, yet an “optimum” value will depend strongly on the considered geometry and scattering elements. In the classical sense and without the IMS correction, the number of Legendre terms and azimuthal components is capped in the simulation to 2M, so $N_{MAX}=L_{MAX}/2$. For a phase function with HG: 0.95 and $L_{MAX}=150$, one would need $N_{MAX}=75$. Such high NMAX would require 52000 times more time than a simulation with $N_{MAX}=2$. If a simulation takes 1 second with $N_{MAX}=2$, it would take ~15 hours with $N_{MAX}=75$. Such requirement is astronomical, and quite impractical. Thankfully to the IMS correction, one can achieve solutions for $L_{MAX}=150$, with $N_{MAX}=5$ at comparable accuracies. In general, a higher value of NMAX is recommended though.

Case / w	1	0.999	0.995	0.99	0.98	0.95	0.9	0.8	0.7
Rayleigh	0.756	0.702	0.641	0.599	0.545	0.453	0.367	0.269	0.206
$N_{MAX}:2$	0.751	0.697	0.637	0.595	0.542	0.451	0.365	0.268	0.205
$L_{MAX}:4$	0.6%	0.6%	0.6%	0.7%	0.6%	0.5%	0.6%	-	-
Isotropic	0.693	0.639	0.579	0.538	0.484	0.394	0.311	0.219	0.162
$N_{MAX}:2$	0.689	0.636	0.575	0.534	0.482	0.392	0.309	0.218	0.162
$L_{MAX}:4$	0.6%	0.5%	0.7%	0.7%	0.5%	0.5%	0.7%	-	-
HG: 0.5	0.653	0.577	0.496	0.442	0.376	0.272	0.188	0.108	0.069
$N_{MAX}:2$	0.649	0.574	0.493	0.44	0.374	0.271	0.187	0.108	0.069
$L_{MAX}:12$	0.5%	0.5%	0.5%	0.5%	0.6%	-	-	-	-
HG: 0.75	0.641	0.537	0.431	0.365	0.289	0.181	0.107	0.051	0.029
$N_{MAX}:3$	0.642	0.537	0.431	0.366	0.290	0.182	0.108	0.052	0.030
$L_{MAX}:36$	-	-	-	-	-	-	-	-	-
HG: 0.8	0.642	0.526	0.411	0.342	0.263	0.157	0.089	0.041	0.023
$N_{MAX}:6$	0.640	0.524	0.410	0.341	0.262	0.157	0.088	0.040	0.023
$L_{MAX}:36$	0.3%	0.4%	-	-	-	-	-	-	-
HG: 0.85	0.639	0.507	0.381	0.307	0.227	0.125	0.066	0.028	0.015
$N_{MAX}:8$	0.639	0.499	0.381	0.308	0.228	0.126	0.067	0.029	0.016
$L_{MAX}:64$	-	1.7%	-	-	-	-	-	-	-
HG: 0.9	0.639	0.481	0.339	0.261	0.180	0.089	0.043	0.017	0.009
$N_{MAX}:12$	0.638	0.481	0.338	0.260	0.180	0.090	0.043	0.018	0.010
$L_{MAX}:80$	-	-	-	-	-	-	-	-	-

Table 1: Geometric albedo as a function of single scattering albedo (w) and scattering anisotropy (HG). The first value is as calculated with PSG, the value below as computed by (Dlugach and Yanovitskij, 1974), and below the corresponding difference in percentage. Differences smaller than 0.001 in intensity are considered to be within the rounding error of the reported values. The PSG simulations were performed using the reported NMAX/LMAX parameterization.

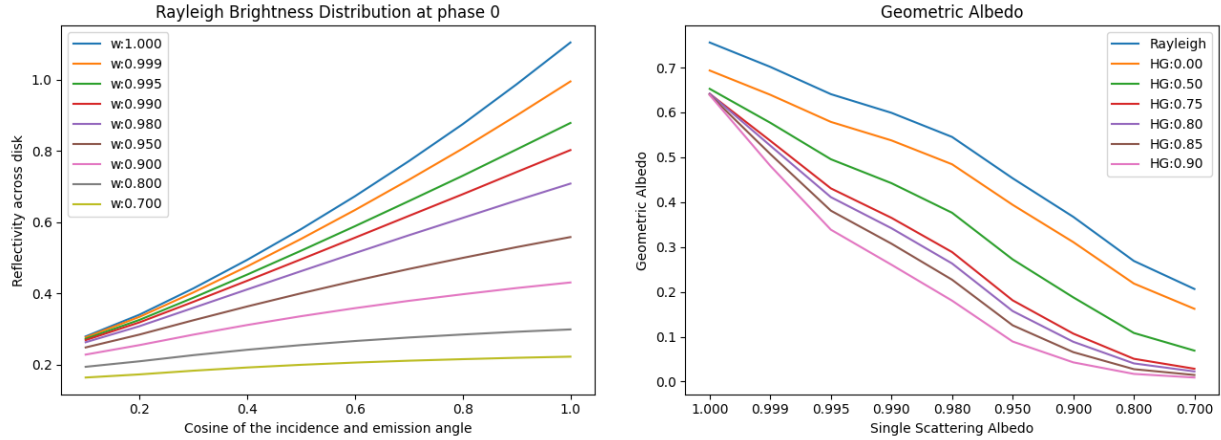


Figure 5: Simulations presenting the brightness distribution for Rayleigh across the disk and of geometric albedo, considering different levels of single scattering albedo and anisotropy. The simulations were performed with the parameters as presented in Table 1, and show the strong impact of the single scattering albedo to the brightness of the planet across the disk and to integrated intensity at phase 0 (geometric albedo).

As a benchmark scenario, we can consider the rigorous calculations by (Dlugach and Yanovitskij, 1974) for a semi-infinite atmosphere having homogenous scattering properties, that reports the dependence of brightness across a disk and also report spherical and geometrical albedos. The simulations were performed for several cases, including Rayleigh, isotropic and highly-anisotropic phase functions (HG: 0.9). We compare these results to simulations performed with PSG (see Figure 5) and obtain generally very good agreement ($<1\%$ in most cases, see Table 1) when using the appropriate NMAX/LMAX requirements. In addition and based on this comparison, we define a general set of recommendations for scattering requirements based on the anisotropy of the phase functions considered in the simulation (see Table 2), reaching up to NMAX : 12 for HG : 0.9.

Level of asymmetry (HG value)	Forward/backward peak ratio $P(0^\circ)/P(180^\circ)$	Number of stream pairs (NMAX) when employing IMS	Number of Legendre phase terms (LMAX)
Rayleigh and $HG \leq 0.1$	< 2	2	4
$HG \leq 0.50$	< 27	2	12
$HG \leq 0.75$	< 343	3	36
$HG \leq 0.80$	< 729	6	36
$HG \leq 0.85$	$< 1,876$	8	64
$HG \leq 0.90$	$< 6,859$	12	80
$HG \leq 0.95$	$< 59,318$	24	80

Table 2: Suggested minimum values of NMAX and LMAX according to asymmetry g and the corresponding forward/backward ratio $[(1+HG)/(1-HG)]^3$. Anisotropy HG values are internally capped to 0.95 in PSG. These are highly hypothetical, and the actual needed values will depend on the parameters of the simulation. Importantly, these have been defined favoring computational speed and performance.

It is nicely shown that the IMS method is quite effective in correcting for the truncation of the phase function with low values of NMAX. When modeling spectra across a full planetary disk over multiple incidence/emission angles (see sub-sampling method in chapter 2), the azimuthal dependence is less relevant since it becomes “smoothed out” and a lower number of NMAX is sufficient.

5. Specifics of multiple scattering simulations

Phase angle definitions: the definition of angles in a simulation are critical, yet each particular geometry and model ingests these parameters occasionally in different ways. A particular inconsistency exists in the community in the definition of scattering phase angle between atmospheric scattering models and surface models. In atmospheric models as discussed in this chapter, $\text{phase}_{\text{atm}}=0$ refers to forward scattering (see Figure 6), typical for Mie models of aerosols. In such sense, a narrow “phase function” for an aerosol/gas indicates how narrow the aureole near the Sun is seen when observing the Sun through an atmosphere from the surface. On the other hand, when modeling surfaces (see Chapter 6), $\text{phase}_{\text{surface}}=0$ refers to back scattering, being typically maximum when observing the surface in opposition (see definition of g in Figure 1 of chapter 6). Therefore, for all downward looking geometries (e.g., observatory, Nadir, limb, occultation) $\text{phase}_{\text{atm}} = 180 - \text{phase}_{\text{surface}}$, while for all looking up geometries, $\text{phase}_{\text{atm}} = \text{phase}_{\text{surface}}$.

High-incidence and observational angles: solving a multiple scattering simulation in a spherical atmosphere is particularly challenging. The foundational methods implemented in PSGDORT have at its core a plane-parallel mathematical representation, which have been adapted for a spherical geometry. Handling of high solar-zenith-angles ($\text{SZA} > 80^\circ$ and beyond $90-98^\circ$ into twilight) is treated accurately in PSG by implementing the methods as discussed in (Dahlback and Stamnes, 1991), which make use of Chapman functions to capture the complex spherical geometry. Computing intensities at high observational-zenith angles ($80 < \text{OZA} < 90^\circ$) with such methods can be on the other hand challenging, and we have observed numerical instabilities in the solutions when highly peaked phase functions ($\text{HG} > 0.8$) and high-scattering opacities prevail in the medium. As such, in PSG we cap the maximum g allowed for the simulation as a function of OZA and SZA to accommodate for this, in which a corresponding warning will be reported.

Limb and tangential simulations: in the current implementation of scattering in PSGDORT, limb and tangential observations ($\text{OZA}=90$) are only possible when employing the single scattering approximation. This stems from the same high geometric demands as previously discussed, and it is ultimately related to the complexities of solving the system of multiple-scattering streams in geometries in which the effects of the sphericity of the planet diverge substantially from a plane-parallel representation.

Fluxes, mean intensities and divergencies: by default, PSG outputs intensities at specific zenith angles (OZA) and azimuths. Yet for example, we may be interested in the total energy crossing the atmosphere at a specific altitude per unit time, which is of relevance to climatic energy budget studies. Therefore, when performing multiple-scattering simulations ($\text{NMAX} > 0$), the user can select four additional output units: downward direct flux ($F_{\text{dir}}^{\downarrow}$), downward diffuse flux (F^{\downarrow}), upward

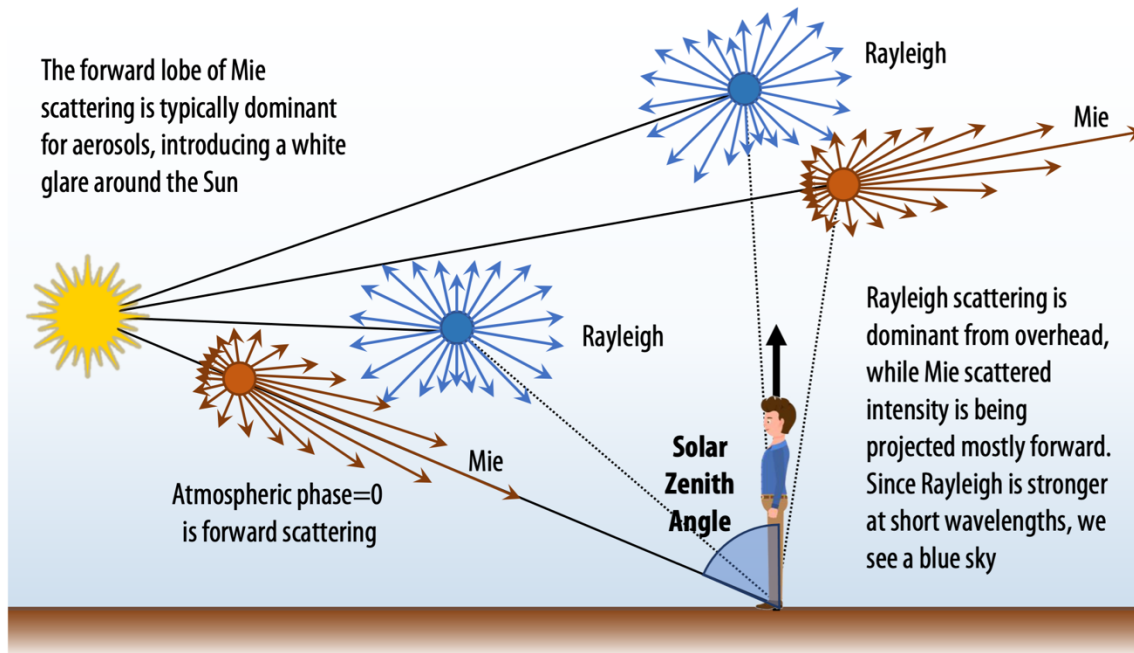


Figure 6: Molecular Rayleigh and aerosols Mie scattering have typically very different phase functions, which lead to notable wavelength dependent scattering effects. Aerosols Mie scattering tends to lead to forward scattering ($\text{phase}_{\text{atm}}=0$), which differs from the definition of surface phase function (see Figure 1 in Chapter 6), which is relative to backscattering.

diffuse flux (F^\uparrow), mean intensity (\hat{I}), and flux divergence ($\delta F/\delta \tau$). $F_{\text{dir}}^\downarrow$ reports the total flux coming from the Sun/Star at that specific altitude and across all observing angles. F^\uparrow reports the flux emanating from the planet across all angles, and includes the surface reflected fluxes and all outward looking scattered/emitted fluxes. Mean intensity (\hat{I}) measures the total intensity at that location from all sides, and is of importance to photochemical reactions. The only difference between mean intensity and fluxes is that fluxes are cosine-weighted averages of the intensity while mean intensities are unweighted averages. Finally, the flux divergence ($\delta F/\delta \tau$) reports the change of flux with opacity at that location, and is related to the radiative heating rate, and relevant to energy budget investigations. Further information about these outputs and their mathematical formulation is presented in (Stamnes et al., 2000).

Irregular cloud cover: clouds and hazes form a particular challenge in radiative transfer simulations since their abundance and spatial distribution are not well represented by a spatial average. For instance, clouds on Earth are often very localized, with parts that are fully covered by clouds, and others which are fully transparent. Neither the opaque nor the transparent radiative transfer simulations would provide a satisfactory description of the way the light interaction with the atmosphere. One way to approach simulations of patchy clouds is by performing two separate simulations: the first considering clouds at their maximum opacity throughout the cell, and a second without any clouds present. The way to obtain the final spectrum is then to combine the two considering the cloud fraction, in which the cloud abundance for the cloudy simulation is assumed

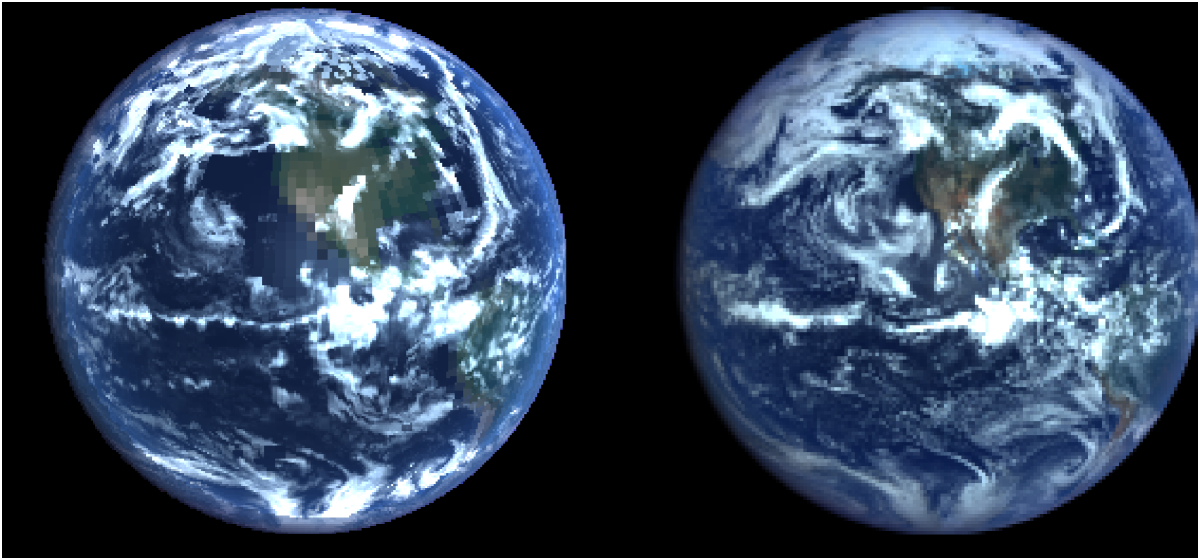


Figure 7: PSG simulations of Earth (left) at the exact same time of the DSCOVR-EPIC observations (right). For these 3D simulations, atmospheric parameters from the MERRA-2 database were adopted, as well as surface cover descriptions from MODIS and National Snow and Ice Data Center. For more information see Kofman et al., 2024.

to inversely scale with the cloud fraction (i.e., $\text{cloud_abundance} = \text{cloud_average_abundance} / \text{cloud_fraction}$). An implementation of this approach is presented in (Kofman et al., 2024), for which meteorological data and cloud coverage information were collected from the MERRA-2 atmospheric database. As demonstrated by the comparisons between the PSG simulations and DSCOVR-EPIC observations (see Figure 7), integrating the localized nature of clouds via the cloud fraction would be critically needed when comparing and matching spectral and spatial variations. In PSG, the cloud fraction parameter is provided via the keyword 'ATMOSPHERE-CLOUDFRACTION', for which PSG will run two simulations, one fully clouded, and one without the aerosols, and the combined spectrum will be reported. This parameter can be also provided for 3D simulations with GlobES, for which one needs to add the keyword cloud fraction to the parameter <ATMOSPHERE-GCM-PARAMETERS> in the configuration file, as well as a 2D cloud fraction array in the binary PSG GCM file. In the simulations, each radiative transfer computation is performed twice, and the weighted average of the spectrum is reported in the output file. The PSG github page provides an example of the code used to produce the images below.



Planetary Spectrum Generator
National Aeronautics and Space Administration

Chapter 6: **Surface Scattering Modeling**

**Villanueva, Protopapa, Liuzzi, Faggi and
PSG team**



1. Surface modeling in PSG

As light arrives to a surface at a particular wavelength, it can either be absorbed or scattered (reflected). Processes such as surface fluorescence or Raman will transfer some of this energy to a different wavelength, but for our treatment in PSG, we simply consider this as an absorption process at this wavelength. The direction and intensity of the scattered light requires of complex modeling, and several methods exist (e.g., Lambert, Hapke, etc.). The light absorbed will heat the surface, and this together with other internal sources of heat will lead to thermal emission (with an associated directionality and effectiveness/emissivity). How effective the surface scatters light is defined by the single scattering albedo w , where 0 means the light is totally absorbed and to 1 the light is totally scattered back.

The reflected flux from an object will ultimately depend on how the surface scatters back, and we would then require information about the observing geometry, the emission direction and the geometry of the incidence fluxes. Three angles are used to define the geometry: i “incidence angle” is the angle between the Sun (or host-star) and the line perpendicular to the surface at the point of incidence, called the normal; e “emission angle” is the angle between the surface normal and the observer; and g “phase angle”, which is the angle between the source and observer (not to be confused with solar azimuth angle, which is the projection of the phase angle).

The quantity that captures how much light is being reflected towards the observer is called $r(i,e,g)$ “bidirectional reflectance” ($r(i,e,g)=I(i,e,g)/J$, where I is the scattered radiance and J is the incidence radiance) which is in units of $[sr^{-1}]$, with steradians $[sr]$ being a unit of solid angle. A common alternative quantity is the BRDF or “bidirectional-reflectance distribution function” $[sr^{-1}]$, which describes the reflectivity of the surface with respect to a Lambertian sphere, and it is simply $r(i,e,g)/\cos(i)$. Similarly for emission, directional emissivity $\epsilon(e)$ is the ratio of the thermal radiance emerging at emission angle e from the surface with temperature T with respect to a black body at the same temperature.

Once the geometry (i,e,g) and the specific scattering properties (e.g., w) are defined, we would then need a scattering model to accurately model the emissions from the target’s surface. In PSG, four core models are available: Lambert (isotropic scattering), Hapke (parametric surface scattering), Lommel-Seeliger (weakly scattering / diffuse surfaces) and Cox-Munk (specular glint scattering model).

2. Lambert model: isotropic scattering

A Lambertian surface is one that scatters isotropically, as an ideal matte or a perfectly diffusive reflecting surface. The emissivity can be defined as $\epsilon = 1 - w$, while the bidirectional-reflectance distribution function is defined as (adapted from Hapke, 2012a [H12 hereafter] eq. 8.12):

$$BRDF = \frac{w}{\pi} \quad (1)$$

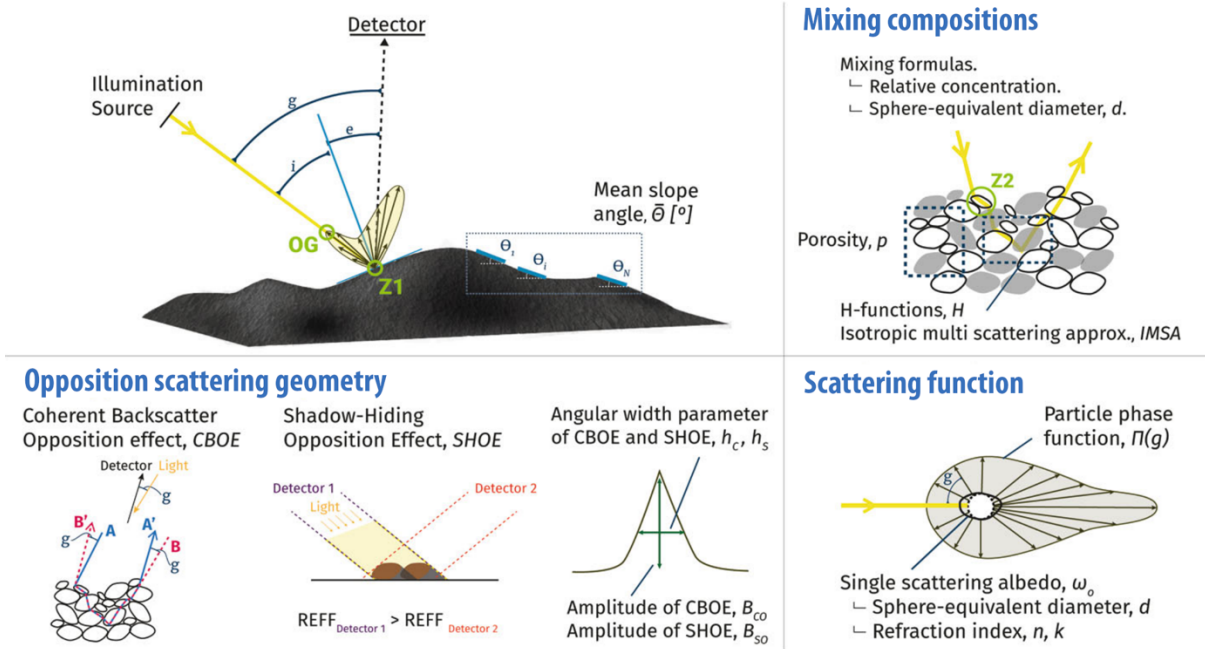


Figure 1: Surface scattering geometry and components of the Hapke surface model. Roughness accounts for the variability of illumination / emission angles, while by combining several components via mixing equations, the heterogeneity of the surface can be captured. The opposition effects are modeling via the CBOE and SHOE terms. Figure adapted from (Pommerol et al., 2019).

3. Hapke model: parametric surface modeling

The Hapke scattering model is a physically motivated model that approximates the solution for radiative transfer for a porous, irregular, and particulate surface. This model has been advancing over the last decades and captures processes and radiative transfer phenomena parameterized with approximations, which are motivated by the basic physical principles of scattering. In PSG, we implement the generic Hapke’s “Isotropic Multiple-Scattering Approximation” (IMSA) model, which is useful if the surface scattering function is not too anisotropic and can be mostly described by a single-scattering term. The implementation also includes Hapke’s shadow-hiding opposition effect (SHOE) factor, the coherent backscatter opposition effect (CBOE) and a compensation for surface roughness. The BRDF can be then modeled following H12 (eq. 12.55) as:

$$\text{BRDF} = K \frac{w}{4\pi} \frac{1}{\mu_{0e} + \mu_e} \left[P(g) [1 + B_{SO} B_S(g)] + H\left(\frac{\mu_{0e}}{K}\right) H\left(\frac{\mu_e}{K}\right) - 1 \right] [1 + B_{CO} B_C(g)] S(i, e, g) \quad (2)$$

where K is the porosity coefficient, μ_{0e} and μ_e are the cosine of the effective incidence and emission angles respectively (see below), $P(g)$ the phase function, B_{SO} is the amplitude of the opposition effect (0 to 1), $B_S(g)$ is the shadow-hiding opposition function, B_{CO} is the amplitude of the coherent backscatter opposition effect (0 to 1), $B_C(g)$ is the backscatter angular function, $H(x)$ is the

Ambartsumian–Chandrasekhar H function, and S is the shadowing/roughness function. The phase function can be characterized using different representations, and in PSG four functions are available: HG1, HG2, HGH and LP2, described here after.

The single lobe Henyey-Greenstein (HG1): has one parameter ξ (asymmetry parameter, -1:backscatterer to 1:forward) defined as (H12 eq. 6.5):

$$P_{HG1}(g) = \frac{1 - \xi^2}{(1 + 2\xi \cos g + \xi^2)^{3/2}} \quad (3)$$

The sign of ξ may differ depending on the definition of the “phase” g angle and the sign of the cosine term used for the HG1 function. In PSG, $g=0$ implies the backward direction, and therefore negative ξ numbers imply backscattering (typical).

The double-lobed Henyey-Greenstein (HG2): has parameters b (asymmetry parameter, 0 to 1) and c (back-scattering fraction, -1 to 1) and it is defined as (H12 eq. 6.7a):

$$P_{HG2}(g) = \frac{1+c}{2} \frac{1-b^2}{(1-2b \cos g + b^2)^{3/2}} + \frac{1-c}{2} \frac{1-b^2}{(1+2b \cos g + b^2)^{3/2}} \quad (4)$$

There are conflicting definitions of the c parameter (some use $[1-c]$ and $[c]$ as scalers), so please consider this carefully when entering this parameter into PSG.

Henyey-Greenstein Hapke/hockey phase function (HGH): It has been observed that for the HG2 function, there is an inverse relationship between the b and c parameters following a hockey stick shape. As such, the HGH phase function can be defined following Hapke, 2012b (eq. 8) as:

$$c = 3.29 \exp(-17.4b^2) - 0.908 \quad (5)$$

The two-term Legendre polynomial function (LP2) has parameters b and c , and it is defined as (H12 eq. 6.3 with P_0 , P_1 , P_2 defined in appendix C.4):

$$P_{LP2}(g) = 1 + b \cos g + c(1.5 \cos^2 g - 0.5) \quad (6)$$

The shadow-hiding opposition function can be approximated following H12 (eq. 9.22) as:

$$B_s(g) = \frac{1}{1 + (1/h_s) \tan g/2} \quad (7)$$

where h_s is the width of the opposition surge. The backscatter angular function can be approximated following H12 (eq. 9.43) as:



$$B_C(g) = \left\{ 1 + [1.3 + K] \left[\left(\frac{1}{h_C} \tan \frac{g}{2} \right) + \left(\frac{1}{h_C} \tan \frac{g}{2} \right)^2 \right] \right\}^{-1} \quad (8)$$

where h_C is the width of the backscatter function. The Ambartsumian–Chandrasekhar H function can be approximated with errors of less than 1% and following H12 (eq. 8.56) as:

$$H(x) = \left\{ 1 - wx \left[r_0 + \frac{1 - 2r_0x}{2} \ln \left(\frac{1+x}{x} \right) \right] \right\}^{-1} \quad (9)$$

where r_0 is the diffusive reflectance, which is calculated from the albedo factor $\gamma = (1-w)^{1/2}$ as (H12 eq. 8.25):

$$r_0 = \frac{1 - \gamma}{1 + \gamma} \quad (10)$$

The porosity coefficient K is dependent on ϕ , the filling factor or fractional volume filled by material (0: loose grains, 1: highly compacted material), given by (H12 eq. 7.45b):

$$K = - \frac{\ln(1 - 1.209\phi^{2/3})}{1.209\phi^{2/3}} \quad (11)$$

When employing the roughness term S , this implementation impacts the effective cosine of the incidence angles ($\mu_0 \rightarrow \mu_{0e}$) and emission angles ($\mu \rightarrow \mu_e$), where $\mu_0 = \cos(i)$ and $\mu = \cos(e)$. The shadowing term and the new μ_{0e} and μ_e are calculated following H12 (eq. 12.63) as: when $i \leq e$:

$$\mu_{0e} = \chi(\theta_p) \left[\cos i + \sin i \tan \theta_p \frac{\cos \psi E_2(e) + \sin^2(\psi/2) E_2(i)}{2 - E_1(e) - (\psi/\pi)E_1(i)} \right] \quad (12)$$

$$\mu_e = \chi(\theta_p) \left[\cos e + \sin e \tan \theta_p \frac{E_2(e) - \sin^2(\psi/2) E_2(i)}{2 - E_1(e) - (\psi/\pi)E_1(i)} \right] \quad (13)$$

$$S = \frac{\mu_e}{\eta(e)} \frac{\mu_0}{n(i)} \frac{\chi(\theta_p)}{1 - f(\psi) + f(\psi)\chi(\theta_p)[\mu_0/\eta(i)]} \quad (14)$$

when $e \leq i$:

$$\mu_{0e} = \chi(\theta_p) \left[\cos i + \sin i \tan \theta_p \frac{E_2(i) - \sin^2(\psi/2) E_2(e)}{2 - E_1(i) - (\psi/\pi)E_1(e)} \right] \quad (15)$$

$$\mu_e = \chi(\theta_p) \left[\cos e + \sin e \tan \theta_p \frac{\cos \psi E_2(i) + \sin^2(\psi/2) E_2(e)}{2 - E_1(i) - (\psi/\pi)E_1(e)} \right] \quad (16)$$

$$S = \frac{\mu_e}{\eta(e)} \frac{\mu_0}{n(i)} \frac{\chi(\theta_p)}{1 - f(\psi) + f(\psi)\chi(\theta_p)[\mu/\eta(e)]} \quad (17)$$

Hapke parameter	Range	Hapke parameters for objects in our solar system					
		Pluto P2020	Europa B2020	Mars F2015	Moon S2014	C-type asteroids HV1989	S-type asteroids HV1989
P(g) phase function	HG1, HG2, HGH, LP2	HG1	HG2	HG2	HGH	HG1	HG1
ξ or b phase coefficient	-1 to 1	-0.36	0.2 to 0.6	0.2 to 0.6	0.1 to 0.3	-0.47	-0.27
c phase coefficient	-1 to 1	-	0.1 to 0.9 alternative	0.1 to 1.0	-	-	-
B _{so} opposition surge scaler	≥ 0	0.307	0.2 to 0.9		1.5 to 2.1	1.03	1.6
h _s opposition surge width	≥ 0	0.206	0.2 to 0.7		0 to 0.12	0.025	0.08
θ roughness mean slope angle [degree]	0 to 40	20	6 to 27	5 to 25	23.4	20	20
ϕ filling factor	0 to 0.75	0.0	0.0	0.0	0.0	0.0	0.0
B _{co} coherent backscattering scaler	0 to 1	0.074	0.0	0.0	0.0	0.0	0.0
h _c width of coherent backscattering	≥ 0	0.0017	0.0	0.0	0.0	0.0	0.0

Table 1 Summary of PSG accepted input parameters for the Hapke model. In yellow the range of each parameter is reported.

where

$$\theta_p = (1 - r_0)\theta \quad (18)$$

$$\psi = \arccos\left(\frac{\cos g - \cos i \cos e}{\sin i \sin e}\right) \quad (19)$$

$$f(\psi) = \exp(-2 \tan(\psi/2)) \quad (20)$$

$$\chi(\theta_p) = (1 + \pi \tan^2 \theta_p)^{-1/2} \quad (21)$$

$$E_1(y) = \exp(-2/\pi \cot \theta_p \cot y) \quad (22)$$

$$E_2(y) = \exp(-1/\pi \cot^2 \theta_p \cot^2 y) \quad (23)$$

$$\eta(y) = \chi(\theta_p)[\cos y + \sin y \tan \theta_p (E_2(y)/(2 - E_1(y)))] \quad (24)$$



Thermal emission from a scattering surface will also have directionality, and the directional emissivity of an optically thick particulate medium can be defined following H12 (eq. 15.19) as:

$$\varepsilon = \gamma H(\mu) \quad (25)$$

Table 1 summarizes the parameters needed by PSG when performing Hapke modeling and their typical range. For comparison Hapke parameterizations and derivations for objects across our solar system are also listed, in which P2020: (Protopapa et al., 2020), B2020: (Belgacem et al., 2020), F2015: (Fernando et al., 2015), S2014: (Sato et al., 2014), HV1989: (Helfenstein and Veverka, 1989), and L2015: (J.-Y. Li et al., 2015).

4. Lommel-Seeliger: dark and weakly scattering Lunar/asteroid/comet surfaces

For relatively dark objects with weakly scattering surfaces, the Lommel-Seeliger model performs well in capturing the variation of the scattered fluxes with respect to the source/observational angles. It is therefore the preferred model when interpreting the Moon, asteroids and other small bodies. The generalized Lommel-Seeliger is defined as (adapted from H12 eq. 8.35a):

$$\text{BRDF} = \frac{w}{4\pi} \frac{1}{\mu + \mu_o} P(g) \quad (26)$$

where w is the surface single scattering albedo and $P(g)$ is the single-scattering phase function. Several disk-resolved models are based on this basic formalism (e.g., ROLO), and since this model is suitable for small unresolved dark bodies, it is the preferred method in PSG for modeling the disk-resolved BRDF of asteroids and comets. In the literature, there are several measurements and derivations of the “phase function” for unresolved bodies, but these refer to the integral phase function $\Phi(g)$, not to $P(g)$. We can re-normalize the empirically derived $\Phi(g)$ to an effective surface $P(g)$ by dividing by the integrated reflectance of a perfect Lommel-Seeliger object (adapted from H12 eq. 6.14):

$$\frac{\Phi(g)}{P(g)} = \left[1 - \sin \frac{g}{2} \tan \frac{g}{2} \ln \left(\cot \frac{g}{4} \right) \right] \quad (27)$$

Lumme-Bowell phase function (HG): The Lumme-Bowell model is a scattering model typically used in asteroid research and presented in Lumme and Bowell (1981). A simplified empirical version of the integral Lumme–Bowell model was adopted by the International Astronomical Union (IAU) in 1985 to describe the integral phase function of asteroids, and this function with slope parameter is adopted as (H12 section 12.5.2):

$$\Phi(g) = (1 - G)\Phi_1(g) + G\Phi_2(g) \quad (28)$$

$$\Phi_1(g) = \exp[-3.33(\tan g/2)^{0.63}] \quad (29)$$

$$\Phi_2(g) = \exp[-1.87(\tan g/2)^{1.22}] \quad (30)$$



Figure 2: Lommel-Seeliger surface modeling of the Moon with PSG. The simulation was performed employing a constant phase function, $P(G)=1$. The Lommel-Seeliger scattering model captures the quite homogeneous brightness observed on the Moon across the illuminated regions, while also models the significant brightening occurring at the illuminated limb.

where $\Phi_1(g)$ is the single scattering component (steep function, ~ 0.043 mag/deg), $\Phi_2(g)$ the multiply scattered component (shallower, ~ 0.014 mag/deg), and G is the slope parameter ($0 \leq G \leq 1$). Considering that the geometric albedo (A_{geo}) of a LS object is $w/8$, the single scattering albedo w can be determined from A_{geo} and the disk-integrated absolute magnitude H_0 value and the object's diameter (D) as (Tedesco et al., 1992):

$$A_{\text{geo}} = \frac{w}{8} = \left(\frac{1329}{D[\text{km}]} 10^{-0.2H_0} \right)^2 \quad (31)$$

Muinsonen 3-parameters (HG_1G_2): over the last decades, it was observed that several bodies could not be properly described with the HG phase function, and a new system with three parameters was developed (Muinsonen et al., 2010). In 2012, the IAU replaced the HG system with the HG_1G_2 system. The integral phase function, with splines coefficients listed in (Penttilä et al., 2016), is described as:

$$\Phi(g) = G_1\Phi_1(g) + G_2\Phi_2(g) + (1 - G_1 - G_2)\Phi_3(g) \quad (32)$$

$$\text{Splines of } \Phi_1(g) = 1 - 6g/\pi \quad (33)$$

$$\text{Splines of } \Phi_2(g) = 1 - 9g/(5\pi) \quad (34)$$

$$\text{Splines of } \Phi_3(g) = \exp(-4\pi \tan^{2/3} g/2) \quad (35)$$



Penttila 2-parameters (HG₁₂): Penttilä et al. (2016) determined an improved relationship between the G1 and G2 parameters, which is applicable to all types of asteroids with the exception of E- and D-types:

$$G_1 = 0.5351335 \cdot G_{12} \quad (36)$$

$$G_2 = 0.84293649 - 0.5351335 \cdot G_{12} \quad (37)$$

where G_{12} is only valid between 0 and 1.

Exponential (EXP): an exponential empirical series was investigated for the OSIRIS-REx mission to asteroid Bennu (Takir et al., 2015) as:

$$P(g) = \exp(\beta g + \gamma g^2 + \delta g^3) \quad (38)$$

Lunar/ROLO: The ROLO model was developed by (Buratti et al., 2011), using the USGS's ROLO data from NASA's Moon Mineralogy Mapper (M3), and the surface phase function and single scattering albedo can be described following (Buratti et al., 2011) as:

$$P(g) = C_0 \exp(-C_1 g) + A_1 g + A_2 g^2 + A_3 g^3 + A_4 g^4 \quad (39)$$

$$w = 4(A_0 - C_0) = 8 A_{geo} \quad (40)$$

The Table 2 summarizes the parameters needed by PSG when employing the LS model and their typical value ranges. For comparison, parameterizations and derivations for objects across our solar system are also listed, in which T2015: (Takir et al., 2015), C2017: (Ciarniello et al., 2017), B2011:(Buratti et al., 2011), V2015: (Vereš et al., 2015).

LS model parameter	Range	Parameters for objects in our solar system					
		Bennu T2015	67P C2017	Ceres C2017	Moon B2011	C-type asteroids V2015	S-type asteroids V2015
$\Phi(g)$ Phase function	HG, HG1G2, HG12, EXP, ROLO	EXP	HG	HG	ROLO	HG12	HG12
$G, a_1, G_{12}, \beta, C_0$	See text	-0.043	-0.09	0.02	$0.2-0.4 \cdot 10^{-2}$	0.58	0.47
a_2, γ, C_1		$2.6 \cdot 10^{-4}$			0.04 to 0.23		
a_3, δ, A_1		$-9.7 \cdot 10^{-7}$			-0.6 to $0.1 \cdot 10^{-2}$		
A_2					-1 to $1 \cdot 10^{-4}$		
A_3					-4 to $2 \cdot 10^{-6}$		
A_4					-1 to $2 \cdot 10^{-8}$		

Table 2 Summary of PSG accepted input parameters for the Lommel-Seeliger model. Few examples reporting small bodies of the solar system and the Moon are shown in each column.

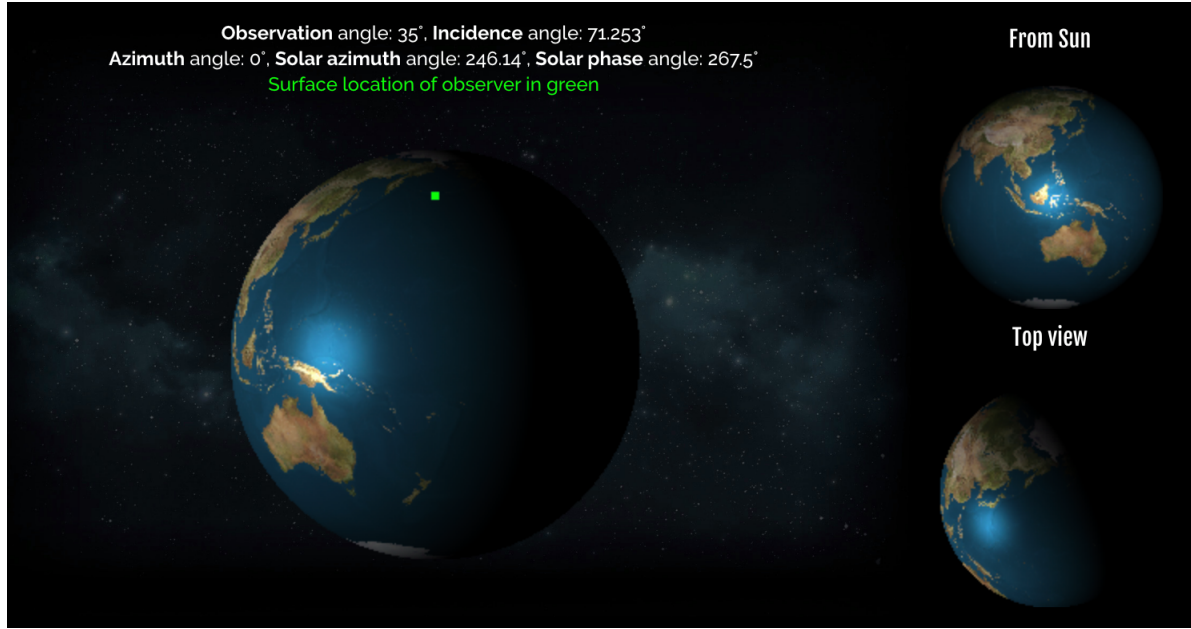


Figure 3: Ocean glint modeling with PSG. Typically, ocean glint leads to a notable and localized enhancement of the planetary brightness near the sub-solar point, yet the location and shape of the feature depends on the wind speed and specific observational angles. This enhancement is particularly bright and contrasted considering the typical dark / low-albedo properties of the deep oceans.

5. Cox-Munk model: glint and ocean's reflections

The Cox-Munk model is a scattering model of glitter on a water surface. The model employs geometric optics model with the assumption of a Gaussian distribution of the slopes of the wave facets. In the implementation of the glint model in PSG, the BRDF includes two terms, the pure glint term (Cox and Munk, 1954; Jackson and Alpers, 2010; Ma et al., 2015; Spurr, 2002), and the classical non-glint Lambert term for the surface:

$$\text{BRDF} = \text{BRDF}_{\text{glint}} + \text{BRDF}_{\text{Lambert}} \quad (41)$$

$$\text{BRDF}_{\text{glint}} = \frac{r_p s_{\Lambda} (1 + \tan^2 \beta)^2}{4 \cos e} \quad (42)$$

where r is the Fresnel reflection coefficient for an unpolarized source and computed as:

$$g_r = \text{asin}(\sin g / 1.34) \quad (43)$$

$$r = \frac{1}{2} \left[\left(\frac{\sin(g - g_r)}{\sin(g + g_r)} \right)^2 + \left(\frac{\tan(g - g_r)}{\tan(g + g_r)} \right)^2 \right] \quad (44)$$



Cox and Munk (1954) found that the probability density function of the wave slopes depends on the wind speed (U_{wind} , assumed 4 m/s when not provided), and the probability determining glint reflections can be approximated by a Gaussian function as:

$$\sigma^2 = 0.003 + 0.00512 U_{\text{wind}}[\text{m/s}] \quad (45)$$

$$\cos \beta = \frac{\cos i + \cos e}{2 \cos g} \quad (46)$$

$$p = \frac{1}{\pi \sigma^2} \exp \left(-\frac{\tan^2 \beta}{\sigma^2} \right) \quad (47)$$

As we approach high incidence angles, not all facets are visible, and the “shadow” term compensates for this:

$$s_{\Lambda} = \frac{1}{1 + \Lambda(i) + \Lambda(e)} \quad (48)$$

$$\Lambda(x) = \frac{1}{2} \left\{ \frac{1}{\sqrt{\pi}} \frac{\sigma}{\cot x} \exp \left(-\frac{\cot^2 x}{\sigma^2} \right) - \text{erfc} \left(\frac{\cot x}{\sigma} \right) \right\} \quad (49)$$

where $\text{erfc}(x)$ is the complementary error function.

6. Cometary dust/icy grains

Dust and icy particles in an extended coma are typically the main source of continuum radiation in small bodies and in comets. Several properties impact the scattered light from dust grains, with the main being: the amount of dust present in the coma, the size distribution and its variation across the coma, and the shape and scattering properties (e.g., phase function) of the dust grains. A metric to quantify the amount of dust in the coma is the dust/gas mass ratio [Q_d/Q_g], in which Q_d and Q_g are described in units of mass ejected per second (e.g., kg/s). Inferring this quantity from cometary observations can be quite challenging, since this would require precise knowledge of the kinematics, specific mass densities, scattering properties and 3D distribution for all possible size bins. For instance, this ratio can vary by orders of magnitude depending only on the assumed size distribution of the dust particles (Marschall et al., 2020), yet observations of comets in many cases suggest mass ratios Q_d/Q_g ratios near ~ 1 (e.g., Marschall et al., 2020; Weiler et al., 2003).

Ultimately, the dust particles that make up the extended coma are only those allowed to escape, with large particles following ballistic trajectories and falling back to the surface due to the nucleus gravity. The size of the particles allowed to escape will primarily depend on the thermodynamic properties of the gas, the surface temperature, and the specific density of the dust particles. Interestingly many of these quantities are related to the available solar radiation, and therefore the size distribution will be typically connected to the heliocentric distance, with larger dust grains favorably lifted at smaller heliocentric distances (Weiler et al., 2003). The available scattering surface

(S) relative to the particle's mass (M) decreases linearly with the radius (r) of the particle ($S[r]/M[r] \propto 1/r$), so a size distribution containing larger particles will have less available scattering surface to scatter and emit radiation per unit mass. This effect is compounded by the fact that different particle sizes will have different velocities, leading to a noticeable effect on the available scattering surface area with heliocentric distance and along the coma. In addition, the scattering properties will depend strongly on the size of particles (Fink and Rubin, 2012), with larger particles behaving more like a solid body, and smaller particles with pronounced Mie forward/backward scattering responses.

Modeling of dust emission in comets have been motivated from decades of observations of comets, historically primarily done at optical wavelengths and quantified via the comet's apparent magnitude. The apparent magnitude (m_V) can provide a first order quantification to the level of activity, yet comets are diffuse objects, and the integrated flux and herewith observed magnitude will depend on the considered integration aperture (i.e., field of view). In order to mitigate this issue, A'Hearn et al. (1984) introduced the quantity $Af\rho$ [cm], which provides a metric to the comet brightness corrected by the observing aperture. A is the average albedo of the dust particles and dependent on phase and wavelength, ρ is the aperture radius [cm] and f is the filling factor, which is the total cross section (S_{dust} [cm²]) of the grains within the field of view divided by the area of the field of view ($S_{\text{FOV}} = \pi\rho^2$ [cm²]). The total scattering cross section in an optical thin case can be related to total the number [N] of particles as $S_{\text{dust}} = N\sigma$, where σ [cm²] is the cross section of a single dust particle. The total luminosity of a comet is then $AN\sigma F_\star / r_H^2$, where F_\star is the solar flux at 1 AU and r_H [AU] is the heliocentric distance. $Af\rho$ is then defined as:

$$Af\rho = 4 \frac{F_{\text{comet}}}{\rho} \frac{(\Delta r_H \text{AU})^2}{F_\star} \quad (50)$$

where Δ [AU] is the geocentric distance and AU [cm] is the astronomical unit. The apparent magnitude in the V-band with a field-of-view diameter of θ [arcsec] ($\theta = 2.7576E-08 \rho/\Delta$) can be calculated from $Af\rho$ as:

$$m_V = -2.5 \log \left(\frac{F_{\text{comet}}}{F_{\text{ref}}} \right) = -2.5 \log \left(1.6204E-15 [Af\rho] \frac{\theta F_\star}{F_{\text{ref}} \Delta r_H^2} \right) = -2.5 \log \left(\frac{1.9602E-9 [Af\rho] \theta}{\Delta r_H^2} \right) \quad (51)$$

The relationship between these observational quantities and the actual amount of dust ejected by the comet is highly model dependent as explained above, yet a higher $Af\rho$ would in principle be associated with a higher amount of dust. Observational data do point to some particular relationships between the $Af\rho$ (e.g., A'Hearn et al., 1995), the visual magnitude (e.g., Jorda et al., 2008), the water production rate, the geocentric distance and the heliocentric distance. Some of the scattering processes discussed above would be responsible for these relationships, and in PSG we implement an empirical approach to relate gas activity and dust cometary emission intensity.

Specifically, A'Hearn et al. (1995) noticed a pronounced relationship between $Af\rho/Q(\text{OH})$ and heliocentric distance and perihelion distance, which is consistent with a lower scattering area when closer to the Sun (see Figure 4) as previously discussed. The molecular production rates reported in that work were computed assuming a constant expansion velocity of 1 km/s, yet it has been observed

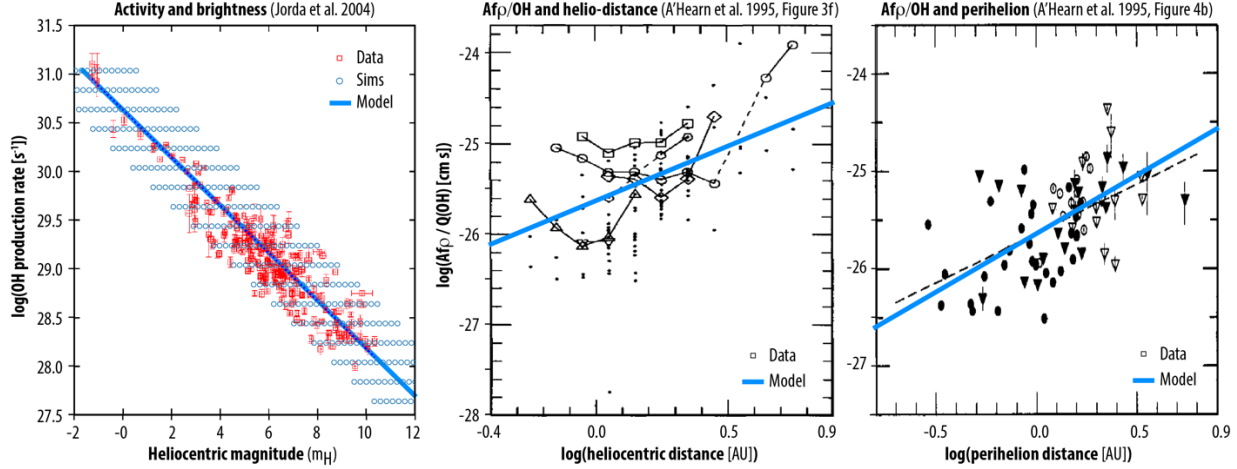


Figure 4: Relationships between optical magnitude and $Q(\text{OH})$ as determined by Jorda et al. (2008) and between $Afp/Q(\text{OH})$ and heliocentric distance and perihelion distance as determined by A'Hearn et al. (1995). The observed relationship can be relatively well described by equations (52) and (51). The model trends for $Afp/Q(\text{OH})$ also include a correction factor of $0.8r_H^{-0.5}$ to capture the typical variation of the expansion velocity with heliocentric distance and a common $P_{HM}(g)$ phase function value of 0.5.

that the expansion velocity in comets is generally best described with a $\sim 0.8r_H^{-0.5}$ relationship (Biver et al., 1999), so part of that trend could be explained by that effect. Yet, we observe that a remnant $r_H^{0.7}$ factor could further assist to fully describe the observed $Afp/Q(\text{OH})$ trend (see Figure 4). This relationship with heliocentric distance is consistent with larger particles having lower scattering efficiency and being lifted more effectively when closer to the Sun. In Figure 4, we show model slopes under these considerations which nicely overlap with the observations. We further validated this relationship by comparing to the $Q(\text{OH})$ versus heliocentric magnitude determined by Jorda et al., (2008) for a selection of observations, and also obtain a relatively good agreement to the observed slope between the points. The empirical relationship that we obtain between $Q(\text{H}_2\text{O})$ [s^{-1}] and Afp [cm] can be described as, where $P_{HM}(g)$ is the Halley-Marcus phase function at phase angle g :

$$Afp = P_{HM}(g) \left(\frac{Q(\text{H}_2\text{O})}{3E25} \right) r_H^{0.7} \quad (52)$$

Cometary dust is known to display a strong phase relationship, and in PSG we integrate the Halley-Marcus (H-M) integral phase function $P_{HM}(g)$ compiled by (Schleicher and Bair, 2011) to model the scattering properties for the dust grains at other phases, independently of the selected nucleus scattering and phase models. The user can then select from three different options to define the dust continuum intensity:

$A(g)fp$: the user may directly provide the Afp for this phase, effectively providing $AfpP_{HM}(g)$, and since this quantity intrinsically includes a phase correction, the reflected fluxes are not corrected by the H-M phase curve, yet the thermal fluxes are corrected by $1/P_{HM}(g)$.

$\log[A(g)f_p/Q]$: in this case the user is providing Afp for this phase yet relative to the user-provided activity of the comet. Typical values would be in the -25 to -27 range.

Dust/gas: this input behaves as a scaler to the empirical relationship of Afp vs. Q described by equation (52). A typical comet would have dust/gas=1, while a “dusty” comet would have values higher than 1.

Beyond the previously discussed continuum intensity considerations, small bodies and dusty coma are known to show a strong **phase reddening effect** (Bockelée-Morvan et al., 2019; Fornasier et al., 2020; Sanchez et al., 2012). This phenomenon has been attributed to small-scale surface roughness on large bodies, space weathering, and multiple scattering on dusty environments. This effect is particularly prominent in the near-IR/optical, and in PSG the user can select the “RED” phase function with a reddening a slope [%/μm] that will be used to correct the synthetic spectra at wavelengths shorter than 2.5 μm. When employing this spectral phase function, the user provided albedo values are those describing the spectral point at 0.5 μm.

7. Mixing compositions

A planetary surface is typically not composed of a single homogenous constituent with specific optical properties, but of a mixture of constituents. The optical properties of the aggregate would vary depending on how the constituents are organized and the shape/scattering properties of the individual constituents (Figure 5). Several mixing models (e.g., areal, intimate, intraparticle) do exist, approximating the effective optical properties of the aggregate. In the simplest case, the areal mixing model assumes that the surface is composed of several unresolved smaller patches having each a homogenous composition. One can then treat each patch separately, and compute BDRFs and optical properties individually, which are then aggregated as a linear sum weighted by their corresponding area.

Other mixing models, as the intraparticle mixing models, operate with the individual optical constants of the constituents, and determine an effective set of optical constants for the mixture. In PSG, the optical properties of the constituents can be defined in several forms (e.g., reflectance, attenuation coefficient), and these need to be converted to optical constants in order to perform the mixing operations. When operating with intraparticle mixing models and when one of the constituents is not described via optical constants, the n refraction coefficient is assumed to be 1.0, while the extinction coefficient is determined using the following conversions:

$$k_{refl} = -\frac{\ln(r)\lambda[\mu m]}{4\pi h[\mu m]} \quad k_{alpha} = 10^{-4} \frac{\alpha[cm^{-1}]\lambda[\mu m]}{4\pi} \quad (53,54)$$

where r is the tabulated reflectance for the constituent, α is the alpha attenuation coefficient, λ is the wavelength of the extinction and h is the thickness of the main constituent of the mixture. Mixing is defined when N or more endmembers are combined together in different concentrations f_j . Two physical constraints define the concentrations: 1) The sum of the concentrations must be equal to one. If the sum of the concentration is lower than 1, PSG will complement the mixture with the

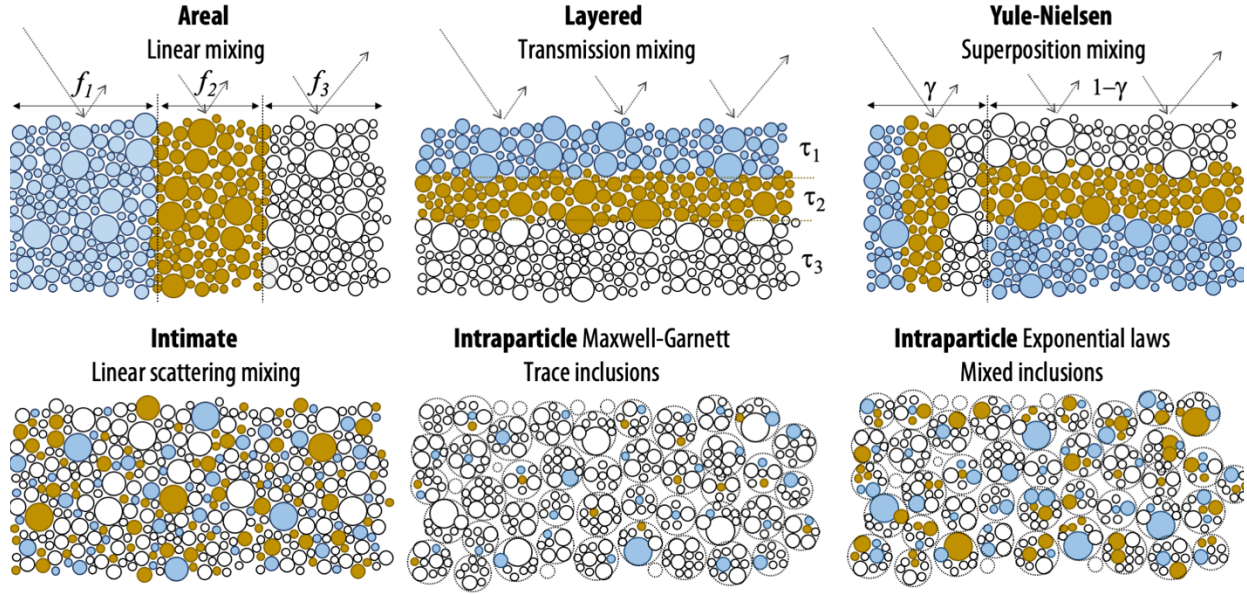


Figure 5: Depending on how the components are organized on the surface, the mixing and combination of the optical properties of the components need to be handled differently. PSG integrates several mixing models that approximate the average and effective scattering properties of the total mixture. A common mixing model is the “areal” combination, in which the effective BRDF is computed as a linear mixture of the BRDF of the individual constituents, while in an intraparticle Maxwell-Garnett mixture, the scattering properties are assumed to be dominated by a specific component with inclusions of a set of trace constituents.

average “albedo” and “emissivity” values provided for the surface. If the sum is greater than 1, then the abundances will be normalized so the sum is 1. 2) Negative concentrations do not have a physical meaning, and therefore all the concentrations must be equal to or greater than 0.

Areal linear mixing: in this mixing model, the surface radiative transfer for each constituent is computed separately and the total resulting BRDF is calculated as a linear sum of the scattering properties (single scattering albedo w_i and emissivity ϵ_i) for each constituent weighted the concentration f_j :

$$\text{BRDF}_T = \sum_{j=1}^N f_j \text{BRDF}(w_j) \quad \epsilon_T = \sum_{j=1}^N f_j \epsilon(\epsilon_j) \quad (55,56)$$

Layered transmission mixing: if the constituents are organized on top of each other forming layers, the optical properties of the aggregate can be modeled as a succession of filters (Grillini et al., 2020). This model is also called “subtractive”. The single scattering albedo of the mixture is then obtained as the consecutive products of the single endmembers’ w_j , implementing the concentrations in a geometric mean fashion:

$$w_T = \prod_{j=1}^N w_j^{f_j} \quad (57)$$

Yule-Nielsen superposition mixing: this mixing model is a hybrid between the layered (subtractive) and linear (additive) mixing models, which was developed in the study of half-toning, since neither subtractive nor additive models could explain such colors (Yule and Nielsen, 1951). It approximates the layered model when γ approaches 0 asymptotically, and the linear mixing when γ is 1.

$$w_T = \left(\sum_{j=1}^N f_j w_j^\gamma \right)^{\frac{1}{\gamma}} \quad (58)$$

Intimate linear scattering mixing: Intimate mixture models describe surfaces where grains of different materials are mixed on a small scale rather than being spatially segregated. The combined single scattering albedo is calculated for the mixture using a weighted average. The weight of each constituent is computed as $f_j = X_j \sigma_j$, where X_j is the volume fraction and σ_j its cross-sectional area. In PSG, the user input describes f_j . When employing scattering models that linearly depend on the single scattering model, as Lambert and Lommel-Seeliger, areal and intimate mixtures are indistinguishable when employing the same weights.

$$w_T = \sum_{j=1}^N f_j w_j \quad (59)$$

Intraparticle Maxwell-Garnett: this type of mixing describes the situation where a small fraction (<20%) of contaminating material is present as inclusions embedded in a host matrix material with different optical properties. This type of mixing model has precedent in the spectral interpretation of many icy solar system objects (e.g., Molyneux et al., 2020). For a comprehensive set of criteria for mixing rules application for inhomogeneous astrophysical grains and planetary surfaces, please refer to (Maron and Maron, 2008). As nicely demonstrated by Mallet et al. (2005), if single scattering is the dominant mechanism, the coherent and incoherent scattering cross sections of the finite random media are accurately described by the scattering and absorption cross sections of the homogenized test volume with Maxwell-Garnett permittivity. This is true whichever the statistical distribution of the particles is, as long it is uniform. On the other hand, if multiple scattering is important, the effective permittivity depends strongly on the n-point probability distribution function of the aggregate. Yet, if the particle positions can be considered uncorrelated, the effective permittivity reduces to the Maxwell-Garnett expression. Thus, this mixing rule remains valid in a regime where it is usually not expected to hold - that is, for a high density of scatterers with strong electromagnetic interaction. The Maxwell-Garnett model was originally designed for two constituents, but it can be readily generalized to N constituents (Sihvola, 2000) as:

$$\varepsilon_T = \varepsilon_e + 3\varepsilon_e \frac{\sum_{j=1}^N \left(f_j \frac{\varepsilon_j - \varepsilon_e}{\varepsilon_j + 2\varepsilon_e} \right)}{1 - \sum_{j=1}^N \left(f_j \frac{\varepsilon_j - \varepsilon_e}{\varepsilon_j + 2\varepsilon_e} \right)} \quad (60)$$

where ε_j is the inclusion dielectric constant and ε_e is the medium dielectric constant (defined in PSG as the constituent with the highest concentration). This mixing operation is computed numerically employing complex math and considering the following Kramers-Kronig relations:

$$\varepsilon = \varepsilon_{Re} + \varepsilon_{Im}i \quad \varepsilon_{Re} = n^2 - k^2 \quad \varepsilon_{Im} = 2nk \quad (61,62,63)$$

$$n = \sqrt{\frac{\varepsilon_{Im} + \varepsilon_{Re}}{2}} \quad k = \sqrt{\frac{\varepsilon_{Im} - \varepsilon_{Re}}{2}} \quad (64,65)$$

Intraparticle Exponential laws: when the particles are oriented in a particular way relative to the incident field or when the abundance of the inclusions is comparable to that of the medium, other mixing rules better describe the optical properties of the aggregate. A flexible mixing model is that in which the dielectric constant of the constituents are added as a summation of terms affected by an exponential power law. Several effective mixing models can be described with this model.

$$\varepsilon_T = \left(\sum_{j=1}^N f_j \varepsilon_j^{\frac{1}{m}} \right)^m \quad (66)$$

- **Arithmetic linear volumetric mixing formula ($m = 1$, high Wiener bound):** this is the most intuitive model among the exponential models, in which the aggregate's dielectric constant is based on the linear proportion of the constituents. This mixing formula describes an anisotropic mixture where inclusions are oriented along the incident flux, corresponding to the upper-bound in permittivity for the aggregate, also called the high “Wiener bound”.
- **Harmonic average mixing formula ($m = -1$, low Wiener bound):** this mixing is based on the rules of inverses, and it is suitable for constituents having diametrical opposite permittivities. This mixing formula describes an anisotropic mixture where inclusions are oriented perpendicular to the incident flux, corresponding to the lower-bound in permittivity for the aggregate, also called the low “Wiener bound”.
- **Complex Refractive Index mixing formula ($m = 2$, Beer's or Birchak's mixing):** this mixing is based on the average transit time across the constituents. This type of mixture is valid when the wavelength is smaller than the thickness of the inclusion layers (Seleznev, 2005).
- **Looyenga ($m = 3$, Looyenga-Landau-Lifshiz mixing):** this mixture is suitable for low dielectric contrast between different inclusion phases, or small volume fraction of the inclusions with higher dielectric contrast, and it is thus not appropriate in the metallic limit. The Looyenga mixing rule gives best results for porous ice (Maron and Maron, 2008). In the case of interstellar or circumstellar grains, the processes leading to their nucleation and growth are complicated and depend on not always known conditions, which can change in time and space, physical and chemical nature.

8. Calculation of the single scattering albedo: reflectances, optical constants and albedos

For each of the models described above, a key parameter is the single scattering albedo (w). This parameter can be calculated for a specific surface from optical constants, or it can be determined

from laboratory measurements of reflectance of that component, or it can be derived from astronomical measurements (e.g., geometric albedo). Scattering albedo, geometric albedo, Bond albedo, reflectance, absorptivity are all related quantities, yet they have very different meaning and their values can differ greatly for the same component. For instance, how can one use a “reflectance” laboratory spectrum with the models previously described? One would need to convert these to a wavelength dependent single scattering albedo (w), and for that we would need the exact sample properties (e.g., compactness) and observing conditions as employed in the laboratory experiment.

Reflectances: if the user provides “albedo”, “reflectance” or employs reflectance databases (e.g., USGS), PSG will normally assume this to be single scattering albedo (w). For the RELAB database, PSG integrates their most spectrally complete spectrum for each sample and measurements taken at the nominal phase $g=30^\circ$. The raw RELAB spectra have been converted from measured reflectance to Hapke’s diffusive reflectance (r_0) employing look-up tables based on equation 2, assuming $K=1$, $B_{SO}=0$, $B_{CO}=0$, $S=1$, and an empirical phase function as reported in equation 6 of Mustard and Pieters (1989), $P(30^\circ)=1.65-0.75w$. Specifically and only when utilizing the Hapke model with reflectances, PSG considers that the reflectance inputs are Hapke’s diffusive reflectances (r_0), not single scattering albedos (w). The relationship between the single scattering albedo (w) and the Hapke’s diffusive reflectance parameter (r_0) is:

$$w = \frac{4r_0}{(1+r_0)^2} \quad r_0 = \frac{1 - \sqrt{1-w}}{1 + \sqrt{1-w}} \quad (67,68)$$

Alpha parameter (attenuation coefficient): for species described with an “attenuation coefficient” (α), the single scattering albedo is calculated as $w = \exp(-\alpha h)$, where h is the thickness (or mean ray path length) of the material on the surface.

Optical constants: when optical constants (n and k) are provided, the single scattering albedo (w) at wavelength λ for a slab of thickness h is calculated following H12 (section 6.5.3, w from eq. 6.20, S_e from eq. 5.37, S_i from eq. 6.23, θ from eqs. 5.56 and 5.8):

$$w = S_e + (1 - S_e) \frac{1 - S_i}{1 - S_i \theta} \quad (69)$$

$$S_e = 0.0587 + 0.8543 \Gamma + 0.0870 \Gamma^2 \quad (70)$$

$$S_i = 1 - \frac{1}{n^2} [0.9413 - 0.8543 \Gamma - 0.087 \Gamma^2] \quad (71)$$

$$\Gamma = \frac{(n-1)^2 + k^2}{(n+1)^2 + k^2} \quad (72)$$

$$\theta = \exp \left[-4\pi k \frac{h[\mu\text{m}]}{\lambda[\mu\text{m}]} \right] \quad (73)$$



Geometric albedo (A_{geo}) or physical albedo: this is an apparent quantity that specifies how bright the whole planet/object appears for its size (idealized flat disk) at phase=0 (as seen from the Sun/star). $A_{geo}=1$ means that all the light arriving is reflected back, and A_{geo} can also be greater than 1 if the object has a strong opposition effect. Considering that a planetary disk encounters the full range of incidence / emission angles, the relationship between A_{geo} and w will differ depending on the assumed surface scattering model (Shepard, 2017, H12 eq. 11.34):

$$A_{geo}^{Lambert} = \frac{2}{3} w \quad A_{geo}^{LS} = \frac{1}{8} w P(0) \quad (74,75)$$

$$A_{geo}^{Hapke} = \left\{ \frac{w}{8} [P(0)(1 + B_{s0}) - 1] + (0.49 r_0 + 0.19 r_0^2) \right\} (1 + B_{s0}) \quad (76)$$

Bond albedo (A_{Bond}): this quantity defines how much radiation the surface scatters across all wavelengths and all directions. The Bond albedo is a value strictly between 0 and 1, as it includes all possible scattered light (but not radiation from the body itself). Bond albedo is particularly relevant when investigating the energy balance of a planet, yet it should not be used when predicting the brightness of an object at a certain wavelength, since this quantity effectively describes the average response cross all wavelengths.

Emissivity (ϵ): this quantity defines the efficiency of a surface in radiating its thermal energy. Considering energy conservation and Kirchhoff's law, the emissivity could be defined to be equal to 1 minus the absorptivity when integrating across all wavelengths, yet emissivity could exceed unity at certain wavelengths and directions. Absorptivity and Bond albedo are closely related, but not exactly the same, and in many cases the relationship 1-albedo can be assumed. In a general case, emissivity can have “direction” and specific response at a certain wavelength, and as reported above, for each scattering we define a method to compute emissivity from the scattering albedo.

9. Disk integrated quantities: albedos and phase integrals

One important aspect of the BRDF quantity is that it refers to a spatially defined location on the planet's surface, with a specific bi-directionality between the source (i angle) and the observer (e and g angles). In many cases, the observer's field-of-view (FOV) may encompass a broad range of incidence and emission angles, as when we measure the spectra of unresolved small-bodies. We would then need the integral of the bi-directional reflectance across the sampled region, or disk-integrated reflectance when the whole hemisphere is sampled. One important quantity is then the integral phase function $\Phi(g)$, which defines how the brightness of the planet/object changes when observed at different phases with respect to opposition ($g=0$). As we discussed above, at phase $g=0$, A_{geo} defines the average reflectivity at opposition, while $\Phi(g)$ operates as a scaling factor for other phase angles and normalized to 1.0 for $g=0$. The phase integral is defined for each scattering modeling as following (Shepard, 2017, H12 eq 11.42):

$$\Phi(g)_{Lambert} = \frac{1}{\pi} (\sin g + (\pi - g) \cos g) \quad (77)$$

$$\Phi(g)_{LS} = P(g) \left[1 - \sin \frac{g}{2} \tan \frac{g}{2} \ln \left(\cot \frac{g}{4} \right) \right] \quad (78)$$

$$\begin{aligned} \Phi(g)_{Hapke} = \frac{r_0}{2A_{geo}} & \left\{ \left[\frac{(1 + \gamma)^2}{4} \{ [1 + B_{s0} B_s(g)] P(g) - 1 \} + [1 - r_0] \right] \right. \\ & \times \left[1 - \sin \frac{g}{2} \tan \frac{g}{2} \ln \left(\cot \frac{g}{4} \right) \right] \\ & \left. + \frac{4}{3} r_0 \frac{\sin g + (\pi - g) \cos g}{\pi} \right\} [1 + B_{c0} B_c(g)] \end{aligned} \quad (79)$$

These integral formalisms are only provided for reference, since PSG performs the integrals across the field-of-view numerically. Specifically, the geometry module in PSG computes a scaling factor to the discrete reflectance at the (i,e,g) employed by the radiative transfer module, with respect to the integrated reflectance when diverse angles encompassed by the FOV are considered. This integration is performed numerically for the average w by dividing the disk in 140×140 pixels (19600 pixels), and a scaling factor between the FOV/disk-integrated and disk-resolved scattering model is determined. This allows PSG to compute accurately the radiating fluxes even when the FOV encompasses a large fraction of the disk and is offset from the object center.

10. Thermo-physical Modelling (PSGTM)

The temperature across a planetary surface is governed by a balance between insolation, surface properties (e.g., roughness), climatological recirculation of thermal energy and the inertia of the surface and the atmosphere to conserve/release heat. Detailed 3D surface and climate models would be needed to fully capture the redistribution of thermal fluxes, yet several analytical expressions and simplified thermo-physical models exist that are based on first principles and capture the main thermal anisotropies across a planet. On irradiation alone, the temperature of a surface can be defined as:

$$T_{irr} = T^* \sqrt{\frac{R^*}{r_h}} \quad (80)$$

where T^* [K] is the host stellar temperature, R^* [m] is the stellar radius and r_h is the planet-star distance [m]. If the planet does not absorb all the incoming irradiation (with A describing the bond albedo) and emits only a fraction (ϵ is emissivity), the equilibrium temperature at a surface is described as:

$$T_0 = T_{irr} \left(\frac{1-A}{\epsilon} \right)^{1/4} \quad (81)$$

For a spherical planet in which heat is perfectly re-distributed across the planet, it will have a uniform temperature at all locations, and this uniform and global equilibrium temperature can be calculated as (Cowan and Agol, 2010):

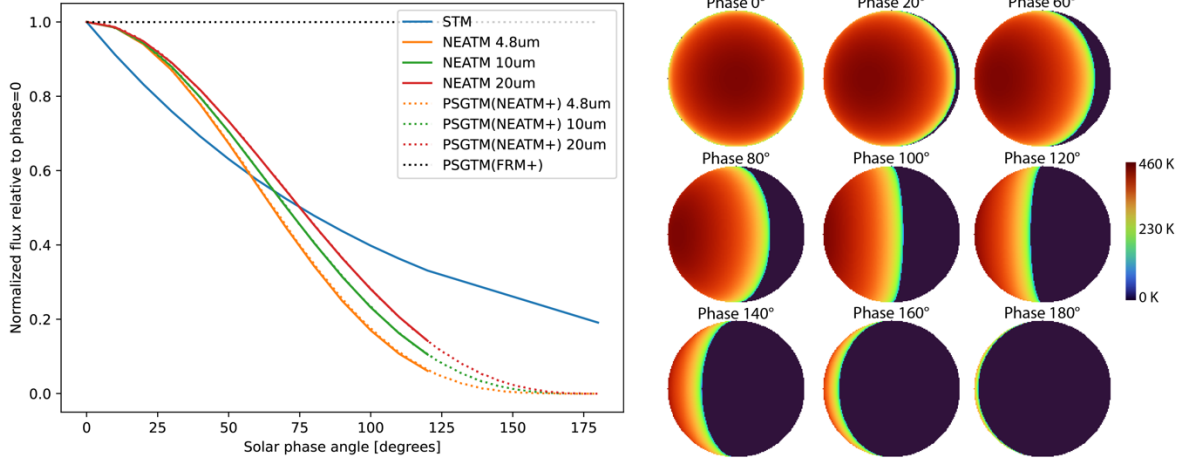


Figure 6: Comparison between the Standard Thermal Model (STM, Lebofsky et al., 1986), the Near-Earth-Asteroids Thermal Model (NEATM, Harris, 1998) and PSG’s Thermophysical Models (PSGTM). Excellent agreement is observed between NEATM and PSGTM(NEATM+), when selecting a spherical surface, a minimum temperature of 0K, and the same sub-solar temperature (425.3 K) and beaming factor η (0.756) as defined in (Harris, 1998). One can also see that a phase correction of $0.01 \text{ mag deg}^{-1}$ as implemented in STM greatly mismatches the phase response of a phase rotated sphere. The different thermal regions computed by PSGTM across the surface (see right panels for different phases) are captured in the radiative transfer of PSG by selecting the sub-sampling mode (see chapter 2). The Fast-Rotating-Model PSGTM(FRM+) is isothermal across longitude, so for a planet seen from the equator, the thermal fluxes do not change with phase.

$$T_{\text{uni}} = T_0(1/4)^{1/4} = \frac{T_{\text{irr}}}{\sqrt{2}} \left(\frac{1-A}{\epsilon} \right)^{1/4} = T^* \sqrt{\frac{R^*}{2r_h}} \left(\frac{1-A}{\epsilon} \right)^{1/4} \quad (82)$$

If the radiation time is much shorter than the rotation timescales, as in tidally-locked objects with thin atmospheres or with very low surface thermal inertia, then each point on the planetary surface will be in local thermal equilibrium. The nightside hemisphere will then have a temperature T_n of 0K, and the dayside temperature at each location is defined by (Hansen, 2008):

$$T_{\text{aniso}}(i) = T_0(\cos i)^{1/4} \quad (83)$$

$$T_{\text{d,aniso}} = T_0(2/3)^{1/4} \quad (84)$$

with i being the solar incidence angle, and $T_{\text{d,aniso}}$ being the average temperature across the whole dayside hemisphere. In the case of fast rotating planets (FRP), or planets with strong zonal winds or very high thermal inertia, the incoming radiation is homogenized across longitude, leading to zonal isothermal bands across the planet. The dayside and nightside hemispheres will now have the same distributions, and the local temperatures at the bands for latitude θ are defined by (Cowan and Agol, 2010):

$$T_{\text{FRP}}(\theta) = T_0 \left(\frac{\cos \theta}{\pi} \right)^{1/4} \quad (85)$$

$$T_{\text{d,FRP}} = T_0 \left(\frac{8}{3\pi^2} \right)^{1/4} \quad (86)$$

with $T_{\text{d,FRP}}$ being the average temperature across the rotation hemisphere (dayside or nightside).

In the study of asteroids and airless objects, thermo-physical models progressed from highly tailored models applicable to certain rotation states to more generalized models, which were parameterized to match different spin orientations, rotation periods, thermal inertias and surface roughness.

Historically, the Standard Thermal Model (STM, Lebofsky et al., 1986) was the most commonly applied for asteroid analysis, with the model assuming temperature solely defined by insolation (as in T_{aniso} above) but only accurately tailored for phase 0 (dayside hemisphere). Alternatively and for objects with large thermal inertia and/or having short periods, the fast rotating model (FRM, Lebofsky and Spencer, 1989) was employed, with thermal distributions similarly to those described for T_{FRP} . It was soon realized that neither of these models worked well with Near-Earth-Asteroids (NEAs), in particular because these objects are small, have low surface gravities, display large thermal inertias and are typically observed at phases far from 0. The NEATM (Harris, 1998) was then introduced, in which the STM model was primarily advanced by implementing a better prescription of the thermal phase function of these objects (see comparison between NEATM and STM in Figure 6). Specifically, in the NEATM model, the solar phase angle is taken into account by numerically calculating the thermal flux originating from points visible to the observer, in which the temperature is calculated at each point based on anisotropic emission (similar to equation 83), with no emission originating on the night side.

These models have been widely used by the community and remain at the core of many modern standards. As such, PSG's Thermo-physical Model (PSGTM) is built to ensure reproducibility of these models, while this module also adds certain important advances (NEATM+, FRM+) increasing the realism of the modeled temperatures and fluxes across a wide of range of objects. Specifically, PSGTM includes these additional capabilities and flexibilities: 1) a full non-spherical 3D model of irregular objects employing realistic shape models, which permits to properly compute with fine detail, the incidence, emission and equilibrium temperature on millions of facets across a planetary surface (see Figure 7). 2) A minimum temperature (T_{min}) can be now defined, which can be used to roughly characterize thermal inertia, energy redistribution and the nightside state – It is interesting to note, that if only 1% of the dayside radiation is transported to the nightside, the nightside temperature will be $(0.01)^{1/4} = 0.32$ of the dayside (e.g., 95K at night for a 300K dayside planet). Lastly 3) the structure of the longitudinal temperature maps across the planet of FRM+ is defined by the shift between the sub-solar point and rotational axis. For instance, FRM+ would become NEATM+ when the sub-solar latitude is at the poles. Importantly, we have made sure that these advances did not affect the reproducibility of the original models, and when considering a spherical planet and $T_{\text{min}}=0\text{K}$, PSGTM(NEATM+) becomes NEATM (see Figure 6); while for a spherical planet, $T_{\text{min}}=0\text{K}$ and the sub-solar at the Equator, PSGTM(FRM+) becomes FRM.

The three parameters that primarily define the functioning of PSGTM are:

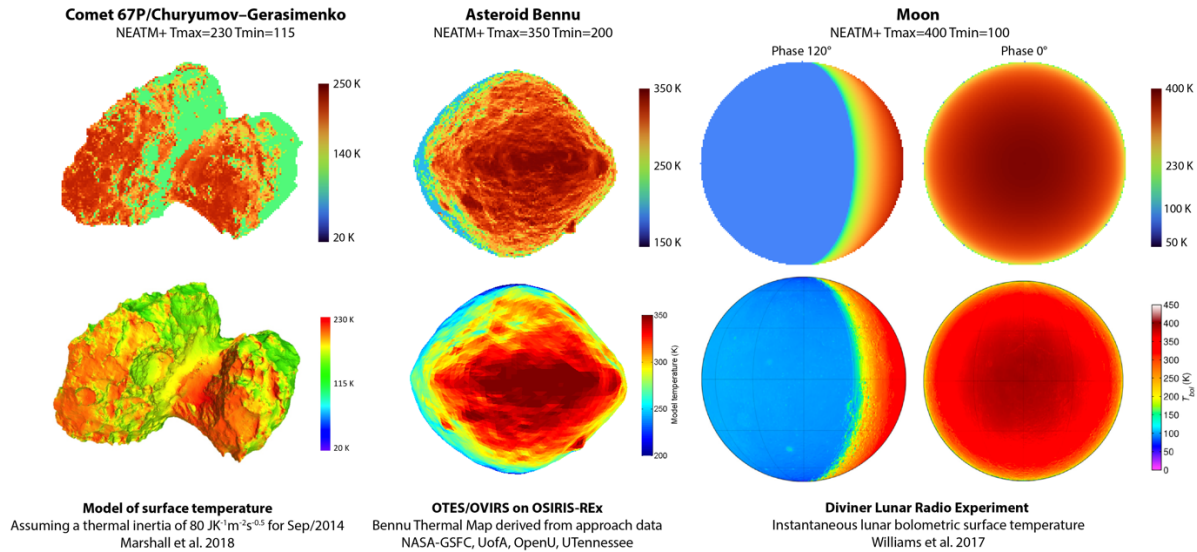


Figure 7: Comparison between surface temperatures as computed with PSGTM and observed/modelled on several objects across our solar system: comet 67P (Marshall et al., 2018), asteroid Bennu and the Moon (Williams et al., 2017). The color-bars are not exactly the same, so these comparisons are simply done to explore the adaptability of the PSGTM models to a wide range of objects and insolation/rotation/thermal states, in particular when investigating complex 3D objects. Detailed thermo-physical modeling, beyond the scope of the simple models implemented in PSGTM, would be needed to fully capture the complex energy balance occurring at the surface of these objects.

Fiducial temperature (T_0) and beaming parameter (η): the temperature in these models is always defined relative to the sub-solar maximum temperature. In principle, the sub-solar temperature should follow equation 81 (T_0), yet surface roughness and thermal inertia may lead to greater or lower values in this region. The STM and NEATM models therefore incorporate the beaming parameter (η) as a means to account for observed discrepancies in the thermal emission ($T_0' = T_0 \eta^{-1/4}$) at different phases angles. This parameter is in principle related to the thermal properties of the object, but it can also change due to the observational geometry, rotational properties of the object and the wavelength of the observation. For instance, as the surface roughness increases, a facet has more absorption area leading to an increase in the local temperature, which would correspond to η values lower than 1. On the contrary, a large thermal inertia would lead to lower temperatures at the sub-solar region, and η larger than 1 can be used to capture this effect, with theoretical maximum values of ~ 3.5 (Delbo et al., 2015). In PSG, the user can enter any value of T_0 and η , yet the web interface of PSG will make a recommendation of T_0 based on equation 82.

Minimum temperature: the STM, NEATM and FRM models operate under simplified regimes of thermal balance and energy redistribution, which do not fully capture the non-illuminated regions. On the other hand, surfaces with temperatures lower than 100K radiate much less than the sub-solar regions at wavelengths lower than 20 μm , so the contribution to modelled fluxes from non-illuminated regions tend to be small/insignificant in many cases. Modelling nightside temperatures and the evolution of temperature across a planet requires a large range of parameters (e.g., thermal



conductivity, thermal inertia, rotation axis and period, surface depth composition) which are in many cases not available, yet by implementing a single parameter parameterization for the nightside temperature (T_{\min}), PSGTM can roughly capture the general thermal anisotropies observed on many objects across our solar system (see Figure 7).

Rotational axis: NEATM only depends on the local illumination, so this module is ultimately agnostic to the rotation period and axis. FRM, on the other hand, requires information about the rotation axis, in reference to the Sun and to the observer. If we consider that the rotation axis is established relative to longitude, the location of the sub-solar latitude (θ_{ss}) would then define the temperature for the different meridional bands. A sub-solar latitude at the equator ($\theta_{ss}=0$) would lead to a temperature distribution as equation 85, yet if the sub-solar latitude is at a pole ($\theta_{ss}= \pm 90^\circ$), only one hemisphere becomes illuminated, and the temperature distribution transitions to equation 83 (similar to NEATM). The temperature distribution for the PSGTM(FRM+) model is then described as:

$$T_{\text{FRM+}}(\theta) = T_0 \left(\frac{\cos(\theta - \theta_{ss})}{1 + (\pi - 1)\cos\theta_{ss}} \right)^{1/4} \quad (87)$$



Planetary Spectrum Generator
National Aeronautics and Space Administration

Chapter 7:

Mass spectrometry

**Villanueva, Kofman and
PSG team**

1. Mass spectrometry and its implementation in PSG

Mass spectrometry is a technique in which the elemental components of a sample (molecules) are described according to the mass per charge (m/z) of its constituents (atoms/isotopes/ions) to infer its fundamental building blocks and composition. Mass spectrometers are differentiated by the choice of (1) ionization source, which converts the neutral analyte to charged fragments, (2) mass analyzer, which separates ions by m/z , and (3) detector, which measures the number of ions produced at each m/z value.

In this chapter, we focus on the interpretation and modeling of atmospheric and surface planetary samples (e.g., MAVEN/NGIMS, Rosetta/ROSINA, LADEE/NMS, Curiosity/MSL), in which the ionization and fragmentation of the species to be analyzed is induced by electron impact, a common method used by mass spectrometers for planetary missions. This consideration is mostly defined by the calibration laboratory datasets employed by the PSG/MASS module, which fundamentally relies on the electron ionization mass spectra for over 21,000 species as compiled in the NIST database.

Contrary to remote sensing techniques (e.g., molecular spectroscopy), mass spectrometry is an in-situ measurement, meaning that it requires physical access to the sample to analyze its composition. It might be surprising that a radiative transfer spectroscopic suite such as PSG has a mass spectrometry module, yet some core simulation building blocks of PSG are common to both the remote sensing techniques and the in-situ mass spectrometry. Specifically, PSG has an advanced set of orbital and atmospheric models, which provide realistic information of the local densities and kinematics at the different locations in an atmosphere. By placing a simulation “probe” at a specific location, all the needed input parameters for a mass spectrometry atmospheric simulation are provided. As we discuss further in this chapter, the fragmentation or fundamental mass spectrum of a compound also relies on laboratory and theoretical information, similar to radiative transfer simulations, and therefore similar analytical methods can be used to synthesize mass spectra for a broad range of mixtures and configurations. Furthermore, the calculation of noise in mass spectrometry measurements also relies on similar Poisson statistics as applies to the calculation of noise in measurements made by a photon counting device (e.g., imaging CCDs), so similar mathematical and physical principles can be adopted when simulating mass spectrometry noise. The PSG/MASS module includes a noise model simulator that is particularly relevant when constraining the detectability of species with a proposed space instrument or when determining the limiting factors affecting a currently available planetary mass spectral dataset.

Importantly, mass spectrometry is a common technique used by orbiters to probe planetary atmospheres, often working in tandem with remote sensing instruments. Interpretation of planetary mass spectrometry data obtained by flight mission instrumentation requires in-depth knowledge of the technological processes that lead to a mass spectrum. This also requires versatile and advanced analytical tools that can access a broad range of mass fragment databases, chemical models, and retrieval or fitting algorithms. Most of the tools employed by the community to interpret complex mass spectrometry data are based on proprietary (e.g., non-public) and expensive software packages, which are in most cases designed for industries applications or tailored to specific laboratory instruments. In many cases, the challenges affecting the interpretation and modeling of mass-

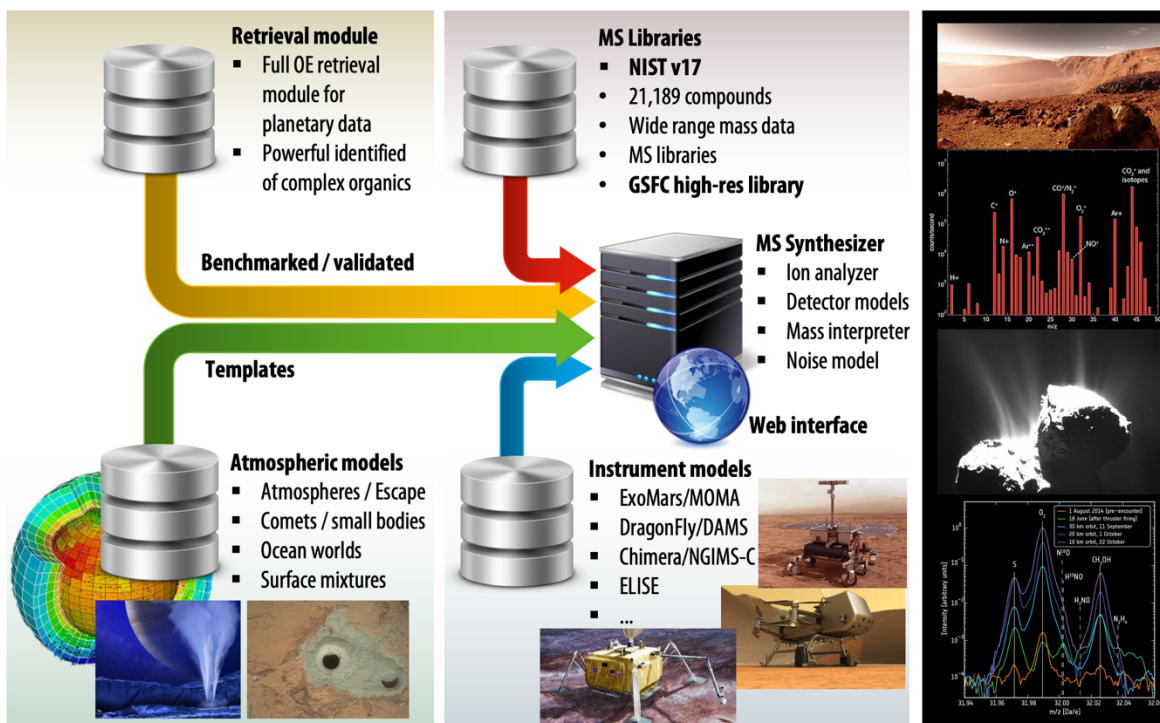


Figure 1: By combining an advanced set of mass-spectrometry models with the PSG versatile online planetary suite, the PSG/MASS module can greatly assist with the interpretation and simulation of planetary missions.

spectrometry for planetary science applications are poorly addressed by these industry analytical tools, and an advanced and versatile mass spectrometry planetary modeling and retrieval suite tailored to planetary science is needed. These are the founding principles and aspirations behind this module in PSG, a publicly available mass spectrometry tool specifically designed for planetary missions, which is open access and based on realistic and well-proven methods. In this initial implementation of the MASS module for PSG, we developed an algorithm that, by employing permutation theory, synthesizes all possible fragments for 21,000+ species (see Section 2). This information is then fed to the mass interpreter and modeler (see Section 3), that was exhaustively tested on data collected from several in-situ planetary missions (e.g., LADEE, MAVEN, Rosetta) – see Section 4. Finally, a retrieval or fitting method (e.g., employing the latest search engines and other statistical methods) was developed and tested on laboratory data for the identification of complex organics (see Section 4).

2. Fragmentation model and an accurate high-resolution mass fragment database

The advantage of having line lists in radiative transfer modeling is that it is possible to compute spectra at any resolution, ambient conditions, and radiative regime. Unfortunately, there is no equivalent publicly available fragmentation line lists applicable to mass spectrometry, only databases of mass spectra measured at modest mass resolutions (≥ 1 [Da]) and collected for different species in specific ionization and fragmentation regimes. However, we can use this information in combination with a theoretical model to compute accurate an accurate high-resolution mass fragmentation

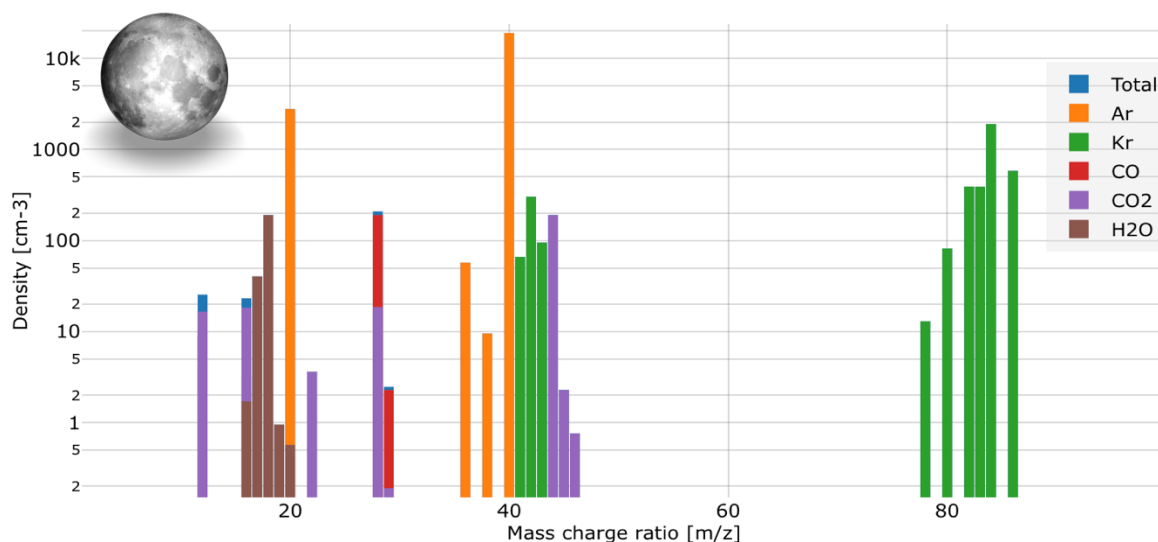


Figure 2: Simulated spectrum in the Moon exosphere at 55 km altitude, in the hypothetical case that it had trace amounts of H₂O, CO₂, and CO, while also considering probable abundances of Ar and Kr as observed with a mass spectrometer like the NMS onboard LADEE. Such theoretical investigations permit to quantify the detectability of species and their overlap with other signatures.

database for mass spectrometry. Specifically, as part of the PSG/MASS module, we developed a novel fragmentation model for mass spectrometry that generates lists of mass fragments at very high mass resolution (<1 [mDa]). At the core of our model in PSG, there is a permutation and fragmentation algorithm that divides a species into all its possible fragments. The algorithm first determines the fundamental elements of the molecule, exploring all possible isotopologues and considering natural isotopic abundances. For instance, the diatomic CO molecule would have the possible following 10 fragments (in order of increasing mass): $^{16}\text{O}^+$ (15.994915 Da), $^{17}\text{O}^+$, $^{18}\text{O}^+$, $^{12}\text{C}^+$, $^{12}\text{C}^{16}\text{O}^+$ (27.994915 Da), $^{17}\text{C}^{16}\text{O}^+$ (28.999132 Da), $^{12}\text{C}^{18}\text{O}^+$, ^{13}C , $^{13}\text{C}^{16}\text{O}^+$ (28.998269 Da), $^{13}\text{C}^{17}\text{O}^+$, $^{13}\text{C}^{18}\text{O}^+$. This list is obtained by taking into account only the 3 most abundant isotopes of O (with masses of 16, 17, and 18 [amu]) and 2 most abundant isotopes of C (with masses of 12 and 13 [amu]). Such lists of fragments can include thousands of possible combinations for species containing dozens of atoms with many abundant isotopes.

The probability of producing any possible fragment from a molecule will depend on the relative abundances of isotopes it may contain (fragments with many isotopic permutations are less abundant following the law of mixing) and the number of times that fragment occurs in the molecule. For instance, the CO₂ molecule contains two O atoms and one C atom, so if one were to fragment millions of CO₂ molecules in a mass spectrometer, there is twice the chance that one would observe an O⁺ fragment than a C⁺ fragment. Taking into consideration these two basic principles (i.e., isotopic probability of the fragment and abundance of the fragment in the molecule), the fragmentation module will compute a fragment list for each compound. Importantly, each fragment will have a precise mass (saved in a model database with a precision of 6 digits in [Da]) defined by the total mass of the fragment. Let us consider the example of CO analyzed using a spectrometer with a mass resolution of 1 [Da]. In this case, the fragments $^{12}\text{C}^{17}\text{O}^+$ and $^{13}\text{C}^{16}\text{O}^+$ would fall in the

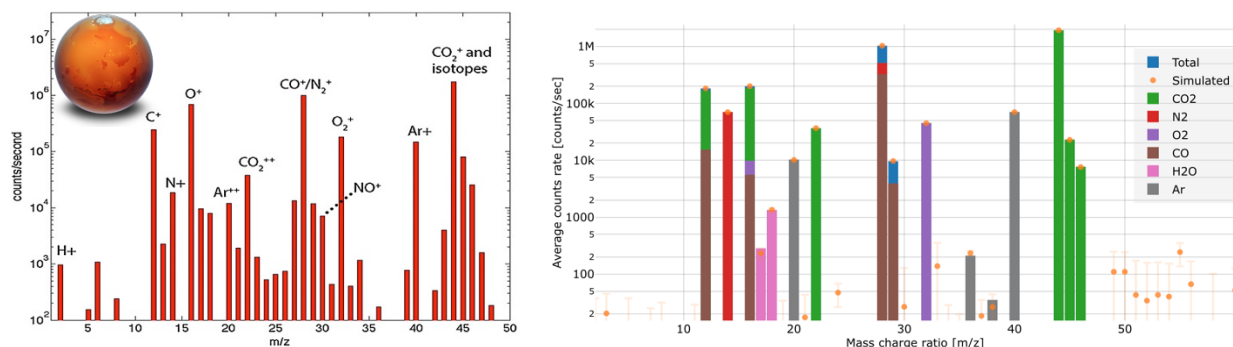


Figure 3: Comparison of a fully synthetic mass spectrometry PSG/MASS simulation (right) with orbital Mars data (left) as collected with MAVEN/NGIMS (Mahaffy et al., 2015). Even though the simulations were not done for the exact same conditions and the data includes background signal, the general morphology and intensity of the features is well replicated by the simulation. The noise simulated by PSG is comparable to the detection “floor” as depicted in the left panel.

same bin because both have a mass of 29 [Da], yet if the analysis is performed using a very high-resolution spectrometer, then it is possible to differentiate between the two isotopologues. This example illustrates the great advantage of having line lists of possible fragments for many species that can be used to synthesize and interpret mass spectrometry data at different resolutions.

In reality, the situation is more complex than the example described in the previous paragraph, because the selected fragmentation method and the energies involved in the ionization process will determine which fragments have a higher probability of detection. For instance, if one performs electron ionization at a specific velocity and temperature, certain fragments will be preferentially produced, and the fragmentation pattern would not be accurately reproduced by a natural occurrence probability based on the number of times a fragment exists in a molecule. On the other hand, the fragmentation pattern within constrained mass ranges can be assumed to follow the laws of isotopic mixing, so a simple a priori fragmentation model as described above could be used to determine the fragments within a 1 [Da] wide mass bin and their relative proportions.

To calibrate our fragmentation model to experimentally measured mass spectra, we bin our high-resolution fragmentation database for each molecule into a spectrum with a mass resolution of 1 [Da], or in other words, we round the mass of each fragment to the nearest integer. We then take this binned line list and calibrate or scale each bin to the mass spectra reported in the NIST Standard Reference Database Number 69. NIST provides mass spectra for 21,000+ species with masses up to 200 [Da] and a mass resolution of 1 [Da]. For instance, if the proportion of fragments measured at an m/z of 20 is 0.5 in the NIST database, we scale all fragments with rounded m/z of 20 to have a total intensity of 0.5, with each fragment scaled by its relative intensity/probability within the bin. All of our mass fragments lists are normalized to the maximum in the list. This combination of theoretical and laboratory data allows for the compilation of an effective and versatile mass spectral database that can be used to synthesize a wide range of mixtures at low and high resolutions.

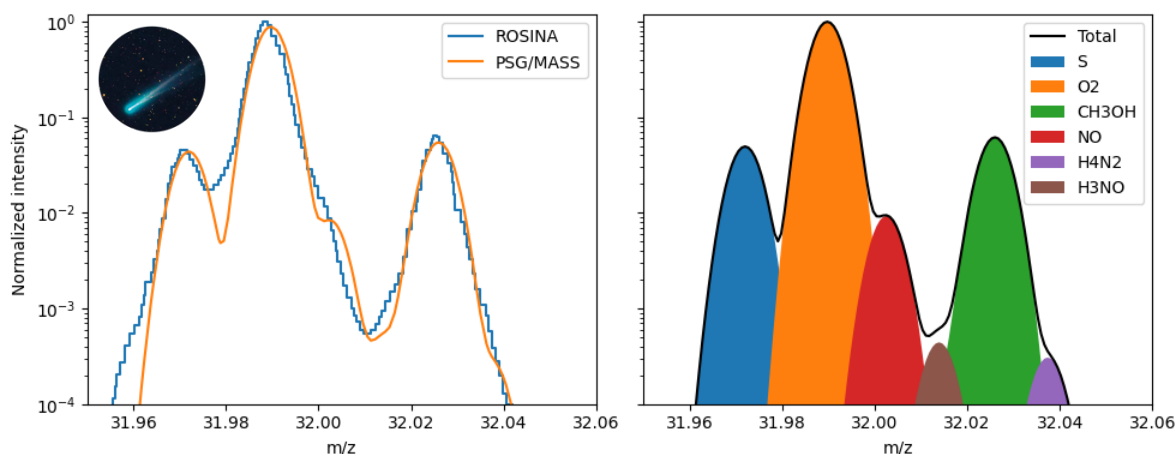


Figure 4: Retrieval with PSG/MASS of the composition of comet 67P as measured with the ROSINA mass spectrometer (Rubin et al., 2019) onboard Rosetta. ROSINA is a Double Focusing Mass Spectrometer (DFMS) capable of extremely high mass resolution ($M/dM > 3000$), in which one can identify the multiple constituents with a mass of 32 [Da]. The PSG/MASS simulation retrieval (convolved with a Gaussian kernel) provides a very good match data and allows to properly quantify the abundance of the components found in the coma.

3. Simulating mass spectrometry and its noise

There are two general possible scenarios when synthesizing and interpreting mass spectrometry with PSG: (1) in-situ atmospheric measurements obtained by orbiting probes (e.g., by MAVEN/NGIMS or Rosetta/ROSINA) and (2) in-situ rover or laboratory measurements (e.g., obtained by Curiosity/MSL, by ExoMars/MOMA, or in a laboratory). Typically, mass spectrometry investigations operate with relative or dimensionless intensities, but PSG internally operates with values of [molecules/cm³] (or [cc]) which are then converted to any desired output unit by the MASS module.

For in-situ rover or laboratory measurements, the user can choose to be in “cell mode” (which refers to a gas cell) or “sample mode” (for a sample collected by a rover or a laboratory sample), which requires the user to supply the ambient atmospheric density. For in-situ atmospheric obtained by orbiting probe investigations, the MASS module will determine the input atmospheric density [molecules/cm³] at the desired probe location by passing the user-defined geometry and atmosphere information, provided in the configuration file, to the GEOMETRY and ATMOSPHERE modules (see Chapters 2 and 3).

Using the provided molecular mixing ratios [molecules/molecule], the MASS module will then compute the specific density [molecules/cm³] for each selected molecule. As presented in Chapter 3, PSG calculates the local density for each molecule by employing a realistic 2-stage photodissociation model for comets/exospheres or the hydrostatic integration to determine densities in an equilibrated planetary atmosphere. Using the selected mass ranges and resolution, the MASS module will compute a spectral grid and create a spectrum for each compound by summing the signal collected in each bin from the high-resolution reference mass fragment database as presented in section 2. The



total signal will then be calculated as the integral across all species, in which each spectrum is multiplied by the specific molecular density of each component. The natural unit of the simulated spectra is then in units of [molecules/cm³] (since the line-lists are normalized to unity).

The generated mass spectrum (R) can be converted from [molecules/cm³] to [counts/second] by multiplying the spectrum by the instrument sensitivity (Γ), which is typically reported in units of [counts/second/cm³]. If the user provides the total integration time of the measurement (Δt in [seconds]), PSG will compute the total integrated counts (via $S = R \cdot \Gamma \cdot \Delta t$) across that time and will produce a spectrum in similar format and units as reported by the instrument. For instance, a typical efficiency for MAVEN/NGIMS and LADEE/NMS is 0.03 [counts/second/cm³]. Similar to imaging CCDs, detectors used in mass spectrometers typically have strong background signatures (I_{dark} or “dark” [counts/second]) and add counts/noise upon every read (I_{read} “read” [counts/read]). This background signal can be added to the generated count rate to accurately determine and estimate the effect of noise in the data. As will be discussed in Chapter 8, in Poisson statistics, the noise follows the square root of the total measured counts [$N = \sqrt{S_T}$], where $S_T = S + n_{\text{read}}(I_{\text{read}} + I_{\text{dark}} \cdot \Delta t_{\text{read}})$, n_{read} is the number of reads, and Δt_{read} is the integration time per read [s/read]. Finally, the MASS module will compute noise following these equations and employing the specific instrument sensitivity and detector readout characteristics as described above. Performance parameters for several planetary mass spectrometers have been collected and included as loadable instrument templates in the online PSG’s instrument section.

4. Mass spectrometry retrievals and complex organics identification

To demonstrate the module and explore its regimes of operability, we analyzed several important planetary mass spectrometry datasets and interpreted these data by using the MASS module. The datasets were selected to explore different input atmospheric regimes (e.g., atmosphere, comet, laboratory), different mass ranges and spectral resolutions, and these are:

Lunar exosphere (Figure 2): The Lunar Atmosphere and Dust Environment Explorer (LADEE) was a NASA lunar exploration and technology demonstration mission that launched in September 2013. This orbiter had a Neutral Mass Spectrometer (NMS) that targeted several species in the exosphere of the Moon, ultimately leading to the characterization of the noble gas cycle on the Moon (Benna et al., 2015) and to the discovery of several ions related to the solar wind interaction with the Moon exosphere (Halekas et al., 2015). We simulated the detectability of these noble gases together with the potential signature of other common atmospheric volatiles with PSG/MASS employing instrument parameters as those of LADEE/NMS (see Figure 2). The simulation nicely shows the strong noble signatures (for all the isotopes) and the potential overlap between the different fragments for CO, CO₂, and H₂O.

Martian atmosphere (Figure 3): The Neutral Gas and Ion Mass Spectrometer (NGIMS) onboard the Mars Atmosphere and Volatile Evolution (MAVEN) orbiter has provided key insights about the Martian atmosphere. The spectrometer targets several key Mars volatiles and enables the characterization of their vertical, spatial, and seasonal dependence by in-situ probing, in particular, due to the “deep dip” campaigns in which the orbiter penetrated deeply into the Martian

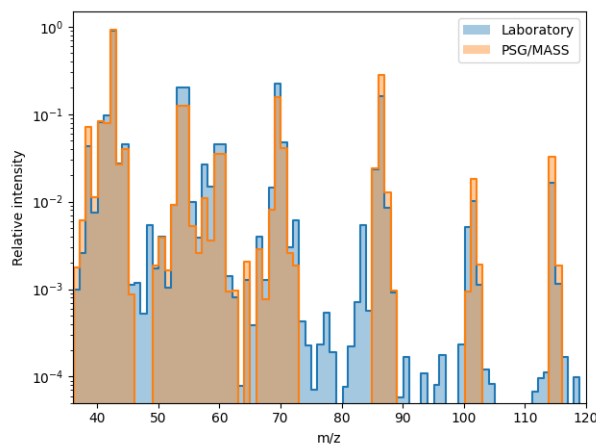


Figure 5: Identification of complex organics with PSG/MASS on laboratory samples. As a blind test experiment, the data were provided to us by Goddard’s Astrobiology Analytical Laboratory to determine its composition. We obtained the highest match (98.69%, right panel as shown by the retrieval web interface) with acetate 2-pentanol, consistent with the original source, while the model also identified several related species with similar structure and composition. The PSG/MASS search algorithm is extremely effective and fast (only taking ~1 second to obtain the results shown here), which enables rapid identification of complex species among a database of 21,000+ species at a broad range of masses and resolutions.

atmosphere. An example measurement is presented in (Mahaffy et al., 2015), which we compare to a simulation at a similar altitude using our tool. The conditions of the simulation are not exactly the same as those of the measurement and the simulations were not fitted to match the data, but one can see a close resemblance in the peaks’ intensity between model and data. Importantly, the PSG/MASS module provides detailed information about the contribution of the different atmospheric constituents to every mass peak, enabling analysis of overlapping signals and thus the potential significance of each individual signature.

Cometary coma of 67P (Figure 4): Onboard the ESA/Rosetta mission orbiting around comet 67P, the ROSINA (Rosetta Orbiter Spectrometer for Ion and Neutral Analysis) mass spectrometer contained two sensors which were used to determine the composition of the comet’s atmosphere and ionosphere, the velocities of electrified gas particles, and the reactions in which they took part. A particular mode of the instrument is its double focusing mass spectrometer (DFMS) that has a mass range from 1-150 [amu] and a mass resolution higher than 3000. The DFMS channel has been optimized for very high mass resolution and large dynamic range. It can thus be an extremely useful tool for the exploration of isotopic compositions and the overlapping signatures from many species in a narrow mass range. In Figure 4, we perform a retrieval on Rosetta/ROSINA data (Rubin et al., 2019) by employing PSG/MASS, in which several species are revealed and separated. We have used a Gaussian kernel to convolve data, though this channel is known to have a peculiar/asymmetric ILS (Instrument Line Shape) function, and that would explain many of the observed differences. In particular, the unique value of having a high- resolution mass fragment database, as presented in Section 2, is nicely demonstrated in this retrieval, that a NIST 1 [Da] database would not permit.



Complex organics and surface/laboratory samples (Figure 5): We have added a powerful molecular search engine to PSG that allows for the comparison of observed data with a large sample of spectra. To test this capability, we asked NASA Goddard's Astrobiology Analytical Laboratory to provide us with a mass spectrum of a single large organic molecule. We asked them not to inform us of the nature or properties of the sample. We used PSG/MASS to infer and detect its composition. The search algorithm only took a second to identify an accurate match with acetate 2-pentanol among a database of 21,000+ species. The algorithm also identified several related species with similar structure and composition, which can be helpful when exploring planetary samples of processed, unknown materials.



Planetary Spectrum Generator
National Aeronautics and Space Administration

Chapter 8: **Instruments and Noise Modeling**

**Villanueva, Mandell, Liuzzi and
PSG team**

1. Principles of noise modeling

Noise in an observation/measurement is introduced by a wide range of effects, and computing it requires a precise accounting of the fluxes arriving to the instrument, the instrument losses and the intrinsic components of the instrument/telescope affecting the overall sensitivity. PSG has been designed at the core to keep full accounting of the photons and fluxes at all stages of a simulation, ensuring a proper tracking of signals and their respective associated noises. In particular, the noise simulations in PSG are done by the GENERATOR module after performing the integration of the spectral radiances across the corresponding selected simulation field-of-view, spectral wavelengths range and instrument properties (see Figure 1).

The total noise in a simulation can be generally defined as a linear combination, typically a sum of squares, of three main noise sources: scene (or target) fluxes (planetary and stellar fluxes), background fluxes (e.g., zodiacal, telluric) and detector or systematic instrument sources. At short wavelengths (e.g., optical or near IR), the background photon counts follow a Poisson distribution, and the fluctuations are given by the square root of the mean number of photons received (Tables 1 and 2). A Poisson distribution holds only in the case that the mean photon mode occupation number is small, $n \ll 1$. For a thermal background, the occupation number is given by the Bose-Einstein formula, $n_{th}(v, T) = [\exp(hv/kT) - 1]^{-1}$, so the opposite classical limit $n \gg 1$ is the usual situation at longer wavelengths for which $h\nu \ll kT$. When $n \gg 1$, the photons do not arrive independently according to a Poisson process but instead are strongly bunched, and the fluctuations are linearly related to the received photons. Therefore, the Dicke equation is used to calculate sensitivities for the receiver temperature mode (e.g., ALMA and sub-mm receivers), which states that the noise is proportional to the background power rather than its square root. The formalism employed for this mode in PSG is based on the ALMA sensitivity calculator (Table 1).

As we explore the concept of noise calculations in this chapter, it is important to establish a key parameter affecting the calculations, R as number of photons per second arriving to the detector (see additional details in Table 2). If we know the integration time (T), then the total number of observable photons is simply $S = RT$. Let us now consider that we have calculated an effective spectral radiance L [$W/m^2/\mu m/sr$] for our simulation scene, then R is calculated as:

$$R [\text{photons} / \text{s}] = \eta \cdot L [W/m^2/\mu m/sr] \cdot A_{\text{tele}} [m^2] \cdot \Delta\lambda [\mu m] \cdot \Omega [sr] \cdot (\lambda/hc) [\text{photons} / \text{s} / W] \quad (1)$$

where η is the instrument throughput (1.0 is a perfect instrument), A_{tele} is the collecting area of the telescope (bigger telescopes collect more photons), $\Delta\lambda$ is the spectral width of the simulation pixel, Ω is the steradian area of the field-of-view (FOV), and the last term is simply a scaler of the number of photons/s for every Watt. A few key important points are to be made here: R is independent of distance to the object (that is captured in L); the per $/\mu m$ in L refers to the width of the pixel, not to its wavelength (wider or lower “resolution” pixels collect more photons); wide FOVs (greater Ω) leads to higher photon rates, but only if L is constant across the FOV. It is then key that we capture the differences in L for an extended source versus a point source. If the FOV is smaller or within the size of an extended source (e.g., large nearby planets or a background source like the zodiacal dust), then L does not change. In that sense, having a larger FOV that still encompasses the source will lead

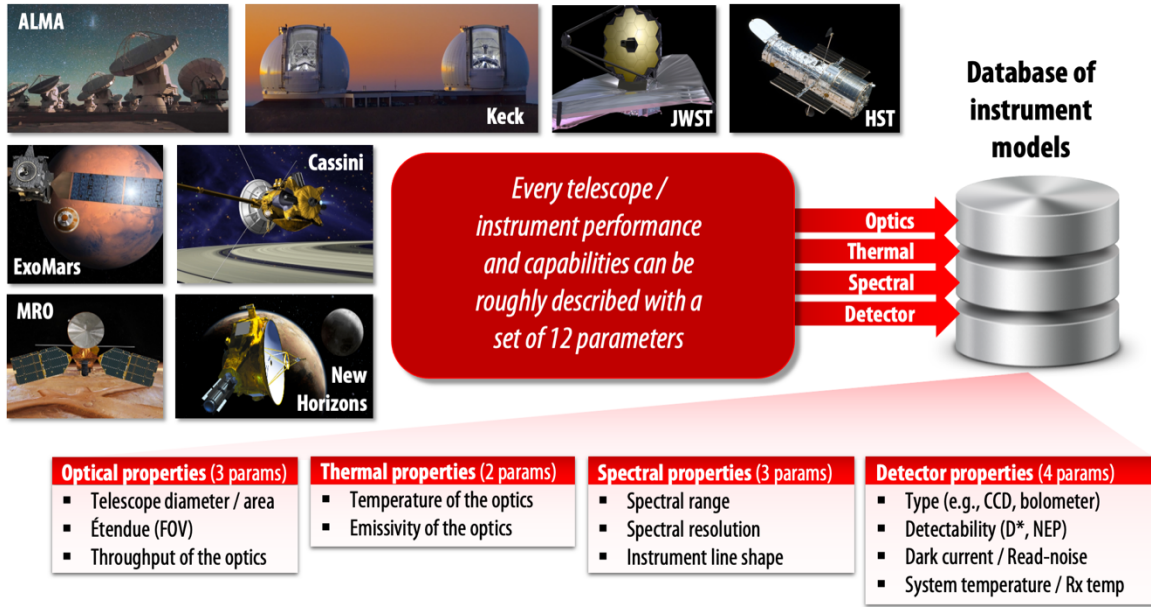


Figure 1: The basic elements of any noise simulation require 12 core parameters as summarized in this figure. In PSG, we have prepared templates for a wide range of instruments, observatories and missions that capture their noise performances, which can be selected/uploaded in the instrument section of PSG. A user-custom instrument simulator can also be created.

to a higher count rate. On the other hand, if the source is smaller than the FOV (e.g., a point source or a distant star), then L will scale with inversely with Ω , and then the count rate will remain the same (more details in section 2). Another key metric identified in equation 1 is η , or the total throughput of the instrument. The higher the number the more photons from the source we collect (S), and then the higher the S/N . For instance, if a mirror in an instrument optical setup has a transmissivity of 0.95, having 10 reflecting surfaces will lead to a total transmissivity of $0.95^{10} = 0.6$. Furthermore, some instruments may be designed to greatly reduce the signal for only certain regions of the scene, as in a coronagraph, where the stellar signatures have a particular η_{star} and the planet/background signatures has a different η_{planet} (more details in section 6).

With equation 1, we have identified the core formalism for computing the first two components of noise (planetary, stellar and background sources, more details in Table 2), now remaining the modeling of detector and systematic instrumental noise. Each detector technology introduces noise in a particular way, and it also responds differently to the observed fluxes. As such in PSG, several detector and instrument models are available to capture this diversity (see Table 1). Imaging sensors (e.g., CCDs) introduce noise upon reading the detector (read noise, typically quantified in e-/pixel/read) and via a background current which increments over time (dark current, quantified as e-/pixel/s). The dark current is added to any frame but can be removed by doing (science frame – dark frame), in which dark is a no-signal frame taken over the same exposure time as the data. The dark current can be then removed, but not its noise, and therefore this type of detector noise needs to be included in any astronomical simulation. In the case of read noise, it can be reduced for certain detectors by performing multiple reads before emptying the detector well, a process normally defined

Type of noise	Parameters	Detector specific noise equations
TRX Receiver temperature (radio)	T_{RX} [K]: noise of receiver g: sideband (0:SSB, 1:DSB) n_{pol} : 1 (# of polarizations) f_N : 1 (# of baselines) For interferometric systems (e.g., ALMA): n_{pol} : 2 (assuming dual / full configuration) $f_N = n_{tele} \cdot (n_{tele}-1)$	$L_{RJ} = 1E-18 \cdot \lambda^4 / 2kc$ $T_{source} = L \cdot L_{RJ}$ $T_{back} = L_{back}L_{RJ} + T_{ground}(1 - \tau_{n_{ground}})$ $k_{sys} = (1+g)/(\eta_{Total} \tau_{n_{ground}})$ $T_{sys} = k_{sys} [T_{RX} + \epsilon_{optics}T_{optics} + T_{source} + T_{back}]$ [K] $f_{\Omega} = (\Omega_{Tele} / \Omega)$ Diffraction / FOV correction $D_v = 1E6 \cdot c \cdot d\lambda / \lambda^2$ $N_{total} = T_{sys} \cdot f_{\Omega} / \sqrt{(f_N \cdot n_{pol} \cdot d_v \cdot n_{exp} \cdot t_{exp})}$ [K]
NEP Noise Equivalent Power	NEP [W / \sqrt{Hz}]: sensitivity	$N_D = n_{pixels} \cdot n_{exp} \cdot t_{exp} \cdot (NEP \cdot \lambda \cdot 1E-6 / hc)^2$ [e ⁻²]
D* - Detectivity	D^* [cm \sqrt{Hz} / W]: detectivity S [μm]: pixel size	$N_D = n_{pixels} \cdot n_{exp} \cdot t_{exp} \cdot ((S \cdot 1E-4 / D^*) \cdot \lambda \cdot 1E-6 / hc)^2$
NETD Noise-Equivalent Temperature difference	NETD [mK] at $T=300K$, $f=50$ Hz and $\Delta\lambda=1 \mu m$ S [μm]: pixel size <i>This value is measured by the detector manufacturer by performing a defined measurement on a source of temperature T (e.g., 300K), with a repetition f (e.g., 50 Hz). The noise will be dependent on the operating spectral coverage of the detector (e.g., $\Delta\lambda=1 \mu m$ for a 12-13 μm response).</i>	<i>To convert from a NETD obtained with another source temperature T [K], sampling frequency f [Hz] or detector bandwidth $\Delta\lambda$ [μm]:</i> $NETD = NETD(T, f) \cdot dPB/dT(300, 50) / dPB/dT(T, f) \cdot \sqrt{(50/f) \cdot \Delta\lambda}$ $dPB/dT = hc/(\lambda kT^2) \cdot PB$ $PB = A \cdot \Omega \cdot \Delta\lambda \cdot 2hc^2/\lambda^5 \cdot [\exp(hc/(\lambda kT)) - 1.0]^{-1}$ $A = S^2$ (area of pixel) $\Omega = \pi/(4F\#^2 + 1)$ (solid angle of pixel) $NEP = NETD \cdot dPB/dT / \sqrt{f}$
Imager – (e.g., CCD, CMOS, EMCCD, ICCD / MCP)	Read-noise [e- / pixel] Dark [e- / s / pixel]	$N_D = n_{pixels} \cdot n_{exp} \cdot [N_{read}^2 + (Dark \cdot t_{exp})]$ [e ⁻²]

Table 1: Mathematical formalisms for the different detector models.

as multiple nondestructive readout (NDR). This can lead to a reduction of the read noise by \sqrt{K} (where K is the number of reads), yet this may also notably increase the read/integration times leading to other systematic (e.g., saturation) issues. In summary when performing noise calculations, it is critical to validate the detector parameters used for the simulation and to define an optimum integration method (i.e., number of exposures, and integration per exposure).

2. Field-Of-Views (FOVs), diffraction limits and planetary filling factors

The GEOMETRY module of PSG will compute several key parameters which permits to accurately quantify the relationship between the size and location of the planet and stars (e.g., host-star and any stellar background) with respect to the FOV. As shown in Figure 1 of chapter 2, if the distance to



General formalism for the noise components under Poisson statistics (i.e., UV, optical, IR)

$$\begin{aligned}
 L_{e-} &= \Omega \cdot A_{\text{Tele}} \cdot \eta_{\text{eff}} \cdot d\lambda \cdot \lambda \cdot t_{\text{exp}} \cdot n_{\text{exp}} \cdot 1\text{E-6} / hc \quad \text{Radiance to detector electrons conversion factor} \\
 N_{\text{source}} &= L \cdot L_{e-} \quad \text{Noise introduced by the source itself [e-}^2\text{]} \\
 N_{\text{back}} &= (L_{\text{back}} + n_{\text{ezo}} \cdot L_{\text{zodi}}) \cdot L_{e-} \quad \text{Noise introduced by background sky sources [e-}^2\text{]} \\
 N_{\text{optics}} &= \epsilon_{\text{optics}} \cdot L_{e-} \cdot (2E24 \cdot h \cdot c^2 / \lambda^5) / (\exp(1E6 \cdot h \cdot c / (k \cdot T_{\text{optics}} \cdot \lambda)) - 1) \quad \text{Noise by the telescope [e-}^2\text{]} \\
 N_{\text{ground}} &= L_{e-} \cdot (1 - \text{trn}_{\text{ground}}) \cdot (2E24 \cdot h \cdot c^2 / \lambda^5) / (\exp(1E6 \cdot h \cdot c / (k \cdot T_{\text{ground}} \cdot \lambda)) - 1) \quad \text{Noise for ground [e-}^2\text{]} \\
 N_{\text{Total}} &= \sqrt{(2N_D + N_{\text{source}} + 2N_{\text{back}} + 2N_{\text{optics}} + 2N_{\text{ground}})} \quad \text{Total noise [e-]}
 \end{aligned}$$

Parameters and constants:

L [W / sr / m² / μm]: spectral radiance of the source
 L_{back} [W / sr / m² / μm]: spectral radiance of the background sources
 t_{exp} [s]: time per exposure
 n_{exp} : total number of exposures
 n_{pixels} : total number of pixels for Ω and $d\lambda$.
 n_{ezo} : Exozodiacal dust scaler relative to Solar System zodiacal dust
 T_{optics} [K]: temperature of the optics
 ϵ_{optics} : emissivity of the optics
 η_{eff} : total throughput of the system (including quantum efficiencies)
 Ω [steradian]: is the solid angle of the observations. It is wavelength dependent.
 A_{Tele} [m²]: is the total collecting area of the observatory ($n_{\text{Tele}} \cdot \pi \cdot [D_{\text{Tele}}/2]^2$)
 λ [μm]: is the wavelength in microns
 $\text{trn}_{\text{ground}}$: terrestrial transmittance
 T_{ground} [K]: temperature of the terrestrial atmosphere - 280
 h [W s²]: is Planck's constant - 6.6260693E-34
 c [m / s]: is the speed of light - 299792458
 k [J / K]: is Boltzmann's constant - 1.380658E-23

Table 2: Mathematical formalisms for the computation of noise for Poisson statistics detectors.

the system is greater than 0.1 parsec, PSG will compute the planetary orbit and the projected distance between the planet and the host-star in the observer's reference frame. This information is recorded in the field GEOMETRY-STAR-DISTANCE (Δ_{star}), in which a negative value (e.g., -1) would indicate the star is not in the scene (all cases with distances < 0.1 pc), a 0 value indicates that star is fully in the FOV, and a value larger than 0 indicates the distance in arcseconds between the center of the FOV and the center of the star. If the star is within the FOV ($\Delta_{\text{star}}=0$), the planet may too, and it may cover the star (e.g., primary transit), in which the field GEOMETRY-STAR-FRACTION indicates the fraction of the star being covered by the planet. The GEOMETRY module employs a full 3D orbital calculation of the orbit, the star, and the planet, to determine the exact fraction of the star being covered by the planet. These parameters are used to determine the amount of stellar background flux to include in the simulation by the GENERATOR module.

As discussed in section 1, the definition of the average spectral radiance of the scene (L [W/m²/μm/sr]) and the area of the FOV (Ω [sr]) defines the actual total integrated fluxes and ultimately the count rates. The field GEOMETRY-PLANET-FRACTION (f_{planet} , sometimes referred as the “filling factor”, a value ranging from 0 to 1) quantifies how much of the planet surface area is included in the FOV, which is computed by the GEOMETRY module and includes information regarding the shape/orientation of the FOV, distance to the object, size of the planet

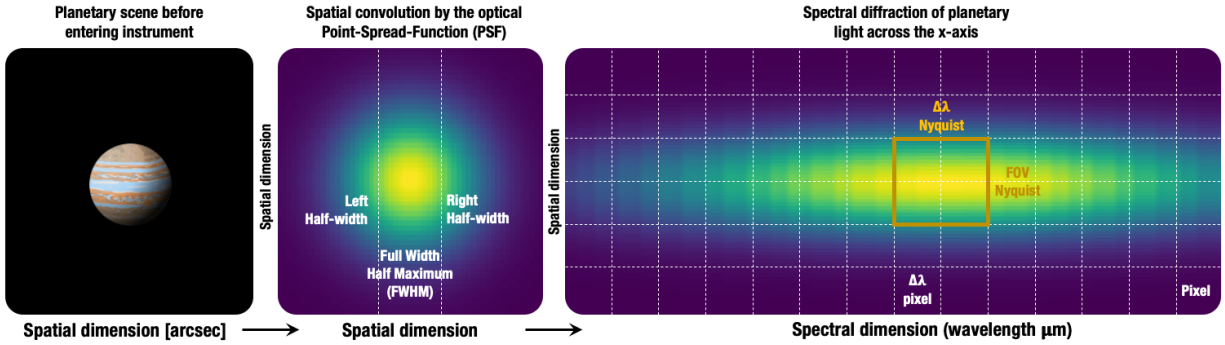


Figure 2: As the planetary light enters the instrument and it is sampled by the detector, the signal is first convolved spatially, then diffracted spectrally and ultimately projected on the detector. The spectral width of every detector pixel depends on the specific instrument configuration, which samples the optical resolution with at least two detector pixels. In this configuration, a “boxcar” pixel as simulated with PSG would correspond to the orange box with 4 detector pixels per instrumental resolution.

and any possible offsets. If the planet is bigger than the FOV, then in principle $f_{\text{planet}} = \Omega / \Omega_{\text{planet}}$. The effective scene spectral radiance is then $L = f_{\text{planet}} \cdot (\Omega_{\text{planet}} / \Omega) \cdot L_{\text{planet}}$, where L_{planet} is the intrinsic radiance of the planet. This is consistent with what was discussed in section 1, in which for extended objects L remains constant and equal to L_{planet} since the first terms cancel out. For diffraction limited telescopes, the FOV [rad] of a telescope of diameter D scales with wavelength λ as $\text{FOV} \sim 1.22 \lambda / D$, and therefore $\Omega = (\pi/4)\text{FOV}^2$ scales quadratically with wavelength. Such considerations are taken into account by PSG when computing filling factors and count rates (equation 1) for each simulation pixel.

3. Spectral grids, sampling and convolutions

Equation 1 and those in tables 1 and 2 make use of finite and quantifiable parameters, all derivable from the simulation input parameters or from the specifications of the instrument. Yet a challenging parameter to conceptualize is “number of pixels”. As summarized in section 1 and in Table 1, the detector noise is per/pixel, and for that one needs to fully understand how the simulated spectra projects onto the detector. If one selects “**boxcar**” for the resolution type in the PSG/GUI Telescope and Instrument section, the separation/spacing between each simulation spectral point will be as defined by the resolution. For instance, if the user chooses a “boxcar” and a resolution of $0.1 \mu\text{m}$, then each simulation point will be spaced by $0.1 \mu\text{m}$, and $\Delta\lambda$ in equation 1 will be $0.1 \mu\text{m}$. However, if the user selects “**gaussian**” for the resolution type, then in PSG the spectral points will be computed at intervals of the selected resolution divided by 10, so at spacings of $0.01 \mu\text{m}$ for this example, and the spectra will be convolved with a Gaussian kernel having a Full-Width-Half-Maximum (FWHM) of $0.1 \mu\text{m}$. In spectroscopic terms, this means that for the “boxcar” method the sampling resolution is equal to the spectral resolution, and for the “gaussian” method the sampling resolution is 10 times higher than the spectral resolution. This higher sampling rate for the gaussian method is needed to ensure proper characterization of the instrument line shape in PSG and it is



well beyond the Nyquist limit (sampling at least twice as the resolution). Yet, this also means that for the “gaussian” method, $\Delta\lambda$ in equation 1 will be $0.01\ \mu\text{m}$, and the count rates 10 times lower.

Now that we have introduced the concepts of “sampling” and “resolution” pixels, we can proceed further with the interpretation of instrument (or optical) and simulation pixel (see Figure 2 for a graphical interpretation of these concepts). It is highly recommended that the user chooses “boxcar” pixels for noise simulations in PSG, so resolution in PSG would then mean “optical” or actual instrument resolution (as reported in their specification tables). Then we need to understand what is the sampling rate that the instrument has for that optical resolution, defining the “number of pixels” (n) entry in PSG Telescope and Instrument section. Most instrument developers, try to squeeze as much information in an array as possible, so this means making the instrumental sampling rate as close to the Nyquist limit as possible. This would mean $n=2$, yet many instruments project into 2D arrays, and herewith we would have $n \sim 2 \times 2 = 4$ pixels per “boxcar” PSG resolution or instrument’s actual resolution. For grating instruments, a value of $n=8$ is recommended (to allow for a typical spread among more pixels), while for linear dispersive instruments $n=2$ to 4 is recommended.

Depending on the dispersive/diffractive method used by the instrument to separate light, some wavelengths may project onto less or more pixels. In PSG, the keyword GENERATOR-NOISEPIXELS allows to provide the number of pixels (e.g., n_A , n_B , n_Z) at specific wavelengths (e.g., λ_A , λ_B , λ_Z) of the instrument, in the format $n_A@ \lambda_A, n_B@ \lambda_B \dots, n_Z@ \lambda_Z$ (see example of JWST/MIRI-LRS template configuration file for details). If this information is not provided, and a diffraction limited configuration is defined, PSG assumes that the number of pixels grows with wavelength due to the larger diffraction pattern, and herewith the number pixels scales as λ^2 .

4. Radiation and intensity output units

In PSG, the user can select from a wide variety of generally used astronomical units for the calculated fluxes, radiances and output intensities (see full table at <https://psg.gsfc.nasa.gov/helpmodel.php#units>). When employing absolute units, the output intensities are specific and clearly defined, yet there are some ambiguities for certain units, and in this section we will establish the formalisms for each of them as defined in PSG:

Spectral radiances (e.g., $[\text{W}/\text{m}^2/\mu\text{m}/\text{sr}]$): this is the baseline of the simulation units, in which the instrument parameters less affect the output results. The reported values by PSG will contain corrections for filling factors/planet fraction (see section 2), so the spectral radiances will depend on the assumed size of the FOV and the projected size of the planet in it. This unit is convenient when comparing simulation results between different instruments or configurations (e.g., independent of spectral resolution or collecting area).

Radiances, intensities, and fluxes: as the spectral radiances get multiplied by specific properties of the instrument – by FOV resulting in spectral irradiance (e.g., $[\text{Jy}]$); by collecting area resulting in spectral intensity (e.g., $[\text{W}/\text{cm}^2/\text{sr}]$); by FOV, collecting area and spectral resolution [photons/second] as in equation 1 – they start to resemble more the values actually measured by an instrument/observatory. Jansky $[\text{Jy}]$ is a particular useful unit when reporting integrated fluxes of

small and distant objects (e.g., asteroids, exoplanets, stars, or objects having filling factor = 1 as described in see section 2), since it is generally invariant with FOV (when larger than the object), resolution and collecting area, and the numerical values are normally “legible” and closer to 1 for many sources.

Brightness temperature [K]: is a typical unit used in radio astronomy, which refers to the effective blackbody temperature of the observed flux, if the source would fill the FOV and it would have an emissivity of 1. Effectively, brightness temperature is the inverse of the Planck function, yet this inverse transformation is highly non-linear and rather numerically instable, so it should be used only for specific and selected cases. An alternative and more stable transformation is the Rayleigh-Jeans Brightness temperature [K], which is based on the first Taylor term of the Planck function and relates linearly with spectral radiance [L]. The Rayleigh-Jeans approximation starts to depart greatly from the Planck function at wavelengths shorter than the sub-mm, and it should be only considered at radio wavelengths.

Magnitude (m): this logarithmic unit normalizes the simulated irradiances to those of the star Vega, considering a radius of $1.65e9$ [m], a distance of 7.68 [pc], and a spectral energy distribution closely approximating that of a black body for a temperature of $11,000$ [K].

Contrast: when a star is in the simulation scene (e.g., transit, coronagraphy, occultation, object > 1 [pc]), PSG can compute the fluxes with respect to the background star ($I = L/L_{\text{star}}$). In transit mode (see section 2), the values report the relative stellar flux lost due to the transit as, $I = (R_p / R_{\text{star}})^2$ equivalent in fluxes as $I = (T \cdot L_{\text{star}} - L) / L_{\text{star}}$, where T is the transit transmittance. It is important to note that L is the intrinsic self-emitted flux of the planet, and this means that the “total” column in PSG contains the net lost flux, which is the sum of the lost flux ($T \cdot L_{\text{star}}$) minus the self-emitted flux (L). The “transit” column reports T . By definition, R_p and T include the solid surface radius (R_{surf}) and the opaque component of the atmosphere ($R_p = R_{\text{surf}} + H_{\text{atm}}$). In that sense, when requesting the unit [ppm], PSG will only report the H_{atm} component in parts-per-million so $I = 1e6 (H_{\text{atm}}/R_{\text{star}})^2$, while the unit [km] will report H_{atm} in [km], which is determined algebraically from the radiative transfer computed “transit” T term.

Apparent albedo (I/F): is the ratio of the planet brightness relative to that one of an idealized flat, fully reflecting, and perfectly emitting ($\epsilon=1$, with temperature as T_{surf}) disk with the same cross-section as the planet. If the planet/object is at phase=0 and the FOV encompasses the whole planet, this unit then corresponds to the “geometric albedo”. In PSG, fluxes always include reflected and thermal emitted fluxes, and in that sense I/F provides a metric to the reflective and emitting properties of the planet. If the simulation includes leaked star/stellar fluxes (e.g., coronagraphy), these are removed from the “Total” column to provide solely planetary I/F values.

5. Zodiacal light, exozodii, telluric and background sources

As we observe our target planetary object (and possible stellar companion), we also observe several background sources, which are not included in the reported radiances, but they do impact the overall sensitivity of the simulations. Effectively when performing observations, one first samples the object

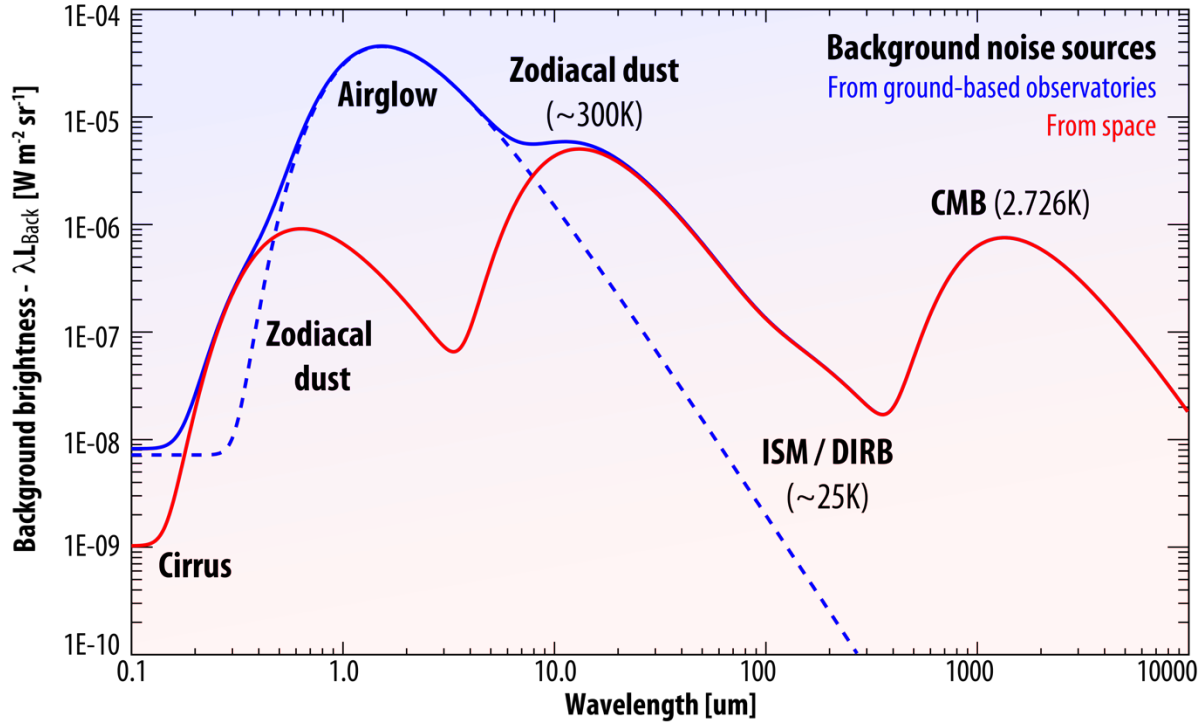


Figure 3: When observing faint astronomical sources, the sensitivity is affected by the shot noise introduced by background and diffuse sources. From space, the background is dominated by the faint and diffuse emission (thermal and scattered sunlight) from zodiacal dust, while airglow (a mixture of photoionization emissions, chemiluminescence and scattered sunlight) dominates the background for ground-based observations. PSG also employs a rudimentary (as shown), yet relatively effective, approximation for atmospheric airglow.

and the background in the A position, then switches to a B position in which only the background is sampled, and then performs the A-B difference to eliminate the background flux from the observations. An optimum sky / background method is to observe in an ABBA sequence to enable second order background cancellation. Even though the observations would no longer include background fluxes, they do unfortunately retain the noise associated with them. This background noise is also added twice (since it exists in the A and B positions), and therefore it must be included twice (see N_{total} equation in Table 2).

There are 3 major sources of background noise:

Instrumental optics (N_{optics}): this is noise originating due to the thermal emission by the instrumental/telescope optics. This value is typically constrained by the temperature and emissivity of the main mirror of the telescope, and it is why so much care is taken to shield the observatory from sunlight when pursuing sensitive infrared observations (e.g., JWST). This term is parameterized in PSG by defining the emissivity and temperature of the optics.

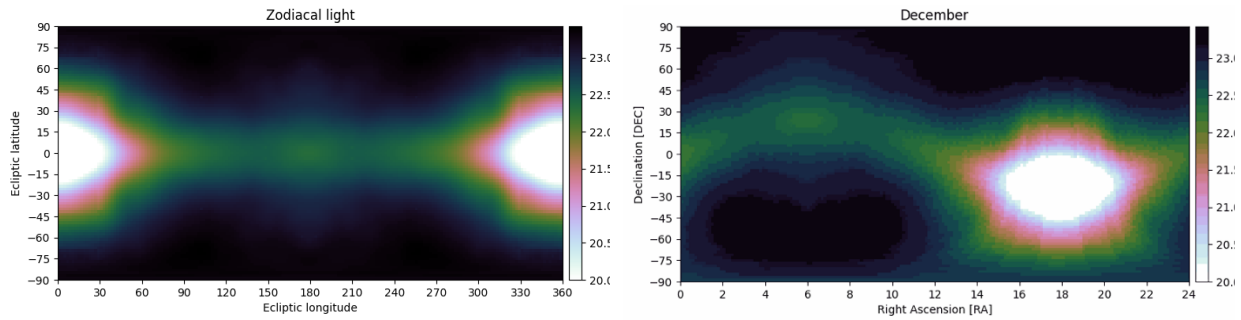


Figure 4: The zodiacal flux decreases notably when away from the Sun, and as the Sun moves across the sky (RA/DEC) during the year, the zodiacal levels change for the same RA/DEC. It is therefore of importance to properly define the zodiacal level at the time of the observations or at the most favorable time/month. The levels shown in these figures were computed by combining data from (Kwon et al., 2004) and from (Leinert et al., 1998). A zodi calculator in PSG (<https://psg.gsfc.nasa.gov/helpmodel.php#noise>) permits to estimate the zodiacal level and the scaler to be used in PSG.

Ground-based background sources (N_{tel}): when performing ground-based observations, thermal emission and airglow by our own atmosphere lead to strong background signatures. Thermal emission and absorption are parameterized in PSG via the definition of the location of the observatory and the total telluric water column for the simulation. PSG works with a database of pre-computed telluric transmittances, that includes 5 altitude regimes (Maunakea/Hawaii [4200 m], Paranal/Chile [2600 m], SOFIA [14,000 m] and balloon observatories [35,000 m]) and 4 water columns established by scaling the tropical water profile by a factor of 0.1, 0.3 and 0.7 and 1. Airglow is a particular important source of radiation at short wavelengths originating from a mixture of photoionization emissions, chemiluminescence and scattered sunlight, and it is modeled in PSG via a simple yet effective parameterization as presented Figure 3.

Background astronomical sources (N_{back}): several background and diffuse sources (e.g., zodiacal dust, exozodi, Cirrus, ISM/DIRB, CMB, Leinert et al., 1998) introduce noticeable levels of noise. Zodiacal light is the faint and diffuse radiation across the ecliptic plane originating from scattered sunlight by interplanetary dust. The brightness of the zodiacal light decreases with distance from the Sun, with a notable increase at opposition due to backscattered sunlight ("gegenschein"). This background radiation is typically the main background radiation term impacting space observations of faint objects, and it is highly dependent on the RA/DEC of the target and the time of the observations. In PSG, the parameterization of the zodiacal level is done by a scaling factor with respect to the polar ecliptic value (23.3 V [mag/arcsec²]), with a scaling of 2 (22.5 [mag/arcsec²]) being the default and the typical value for a general observatory. For exozodis, the surface brightness increases because of the geometry and preferable scattering with an average value of 22 V [mag/arcsec²]. In coronagraphy, the user can scale this by a multiplier (1 being 22 [mag/arcsec²]).

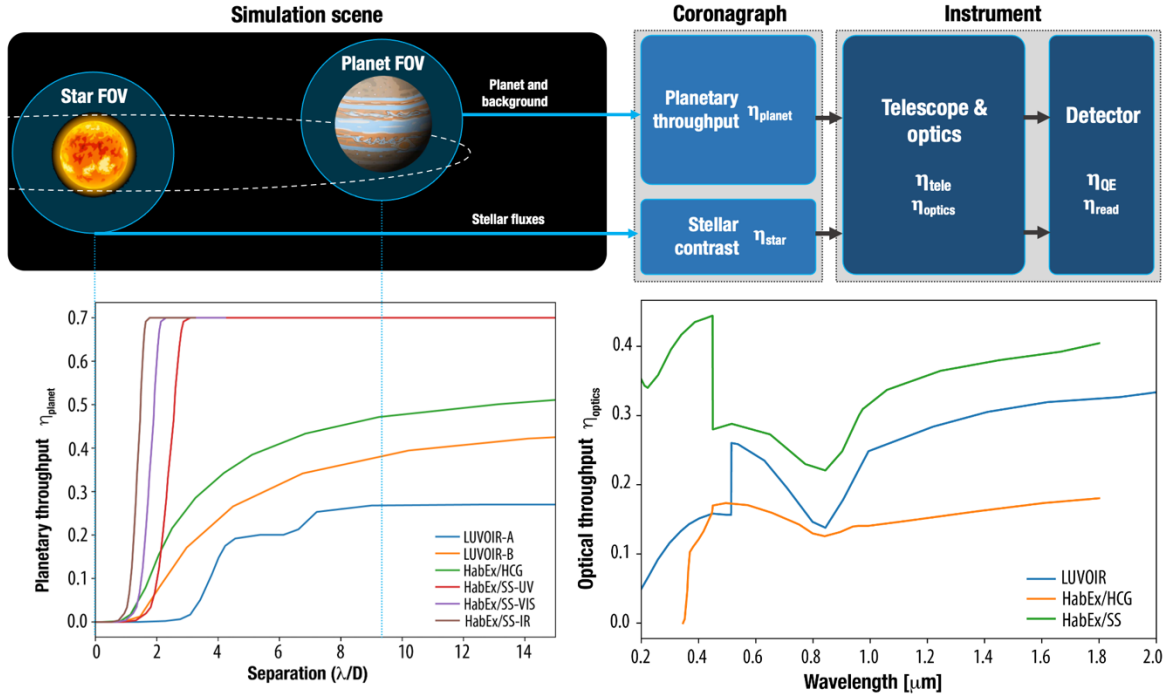


Figure 5: Elements involved in a coronagraphic simulation, and example throughput curves for several blocks as considered by the LUVUOIR (A and B) and HabEx concept missions (star-shade/SS and coronagraph/HCG). The “coronagraph” acts as an additional layer to the standard “instrument” model blocks of PSG, in which the planetary (and background) fluxes are affected by the coronagraph transfer function (η_{planet}), while the stellar fluxes are heavily reduced by orders of magnitude (η_{star}). All these parameters can be provided as inputs to PSG as described in section 6. The value of η_{planet} will depend on the star-planet separation (in radians), the wavelength (λ [m]), the telescope diameter (D [m]) and the planetary throughput curve.

6. Coronagraphic modeling

Coronagraphic simulations are relatively complex simulations, in which several components of a scene are integrated into a cohesive simulated spectrum with a corresponding associated noise (see Figure 5). In practice, these simulations are integrated into PSG by adding a “coronagraph” layer on top of the classical instrument modeling discussed in the previous sections. This layer will provide specific throughputs (η) for the planet and background signals, and another for the stellar signature. These throughputs will depend on the wavelength of the pixel, the diameter of the telescope, the separation between the planet and star and considered coronagraph and contrast transfer curves. The main objective of a coronagraph is to maximize the throughput of the planetary signature and to minimize the fluxes from the stellar companion. This is achieved by placing a blocking element (e.g., star-shade, vortex coronagraph that relies on a phase mask forming a spiraling blocking phase) in front of the star, while also keeping the planet away from this blocking element. The distance between the star and planet then defines how much of the planet flux is permitted to go through.



There are four important parameters in a coronagraph:

Core throughput (η_{core}): this is the maximum throughput of the coronagraph for the planetary signature. The greater this value the higher the performance of the instrument. In figure 5, for instance η_{core} is 0.27 for LUVOIR-A.

Inner Working Angle (IWA): this defines the star-planet separation, defined in radians as λ/D , at which the throughput is half of the core throughput and towards the star. The lower this value, the closer we can observe the planet from the star. In Figure 5, we see that the IWA for LUVOIR-B is 3.5.

Outer Working Angle (OWA): this defines the λ/D at which the throughput drops below half the core throughput beyond the core region. In Figure 5, the OWAs are beyond the limits of the 14 λ/D shown limit, yet we only show a simplified transfer curve in this figure. The greater this value, the further we can observe the planet from the star.

Contrast (C): defines how much stellar leakage remains, and it is defined with respect to the core throughput. In PSG, we assume η_{star} to be constant in wavelength, and only dependent on the reported contrast and the coronagraph core throughput in the form of $\eta_{\text{star}} = \eta_{\text{core}} \cdot C$. For instance, considering the case of LUVOIR-A with C defined as $1\text{e-}10$, the stellar throughput is then $\eta_{\text{star}} = 0.27 \cdot 1\text{e-}10 = 2.7\text{e-}11$.

A particular confusing term is λ/D (as presented in the coronagraph chart in Figure 5), and why it depends on wavelength. This is because coronagraphy is primarily done via interference patterns (not the case of star-shades though), and therefore it is wavelength dependent. For instance, a λ/D of 9 for a 15 meters telescope ($D=15$ [m]) at a wavelength of 0.5 [μm] ($\lambda = 5\text{e-}7$ [m]) is $9 \cdot 5\text{e-}7 / 15 = 3\text{e-}7$ [rad], which is equivalent to a separation of 0.06 [arcsec] ($3\text{e-}7 \cdot 3600 \cdot 180 / \pi$). For a planet at 5 [pc], this would correspond to a separation of 0.3 [au] ($5 \cdot 3\text{e-}7 / 4.84814\text{e-}6$) between the planet and the star. Then, if we are observing a planet at 5 [pc] separated by 0.3 [au] from the star with LUVOIR-A (corresponding to $\lambda/D = 9$), then the throughput would be 0.27.

In the case of star-shades (e.g., HabEx/starshade), the blockage is not done by interference but by physically blocking the stellar light with a spacecraft flying in formation in front of the observatory. As such, the blockage is primarily defined by the physical properties of the star-shade, and it is in principle wavelength independent. The transfer function is then not reported in λ/D , but in actual units of separation [radians] or [arcseconds]. In PSG, the coronagraph transfer function can be provided in units of λ/D or in [arcseconds] depending on the sign of the x-axis – please refer to the LUVOIR and HabEx templates for examples in how to upload your own coronagraph transfer function. If no coronagraph function is provided, PSG assumes that the throughput is minimum (contrast) within half the inner-working-angle (IWA), it reaches 0.5 at the IWA, and reaches 1.0 at 1.5 times the IWA.



Beyond the coronagraph transfer function, several instrument elements will lead to losses in the light path. The more important are: η_{tele} is the telescope main mirror efficiency (0.95 is a typical value); η_{optics} is the optical throughput which is typically wavelength dependent (as shown in Figure 5); η_{QE} is the detector quantum efficiency and depends on the detector technology and sampled wavelength (typically ranges from 0.7 to 0.9); and η_{read} is the read-out efficiency which can be considered 1.0 in many cases, yet a value of 0.75 is commonly used for certain EMCCD detectors. The total instrument throughput includes all these losses, and therefore $\eta_{\text{inst}} = \eta_{\text{tele}} \cdot \eta_{\text{optics}} \cdot \eta_{\text{QE}} \cdot \eta_{\text{read}}$. In PSG, the provided total throughput efficiency refers to this quantity and should include all losses beyond those of the coronagraph.

For further details on coronagraphic simulations with PSG and comparisons to other coronagraph simulators, please refer to Checlair et al., 2021 (LUVOIR/HabEx), Kopparapu et al., 2021 (LUVOIR) and Saxena et al., 2021 (Roman). Importantly, when operating in coronagraphy mode, the noise output of PSG (“noi” file) will include the calculated planetary coronagraphy (η_{planet}) for every simulation pixel, while PSG will also provide the count rates for the different sources in the “cps” file. The count rates allow to quantify the relevance of the different sources arriving to the detector, of key relevance when comparing to other coronagraph models (e.g., Robinson et al., 2016) or when investigating the dominating sources impacting the noise levels.

7. AOTF and grating modeling

Acousto Optical Tunable Filters (AOTF) allow to select a certain wavelength range of the light traversing an optical path by injecting a specific frequency to a tunable crystal. These filters are relatively compact and quick flexible, and therefore a common feature in many instruments, in particular, for mass/volume/power efficient space instruments (e.g., ExoMars-TGO/NOMAD). When performing simulations of AOTF images in PSG, there is no need to select this mode – simply selecting a resolution that corresponds to the spectral width of the filter is sufficient.

The AOTF mode in PSG refers to a special configuration, in which the AOTF operates as an order sorting device for a high-resolution grating system. In an echelle grating spectrometer, all diffraction orders overlap at the same location, and a cross-disperser or filter is used to select the main order of interest. The challenge in an AOTF + grating system is that the AOTF has a complex transfer function, and the contribution of nearby orders overlap to the main selected order. This would mean that when modeling a spectrum for order X, one sees lines spanning a broad range +/- N orders around X.

In PSG, we have implemented a realistic AOTF and grating model that captures the subtleties of order addition and allows for a complex AOTF transfer function scheme. Specifically, the AOTF function is modelled as an asymmetric sinc function complemented by a Gaussian core and a systematic offset. For further details regarding the implementation and modeling of the AOTF in PSG, please refer to (Liuzzi et al., 2019; Villanueva et al., 2021).

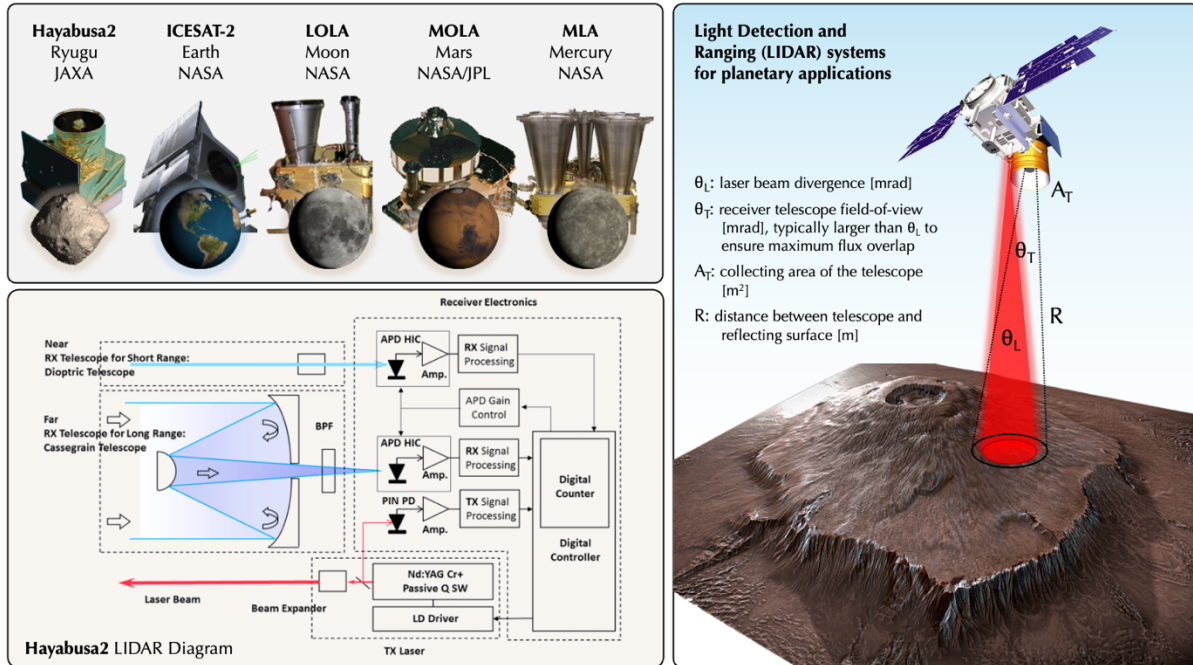


Figure 6: Active remote sensing via Light Detection and Ranging (LIDAR) spectroscopy permits to characterize the surfaces and atmospheres of planets and small bodies over a wide range of illumination conditions. The technique involves deploying an active source, typically a laser, which is complemented with a receiver telescope. Several planetary LIDAR systems have been flown successfully across the Solar System, including the LIDAR in Hayabusa 2 (Mizuno et al., 2017), the Advanced Topographic Laser Altimeter System (ATLAS, Markus et al., 2017) onboard ICESAT-2, the Lunar Orbiter Laser Altimeter Investigation (LOLA, Smith et al., 2010) on the Lunar Reconnaissance Orbiter Mission (LRO), the Mars Observer Laser Altimeter (MOLA, Zuber et al., 1992) onboard Mars Global Surveyor (MGS), and the Mercury Laser Altimeter (MLA, Cavanaugh et al., 2007) onboard the MESSENGER mission.

8. Light Detection and Ranging (LIDAR) spectroscopy

A powerful way to probe planets and small bodies is via Light Detection and Ranging (LIDAR) spectroscopy, in which an active source (e.g., a laser) is sent through a planet's atmosphere and the returning signal can be used to infer the properties of the atmosphere and surface, and also to determine distance and topography. The most common configuration is in nadir geometry, in which a collimated laser beam is sent straight-down (0 degrees inclination) from a satellite, and the reflected signal is measured by a co-located telescope. The peak power of the laser P_L [W] is defined by the energy E of the laser [J] and the pulse duration Δt [s], $P_L = E/\Delta t$. The outgoing laser beam is collimated, so if the receiver telescope would be able to capture the full extent of the collimated beam, then there would no losses due to range and flux distance dilution. Yet, once the collimated beam hits the surface, it is emitted across all directions (e.g., uniformly as in Lambert), and then the received signal will drop by $1/R^2$, where R is the distance to the surface. In that sense and to maximize energy recovery, the receiver telescope FOV (θ_T) should be larger or comparable to the laser beam (θ_L) on the surface, and that is the typical design configuration used by most planetary

LIDARs. As shown in Figure 6, R defines the satellite's altitude, and the larger the altitude, the larger the requirements in sensitivity for the receiving telescope (e.g., the collecting area A_T). For a nadir system, the received power (P_r) can be estimated employing the LIDAR link equation:

$$P_r = P_L \frac{A_T}{\pi R^2} \eta_L \eta_T r_{surf} T_{atm}^2 \gamma_{LT} \quad (2)$$

where η_L is the laser emission efficiency (0 to 1), η_T is the telescope receiving efficiency (0 to 1), r_{surf} is the surface reflectance at phase 0 (incidence laser and emission angles are the same), T_{atm} is the one-way atmospheric transmittance from the satellite to the surface (squared in equation 2 due to double-path absorption), and γ_{LT} is the overlap between the laser and receiver beams (0 to 1). The definition of γ_{LT} would depend on many factors, including the accuracy of the alignment of the beams, the beams parallax, the speed of the spacecraft relative to the distance and time delay, and the size of the laser beam divergence relative to the telescope FOV. If the telescope FOV is smaller than the laser beam, then $\gamma_{LT} \sim (\theta_T/\theta_L)^2$. See below the link equation applied to two planetary LIDAR systems:

Hayabusa 2 (Mizuno et al., 2017): the LIDAR system onboard the Hayabusa 2 (see Figure 6) mapped the topography of asteroid Ryugu over a wide range of distances ($R=30\text{m}$ to 25 km), since it was used as a navigation sensor for rendezvous, approach, and touchdown procedures. At large distances ($R>1\text{ km}$), a compact $D=110\text{ mm}$ Cassegrain telescope ($A_T=\pi D^2/4$) with an efficiency of $\eta_T=0.678$ had an observing FOV of $\theta_T=1.5\text{ mrad}$, which overlapped with 35% ($\gamma_{LT}=0.35$) of the $\theta_L=2.5\text{ mrad}$ laser beam. At short distances, beam parallax effects and saturation of the APD required a secondary smaller telescope with an aperture of $D=3\text{ mm}$, $\eta_T=0.728$ and $\theta_T=20\text{ mrad}$ ($\gamma_{LT}=1.0$). The laser produced 15 mJ of pulse energy over 7 ns at 1064 nm , resulting in a peak power of $P_L = 2.1\text{e}6\text{ W}$. When considering a reflectance of $r_{surf}=0.06$, the link equations for both channels can be reduced to $P_r=92.3/R^2\text{ [W]}$ for the long-range channel and $P_r=0.211/R^2\text{ [W]}$ for the short-range channel. Detection was performed employing an avalanche photodiode–hybrid IC (APD-HIC), with a minimum detectable signal of $6\text{e-}8\text{ W}$, restricting the maximum R to 39.2 km for the long-range and R to 1.9 km for the short-range.

Mars Observer laser altimeter (MOLA) (Zuber et al., 1992): the laser altimeter onboard the Mars Global Surveyor (MGS) spacecraft delivered high-quality topographical maps of Mars with a vertical resolution of 1.5 m from an typical spacecraft altitude of $R = 400\text{ km}$. The laser transmitter was a diode-laser pumped, Q-switched, Cr:Nd:YAG slab laser, delivering a pulse energy of 45 mJ over 8 ns ($P_L=5.6\text{e}6\text{ W}$), while the laser beam had a full width divergence of $\theta_L=0.37\text{ mrad}$. The receiver was composed of a large $D=465\text{ mm}$ telescope with an efficiency of $\eta_T=0.565$ and a FOV of $\theta_T=0.85\text{ mrad}$ ($\gamma_{LT}=1.0$). Considering a typical reflectance of $r_{surf}=0.2$ and an atmospheric transmittance of $T_{atm}=0.6$, the typical received power was $P_r = 7.7\text{e-}8\text{ W}$.



Planetary Spectrum Generator
National Aeronautics and Space Administration

Chapter 9: **Retrieval Methods**

**Liuzzi, Villanueva, Mandell and
PSG team**

1. Retrievals general elements

Retrieving information from planetary observations can be approached in many ways, which can rely to a different degree on radiative transfer or the data themselves. In any case, any retrieval problem is defined in terms of an input (the “data”), a series of unknown variables to retrieve (the “parameters”) and a model that correctly accounts for the physics of the observed system. The objective of a retrieval scheme is to minimize the difference between the data and the model, and to find the corresponding set of parameters.

In most cases, as many inverse problems, this is an ill-posed problem, as many different solutions could represent the observations as well: a classical example is the problem of simultaneously estimating the surface temperature and emissivity of a planetary body, which even in absence of atmospheric absorption does not have an obvious solution. Therefore, one of the main challenges in retrievals is to resort proper ways to optimize the solution towards a set of parameters that is physically coherent with the observed system. Modern algorithms and schemes are accustomed to providing such optimal solutions, by using statistical constraints and heavily relying on climate models as a starting point for the search of the solution.

According to the degree of constraint that can be applied to the search for the optimal solution, retrieval schemes can be roughly divided into two large categories: 1) (pseudo-)analytical schemes, which foresee the possibility to work with strong constraints to the solution, and 2) statistical schemes, in which the search for the solution is performed by exploring a large region of the parameters space and minimizing proper metrics related to the difference between data and model.

PSG currently has two packages that implement two of the most widely used retrieval techniques for each category: an Optimal Estimation (OE) method module (Rodgers, 2000), which has been widely applied and well consolidated in the context of Earth and the other planetary bodies of the Solar System; and a Nested Sampling (NS) scheme (Buchner, 2021) which is widely employed in the context of exoplanetary research to, e.g., look for signatures of molecular absorption in atmospheres.

2. Optimal Estimation

OE retrievals are particularly suitable in cases where a wealth of prior information about the parameters to retrieve is available and can be used to constrain the solution of the parameters. In fact, any OE algorithm and its variations include the necessity to use a-priori as an integral part of the mathematical equations that yield the minimization of the residuals between the model and the data. This objective is always sought in an iterative fashion through a form of a Gauss-Newton approach, exploring the minimization of a cost function.

The OE package in PSG is fully integrated with the radiative transfer model, meaning that they are completely inter-operable, and that the data and the parameters set in PSG can be part of the set of parameters to retrieve. The OE scheme in PSG is based on the original formulation of OE (Rodgers, 2000) with specific regularization mechanisms and planetary parameterizations which are summarized here. Optimal estimation is a Bayesian method, in that it employs probability

information on the data (e.g., error-bars) and the possible solution (e.g., a-priori, possible parameter range) to condition and balance the solution to reach the most probable and optimal solution. The principle of OE is to link the data space with the parameter space by a set of linear equations that are solved iteratively by exploring the minimization of a cost function. In the retrieval, we have a dataset (y) with one sigma error-bars (ε) described as vectors of length of m , which is compared to model f parameterized with n values (x). Following Bayes theorem for the most optimal solution, the cost function (Q) can be then defined as (based on equation 5.3 from Rodgers, 2000 defined as R5.3 hereafter):

$$Q = (y - f)^T S_\varepsilon^{-1} (y - f) + (x - x_a)^T \gamma S_a^{-1} (x - x_a) = \chi^2 + \xi^2 \quad (1)$$

where S_ε is the signal covariance matrix [$m \times m$], S_a is the parameter covariance matrix, γ is a regularization parameter and x_a is the a-priori state vector. The first term of the equation is the χ^2 reduced of the solution and the second quantifies the cost ξ^2 of deviating too far from the a-priori prescription. Neglecting correlated noise, the signal covariance matrix can be established based on the signal variance as $S_\varepsilon = \varepsilon^T \varepsilon$, only filling the diagonal terms, and its inverse S_ε^{-1} trivially computed as the inverse of the diagonal terms. This is the formulation adopted in PSG, yet in the more general case, complex formulations considering effects such as inter-channel correlations can be adopted. The vector x (of dimension n) contains the needed parameters for model function f in order to match the data y . The x array could include, the surface parameters (e.g., temperature, reflectance), the atmospheric parameters in terms of the total column observed of a particular constituent (e.g., gas abundance, aerosol properties, temperature), or the full, or a portion of the vertical profile of those parameters along the line of sight.

At first, one also must define an initial guess for the values of the parameters, which is denoted as x_a , which contains values for the parameters defined on a-priori information, such as climate models, or educated guesses on the parameters from past observations. Information on the statistical variability of the parameters and their degree of correlation is defined by the covariance matrix S_a [$n \times n$]. The simplest choice for it is a diagonal matrix, which corresponds to assuming total independence of all the parameters from each other. Yet, in many cases, this is a non-realistic assumption, especially when dealing with vertical profiles of atmospheric parameters, which can be characterized in PSG by defining a vertical correlation coefficient (see Section 4).

In order to determine the direction towards the solution at step i , the algorithm utilizes the Jacobian matrix K_i [$m \times n$], which contains the derivatives of the model function near the latest solution state $K_i = \partial f / \partial x$. The Gauss-Newton iteration for solving the OE systems of equations can be described as (based on R5.9):

$$x_{i+1} = x_a + \boxed{(\gamma S_a^{-1} + K_i^T S_\varepsilon^{-1} K_i)^{-1}} K_i^T S_\varepsilon^{-1} [y - f + K_i(x_i - x_a)] \quad (2)$$

that involves the inversion of a matrix of order [$n \times n$], highlighted in the equation with a rectangular box. For the inversion of this matrix and of S_a , PSG employs the Cholesky decomposition method since these matrices are positive-definite and symmetric. In all cases, the algorithm is initialized adopting the a-priori state vector ($x_0 = x_a$), and the parameters are operated

internally using normalized and positive transformed forms of them. The regularization parameter γ defines how much the solution is dependent on the a-priori, with a value of 1 being the default and consistent with the classical (Rodgers, 2000) optimal estimation formalism. A value of 0 would correspond to a direct least-squares (e.g., MPFIT), and values greater than 1 implying a solution heavily directed towards the a-priori values.

In the case that the true solution is far from the current iteration point, the algorithm may overshoot or diverge from the desired path of convergence. PSG employs two stabilizations approaches to control the evolution of the retrieval: 1) by employing a “braking” Levenberg-Marquardt coefficient λ and 2) by increasing the scaling of the γ parameter to further direct the solution towards the a-priori (similar to R5.36). The first approach regulates the size of the jumps, which can be particularly misjudged by the OE algorithm for heavy ill-posed and non-linear problems, since at the core, the algorithm estimates the jumps based on a linearized form of the function $K_i(x_i - x_0)$. The braking λ coefficient is based on the formalism by (Irwin et al., 2008) as:

$$x_{i+1}' = x_i + \frac{x_{i+1} - x_i}{1 + \lambda} \quad (3)$$

At each iteration, λ is initialized at 0, and increases to 1 and then to 10 and then 100, exploring a lower cost function. If the cost function still did not improve, PSG will then scale γ by 10 and then 100 to explore if directing the solution towards the a-priori solves the divergence problem. Convergence is assumed to be reached when the rate of change of Q is lower than $1e-3$ and λ is close to 0. The resulting covariance of the parameters can be determined directly from the inverted matrix in equation 2 following R5.13 as:

$$S = (\gamma S_a^{-1} + K_i^T S_\epsilon^{-1} K_i)^{-1} \quad (4)$$

At a first order, the reported error-bars (σ) of the parameters can be determined from the square-root of the diagonal terms of S , and that is the approach implemented in PSG. Another important quantity is the averaging kernels (A) of the derived parameters, which are defined as the sensitivity of the retrieved parameters with respect to their “real” value (based on R3.28):

$$A = S K_i^T S_\epsilon^{-1} K_i = (\gamma S_a^{-1} + K_i^T S_\epsilon^{-1} K_i)^{-1} K_i^T S_\epsilon^{-1} K_i \quad (5)$$

The diagonal of the A matrix contains values between 0 and 1, which indicate the sensitivity of the retrieval to each parameter. Low values could indicate either poor intrinsic sensitivity of the data themselves to the retrieval parameters (low K), or too stringent constraints imposed to the variability of the retrieved parameters (very high S_a^{-1}), and that the retrieved information will be dominated by the a-priori. Instead, diagonal elements of A equal to 1 will indicate that the retrieved values are fully constrained by the data. The non-diagonal elements indicate the degree of correlation between parameters; ideally, these values are close to 0, or negligible with respect to the diagonal elements. The averaging kernels can be negative in the non-diagonal terms, indicating a negative correlation between parameters.

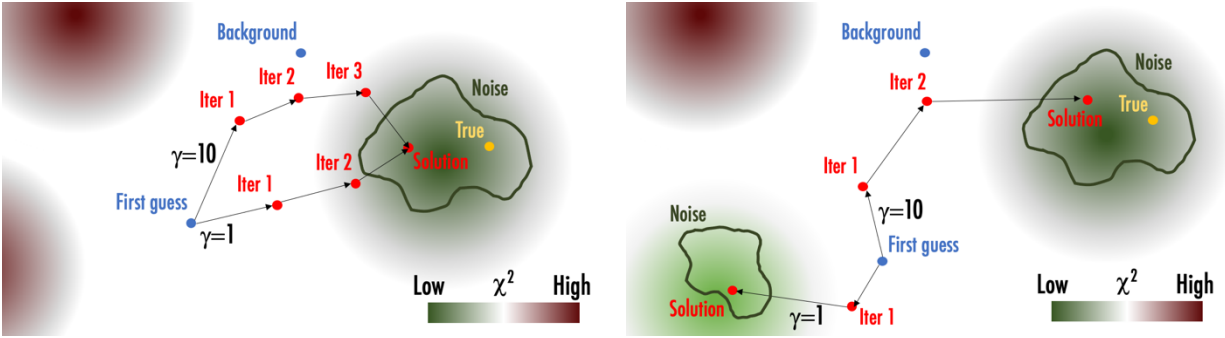


Figure 1: Scheme to illustrate the walk of OE between the First Guess and the solution. The background color represents the χ^2 , while the green lines represent the limit at which the solutions are all equal within the spectral noise (i.e., every model in that contour differs from the data by at most the noise). According to the value of gamma, the walk to the solution happens in different paths at different distances from the background. **Left:** a case in which the First Guess is relatively close to the truth. **Right:** a case where the First Guess is closer to another local minimum in the χ^2 , where other settings in the OE can steer the walk to the solution to the correct one.

The behavior of the OE scheme can be conceptually summarized in the scheme in Figure 1. Depending on the value of γ , the walk between the first guess and the solution is influenced by the background and can be slower or faster. However, it is important to note that the OE works at its best only when the first guess is reasonable with respect to the truth. When this is not the case, the presence of local minima in the χ^2 close to the first guess could yield the solution to collapse into such local minima, unless the background is properly chosen to make sure that the solution ends up in a domain close to the truth.

3. Implementation of OE in PSG

The implementation of OE in PSG benefits of some extra elements borrowed from simpler approaches, such as the regularized Levenberg-Marquardt (LM) minimization method. PSG relies on defining many parameters in the previous equations implicitly in the code, with minimal input from the user. The scheme for the implementation of OE in PSG is shown in Figure 2. Specifically, the following aspects and variables are implicitly defined in the code:

- For every retrieved parameter, PSG accepts in input from the user minima and maxima for their variability, v_{min} and v_{max} , similarly to what is usually done in a LM regularized approach. Those are then used to define the a-priori covariance matrix S_a , whose diagonal elements are computed as 10% of the difference between v_{min} and v_{max} .
- The algorithm is initialized adopting the a-priori state vector ($x_0 = x_a$), which is also the background state vector.
- To make the convergence and the inversion of the matrices smoother, the parameters are operated internally using normalized and positive transformed forms of them.

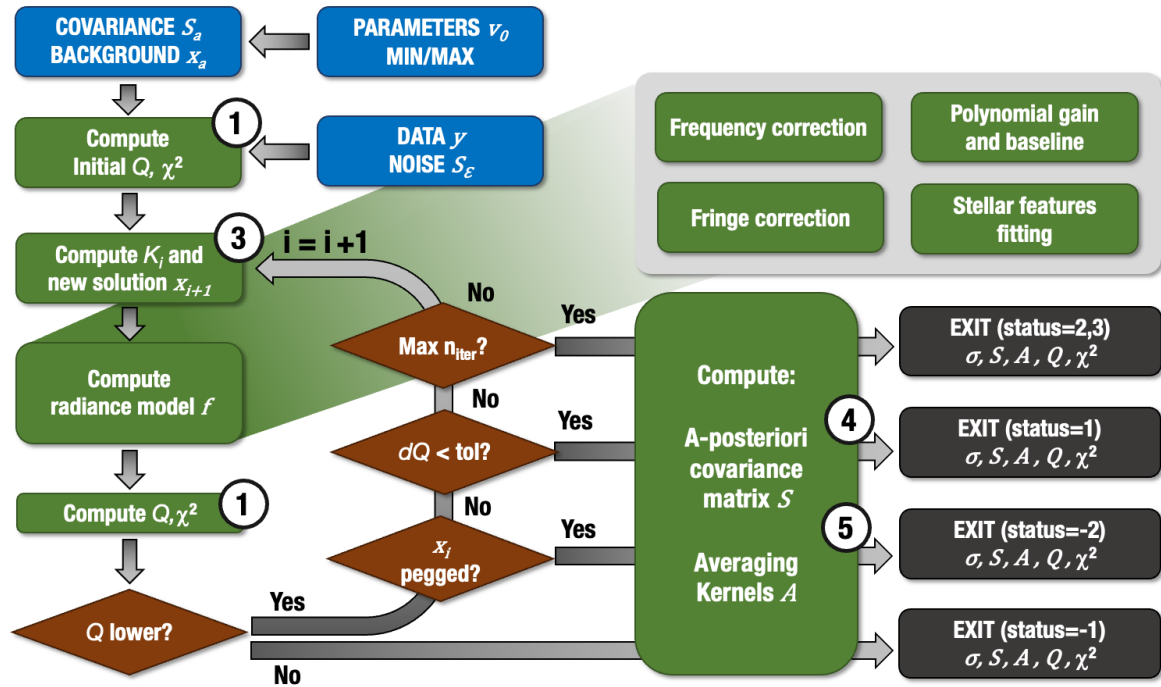


Figure 2: Scheme summarizing how OE is implemented in PSG. The blue boxes represent the user inputs, the green boxes are the internal PSG operations (and related equation numbers in the circle), in grey the outputs are shown.

- The maximum number of iterations is 20. While it is common for OE to rely on a fixed threshold for the Q below which the scheme exits with the solution, this would imply relying on accurate knowledge of the input noise and a-priori covariances. Given the general applicability of PSG, this is not always the best choice. Instead, it is checked whether the relative change of Q at the n -th iteration is lower than the one at the $(n-1)$ -th iteration by a factor.
- Retrieved parameters are checked by looking at whether the retrieval pegs them to their extremes. If that occurs several consecutive times the scheme excludes them from the retrieval.

The retrieval module can also correct for specific instrumental effects, which are iteratively accounted for through the radiative transfer function. This is necessary as at every iteration the model corresponding to the updated retrieval parameters changes, and with that the estimation of instrument-induced effects (more on this in Villanueva et al., 2013). A schematic view of such effects is given in Figure 3:

Frequency correction: frequency shifts can be induced by a myriad of instrumental effects, such as flexing of detectors and gratings caused by temperature changes. Correction of this effect is performed in PSG via a brute-force approach. Once the radiative transfer produces a model at the same spectral resolution as the data, the model is interpolated on the same sampling points as the data. To search for eventual frequency corrections, the data spectral grid is shifted, stretched and bended in regular steps, circling to the optimal solution which is sought by evaluating the correlation coefficient between the data and the frequency-corrected model.

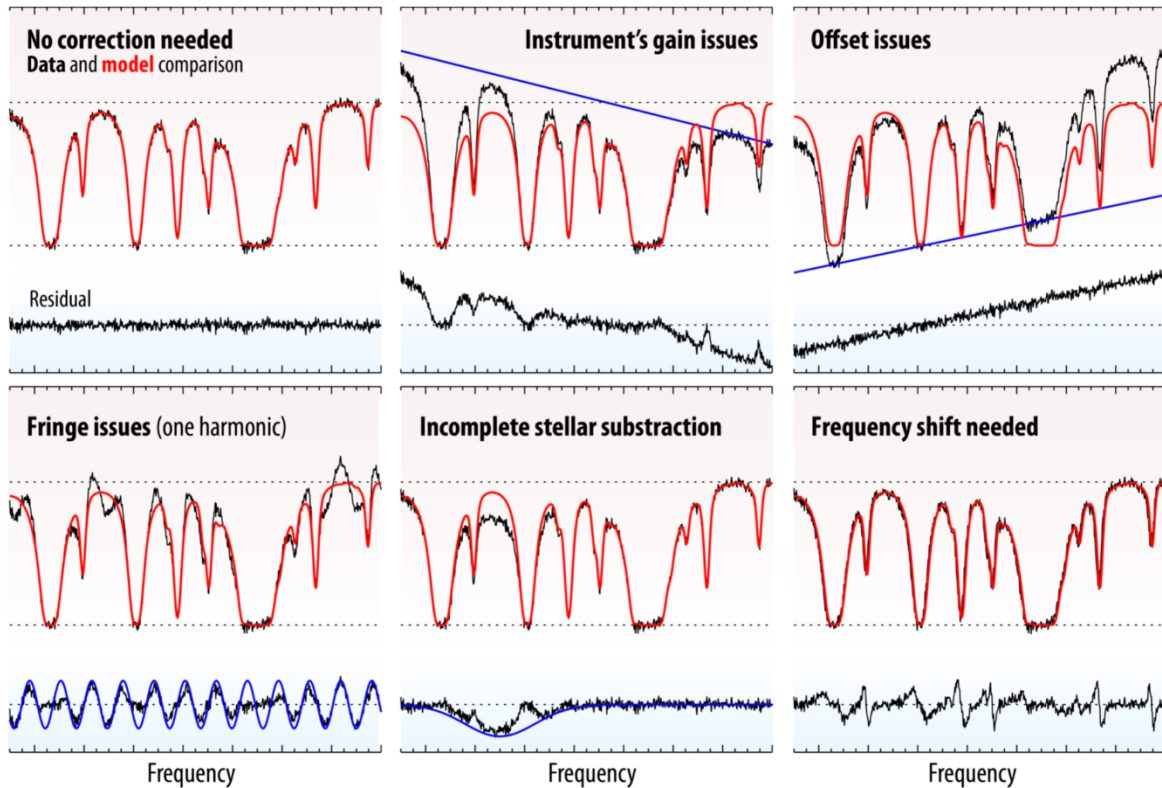


Figure 3: Illustration that shows the corrections that the PSG retrieval module is capable of accounting for and modeling.

Fringe correction: Several types of data (e.g., grating-based spectrometers, interferometers) are commonly affected by fringing. Spectral fringes arise from multiple reflections between two optical surfaces, and interference of the resulting wave fronts. The fringe spacing is $1/nL$, ('n' is the index of refraction in the medium, and L is the separation of the two surfaces). When this happens multiple times in an instrument, multiple fringes of different frequency will show up in the data. Correction for spectral fringing is performed as follows. First, a Lomb–Scargle periodogram analysis on the residual spectra is performed, from which period, amplitude, and phase are determined for each fringe. This information is used to compute a synthetic model for each fringe, whose amplitude is fitted to the spectra through a LM fit and subtracted from the spectra pixel-by-pixel.

Polynomial gain and offset: Gain effects are oscillations in the continuum around an average value and are quite common in observed spectra from any kind of instrument and at any wavelength. Excluding those modeled by radiative transfer as intrinsic to the observed system (e.g., emissivity or reflectance of the surface, atmospheric aerosols), the residual continua are modeled by PSG by LM fitting of a polynomial of degree specified by the user, which multiplies the model. An offset, instead, occurs as external flux added in the observations (e.g., by straylight), and is fitted by LM as a polynomial additive component to the model.

Parameter	Brief description	Optimal value	Optional?
Q and χ^2	As in Eq. (1)	$<N$ (residuals average is $<\epsilon_R$)	NO
Reduced χ^2	$\chi^2/(N- M)$	<1	NO
DOF	$\sum_{i=1}^N A_{ii}$	M (Information fully constrained by data)	It is 0 if no parameters are retrieved
NITER NFEV	Number of iterations Number of forward calculations	Max NITER is 20 The lower, the faster	NO
Status	Status of convergence	-2: Error in matrix inversion -1: Divergence in Q (does not decrease) 0: bad input or nothing to retrieve 1: convergence in Q (OPTIMAL) 2: max. NITER reached 3: Diverging but a better solution was found	NO
Frequency correction	Polynomial coefficients for shift, stretch and bending of the freq. correction	0 for all (i.e., the frequency solution is already optimal)	YES
A	As in Eq. (5)	Unity matrix (Information fully constrained by data, parameters independent of each other)	NO

Table 1: List of the PSG retrieval output parameters, their definitions, and their significance.

Stellar features fitting: in some cases, such as ground-based or nadir observations of a rocky planet, stellar lines and features can show up in the data if not previously corrected, and there are cases in which fitting their amplitude can give information about atmospheric absorption (as stellar radiation transverses two paths before reaching the observer in many geometries), or surface reflectance. There are also cases in which stellar lines are previously subtracted from the data, but the subtraction is not complete or generates micro-dispersion features related to incorrect frequency calibration. In any case, the forward module in the retrieval is capable of modeling and taking out stellar features by LM fitting of their amplitude.

Examples of retrieval applications are shown in Figure 4. In the examples of ExoMars Trace Gas Orbiter data, the single components of the retrieval scheme in PSG are highlighted. On the bottom we also show a sample calculation of Averaging Kernels of the atmospheric temperature profile. Since these data are taken in Solar Occultation geometry at a specific altitude (13 [km]), the Averaging Kernels show that no information related to the temperature is present below that altitude, and that most of the information is concentrated in the proximity of the tangent altitude. PSG does not output the full a-posteriori covariance matrix, showing only the estimated uncertainty of each parameter (square root of the diagonal elements S). A summary of the quantities that are

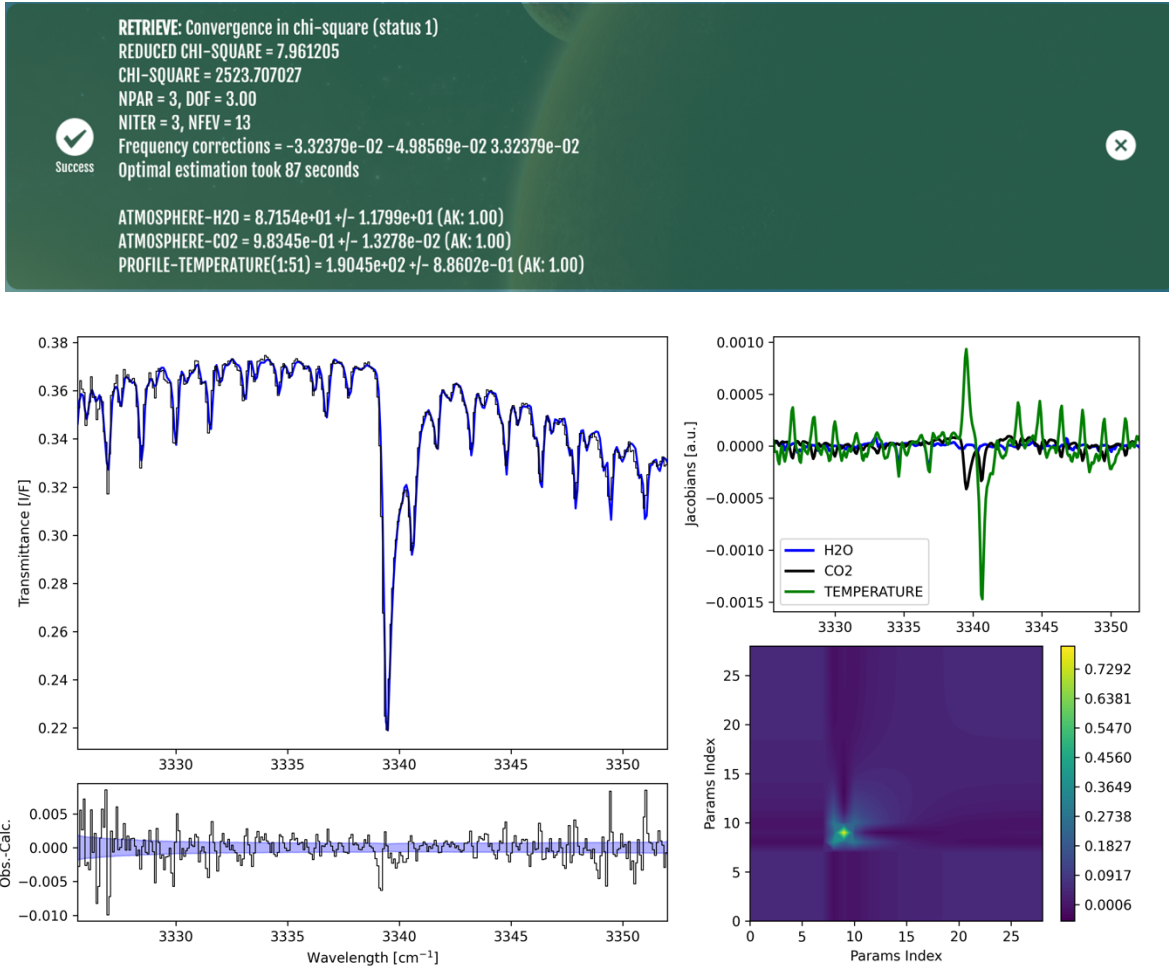


Figure 4. Sample results of a retrieval of water vapor, CO₂ column and average temperature along the line of sight for ExoMars NOMAD data (as in Liuzzi et al., 2021). **Top:** summary of the retrieved values and the main metrics computed by PSG. **Middle left:** data R (black) and best fit model f (blue). **Bottom left:** spectral residuals (black) and noise envelope ϵ_R (blue). **Middle right:** Jacobians, a.k.a. the derivatives of the model with respect to the parameters to retrieve (lines of the matrix K). **Bottom right:** Averaging Kernels of the temperature profile.

provided in output by PSG is given in Table 1. This serves as reference to interpret the results of a retrieval, to clarify what outputs are optional, and to have a clear idea of what is the optimal value of each quantity in relation to the quality of the data and resulting fit.

4. Retrieval of vertical profiles

Retrievals of vertical profiles can be quite more complicated than cases when OE is applied to retrieve scalar parameters across the full atmosphere. Complications arise essentially because of three reasons: (1) the retrieval of vertical profiles require a significant increase in the number of parameters to retrieve (hence in the computational load); (2) the vertical sensitivity of the data to the properties of the atmosphere may not necessarily be obvious, and could depend on the specific spectral interval and observation geometry; (3) the value of a specific parameter in an atmospheric layer depends on

the value of – at the very least – that parameter in nearby layers, and this must be properly accounted for in the OE equations. This is at the core of any *regularization* strategy, whose aim is to obtain physically meaningful vertical profiles of the specific parameter of interest. As an example, let us suppose that one wants to retrieve the vertical temperature profile of a terrestrial planet from nadir observations. The same data could be as well represented by a smooth vertical profile centered around an average value, but also by a vertical profile with large unphysical fluctuations, layer by layer, around the same average value. The objective of regularization is to correctly establish the solution filtering unphysical fluctuations out, yielding a profile at a desired vertical resolution.

There is a variety of methods for regularization of vertical profiles, based either on weighing the information from different spectral intervals (e.g., Serio et al., 2016), or on a-posteriori smoothing of the solution (e.g., Quémerais et al., 2006). The latter approach is particularly useful to limit unphysical and amplified oscillations in the retrieved profile, by imposing a smoothness constraint which will decrease the effect of the noise in the profile. At the core of any regularization there is a proper choice of the covariance matrix S_a . It is particularly important that S_a is structured to contain all the information related to the expected variability of the vertical profiles of the parameters to retrieve, and properly enhances the elements of the profile to which the data are less sensitive to. This last specific aspect will depend on the observation geometry and the wavelength of the observation.

As an example, let us consider the case of data acquired in nadir-looking geometry, and that one wants to retrieve the vertical profiles of temperature and of a specific gas, together with n scalar parameters (i.e., column amounts of other gases, aerosols, or surface temperature). If possible, a full covariance matrix for these parameters could be derived directly from climatology or circulation models, by selecting a subset of locations and times, and computing the covariance of the vertical profiles and scalar parameters of interest. This approach would also account for correlations between different parameters and profiles, producing a non-diagonal covariance matrix, and it is customary in many Earth science applications (e. g., Masiello & Serio (2013); Yang & Liu (2019)). In absence of climatology-specific a-priori information about the covariance of the profiles, S_a takes the form of a block-diagonal matrix, that for the specific example considered here has the following structure:

$$S_a = \begin{pmatrix} S_T & \mathbf{0} & \mathbf{0} \\ \mathbf{0} & S_{gas} & \mathbf{0} \\ \mathbf{0} & \mathbf{0} & \begin{matrix} s_1 & \cdots & 0 \\ \vdots & \ddots & \vdots \\ 0 & \cdots & s_n \end{matrix} \end{pmatrix} \quad (6)$$

where the values $s_{i=1,\dots,n}$ represent the variances of the scalar parameters, S_T is the covariance matrix of the temperature profile, and S_{gas} is the covariance matrix of the gas profile, both of them matrices of size $n_L \times n_L$, where n_L is the number of atmospheric layers on which the profile is retrieved. To regularize retrievals, these two matrices need to be structured in a way that each atmospheric layer has some degree of dependency from the nearby layers. A good way to do that is to assign a Markovian formalism to these matrices (as done, e. g., in Irwin et al. (2008); Serio et al. (2019)), such that their elements of S_T (or S_{gas}) can be written as:

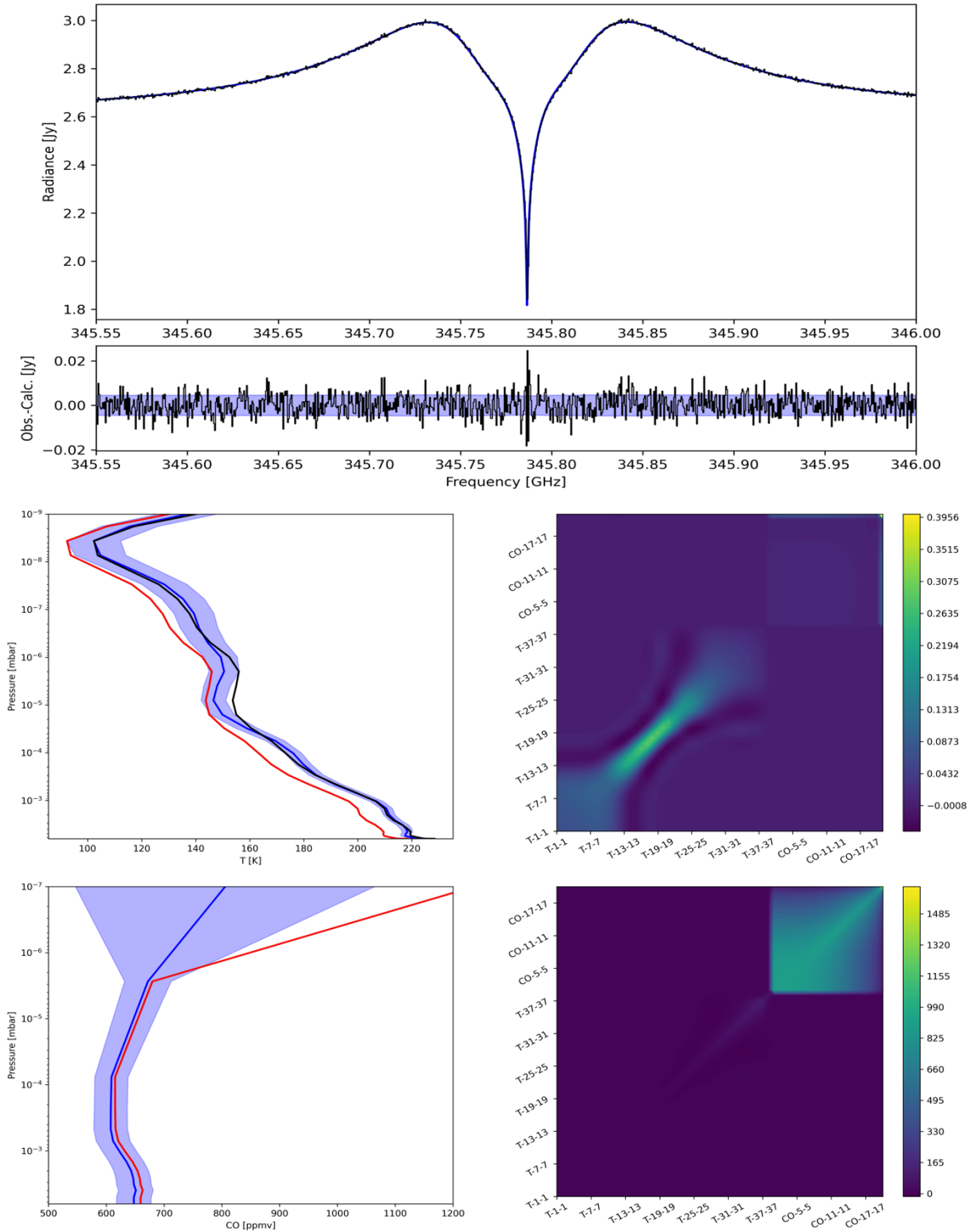


Figure 5: Vertical profile retrievals with PSG. **Top:** best fit to simulated ALMA data (black) and residuals on the bottom compared to the simulated noise. **Bottom left:** vertical profiles of temperature and CO: true (black), first guess and background (coincident: red) and retrieved with error bars (blue with the shaded area). **Bottom right:** a-posteriori Averaging Kernel matrix (top), and covariance matrix (bottom). It can be seen the block structure divided between the temperature profile (also on the axis with the layer number) and the CO one. The latter is less constrained (lower A values, higher covariance).

$$S_{ij} = (S_{ii}S_{jj})^{1/2} \cdot \exp \left(-\frac{|\log(p_i/p_j)|}{\alpha} \right) \quad (7)$$

where S_{ii} is the variance assigned to the parameter in the i -th layer, p_i the pressure of that layer, and α is a scaling factor that defines the scale of the correlation between nearby layers, in units of atmospheric scale heights. The higher the value of α , the more the profile will be vertically correlated and tend to a constant with altitude. Typical choices of α are around 1.5 for most temperature profiles, while there are also cases in which alpha varies with the pressure itself to account for expected local steep gradients of the profile to retrieve. The values of S_{ii} instead, depend strictly on the nature of the parameter (its vertical variability), the observation geometry (e.g., nadir vs. looking up), and the specific wavelength (i.e., the expected information content) of the observation. According to these aspects, one could choose to increase the standard deviation values with the altitude, keep it constant, or decrease it, and this is a very problem-specific decision.

Without any further specific modification these terms can be plug into the OE retrieval equations to obtain a solution. An example of retrieval is given in Figure 5, where a vertical profile of temperature and CO is retrieved from simulated ALMA observations of a CO line of Mars. It can be seen that the T vertical profile is well constrained to the true one, and because the CO and T are heavily interdependent, it is difficult to obtain vertically resolved CO measurements. This is also indicated by the Averaging Kernel matrix, which shows low information content for CO.

5. Nested retrievals: principles

The mathematical basis of OE theory is centered on the idea that a solution for the geophysical parameters can be sought by exploiting a-priori information derived from circulation models or other sources of knowledge. The a-priori plays an essential role in driving the solution to the most likely one and in the way the parameter space is explored, and when no reliable a-priori information is available, or when the First Guess is poorly constrained, OE can struggle in finding a physical solution. In these cases, other approaches that rely less on a-priori knowledge, can be adopted to explore the parameter space. A large class of these models are based on randomly sampling the parameter space, to iteratively establish a region of likely solutions. While the OE seeks to minimize the number of iterations and maximizes the constraints to get to the solution, such statistical methods use large numbers of random realizations in the parameter space with little to no a-priori constraints.

The simplest framework in this sense is the Markov-Chain Monte-Carlo (MCMC, see van Ravenzwaaij et al. (2018)). A Monte-Carlo approach consists in drawing several random samples from a normal distribution and calculate their sample average. The benefit of working in this way is that, instead of computing the mean from the distribution properties, which may be unknown, the mean is computed directly by probing its statistical properties. The Markov-Chain property of MCMC, instead, consists in generating the random samples in a specific sequential framework: each random sample is in fact the steppingstone to draw the following random sample (therefore, the

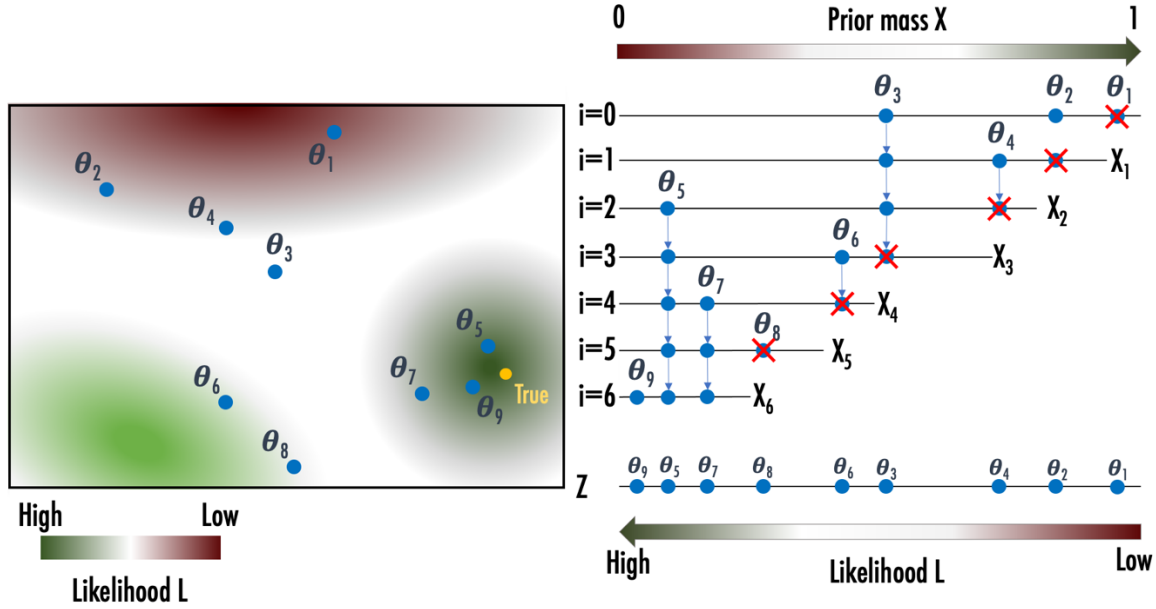


Figure 6: Schematic representation of the NS method. On the left, a simple parameter space (two-dimensional, $N=2$) is represented, in which the solution (yellow) is in a high-likelihood region (color scale on the bottom). On the right, it is shown how high likelihood regions correspond to low mass ones and vice versa. At initialization, the scheme is started with $n=3$ live points, each one characterized by a set of parameters θ_j . At each iteration, the lowest-likelihood point is replaced with a new one, until convergence. Adapted from Skilling (2006).

chain). The “Markov” property of the chain is that each new sample depends on the previous one, but new samples are independent of any samples before the previous.

As said, MCMC comes particularly in handy in Bayesian inference, because MCMC is focused on posterior distributions which are often difficult to handle by analytic examination (van Ravenzwaaij et al., 2018). In this sense, MCMC allows the user to approximate aspects of posterior distributions that cannot be directly calculated. If we consider the context of planetary observation, Bayesian inference uses the *information* provided about a set of planetary parameters, that is the *likelihood*, to update a prior state of beliefs about those parameters to become a posterior state of knowledge about them. The fact that many samples are drawn allows to evaluate the likelihood on the average of them and to estimate their standard deviation as an analog for uncertainty.

Let us continue to consider only the problem of retrieving planetary parameters from observed spectra. The MCMC essentially performs a walk, point by point, from an initial random realization of the parameters to the final solution. Depending on the number of parameters and the complexity of the radiative transfer, the convergence of the MCMC to a solution could be quite slow and require many iterations. With time, several more refined approaches have been resorted to make MCMC more efficient. One way to do that is to initialize the exploration of the parameter space with a larger number of points, and then use them to iteratively increase the likelihood of their average. This is the basic principle behind *nested sampling* (NS, Skilling, 2006). Let us introduce some elements of the NS; first, let us indicate with θ a set of N parameters (e.g., atmospheric and

surface parameters of interest), and with D the M -dimensional observed data array (a spectrum). Let us also indicate with H some model or hypothesis for the data D . This is clearly the nexus between data and parameters.

According to the Bayes' theorem:

$$\Pr(\theta|D, H) = \frac{\Pr(D|\theta, H) \Pr(\theta|H)}{\Pr(D|H)} = \frac{L(\theta)\pi(\theta)}{Z} = P(\theta) \quad (8)$$

where:

- $\Pr(\theta|D, H)$ is the posterior probability distribution of the parameters θ , given the data D . This represents also the final result of the retrieval, and can be synthetically indicated with $P(\theta)$.
- $\Pr(D|\theta, H)$ is the likelihood of the data D given the parameters θ , and responds to the question: how likely are the data D to be reproduced by the parameters θ with the model hypothesis H ? It can be indicated with $L(\theta)$. *To trace a parallel with OE, this has a similar role as the cost function, or a chi-square.*
- $\Pr(\theta|H)$ is the prior state of knowledge of the parameters θ before analyzing the data. For example, it can be an N -dimensional uniform distribution limited by ranges in which the parameters are searched, and it can be indicated with $p(\theta)$.
- $\Pr(D|H)$ is the evidence. This is a key quantity in NS, as it represents not only a normalization factor for the posteriors, but also a natural quantification of the progression of NS retrievals through the solution, as it inherently tells how well data D are reproduced under hypotheses H . It is commonly indicated with Z .

The question that NS tries to answer is: which set of models best describe the data? The key quantity to get to an answer is the evidence Z . From Eq. (8), for a set of models θ , Z can be defined as:

$$Z = \int L(\theta)\pi(\theta)d\theta \quad (9)$$

which is particularly challenging given the multi-dimensionality of the problem. To limit this complexity, NS starts from n initial models, each one specified by a set of planetary parameters $\{\theta\}_{i=1,\dots,n}$ sampled from the prior distribution. For these initial set of models, let us compute their hyper-volume X in the parameter space including only those sets of parameters whose likelihood is above a certain threshold L' :

$$X(L') = \int_{L(\theta) > L'} \pi(\theta)d\theta \quad (2)$$

This integral sometimes is also referred to as (*cumulant*) *prior mass* including all likelihood values greater than L' . If one imagines the variable L' to increase, the integral in Eq. (10) goes from 1 to 0 (because of the normalization in Eq. (8) that is not explicitly reported). The introduction of the prior mass allows to simplify greatly the calculation of Z , which now becomes a one-dimensional integral:



$$Z = \int_0^1 L(X) dX \quad (3)$$

In this way, also, the problem regularizes naturally, as the likelihood calculation is not done on single samples, but on volumes in the parameter space, making L a monotonic, well-behaved function. Its integration then becomes easy to discretize as a sum over finite elements in the space of mass X . The NS objective becomes to modify in successive steps the initial sample to increase the evidence, and given the relation established between X and the parameter space $\pi(\theta)$, this can be done in one of the two spaces equivalently. The basic scheme of NS to work this out is summarized in the following and illustrated graphically in Figure 6, which can be compared to Figure 1 for OE.

- Start with n initial sets of parameters $\{\theta\}_{j=1,\dots,n}$ randomly from the parameter space $\pi(\theta)$.
- Set the initial conditions: $i=0$; $X_0=1$; $Z=0$ (or a very small value).

Until convergence is reached:

- Calculate the likelihoods $\{L\}_{j=1,\dots,n}$ of $\{\theta\}_{j=1,\dots,n}$ and record the lowest likelihood L_i . Eliminate this point from the sample.
- Under the hypothesis that the mass function is of gaussian form, with most of the mass concentrated in a small region of the parameter space, set $X_i = e^{-i/n}$. One can also not consider this hypothesis and directly compute Eq. (10) by sampling the parameter space.
- Because the lowest-likelihood point has been canceled out from the sample, one needs to compute how much the evidence has increased from this cancellation. Using the discrete form of (12), one calculates the finite element $\Delta X_i = w_i = (X_{i-1} - X_{i+1})/2$. Then, the evidence is increased by $L_i w_i$.
- Now the lowest-likelihood point is replaced with a new one, which is drawn from the prior distribution $\pi(\theta)$ with the condition that its likelihood is higher than L_i .

At the end, the evidence Z can be incremented by $n^{-1}[L(\theta_1) + L(\theta_2) + \dots + L(\theta_n)]X_i$, to account for the missing intervals in the integral in (11) for all the surviving points in the parameter space. However, this last adjustment is usually less important if either the number of samples n is large, or if the number of steps to convergence is large.

There are two important aspects to clarify about NS mechanics: the choice of the convergence criterion and the choice of the likelihood functional form. For the first one, while the simplest choice would be to terminate NS when a certain number of iterations n is reached, there are much cleverer possible choices that account for the statistical properties of the evidence Z and the likelihood of the samples. While there are no universally valid conditions to terminate NS that ensures always to find the “best” solution, the general idea is to have a condition that translate into “continue the NS iterations until most of the evidence Z has been found” (Skilling, 2006). Two possible criteria to satisfy this are the following:

- Continue until even the largest current likelihood, taken over the current X_i , would not increase the current evidence by more than some small fraction (chosen by the user) α :
 $\max(L_1, \dots, L_n)X_i < \alpha Z_i$

- If an upper bound to the likelihood can be found (or is plausible) and can be quantified with L_{up} , a possible stopping condition would be given by $L_{\text{up}}X_i < \alpha Z_i$. This is particularly applicable in a planetary context, when a tolerance could be established by estimating the noise affecting the observations and used to estimate the maximum likelihood achievable.

The second problem is the definition of the likelihood. As said before, the likelihood could be considered the equivalent of a cost function for OE. Using the same notations adopted for OE, in the context of retrieving planetary parameters from observed spectra a commonly adopted form for the likelihood is using its log (Feroz and Hobson, 2008), as follows:

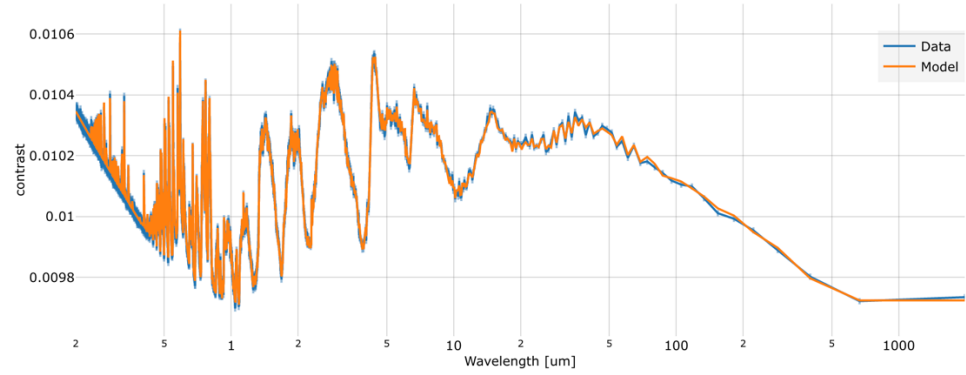
$$L = -\frac{1}{2}\chi^2 - \sqrt{2\pi} \sum_{i=1}^M \sigma_i \quad (4)$$

6. MultiNest and its implementation: PSGnest

The theory of NS and Bayesian retrievals more in general can be greatly refined and improved under many aspects, which have to do with the way in which the sampling is performed, and samples are selected towards convergence. It is known that NS becomes highly inefficient for multimodal posteriors, namely cases where regions of comparable (high) likelihood exist in the parameter space. This led to introducing the notion of clustered nested sampling (Shaw et al., 2007), in which multiple modes in the posterior are detected and defined, and distinct ellipsoidal bounds are constructed around each one of them (Feroz and Hobson, 2008). This approach has a significant positive impact on the sampling efficiency. On this work, Feroz built the MultiNest model (Feroz et al., 2009), which is the standard for nesting algorithms applied to cosmology and planetary science.

Compared to the initial work by Skilling, MultiNest can handle cases like the one schematized in Figure 6 more efficiently, as it is able to identify multiple regions of local maximum likelihood, each one corresponding to a degenerate solution. This is usually done by inserting additional steps in the NS basic scheme, which consist in identifying distinct clusters of live points that are well separated and constructing an individual ellipsoid for each cluster. The fact that the evidence is linear allows to consider each cluster individually and sum the single contributions, provided the correct assignment of prior volumes to each cluster and region of maximum likelihood (Feroz and Hobson, 2008).

In PSG, the tool PSGnest (<https://psg.gsfc.nasa.gov/apps/psgnest.php>) implements the most recent version of MultiNest, and is designed to analyze any kind of planetary data, with particular attention for exoplanets, for which NS is particularly suitable given the frequent lack of background information. Retrievals of exoplanetary parameters usually require tens to hundreds of live points and many iterations, yielding a total of sampled sets of parameters of the order of several thousands. Such large number make it somewhat impractical to compute the spectra corresponding to the sampled parameters using a full radiative transfer model in real time.



```

Computation time [seconds]: 54
Live points: 100
Parameters: 6
Acceptance Rate: 0.149668
Replacements: 4232
Total samples: 28276
Nested Sampling Global Log-Evidence: 50373.805595
Nested Importance Sampling Global Log-Evidence: 50334.856728 +/- 0.600647

```

Param No.	Mean	+/-	1-sigma	best-fit (maxlike)	MAP parameter
Temperature	1.3999e+03	+/-	2.7568e-01	1.4001e+03	1.4000e+03
Gravity	1.0007e+01	+/-	1.6840e-02	9.9973e+00	9.9954e+00
Metallicity	9.9670e-01	+/-	3.5143e-03	9.9644e-01	9.9466e-01
C/O	5.5940e-01	+/-	8.8455e-04	5.5941e-01	5.6000e-01
log(Haze)	1.0003e+00	+/-	1.0665e-03	1.0002e+00	9.9976e-01
Cloud	6.1107e-02	+/-	2.4286e-03	6.0806e-02	6.1860e-02

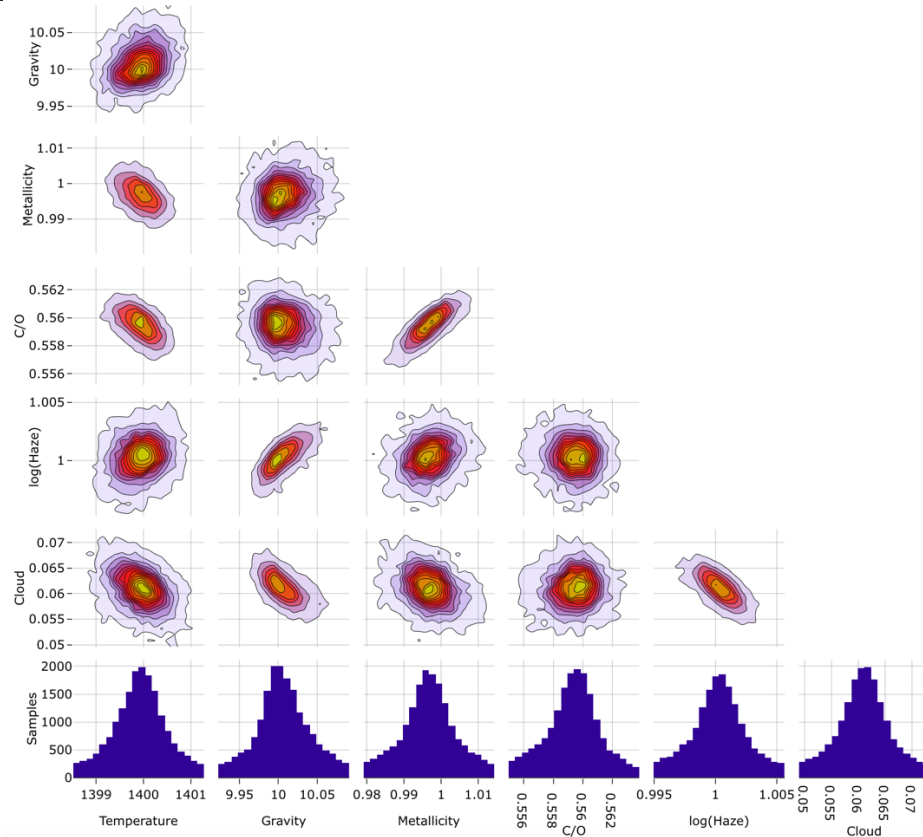


Figure 7: Example of retrieval with PSGnest of a gas-rich exoplanet using the ATMO grid. **Top:** spectrum and best fit (orange). **Middle:** list of retrieved parameters and their uncertainty, evidence, and runtime. **Bottom:** typical corner-plot used to represent posterior distribution of sampled points.

For this reason, it is common to apply this technique drawing the samples from a pre-computed set of spectra organized in the form of a grid. More specifically, once a sample set of parameters θ_j is drawn, PSGnest performs a tri-linear interpolation within the grid to compute an interpolated spectrum corresponding to θ_j . As long as the grid points are distributed in such a way that their variation between couples of them has an effect almost linear on the radiance, this is an effective way to produce synthetic radiances without the need of working directly with radiative transfer. Examples of widely used grids include the ATMO grid (Goyal et al., 2018) applicable to transit observations of giants.

PSGnest provides in output the log evidence $\log(Z)$, the output parameters and their uncertainties, which are estimated from the posterior distribution of the sampled points and their standard deviation. An example of results is shown in Figure 7 on a synthetic spectrum of a hot Jupiter using the ATMO grid (Goyal et al., 2018). The PSGnest can capture multimodal solutions as they occur in exploring the parameter space.



Planetary Spectrum Generator
National Aeronautics and Space Administration

Chapter 10: **Application Program Interface (API) and Installation**

**Villanueva, Liuzzi and
PSG team**



1. Application Program Interface

PSG allows to perform operations remotely by employing a versatile online Application Program Interface (API). The API operates by sending a configuration file to the PSG servers, that can be modified on the user local machine as needed. Upon reception of the configuration file, PSG will compute the spectra and send back the planetary spectra. The great value of the API is that the user does not need to install / update the radiative transfer modules and databases on his/her computer, and by simply performing a 'curl' command, the user will run the simulations on high-performance NASA servers.

The configuration file is a relaxed form of XML (eXtensible Markup Language), the now preferred file type across applications. The spectrum is provided in standard ASCII columns. The resulting units for the columns can be defined with the configuration XML file, while which type of data to provide (e.g., radiance, transmittance, noise) is provided by a POST command.

The communication with the server is performed via HTTPS, and this can be implemented via the 'curl' terminal command. A single line of 'curl', in which the user inputs are provided via a config.txt (example) will lead to spectra. The figure below better explains the inner workings of the PSG modules, and how the user can enable / disable the different modules, and request for different spectral outputs.

2. Calling the API

To compute spectra, one first needs to create / modify a PSG configuration file. The user can choose to edit this file with any text editor or scripting language.

1. Obtain a template configuration file (e.g., config.txt). The easiest way to obtain a configuration file is by parameterizing PSG via the web interface until a desired spectrum is obtained. On the main page of PSG, then click on "Download config-file", this will download the XML configuration file.

2. Modify the config.txt configuration file using a text-editor (e.g. J-edit, Atom, etc), or by using any scripting / programming language. In order to understand what each parameter means, please refer to the PSG documentation.

3. Open a terminal window and type the following command:

```
curl --data-urlencode file@config.txt https://psg.gsfc.nasa.gov/api.php
```

4. By default, the API will run all PSG modules employing this configuration file, and will return the total radiance spectra (**rad** file). One can run only certain modules and request for a different type of spectral output. This is achieved by providing several POST keywords (see section 4). For instance:

To return planetary transmittances (**trn** file) without the header information:



```
curl -d type=trn -d whdr=n --data-urlencode file@config.txt
https://psg.gsfc.nasa.gov/api.php
```

To return only stellar (**str** file) transmittances (the API will only run the module 'continuum'):

```
curl -d type=str --data-urlencode file@config.txt https://psg.gsfc.nasa.gov/api.php
```

5. With the API, the user can also compute ephemerides and/or atmospheric parameters. For instance:

a) Create a text file config.txt with this content:

```
<OBJECT-DATE>2017/01/15 14:30
<OBJECT-NAME>Mars
<GEOMETRY-REF>MRO[74]
```

b) Call the API with this command:

```
curl -d type=cfg -d wephm=y -d watm=y --data-urlencode file@config.txt
https://psg.gsfc.nasa.gov/api.php
```

3. Installing a personal version of PSG in your computer

The user can also install and run a local version of PSG via a virtualization system. PSG is a complex suite of spectroscopic models and databases, coordinated by a general radiative-transfer scheme. Installing the whole suite on a personal system can be a daunting process and would entail a great deal of resources / memory / time. Instead, by employing a virtualization system, the user is saved from this complexity and can easily install a pre-configured Virtual Machine with PSG that provides web/API access as the normal PSG suite.

Fully free: PSG is installable employing the no-cost Docker Engine, which is an open-source containerization technology for building and virtualizing applications. Docker engine is fully free and licensed under the open-source Apache license. To enable the Docker Engine on your machine, you can use the also free Rancher Desktop application, which is open-source and licensed under the public Apache license. Alternatively, Docker Desktop is free for personal use, yet users from large organizations users require a paid license. We encourage users to employ the free and open-source Rancher Desktop and Docker Engine configuration when possible.

In order to provide flexibility, the PSG personal suite is organized in packages. By default, the personal suite of PSG comes with the PROGRAMS and BASE packages, yet the user can install many additional packages, expanding the capabilities of the local version. Specifically, the correlated-k tables for low/moderate spectral resolutions can be quite large, and should be installed only when strictly necessary. The local PSG site also keeps track of any updates of these packages with respect to the current PSG suite, and it will inform you if you are required to update the packages.

1. Install the free Docker Engine on your machine. If in Linux, this can be simply done by performing a 'yum install docker' in Centos/RHEL or with apt-get on Debian and others (more info):



```
yum install docker  
sudo systemctl start docker
```

In Macs or in Windows, you would need to install the Rancher Desktop application on your computer. This is relatively easy and it will establish a virtualization system in which PSG will run. When installing, make sure to select 'dockerd (moby)' for the container runtime, 'Automatic' for path configuration, disable 'Kubernetes', and importantly allow 'sudo access' so the application can properly install the Docker Engine. The application is downloadable at rancherdesktop.io



**Docker
Engine**



**Rancher
Desktop**

Virtualization system: PSG can run in any personal computer (Mac, Linux or Windows based) with the Docker engine and Rancher Desktop. Docker containers wrap up software and all its dependencies (including the operative system) into a standardized package that includes everything it needs to run: code, runtime, system tools and libraries. This guarantees that PSG will always run the same and Docker makes its installation as simple as pulling a container image. This also means that PSG can be easily deployed in cloud computing environments (e.g., Google Cloud, Amazon Web Services).

2. From the command line / terminal, enter the following commands to pull the PSG container from the publicly available Docker hub repository:

```
docker logout  
docker pull nasapsg/psg  
docker tag nasapsg/psg psg
```

3. To run PSG and enable its API interface (add the keyword '--restart always' to keep PSG always running, even after re-booting):

```
docker run -d --name psg -p 3000:80 psg
```

4. To visit the local site of PSG, open your browser and go to **http://localhost:3000**, while to run the local version of the Application-Program-Interface (API), enter the following command:

```
curl --data-urlencode file@config.txt http://localhost:3000/api.php
```

5. The user can install, upgrade and remove packages by visiting **http://localhost:3000**. For performing this from the command line (e.g., inside a VM instance) follow these commands (where 'package' is the package name, all in lower case):

```
curl http://localhost:3000/index.php?install=package  
curl http://localhost:3000/index.php?update=package  
curl http://localhost:3000/index.php?remove=package
```




Some useful docker commands are:

<code>docker stop psg</code>	Stops the current PSG container.
<code>docker restart psg</code>	Restarts the PSG service.
<code>docker start psg</code>	Starts the PSG service if stopped.
<code>docker rm psg</code>	Removes the current container of PSG from docker memory. This operation deletes all updates/installed packages since its initial run, and resets PSG.
<code>docker ps -a</code>	Lists the status (e.g., stopped, started, exited) of all currently available containers. Containers cannot be re-run if they have already been created and therefore appear in this list (independently of the status). Restart, if necessary, while if the user wants to reset PSG to its original image, remove the container (<code>docker rm</code>) and re-run it (<code>docker run</code>).
<code>docker image ls</code>	Lists all the available docker images. The user can spawn multiple instances/containers from the same image. When the user pulls the PSG image from the docker hub, then this image will appear in this list.
<code>docker image rm psg</code>	Deletes the PSG image from memory. Any new PSG container/instance will require a re-pull of the image from the docker hub.
<code>docker system prune -af</code>	Deletes all images and containers/instances from docker memory, fully resetting docker.

4. Types of planetary spectra and special keywords

Requested spectra (type keyword)	
rad	Integrated fluxes, incorporating all planetary and stellar transmittances, and considering the specific instrument / observatory parameters. This file is computed by the module generator. This is the default output setting.
noi	Synthetic observational noise, including the noise introduced by the planet itself, its star (if present within the field), background sources (e.g., exozodii, local zodiacal dust, CMB), the terrestrial atmosphere (if observing from ground), and the instrument performance. This file is computed by the module generator.
trn	Integrated planetary transmittance spectra, including all geometry considerations and requested atmospheric parameters. This file is computed by the module PUMAS only.



atm	Integrated planetary fluxes as observed at the planet in units of $[W/m^2/sr/um]$. This file is computed by the modules PUMAS and CEM.
str	Stellar transmittance spectrum. This file is computed by the module continuum.
tel	Terrestrial transmittance spectrum (telluric).
srf	Surface reflectance and emissivity spectra. This file is computed by the module continuum.
cfg	The API will return the updated configuration file. This file is computed by the modules geometry and atmosphere.
ret	The API will perform a retrieval on the provided data and return all output and input files.
all	This keyword will return all the resulting spectra, and the configuration file.

Requested spectra (type keyword)

wgeo	The geometry module computes the observational angles (GEOMETRY-SOLAR-ANGLE, GEOMETRY-OBS-ANGLE) and the beam/planet ratio (GEOMETRY-PLANET-FRACTION) employing the geometry information provided by the user in the XML configuration file. For exoplanets, it also computes the planet transit factor (GEOMETRY-STAR-FRACTION), and the planet-star distance (GEOMETRY-STAR-DISTANCE). This information is then saved into the configuration file to be used by the other modules. The default is wgeo=y, yet one can disable this computation with wgeo=n.
wephm	This keyword enables the calculation of ephemeris parameters based on the object name and the provided date: <ul style="list-style-type: none">• wephm=y computes ephemeris for the date provided.• wephm=N computes ephemeris for the current date/time.• wephm=T for exoplanets, it searches the next primary transit event, while for Solar System bodies it computes the ephemeris for [date - one day].• wephm=S for exoplanets, it searches the next secondary transit event, while for Solar System bodies it computes the ephemeris for [date + one day].• wephm=P for exoplanets, it searches the next periastron event.• wephm=n disables the ephemerides module (<i>default</i>).
watm	This keyword enables / disables the atmosphere module - Default watm=n.
whdr	This keyword allows to disable outputting the header information - Default whdr=y.
app	Name of the PSG app to call (e.g., globes)



5. Architecture of the API system and setting up a cluster system

The basic principles of remote operation via the API allow for expansion and adaption to a broad range of operational regimes (see Figure 1). As discussed before, the operation of the public PSG server and of the installable Docker version is the same, with only changing the URL in the curl command. The Docker operational scheme can be viewed as a layering system, in which the PSG Docker service “layer” sits above the user’s computer operative system (OS). The interface with the system is done via http ports in all cases. The default port of any http request is via port 80, and in many cases, the local computers may already have a http server running on them (e.g., Apache daemons) or have other services operating at other ports. That is why the PSG Docker system is configured to employ a high port number as default (3000), to avoid interface with local IP ports on the computer. The PSG public server employs Secure Sockets Layer (SSL) certificates for enhanced security, and that is why the communication is done via the encrypted “https” protocol, and not via the classical “http” protocol.

The PSG API commands have been designed to allow for maximum control of the PSG Docker instances, allowing for further automation of the system. For instance, one can have many machines running PSG Docker and organize for them to analyze spectra and data in a coordinated manner. Orchestrating many Docker machines is not a trivial process, and some architectures do exist, such as Kubernetes, yet they can be complex to setup and their configuration for running PSG instances would involve a further layer of customization and setup. For that purpose, we have developed a PSG cluster management tool and integrated it to the PSG Docker service (see Figure 2). The tool is accessible at the page “cluster.php” and it is password (default is “cluster”) controlled to allow for secure remote access.

The manager does not run PSG calculations itself but organizes and sends API requests to the workers in a coordinated manner. The PSG instances should have an operating Docker server with PSG running on them. Their IP or name should be accessible to the manager, since their communication is done via the PSG API protocol. All input config files and resulting files are stored on the manager, so make sure the manager has enough hard-drive resources. The PSG instances need to have enough memory to handle the packages, and at least 8 cores is recommended, in order to take advantage of the multi-threading capabilities of PSG.

The system is configured by providing a list of accessible IP addresses and a tarball containing all the configuration files to process. Only files with extensions “cfg”, “txt” and “set” will be processed. The configs with extension “set” will force a “type=set” API call for those files, while for the others the selected type in the GUI will be used. The manager will uncompress/unpack this tarball, and sequentially go through all the files in the package by sending it to any available machine in the list of PSG computers. The manager keeps track of which machine is free and operating and removes machines from the list if they fail to return valid outputs upon an API call. The GUI to the manager allows to define specifics about the particular batch of PSG operations, types of desired outputs, special keywords and to select specific modules and apps. It is important to note that the manager operations are done via PSG API commands, so no detailed administration of the workers is possible from the manager GUI. One would need to administer them from the specific computer

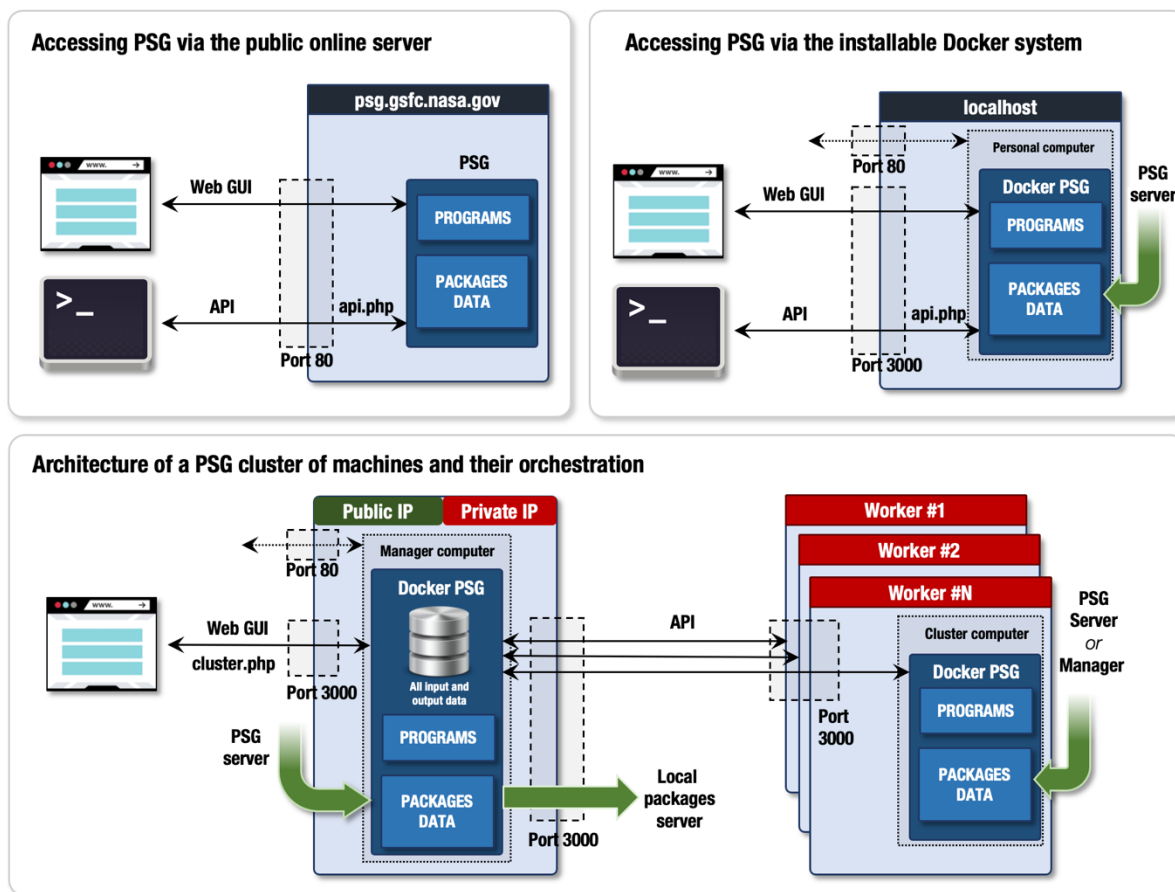



Figure 1: Architectures of three possible PSG configurations controlled via web GUI and API commands: for running the public online server (**upper-left**), for operating locally via the installable Docker system (**upper-right**), and for handling a cluster of PSG machines (**lower panel**). In all cases, the control is done via the HTTP protocol, yet using different ports (80 or 3000), IP addresses, and encryption schemes (e.g., with or without SSL certificates). In a cluster architecture, the manager and workers all operate within a closed intranet network with private IP addresses, yet the manager has an open port with a public address that allow access to the cluster from anywhere in the world. The systems are kept up to date with the latest PSG developments by the installation / update / removal of spectroscopic packages.

management tool, AWS as described in the next section, or via bash commands with password access to the workers.

An optimum way to handle many workers is to give them a sequential name (e.g., psgworker-1, psgworker-2), so they can all be controlled via a single command from the manager. As such, the pdsh Linux command is quite powerful for this, since pdsh being a variant of the remote shell rsh, pdsh can run multiple remote commands in parallel. Below we provide some common commands that can be done sent from the terminal of the manager:





Planetary Spectrum Generator

Cluster Manager

Logout
Change password

This is the *cluster manager* application of the Planetary Spectrum Generator (PSG) tool. It allows to orchestrate and manage a cluster of PSG Docker machines, and to perform coordinated and batch processing of simulations and retrievals.

The PSG instances should have an operating Docker server with PSG running on them. Their IP or name should be accessible to the manager, since their communication is done via the PSG API protocol. All input config files and resulting files are stored on the manager, so make sure the manager has enough hard-drive resources. The PSG instances need to have enough memory to handle the packages, and at least 8 cores is recommended, in order to take advantage of the multi-threading capabilities of PSG.

Type of desired output: ret - Perform retrievals
Application: PSG - No specific app

Geometry module: ☐
Include headers: ☒
Update atmosphere: ☐

Update ephemeris: n - Do not update planet/star parameters

Additional keywords:

Required packages: ATMOSPHERES Add PROGRAMS X BASE X

Check status
Update workers
Upload list of workers

Use local packages: ☒

Last updated: 12/Jan/2022 22:54

psgworker-1	Active	PROGRAMS_2022-01-12	BASE_2022-01-12
psgworker-2	Active	PROGRAMS_2022-01-12	BASE_2022-01-12

Figure 2: Example of the PSG cluster management interface. The user can select what specific PSG modules to run and which packages to use. The tool also permits to handle and update the packages on the workers and keeps track of their functionality when performing orchestrated operations.

```
pdsh -w centos@psgworker-[1-10] systemctl start docker.service
pdsh -w centos@psgworker-[1-10] docker start psg

pdsh -w centos@psgworker-[1-10] docker stop psg
pdsh -w centos@psgworker-[1-10] yum -y update --skip-broken
pdsh -w centos@psgworker-[1-10] shutdown -r now

pdsh -w centos@psgworker-[1-10] systemctl start docker.service
pdsh -w centos@psgworker-[1-10] docker stop psg
pdsh -w centos@psgworker-[1-10] docker system prune -af
pdsh -w centos@psgworker-[1-10] docker logout
pdsh -w centos@psgworker-[1-10] docker pull nasapsg/psg
pdsh -w centos@psgworker-[1-10] docker tag nasapsg/psg psg
pdsh -w centos@psgworker-[1-10] docker run -d --restart always --name psg -p
3000:80 psg
```



6. Setting up a PSG cluster system with AWS

As an example on how to setup a cluster system with PSG machines, we describe in this section how to setup a system with the Amazon Web Services (AWS), yet the same principles can be implemented on many other computational networks. AWS is a collection of computational, storage and web services that allow registered users to perform a wide array of tasks that require scalable and flexible computing resources. In the following paragraphs, we present a series of instructions and indications to work with the EC2 (Elastic Compute Cloud) resources and see how to setup a series of instances.

AWS offers the possibility to create a Free-Tier account as a starting point to learn how to use the AWS resources and to use the basic tier of those resources. To create an AWS account, the user needs to go on the AWS portal and follow the steps of the automated procedure. Once the account is created, it is time to do the first login. By default, the creation of the AWS account does not come with pre-defined users, therefore we need to define them. The starting point is to login as a root user only for the first login. For the following times, logging as root is generally not recommended, as for the inexperienced user this could result into taking unwanted actions. Once logged in, the user needs to create the first administrator IAM user, which will use to login all the other times. It is important to save the password, the user number (a 12-digit code), and the username (typically “Administrator” if the instructions are followed to the letter): those are the three things we will need to login anytime in the future.

6.1 Structurer of the AWS console and instances

Once logged in as admin, the console is our entry point to all the services offered by AWS. The console allows to control the creation of tasks, instances, repositories of memory, clusters, and to check the billing for the services used. From the console we can start creating a single EC2 instance. All the instances we create form the Virtual Private Cloud (VPC) of the user. An instance works effectively as a machine with its own memory and computational resources. Every instance is assigned with:

- **A public IP address**, which makes the machine accessible from users as selected by the security groups (see later). By default, the public IP changes every time the instance is stopped and subsequently restarted.
- **A private IP**, which is not accessible from outside and is only used to communicate with eventual other instances in the VPC. This is static, meaning that once the machine is created, it does not change.

Every EC2 instance comes with basic software and tools already pre-installed, such as python3, and is fully ready to work with Docker containers and functionalities. To create an instance, let's start from the console and click on “Launch a virtual machine” in the “build a solution” panel.



Amazon Linux
Free tier eligible

Amazon Linux 2 AMI (HVM) - Kernel 5.10, SSD Volume Type - ami-0ed9277fb7eb570c9 (64-bit x86) / ami-0a1eddae0b7f0a79f (64-bit Arm)

Amazon Linux 2 comes with five years support. It provides Linux kernel 5.10 tuned for optimal performance on Amazon EC2, systemd 219, GCC 7.3, Glibc 2.26, Binutils 2.29.1, and the latest software packages through extras. This AMI is the successor of the Amazon Linux AMI that is now under maintenance only mode and has been removed from this wizard.

Root device type: ebs Virtualization type: hvm ENA Enabled: Yes

Select

☒ 64-bit (x86)
☐ 64-bit (Arm)

The first screen shows a list of possible architectures for the instance. Among all of them, in the free tier, an Amazon Linux 2 AMI is available at no charge. This configuration is the default one and is good for most basic tests and applications.

Currently selected: t2.micro (- ECUs, 1 vCPUs, 2.5 GHz, -, 1 GiB memory, EBS only)

	Family	Type	vCPUs	Memory (GiB)	Instance Storage (GB)	EBS-Optimized Available	Network Performance	IPv6 Support
<input type="checkbox"/>	t2	t2.nano	1	0.5	EBS only	-	Low to Moderate	Yes
<input checked="" type="checkbox"/>	t2	t2.micro <small>Free tier eligible</small>	1	1	EBS only	-	Low to Moderate	Yes

The second screen lets us choose the resources to use. They vary according to the type of application we want to build. The t2 micro instance comes for free and uses a basic, yet adequate configuration for most starting-level applications. A good guide for other types of applications can be found at the AWS site (<https://aws.amazon.com/ec2/instance-types/>).

Number of instances [Launch into Auto Scaling Group](#)

Purchasing option ☐ Request Spot instances

Network (default) [Create new VPC](#)

Subnet [Create new subnet](#)

Auto-assign Public IP

Hostname type

DNS Hostname

☒ Enable IP name IPv4 (A record) DNS requests

☒ Enable resource-based IPv4 (A record) DNS requests

☐ Enable resource-based IPv6 (AAAA record) DNS requests

Next, we choose the network settings. The first parameter is the number of instances, we can create as many as we want of the same type. Each one will be a machine with its own public and private IP. We can choose the VPC for the instance (typically the same for all of them, yet a user can have more than one VPC). If two instances belong to different VPCs, they will be able to communicate only through their public IP address, and not their private (more on this can be found later).

In the next screen (step 3) we can also choose to create an instance that comes with pre-installed software or some commands to be executed at its creation. For example, we would wish to create an



instance that comes with PSG already installed and running. To do that, on the bottom of the page there is a “User data” field. In the space, we can paste the code that we would use in a bash session:

```
#!/bin/bash
yum update -y
yum install docker -y
sudo service docker start
sudo docker pull nasapsg/psg
sudo docker tag nasapsg/psg psg
sudo docker run -d --name psg -p 3000:80 psg
echo 'sudo service docker start' >> /etc/rc.local
echo 'sudo docker start psg' >> /etc/rc.local
sudo chmod +x /etc/rc.d/rc.local
```

at startup, the machine will come with PSG already running on port 3000. The last 3 commands are used to paste in the file rc.local the instructions to restart the docker daemon and the PSG container anytime the instance is restarted after stopping.

Volume Type	Device	Snapshot	Size (GiB)	Volume Type	IOPS	Throughput (MB/s)	Delete on Termination	Encryption
Root	/dev/xvda		8	General Purpose SSD (gp2)	100 / 3000	N/A	<input checked="" type="checkbox"/>	Not Encrypt

We can then choose the storage amount for the instance. This is equivalent to choosing the amount of space that the machine has in the SSD. There is a 30 GB limitation in the free tier.

Inbound rules for sg-0c1ad65dfa2d317b0 (Selected security groups: sg-0c1ad65dfa2d317b0)				
Type	Protocol	Port Range	Source	Description
HTTP	TCP	80	0.0.0.0/0	
SSH	TCP	22	0.0.0.0/0	
Custom TCP Rule	TCP	3000	0.0.0.0/0	

Before launching the instance, we need to create a security group for the instance. This is crucial since it defines the rules and restrictions to access the instance. Configuring these rules depends only on what we want to do with the instance. For example, if we are not interested in running a website on the instance to be accessed with the https protocol, we won't need to add any HTTPS rule. Adding any extra rule other than those strictly needed will likely result in errors when trying to access the instance. The default given by AWS is the sole SSH, as that is the primary way to access an instance.



Select an existing key pair or create a new key pair

A key pair consists of a **public key** that AWS stores, and a **private key file** that you store. Together, they allow you to connect to your instance securely. For Windows AMIs, the private key file is required to obtain the password used to log into your instance. For Linux AMIs, the private key file allows you to securely SSH into your instance. Amazon EC2 supports ED25519 and RSA key pair types.

Note: The selected key pair will be added to the set of keys authorized for this instance. Learn more about [removing existing key pairs from a public AMI](#).

Choose an existing key pair

Select a key pair

myfirstkey | RSA

☐ I acknowledge that I have access to the corresponding private key file, and that without this file, I won't be able to log into my instance.

Cancel
Launch Instances

The above configuration is quite simple and suitable to run PSG on the instance, and it offers the possibility to access the instance via SSH, HTTP and a custom rule in TCP that opens the port 3000 to listen inbound traffic from any address (0.0.0.0/0).

The next screen gives a review of the properties and the possibility to edit them. Once clicking on “launch”, there is a last important step to complete. The AWS will ask either to generate a key for the instance, or to use a previously generated one. The key is our code of access to enter and use the instance via SSH, and it is possible to generate it and download it ONLY in this moment. For the creation of the first instance, we will need to create a key, and save it as a .pem file, which will be put in a secure location on our computer. For OSX and UNIX, a suitable secure location is ~/.ssh .

Instances (1/3) Info									
<div> <div>Search</div> <div> <div>Refresh</div> <div>Connect</div> <div>Instance state</div> <div>Actions</div> <div>Launch Instances</div> </div> </div>									
	Name	Instance ID	Instance state	Instance type	Status check	Alarm status	Availability Zone	Publ	
<input checked="" type="checkbox"/>	Original		Running	t2.micro	2/2 checks passed	No alarms	us-east-1d	ec2-	
<input type="checkbox"/>	Clone1		Stopped	t2.micro	-	No alarms	us-east-1d	-	
<input type="checkbox"/>	Clone2		Stopped	t2.micro	-	No alarms	us-east-1d	-	



Instance summary for [redacted] **(Original)** [Info](#)

[Refresh](#) [Connect](#) [Instance state ▼](#) [Actions ▼](#)

Instance ID
[redacted] (Original)

IPv6 address
-

Hostname type
IP name: ip-[redacted].ec2.internal

Instance type
t2.micro

AWS Compute Optimizer finding
① Opt-in to AWS Compute Optimizer for recommendations. | [Learn more](#)

Public IPv4 address
[redacted] | [open address](#)

Instance state
✔ **Running**

Private IP DNS name (IPv4 only)
ip-[redacted].ec2.internal

Elastic IP addresses
-

IAM Role
-

Private IPv4 addresses
[redacted]

Public IPv4 DNS
[redacted].amazonaws.com | [open address](#)

Answer private resource DNS name IPv4 (A)

VPC ID
[redacted] [↗](#)

Subnet ID
[redacted]if01 [↗](#)

[Details](#) [Security](#) [Networking](#) [Storage](#) [Status checks](#) [Monitoring](#) [Tags](#)

① You can now check network connectivity with Reachability Analyzer. [Run Reachability Analyzer](#) [✕](#)

▼ Networking details [Info](#)

Public IPv4 address
[redacted] [open address](#)

Public IPv4 DNS
[redacted].amazonaws.com | [open address](#)

IPv6 addresses
-

Carrier IP addresses (ephemeral)
-

Answer RBN DNS hostname IPv4
✔ **Enabled**

Private IPv4 addresses
[redacted]

Private IP DNS name (IPv4 only)
[redacted]

Secondary private IPv4 addresses
-

Outpost ID
-

VPC ID
[redacted] [↗](#)

Subnet ID
[redacted] [↗](#)

Availability zone
✔ **us-east-1d**

Use RBN as guest OS hostname
✔ **Disabled**

▼ Network Interfaces [Info](#)

Now we can launch our instance and check its status on the AWS console at “EC2” under “AWS services”. In the above series of screens, we can see the ID of the instance, the IP addresses and the links to security protocols established for the instance, the subnet and the VPC on which it is running. Clicking on these will open other windows with details about the connectivity for diagnosing purposes as needed. Many network settings can also be accessed by “VPC” under “AWS services”. Once created, the instance can be left running for as much time as we need to perform operations on its computing resources. Then, we have three options, once clicking on “Instance state”:

- **Stop** the instance: this will be the equivalent of turning off the machine. All the content of the instance, the software installed is fully preserved. When restarted, the instance will be assigned a different public IP though by default, unless a static (also known as elastic) public IP is requested. For more info on this see [this guide](#).



- **Reboot** the instance: this is the equivalent of restarting the machine. The same considerations apply as for “stop”.
- **Terminate** the instance: this kills the instance for good. Once terminated, an instance cannot be turned on, and all the content on it is lost.

6.2 Accessing the instances

Any instance in the VPC can be accessed through SSH via its public IP. The private IP is used only once in an instance to access to any other instance in the VPC. To access the instance, we need to use the key that was created with it. Once in the SSH, we can add the key to the keychain:

```
cd ~/.ssh
ssh-add -K mykey.pem    # add the key to the keychain
```

and then the instance can be accessed via SSH:

```
ssh -A ec2-user@ec2-pub-lic-IP-add.compute-1.amazonaws.com
```

the address is in the form of the public Ipv4 DNS taken from the screens shown previously. Once in the machine, we can run any command typical of UNIX terminal. It is good practice to update the instance at the first login.

```
~/ssh > ssh -A ec2-user@ec2-pub-lic-IP-add.compute-1.amazonaws.com
Last login: Thu Jan  6 23:42:04 2022 from pool-IP-add.net

  _|_  _|_  )
 _| (  _|_ /  Amazon Linux 2 AMI
  _|\_|_|_|

https://aws.amazon.com/amazon-linux-2/
```

As previously seen, AMI Linux instances use yum as utility to manage packages on the instance. Once connected by SSH, yum can be used to install, update, and remove packages. More information on this and the options can be found on at the redhat site (https://access.redhat.com/sites/default/files/attachments/rh_yum_cheatsheet_1214_jcs_print-1.pdf).

To verify that the PSG docker container that was installed and started when the instance was created is accessible from any source (internal and external to the VPC) we can check whether the public IP currently in use by the instance directs us to the PSG personal suite page. On the SSH, or on any terminal not connected to the SSH, we can type:

```
curl http://my.pub.lic.IP
```

If the security protocols are correct, that should always give



PROGRAMS - Using latest version (2022-01-03)

BASE - Using latest version (2022-01-03)

If no other PSG package has been installed. The PSG will be also accessible on any browser by typing

```
http://my.pub.lic.IP:3000/api.php
```

As said, if other instances are in the VPC, they can be accessed by their private IP from the SSH session open, by SSH through their private IP:

```
ssh ec2-user@pri.va.te.IP
```

6.2 Configuring AWS on the ssh

It may be quite inconvenient and tedious to look for private and public IPs when many instances are active. To automatize this and other procedures and exploit to the highest level the capabilities of AWS, the aws utility must be configured on the instance. To do that, we need first to obtain a new personal key from the AWS interface. This can be done from the top-right of the AWS console, accessing “security and credentials” once clicking on the user ID. Then, under “AWS IAM credentials” we can click on “Create Access Key” and save it in a .csv file in the local ~/.ssh directory or any other directory. Once we have the key, we can type in the SSH session on the instance

```
aws configure
```

which will ask for the public key, the private key (both just generated) and the region (us-east-1 for the East coast and the DC area). The fourth prompted argument is optional. If no output is returned, the procedure is successful. Now we can quickly obtain all the private or the public IP addresses of all the instances on the VPC by typing on the SSH instance:

```
aws ec2 describe-instances --region your-region --instance-ids --  
query "Reservations[*].Instances[*].PrivateIpAddress" --output text
```

```
aws ec2 describe-instances --region your-region --instance-ids --  
query "Reservations[*].Instances[*].PublicIpAddress" --output text
```

The first IP returned will be the one of the instance we are running on, followed by a single row with all the other IPs of the other instances.

6.2 Cloning an instance

When we need a lot of instances that do the same job, and on which a lot of packages and software needs to be installed on each of them, it may be extremely tedious and inconvenient to create them one by one. In this case, the smartest thing to do is to create a single ec2 instance, customize it with all the software needed, and then from there create an image of the instance. To do that, we need



first to stop the instance. Once stopped, under “actions” we can select “Image and template” and then “create image”. The following screen will be used to name the image, select the volumes to copy (if more than one) and then create it. The image will be available under “Images -> AMIs” in the EC2 dashboard. By entering this menu, we can then launch as many instances as desired from the image, following the exact same procedure as for the creation of the first image.

References

- A'Hearn, M.F., Millis, R.L., Schleicher, D.G., Osip, D.J., Birch, P.V., 1995. The ensemble properties of comets: Results from narrowband photometry of 85 comets, 1976-1992. *Icarus* 118, 223. <https://doi.org/10.1006/icar.1995.1190>
- A'Hearn, M.F., Schleicher, D.G., Millis, R.L., Feldman, P.D., Thompson, D.T., 1984. Comet Bowell 1980b. *The Astronomical Journal* 89, 579–591. <https://doi.org/10.1086/113552>
- Andrews, E., Sheridan, P.J., Fiebig, M., McComiskey, A., Ogren, J.A., Arnott, P., Covert, D., Elleman, R., Gasparini, R., Collins, D., Jonsson, H., Schmid, B., Wang, J., 2006. Comparison of methods for deriving aerosol asymmetry parameter. *Journal of Geophysical Research: Atmospheres* 111. <https://doi.org/10.1029/2004JD005734>
- Appleby, J.F., 1990. CH₄ nonlocal thermodynamic equilibrium in the atmospheres of the giant planets. *Icarus* 85, 355–379. [https://doi.org/10.1016/0019-1035\(90\)90123-Q](https://doi.org/10.1016/0019-1035(90)90123-Q)
- Baranov, Y.I., Lafferty, W.J., 2012. The water vapour self- and water-nitrogen continuum absorption in the 1000 and 2500 cm⁻¹ atmospheric windows. *Philosophical Transactions of the Royal Society of London Series A* 370, 2578–2589. <https://doi.org/10.1098/rsta.2011.0234>
- Batalha, N.E., Marley, M.S., Lewis, N.K., Fortney, J.J., 2019. Exoplanet Reflected-light Spectroscopy with PICASO. *ApJ* 878, 70. <https://doi.org/10.3847/1538-4357/ab1b51>
- Belgacem, I., Schmidt, F., Jonniaux, G., 2020. Regional study of Europa's photometry. *Icarus* 338, 113525. <https://doi.org/10.1016/j.icarus.2019.113525>
- Benna, M., Mahaffy, P.R., Halekas, J.S., Elphic, R.C., Delory, G.T., 2015. Variability of helium, neon, and argon in the lunar exosphere as observed by the LADEE NMS instrument. *Geophysical Research Letters* 42, 3723–3729. <https://doi.org/10.1002/2015GL064120>
- Bensch, F., Bergin, E.A., 2004. The Pure Rotational Line Emission of Ortho-Water Vapor in Comets. I. Radiative Transfer Model. *The Astrophysical Journal* 615, 531. <https://doi.org/10.1086/424439>
- Bernath, P.F., 2020. MoLLIST: Molecular Line Lists, Intensities and Spectra. *Journal of Quantitative Spectroscopy and Radiative Transfer* 240, 106687. <https://doi.org/10.1016/j.jqsrt.2019.106687>
- Biver, N., 1997. Ph.D. thesis.
- Biver, N., Bockelée-Morvan, D., Colom, P., Crovisier, J., Henry, F., Lellouch, E., Winnberg, A., Johansson, L.E.B., Gunnarsson, M., Rickman, H., Rantakyö, F., Davies, J.K., Dent, W.R.F., Paubert, G., Moreno, R., Wink, J., Despois, D., Benford, D.J., Gardner, M., Lis, D.C., Mehringer, D., Phillips, T.G., Rauer, H., 2002. The 1995 2002 Long-Term Monitoring of Comet C/1995 O1 (HALE BOPP) at Radio Wavelength. *Earth* 90, 5–14. <https://doi.org/10.1023/A:1021599915018>

- Biver, N., Bockelée-Morvan, D., Crovisier, J., Davies, J.K., Matthews, H.E., Wink, J.E., Rauer, H., Colom, P., Dent, W.R.F., Despois, D., Moreno, R., Paubert, G., Jewitt, D., Senay, M., 1999. Spectroscopic Monitoring of Comet C/1996 B2 (Hyakutake) with the JCMT and IRAM Radio Telescopes 118, 1850–1872. <https://doi.org/10.1086/301033>
- Bockelée-Morvan, D., 1987. A model for the excitation of water in comets. *Astronomy and Astrophysics* 181, 169.
- Bockelée-Morvan, D., Leyrat, C., Erard, S., Andrieu, F., Capaccioni, F., Filacchione, G., Hasselmann, P.H., Crovisier, J., Drossart, P., Arnold, G., Ciarniello, M., Kappel, D., Longobardo, A., Capria, M.-T., De Sanctis, M.C., Rinaldi, G., Taylor, F., 2019. VIRTIS-H observations of the dust coma of comet 67P/Churyumov-Gerasimenko: spectral properties and color temperature variability with phase and elevation. *A&A* 630, A22. <https://doi.org/10.1051/0004-6361/201834764>
- Bodewits, D., Bonev, B.P., Cordiner, M.A., Villanueva, G.L., 2022. Radiative processes as diagnostics of cometary atmospheres. *Comets III Under review*.
- Bohren, C.F., Huffman, D.R., 1983. *Absorption and scattering of light by small particles*, New York: Wiley.
- Buffa, G., Tarrini, O., Scappini, F., Cecchi-Pestellini, C., 2000. H₂O-H₂O Collision Rate Coefficients. *The Astrophysical Journal Supplement Series* 128, 597–601. <https://doi.org/10.1086/313389>
- Buras, R., Dowling, T., Emde, C., 2011. New secondary-scattering correction in DISORT with increased efficiency for forward scattering. *Journal of Quantitative Spectroscopy and Radiative Transfer* 112, 2028–2034. <https://doi.org/10.1016/j.jqsrt.2011.03.019>
- Buratti, B.J., Hicks, M.D., Nettles, J., Staid, M., Pieters, C.M., Sunshine, J., Boardman, J., Stone, T.C., 2011. A wavelength-dependent visible and infrared spectrophotometric function for the Moon based on ROLO data. *J. Geophys. Res.* 116, E00G03. <https://doi.org/10.1029/2010JE003724>
- Burrows, A., Marley, M.S., Sharp, C.M., 2000. The Near Infrared and Optical Spectra of Methane Dwarfs and Brown Dwarfs. *ApJ* 531, 438–446. <https://doi.org/10.1086/308462>
- Cahoy, K.L., Marley, M.S., Fortney, J.J., 2010. Exoplanet Albedo Spectra and Colors as a Function of Planet Phase, Separation, and Metallicity. *ApJ* 724, 189. <https://doi.org/10.1088/0004-637X/724/1/189>
- Cavanaugh, J.F., Smith, J.C., Sun, X., Bartels, A.E., Ramos-Izquierdo, L., Krebs, D.J., McGarry, J.E., Trunzo, R., Novo-Gradac, A.M., Britt, J.L., Karsh, J., Katz, R.B., Lukemire, A.T., Szymkiewicz, R., Berry, D.L., Swinski, J.P., Neumann, G.A., Zuber, M.T., Smith, D.E., 2007. The Mercury Laser Altimeter Instrument for the MESSENGER Mission, in: Domingue, D.L., Russell, C.T. (Eds.), *The Messenger Mission to Mercury*. Springer, New York, NY, pp. 451–479. https://doi.org/10.1007/978-0-387-77214-1_13
- Checlair, J.H., Villanueva, G.L., Hayworth, B.P.C., Olson, S.L., Komacek, T.D., Robinson, T.D., Popović, P., Yang, H., Abbot, D.S., 2021. Probing the Capability of Future Direct-imaging

- Missions to Spectrally Constrain the Frequency of Earth-like Planets. *AJ* 161, 150.
<https://doi.org/10.3847/1538-3881/abdb36>
- Chin, G., Weaver, H.A., 1984. Vibrational and rotational excitation of CO in comets
 Nonequilibrium calculations. *The Astrophysical Journal* 285, 858–869.
<https://doi.org/10.1086/162565>
- Ciarniello, M., De Sanctis, M.C., Ammannito, E., Raponi, A., Longobardo, A., Palomba, E.,
 Carrozzo, F.G., Tosi, F., Li, J.-Y., Schröder, S.E., Zambon, F., Frigeri, A., Fonte, S.,
 Giardino, M., Pieters, C.M., Raymond, C.A., Russell, C.T., 2017. Spectrophotometric
 properties of dwarf planet Ceres from the VIR spectrometer on board the Dawn mission.
A&A 598, A130. <https://doi.org/10.1051/0004-6361/201629490>
- Clough, S.A., Kneizys, F.X., Davies, R.W., 1989. Line shape and the water vapor continuum.
Atmospheric Research 23, 229–241. [https://doi.org/10.1016/0169-8095\(89\)90020-3](https://doi.org/10.1016/0169-8095(89)90020-3)
- Clough, S.A., Shephard, M.W., Mlawer, E.J., Delamere, J.S., Iacono, M.J., Cady-Pereira, K.,
 Boukabara, S., Brown, P.D., 2005. Atmospheric radiative transfer modeling: a summary of
 the AER codes. *Journal of Quantitative Spectroscopy and Radiative Transfer* 91, 233–244.
<https://doi.org/10.1016/j.jqsrt.2004.05.058>
- Cowan, N.B., Agol, E., 2010. A MODEL FOR THERMAL PHASE VARIATIONS OF
 CIRCULAR AND ECCENTRIC EXOPLANETS. *ApJ* 726, 82.
<https://doi.org/10.1088/0004-637X/726/2/82>
- Cox, C., Munk, W., 1954. Measurement of the Roughness of the Sea Surface from Photographs of
 the Sun's Glitter. *J. Opt. Soc. Am.*, *JOSA* 44, 838–850.
<https://doi.org/10.1364/JOSA.44.000838>
- Crovisier, J., 2007. Cometary diversity and cometary families. *ArXiv Astrophysics e-prints*
 arXiv:astro-ph/0703785.
- Crovisier, J., 1987. Rotational and vibrational synthetic spectra of linear parent molecules in comets.
Astronomy and Astrophysics 68, 223.
- Crovisier, J., Encrenaz, T., 1983. Infrared fluorescence of molecules in comets - The general
 synthetic spectrum. *Astronomy and Astrophysics* 126, 170.
- Daerden, F., Neary, L., Viscardy, S., García Muñoz, A., Clancy, R.T., Smith, M.D., Encrenaz, T.,
 Fedorova, A., 2019. Mars atmospheric chemistry simulations with the GEM-Mars general
 circulation model. *Icarus* 326, 197–224. <https://doi.org/10.1016/j.icarus.2019.02.030>
- Dahlback, A., Stamnes, K., 1991. A new spherical model for computing the radiation field available
 for photolysis and heating at twilight. *Planetary and Space Science* 39, 671–683.
[https://doi.org/10.1016/0032-0633\(91\)90061-E](https://doi.org/10.1016/0032-0633(91)90061-E)
- Delbo, M., Mueller, M., Emery, J.P., Rozitis, B., Capria, M.T., 2015. Asteroid Thermophysical
 Modeling, *Asteroids IV*. https://doi.org/10.2458/azu_uapress_9780816532131-ch006
- Dello Russo, N., Kawakita, H., Vervack, R.J., Weaver, H.A., 2016. Emerging trends and a comet
 taxonomy based on the volatile chemistry measured in thirty comets with high-resolution

- infrared spectroscopy between 1997 and 2013. *Icarus* 278, 301–332.
<https://doi.org/10.1016/j.icarus.2016.05.039>
- Delsemme, A.H., 1982. Chemical composition of cometary nuclei. Presented at the IAU Colloq. 61: Comet Discoveries, Statistics, and Observational Selection, pp. 85–130.
- Devi, V.M., Benner, D.C., Sung, K., Crawford, T.J., Gamache, R.R., Renaud, C.L., Smith, M.A.H., Mantz, A.W., Villanueva, G.L., 2017a. Line parameters for CO₂ broadening in the ν_2 band of HD16O. *Journal of Quantitative Spectroscopy and Radiative Transfer* 187, 472–488. <https://doi.org/10.1016/j.jqsrt.2016.10.004>
- Devi, V.M., Benner, D.C., Sung, K., Crawford, T.J., Gamache, R.R., Renaud, C.L., Smith, M.A.H., Mantz, A.W., Villanueva, G.L., 2017b. Line parameters for CO₂- and self-broadening in the ν_1 band of HD16O. *Journal of Quantitative Spectroscopy and Radiative Transfer* 203, 133–157. <https://doi.org/10.1016/j.jqsrt.2017.01.032>
- Dlugach, J.M., Yanovitskij, E.G., 1974. The optical properties of Venus and the Jovian planets. II. Methods and results of calculations of the intensity of radiation diffusely reflected from semi-infinite homogeneous atmospheres. *Icarus* 22, 66–81. [https://doi.org/10.1016/0019-1035\(74\)90167-5](https://doi.org/10.1016/0019-1035(74)90167-5)
- Edwards, D.P., 1992. GENLN2: A General Line-by-Line Atmospheric Transmittance and Radiance Model. The National Center for Atmospheric Research: Technical Note 367-STR.
- Ehrenreich, D., Tinetti, G., Lecavelier des Etangs, A., Vidal-Madjar, A., Selsis, F., 2006. The transmission spectrum of Earth-size transiting planets. *Astronomy and Astrophysics* 448, 379–393. <https://doi.org/10.1051/0004-6361:20053861>
- Ehrenreich, D., Vidal-Madjar, A., Widemann, T., Gronoff, G., Tanga, P., Barthélemy, M., Lilensten, J., des Etangs, A.L., Arnold, L., 2012. Transmission spectrum of Venus as a transiting exoplanet. *Astronomy and Astrophysics* 537, L2. <https://doi.org/10.1051/0004-6361/201118400>
- Encrenaz, T., de Graauw, T., Schaeidt, S., Lellouch, E., Feuchtgruber, H., Beintema, D.A., Bézard, B., Drossart, P., Griffin, M., Heras, A., Kessler, M., Leech, K., Morris, P., Roelfsema, P.R., Roos-Serote, M., Salama, A., Vandenbussche, B., Valentijn, E.A., Davis, G.R., Naylor, D.A., 1996. First results of ISO-SWS observations of Jupiter. *Astronomy and Astrophysics* 315, L397–L400.
- Fally, S., Vandaele, A.C., Carleer, M., Hermans, C., Jenouvrier, A., Mérienne, M.-F., Coquart, B., Colin, R., 2000. Fourier Transform Spectroscopy of the O₂ Herzberg Bands. III. Absorption Cross Sections of the Collision-Induced Bands and of the Herzberg Continuum. *Journal of Molecular Spectroscopy* 204, 10–20. <https://doi.org/10.1006/jmsp.2000.8204>
- Faucher, T.J., Villanueva, G.L., Schwieterman, E.W., Turbet, M., Arney, G., Pidhorodetska, D., Kopparapu, R.K., Mandell, A., Domagal-Goldman, S.D., 2020. Sensitive probing of exoplanetary oxygen via mid-infrared collisional absorption. *Nat Astron* 4, 372–376. <https://doi.org/10.1038/s41550-019-0977-7>
- Fernando, J., Schmidt, F., Pilorget, C., Pinet, P., Ceamanos, X., Douté, S., Daydou, Y., Costard, F., 2015. Characterization and mapping of surface physical properties of Mars from CRISM

- multi-angular data: application to Gusev Crater and Meridiani Planum. *Icarus* 253, 271–295. <https://doi.org/10.1016/j.icarus.2015.03.012>
- Feroz, F., Hobson, M.P., 2008. Multimodal nested sampling: an efficient and robust alternative to Markov Chain Monte Carlo methods for astronomical data analyses: Multimodal nested sampling. *Monthly Notices of the Royal Astronomical Society* 384, 449–463. <https://doi.org/10.1111/j.1365-2966.2007.12353.x>
- Feroz, F., Hobson, M.P., Bridges, M., 2009. MultiNest: an efficient and robust Bayesian inference tool for cosmology and particle physics. *Monthly Notices of the Royal Astronomical Society* 398, 1601–1614. <https://doi.org/10.1111/j.1365-2966.2009.14548.x>
- Fink, U., Rubin, M., 2012. The calculation of A_{fp} and mass loss rate for comets. *Icarus* 221, 721–734. <https://doi.org/10.1016/j.icarus.2012.09.001>
- Fornasier, S., Hasselmann, P.H., Deshapriya, J.D.P., Barucci, M.A., Clark, B.E., Praet, A., Hamilton, V.E., Simon, A., Li, J.-Y., Cloutis, E.A., Merlin, F., Zou, X.-D., Lauretta, D.S., 2020. Phase reddening on asteroid Bennu from visible and near-infrared spectroscopy. *A&A* 644, A142. <https://doi.org/10.1051/0004-6361/202039552>
- France, K., Loyd, R.O.P., Youngblood, A., Brown, A., Schneider, P.C., Hawley, S.L., Froning, C.S., Linsky, J.L., Roberge, A., Buccino, A.P., Davenport, J.R.A., Fontenla, J.M., Kaltenegger, L., Kowalski, A.F., Mauas, P.J.D., Miguel, Y., Redfield, S., Rugheimer, S., Tian, F., Vieytes, M.C., Walkowicz, L.M., Weisenburger, K.L., 2016. The MUSCLES Treasury Survey. I. Motivation and Overview. *The Astrophysical Journal* 820, 89. <https://doi.org/10.3847/0004-637X/820/2/89>
- Fu, Q., 2007. A New Parameterization of an Asymmetry Factor of Cirrus Clouds for Climate Models. *Journal of the Atmospheric Sciences* 64, 4140–4150. <https://doi.org/10.1175/2007JAS2289.1>
- Gamache, R.R., Renaud, C.L., 2017. Modified Complex Robert-Bonamy (MCRB) calculations of H₂O transitions broadened by H₂ for applications to planetary and exoplanet atmospheres. *J. Phys.: Conf. Ser.* 810, 012032. <https://doi.org/10.1088/1742-6596/810/1/012032>
- Gelaro, R., McCarty, W., Suarez, M.J., Todling, R., Molod, A., Takacs, L., Randles, C.A., Darmenov, A., Bosilovich, M.G., Reichle, R., Wargan, K., Coy, L., Cullather, R., Draper, C., Akella, S., Buchard, V., Conaty, A., da Silva, A.M., Gu, W., Kim, G.-K., Koster, R., Lucchesi, R., Merkova, D., Nielsen, J.E., Partyka, G., Pawson, S., Putman, W., Rienecker, M., Schubert, S.D., Sienkiewicz, M., Zhao, B., 2017. The Modern-Era Retrospective Analysis for Research and Applications, Version 2 (MERRA-2). *Journal of Climate* 30, 5419–5454. <https://doi.org/10.1175/JCLI-D-16-0758.1>
- Gesch, D.B., Larson, K.S., 1996. Techniques for development of global 1-kilometer digital elevation models, in: Pecora Thirteen, Human Interactions with the Environment - Perspectives from Space. Sioux Falls, South Dakota.
- Gordon, I.E., Rothman, L.S., Hargreaves, R.J., Hashemi, R., Karlovets, E.V., Skinner, F.M., Conway, E.K., Hill, C., Kochanov, R.V., Tan, Y., Wcisło, P., Finenko, A.A., Nelson, K.,

- Bernath, P.F., Birk, M., Boudon, V., Campargue, A., Chance, K.V., Coustenis, A., Drouin, B.J., Flaud, J. –M., Gamache, R.R., Hodges, J.T., Jacquemart, D., Mlawer, E.J., Nikitin, A.V., Perevalov, V.I., Rotger, M., Tennyson, J., Toon, G.C., Tran, H., Tyuterev, V.G., Adkins, E.M., Baker, A., Barbe, A., Canè, E., Császár, A.G., Dudaryonok, A., Egorov, O., Fleisher, A.J., Fleurbaey, H., Foltynowicz, A., Furtenbacher, T., Harrison, J.J., Hartmann, J. –M., Horneman, V. –M., Huang, X., Karman, T., Karns, J., Kass, S., Kleiner, I., Kofman, V., Kwabia–Tchana, F., Lavrentieva, N.N., Lee, T.J., Long, D.A., Lukashetskaya, A.A., Lyulin, O.M., Makhnev, V.Yu., Matt, W., Massie, S.T., Melosso, M., Mikhailenko, S.N., Mondelain, D., Müller, H.S.P., Naumenko, O.V., Perrin, A., Polyansky, O.L., Raddaoui, E., Raston, P.L., Reed, Z.D., Rey, M., Richard, C., Tóbiás, R., Sadiek, I., Schwenke, D.W., Starikova, E., Sung, K., Tamassia, F., Tashkun, S.A., Auwera, J.V., Vasilenko, I.A., Vigasin, A.A., Villanueva, G.L., Vispoel, B., Wagner, G., Yachmenev, A., Yurchenko, S.N., 2022. The HITRAN2020 molecular spectroscopic database. *Journal of Quantitative Spectroscopy and Radiative Transfer* 107949. <https://doi.org/10.1016/j.jqsrt.2021.107949>
- Goyal, J.M., Mayne, N., Sing, D.K., Drummond, B., Tremblin, P., Amundsen, D.S., Evans, T., Carter, A.L., Spake, J., Baraffe, I., Nikolov, N., Mannes, J., Chabrier, G., Hebrard, E., 2018. A library of ATMO forward model transmission spectra for hot Jupiter exoplanets. *Mon Not R Astron Soc* 474, 5158–5185. <https://doi.org/10.1093/mnras/stx3015>
- Granate, P., Coelho, P.J., Roger, M., 2016. Radiative heat transfer in strongly forward scattering media using the discrete ordinates method. *Journal of Quantitative Spectroscopy and Radiative Transfer*, Eurotherm Conference No. 105: Computational Thermal Radiation in Participating Media V 172, 110–120. <https://doi.org/10.1016/j.jqsrt.2015.12.011>
- Grillini, F., Thomas, J.-B., George, S., 2020. Linear, Subtractive and Logarithmic Optical Mixing Models in Oil Painting. *Colour and Visual Computing Symposium 2020*, Gjøvik, Norway, September 16-17, 2020.
- Halekas, J.S., Benna, M., Mahaffy, P.R., Elphic, R.C., Poppe, A.R., Delory, G.T., 2015. Detections of lunar exospheric ions by the LADEE neutral mass spectrometer. *Geophysical Research Letters* 42, 5162–5169. <https://doi.org/10.1002/2015GL064746>
- Hansen, B.M.S., 2008. On the Absorption and Redistribution of Energy in Irradiated Planets. *ApJS* 179, 484. <https://doi.org/10.1086/591964>
- Hapke, B., 2012a. *Theory of Reflectance and Emittance Spectroscopy*, 2nd ed. Cambridge University Press, Cambridge. <https://doi.org/10.1017/CBO9781139025683>
- Hapke, B., 2012b. Bidirectional reflectance spectroscopy 7. *Icarus* 221, 1079–1083. <https://doi.org/10.1016/j.icarus.2012.10.022>
- Hargreaves, R.J., Gordon, I.E., Rey, M., Nikitin, A.V., Tyuterev, V.G., Kochanov, R.V., Rothman, L.S., 2020. An Accurate, Extensive, and Practical Line List of Methane for the HITEMP Database. *The Astrophysical Journal Supplement Series* 247, 55. <https://doi.org/10.3847/1538-4365/ab7a1a>
- Harris, A.W., 1998. A Thermal Model for Near-Earth Asteroids. *Icarus* 131, 291–301. <https://doi.org/10.1006/icar.1997.5865>

- Hase, F., Wallace, L., Mcleod, S.D., Harrison, J.J., Bernath, P.F., 2009. The ACE-FTS atlas of the infrared solar spectrum. *Journal of Quantitative Spectroscopy and Radiative Transfer* 111, 521–528. <https://doi.org/10.1016/j.jqsrt.2009.10.020>
- Helfenstein, P., Veverka, J., 1989. Physical characterization of asteroid surfaces from photometric analysis 557–593.
- Hindmarsh, A., 1983. ODEPACK, a Systematized Collection of ODE Solvers, in *Scientific Computing*. Elsevier.
- Horak, H.G., Little, S.J., 1965. Calculations of Planetary Reflection. *The Astrophysical Journal Supplement Series* 11, 373. <https://doi.org/10.1086/190119>
- Huebner, W.F., Keady, J.J., Lyon, S.P., 1992. Solar photo rates for planetary atmospheres and atmospheric pollutants. *Astrophysics and Space Science* (ISSN 0004-640X) 195, 1–289. <https://doi.org/10.1007/BF00644558>
- Humlíček, J., 1982. Optimized computation of the Voigt and complex probability functions. *Journal of Quantitative Spectroscopy and Radiative Transfer* 27, 437–444. [https://doi.org/10.1016/0022-4073\(82\)90078-4](https://doi.org/10.1016/0022-4073(82)90078-4)
- Iro, N., Gautier, D., Hersant, F., Bockelée-Morvan, D., Lunine, J.I., 2003. An interpretation of the nitrogen deficiency in comets. *Icarus* 161, 511–532. [https://doi.org/10.1016/S0019-1035\(02\)00038-6](https://doi.org/10.1016/S0019-1035(02)00038-6)
- Irwin, P. G. J., Teanby, N.A., de Kok, R., Fletcher, L.N., Howett, C.J.A., Tsang, C.C.C., Wilson, C.F., Calcutt, S.B., Nixon, C.A., Parrish, P.D., 2008. The NEMESIS planetary atmosphere radiative transfer and retrieval tool. *Journal of Quantitative Spectroscopy and Radiative Transfer, Spectroscopy and Radiative Transfer in Planetary Atmospheres* 109, 1136–1150. <https://doi.org/10.1016/j.jqsrt.2007.11.006>
- Irwin, P.G.J., Teanby, N.A., de Kok, R., Fletcher, L.N., Howett, C.J.A., Tsang, C.C.C., Wilson, C.F., Calcutt, S.B., Nixon, C.A., Parrish, P.D., 2008. The NEMESIS planetary atmosphere radiative transfer and retrieval tool. *Journal of Quantitative Spectroscopy and Radiative Transfer* 109, 1136–1150. <https://doi.org/10.1016/j.jqsrt.2007.11.006>
- Itikawa, Y., 1972. Rotational Transition in an Asymmetric-Top Molecule by Electron Collision: Applications to H₂O and H₂CO. *J. Phys. Soc. Jpn.* 32, 217–226. <https://doi.org/10.1143/JPSJ.32.217>
- Jackson, Christopher.R., Alpers, W., 2010. The role of the critical angle in brightness reversals on sunglint images of the sea surface. *J. Geophys. Res.* 115, C09019. <https://doi.org/10.1029/2009JC006037>
- Jenouvrier, A., Mérienne, M.-F., Coquart, B., Carleer, M., Fally, S., Vandaele, A.C., Hermans, C., Colin, R., 1999. Fourier Transform Spectroscopy of the O₂ Herzberg Bands . I. Rotational Analysis. *Journal of Molecular Spectroscopy* 198, 136–162. <https://doi.org/10.1006/jmsp.1999.7950>
- Jorda, L., Crovisier, J., Green, D.W.E., 2008. The Correlation Between Visual Magnitudes and Water Production Rates. *Asteroids, Comet, Meteors* 2008 8046.

- Keller-Rudek, H., Moortgat, G.K., Sander, R., Sörensen, R., 2013. The MPI-Mainz UV/VIS Spectral Atlas of Gaseous Molecules of Atmospheric Interest. *Earth System Science Data* 5, 365–373. <https://doi.org/10.5194/essd-5-365-2013>
- Kempton, E.M.R., Lupu, R., Owusu-Asare, A., Slough, P., Cale, B., 2017. Exo-Transmit: An Open-Source Code for Calculating Transmission Spectra for Exoplanet Atmospheres of Varied Composition. *Publications of the Astronomical Society of the Pacific* 129, 044402-. <https://doi.org/10.1088/1538-3873/aa61ef>
- Knollenberg R., Travis L., Tomasko M., Smith P., Ragent B., Esposito L., McCleese D., Martonchik J., Beer R., 2012. The clouds of Venus: A synthesis report. *Journal of Geophysical Research: Space Physics* 85, 8059–8081. <https://doi.org/10.1029/JA085iA13p08059>
- Kofman, V., Villanueva, G.L., 2021. Absorption in exoplanet atmospheres: Combining experimental and theoretical databases to facilitate calculations of the molecular opacities of water. *Journal of Quantitative Spectroscopy and Radiative Transfer* 270, 107708. <https://doi.org/10.1016/j.jqsrt.2021.107708>
- Kofman, V., Villanueva, G.L., Fauchez, T.J., Mandell, A.M., Johnson, T.M., Payne, A., Latouf, N., Kelkar, S., 2024. The Pale Blue Dot: Using the Planetary Spectrum Generator to Simulate Signals from Hyperrealistic Exo-Earths. *Planet. Sci. J.* 5, 197. <https://doi.org/10.3847/PSJ/ad6448>
- Kokhanovsky, A.A., Budak, V.P., Cornet, C., Duan, M., Emde, C., Katsev, I.L., Klyukov, D.A., Korkin, S.V., C-Labonnote, L., Mayer, B., Min, Q., Nakajima, T., Ota, Y., Prikhach, A.S., Rozanov, V.V., Yokota, T., Zege, E.P., 2010. Benchmark results in vector atmospheric radiative transfer. *Journal of Quantitative Spectroscopy and Radiative Transfer* 111, 1931–1946. <https://doi.org/10.1016/j.jqsrt.2010.03.005>
- Kopparapu, R., Arney, G., Haqq-Misra, J., Lustig-Yaeger, J., Villanueva, G., 2021. Nitrogen Dioxide Pollution as a Signature of Extraterrestrial Technology. *ApJ* 908, 164. <https://doi.org/10.3847/1538-4357/abd7f7>
- Kurucz, R.L., 2009. Including All the Lines, in: *AIP Conference Proceedings*. Harvard-Smithsonian Center for Astrophysics, Cambridge, MA 02138, USA, pp. 43–51. <https://doi.org/10.1063/1.3250087>
- Kwon, S.M., Hong, S.S., Weinberg, J.L., 2004. An observational model of the zodiacal light brightness distribution. *New Astronomy* 10, 91–107. <https://doi.org/10.1016/j.newast.2004.05.004>
- Kylling, A., Stamnes, K., Tsay, S.-C., 1995. A reliable and efficient two-stream algorithm for spherical radiative transfer: Documentation of accuracy in realistic layered media. *J Atmos Chem* 21, 115–150. <https://doi.org/10.1007/BF00696577>
- Lebofsky, L.A., Spencer, J.R., 1989. Radiometry and thermal modeling of asteroids. Presented at the Asteroids II.
- Lebofsky, L.A., Sykes, M.V., Tedesco, E.F., Veeder, G.J., Matson, D.L., Brown, R.H., Gradie, J.C., Feierberg, M.A., Rudy, R.J., 1986. A refined “standard” thermal model for asteroids based

- on observations of 1 Ceres and 2 Pallas. *Icarus* 68, 239–251. [https://doi.org/10.1016/0019-1035\(86\)90021-7](https://doi.org/10.1016/0019-1035(86)90021-7)
- Leconte, J., 2021. Spectral binning of precomputed correlated- k coefficients. *A&A* 645, A20. <https://doi.org/10.1051/0004-6361/202039040>
- Leinert, Ch., Bowyer, S., Haikala, L.K., Hanner, M.S., Hauser, M.G., Levasseur-Regourd, A.-Ch., Mann, I., Mattila, K., Reach, W.T., Schlosser, W., Staude, H.J., Toller, G.N., Weiland, J.L., Weinberg, J.L., Witt, A.N., 1998. The 1997 reference of diffuse night sky brightness. *Astronomy and Astrophysics Supplement Series* 127, 1–99. <https://doi.org/10.1051/aas:1998105>
- Lellouch, E., Hartogh, P., Feuchtgruber, H., Vandenbussche, B., Graauw, T. de, Moreno, R., Jarchow, C., Cavalié, T., Orton, G., Banaszkiewicz, M., Blecka, M.I., Bockelée-Morvan, D., Crovisier, J., Encrenaz, T., Fulton, T., Küppers, M., Lara, L.M., Lis, D.C., Medvedev, A.S., Rengel, M., Sagawa, H., Swinyard, B., Szutowicz, S., Bensch, F., Bergin, E., Billebaud, F., Biver, N., Blake, G.A., Blommaert, J. a. D.L., Cernicharo, J., Courtin, R., Davis, G.R., Decin, L., Encrenaz, P., Gonzalez, A., Jehin, E., Kidger, M., Naylor, D., Portyankina, G., Schieder, R., Sidher, S., Thomas, N., Val-Borro, M. de, Verdugo, E., Waelkens, C., Walker, H., Aarts, H., Comito, C., Kawamura, J.H., Maestrini, A., Peacocke, T., Teipen, R., Tils, T., Wildeman, K., 2010. First results of Herschel-PACS observations of Neptune. *A&A* 518, L152. <https://doi.org/10.1051/0004-6361/201014600>
- Li, G., Gordon, I.E., Rothman, L.S., Tan, Y., Hu, S.-M., Kass, S., Campargue, A., Medvedev, E.S., 2015. ROVIBRATIONAL LINE LISTS FOR NINE ISOTOPOLOGUES OF THE CO MOLECULE IN THE $X^1\Sigma^+$ GROUND ELECTRONIC STATE. *ApJS* 216, 15. <https://doi.org/10.1088/0067-0049/216/1/15>
- Li, J.-Y., Helfenstein, P., Buratti, B.J., Takir, D., Clark, B.E., 2015. Asteroid Photometry. *arXiv:1502.06302 [astro-ph]*. https://doi.org/10.2458/azu_uapress_9780816532131-ch007
- Lin, Z., Chen, N., Fan, Y., Li, W., Stamnes, K., Stamnes, S., 2018. New Treatment of Strongly Anisotropic Scattering Phase Functions: The Delta-M+ Method. *Journal of the Atmospheric Sciences* 75, 327–336. <https://doi.org/10.1175/JAS-D-17-0233.1>
- Liou, K.-N., 2002. *An Introduction to Atmospheric Radiation*, 2nd Edition. ed. Academic Press - Elsevier.
- Liou, K.-N., 1973. A Numerical Experiment on Chandrasekhar's Discrete-Ordinate Method for Radiative Transfer: Applications to Cloudy and Hazy Atmospheres. *Journal of the Atmospheric Sciences* 30, 1303–1326. [https://doi.org/10.1175/1520-0469\(1973\)030<1303:ANEOCD>2.0.CO;2](https://doi.org/10.1175/1520-0469(1973)030<1303:ANEOCD>2.0.CO;2)
- Lippi, M., Villanueva, G.L., Mumma, M.J., Faggi, S., 2021. Investigation of the Origins of Comets as Revealed through Infrared High-resolution Spectroscopy I. Molecular Abundances. *The Astronomical Journal* 162, 74. <https://doi.org/10.3847/1538-3881/abfdb7>
- Liuzzi, G., Villanueva, G.L., Mumma, M.J., Smith, M.D., Daerden, F., Ristic, B., Thomas, I., Vandaale, A.C., Patel, M.R., Lopez-Moreno, J.-J., Bellucci, G., 2019. Methane on Mars: New insights into the sensitivity of CH₄ with the NOMAD/ExoMars spectrometer through

- its first in-flight calibration. *Icarus* 321, 671–690.
<https://doi.org/10.1016/j.icarus.2018.09.021>
- Liuzzi, G., Villanueva, G.L., Trompet, L., Crismani, M.M.J., Piccialli, A., Aoki, S., Lopez-Valverde, M.A., Stolzenbach, A., Daerden, F., Neary, L., Smith, M.D., Patel, M.R., Lewis, S.R., Clancy, R.T., Thomas, I.R., Ristic, B., Bellucci, G., Lopez-Moreno, J.-J., Vandaele, A.C., 2021. First Detection and Thermal Characterization of Terminator CO₂ Ice Clouds With ExoMars/NOMAD. *Geophysical Research Letters* 48, e2021GL095895.
<https://doi.org/10.1029/2021GL095895>
- Lopez-Puertas, M., López-Valverde, M.A., 1995. Radiative Energy Balance of CO₂ Non-LTE Infrared Emissions in the Martian Atmosphere. *Icarus* 114, 113–129.
<https://doi.org/10.1006/icar.1995.1047>
- Lumme, K., Bowell, E., 1981. Radiative transfer in the surfaces of atmosphereless bodies. I - Theory. II - Interpretation of phase curves. *The Astronomical Journal* 86, 1694–1721.
<https://doi.org/10.1086/113054>
- Ma, L.X., Wang, F.Q., Wang, C.A., Wang, C.C., Tan, J.Y., 2015. Investigation of the spectral reflectance and bidirectional reflectance distribution function of sea foam layer by the Monte Carlo method. *Appl. Opt.* 54, 9863. <https://doi.org/10.1364/AO.54.009863>
- Mahaffy, P.R., Benna, M., Elrod, M., Yelle, R.V., Bougher, S.W., Stone, S.W., Jakosky, B.M., 2015. Structure and composition of the neutral upper atmosphere of Mars from the MAVEN NGIMS investigation. *Geophysical Research Letters* 42, 8951–8957.
<https://doi.org/10.1002/2015GL065329>
- Mallet, P., Guérin, C.A., Sentenac, A., 2005. Maxwell-Garnett mixing rule in the presence of multiple scattering: Derivation and accuracy. *Phys. Rev. B* 72, 014205.
<https://doi.org/10.1103/PhysRevB.72.014205>
- Markus, T., Neumann, T., Martino, A., Abdalati, W., Brunt, K., Csatho, B., Farrell, S., Fricker, H., Gardner, A., Harding, D., Jasinski, M., Kwok, R., Magruder, L., Lubin, D., Luthcke, S., Morison, J., Nelson, R., Neuenschwander, A., Palm, S., Popescu, S., Shum, C., Schutz, B.E., Smith, B., Yang, Y., Zwally, J., 2017. The Ice, Cloud, and land Elevation Satellite-2 (ICESat-2): Science requirements, concept, and implementation. *Remote Sensing of Environment* 190, 260–273. <https://doi.org/10.1016/j.rse.2016.12.029>
- Maron, N., Maron, O., 2008. Criteria for mixing rules application for inhomogeneous astrophysical grains. *Monthly Notices of the Royal Astronomical Society* 391, 738–764.
<https://doi.org/10.1111/j.1365-2966.2008.13908.x>
- Marschall, R., Markkanen, J., Gerig, S.-B., Pinzón-Rodríguez, O., Thomas, N., Wu, J.-S., 2020. The Dust-to-Gas Ratio, Size Distribution, and Dust Fall-Back Fraction of Comet 67P/Churyumov-Gerasimenko: Inferences From Linking the Optical and Dynamical Properties of the Inner Comae. *Frontiers in Physics* 8.
- Marshall, D., Groussin, O., Vincent, J.-B., Brouet, Y., Kappel, D., Arnold, G., Capria, M.T., Filacchione, G., Hartogh, P., Hofstadter, M., Ip, W.-H., Jorda, L., Kührt, E., Lellouch, E., Mottola, S., Rezac, L., Rodrigo, R., Rodionov, S., Schloerb, P., Thomas, N., 2018. Thermal

- inertia and roughness of the nucleus of comet 67P/Churyumov–Gerasimenko from MIRO and VIRTIS observations. *A&A* 616, A122. <https://doi.org/10.1051/0004-6361/201833104>
- Marten, A., Matthews, H.E., Owen, T., Moreno, R., Hidayat, T., Biraud, Y., 2005. Improved constraints on Neptune’s atmosphere from submillimetre-wavelength observations. *Astronomy and Astrophysics* 429, 1097–1105. <https://doi.org/10.1051/0004-6361:20041695>
- Masiello, G., Serio, C., 2013. Simultaneous physical retrieval of surface emissivity spectrum and atmospheric parameters from infrared atmospheric sounder interferometer spectral radiances. *Applied Optics* 52, 2428. <https://doi.org/10.1364/AO.52.002428>
- Massie, S.T., Hervig, M., 2013. HITRAN 2012 refractive indices. *Journal of Quantitative Spectroscopy and Radiative Transfer* 130, 373–380. <https://doi.org/10.1016/j.jqsrt.2013.06.022>
- McKemmish, L.K., Syme, A.-M., Borsovszky, J., Yurchenko, S.N., Tennyson, J., Furtenbacher, T., Császár, A.G., 2020. An update to the MARVEL data set and ExoMol line list for 12C2. *Monthly Notices of the Royal Astronomical Society* 497, 1081–1097. <https://doi.org/10.1093/mnras/staa1954>
- Meftah, M., Sarkissian, A., Keckhut, P., Hauchecorne, A., 2023. The SOLAR-HRS New High-Resolution Solar Spectra for Disk-Integrated, Disk-Center, and Intermediate Cases. *Remote Sensing* 15, 3560. <https://doi.org/10.3390/rs15143560>
- Mérienne, M.-F., Jenouvrier, A., Coquart, B., Carleer, M., Fally, S., Colin, R., Vandaele, A.C., Hermans, C., 2001. Improved Data Set for the Herzberg Band Systems of 16O 2. *Journal of Molecular Spectroscopy* 207, 120–120. <https://doi.org/10.1006/jmsp.2001.8314>
- Mérienne, M.-F., Jenouvrier, A., Coquart, B., Carleer, M., Fally, S., Colin, R., Vandaele, A.C., Hermans, C., 2000. Fourier Transform Spectroscopy of the O2 Herzberg Bands. II. Band Oscillator Strengths and Transition Moments. *Journal of Molecular Spectroscopy* 202, 171–193. <https://doi.org/10.1006/jmsp.2000.8126>
- Millour, E., Forget, F., Spiga, A., Navarro, T., Madeleine, J.B., Montabone, L., Pottier, A., Lefèvre, F., Montmessin, F., Chaufray, J.Y., López-Valverde, M.A., González-Galindo, F., Lewis, S.R., Read, P.L., Huot, J.-P., Desjean, M.-C., Team, M.G. development, 2015. The Mars Climate Database (MCD version 5.2). *European Planetary Science Congress 2015* 10, EPSC2015-438.
- Mizuno, T., Kase, T., Shiina, T., Mita, M., Namiki, N., Senshu, H., Yamada, R., Noda, H., Kunimori, H., Hirata, N., Terui, F., Mimasu, Y., 2017. Development of the Laser Altimeter (LIDAR) for Hayabusa2. *Space Sci Rev* 208, 33–47. <https://doi.org/10.1007/s11214-015-0231-2>
- Molyneux, P.M., Nichols, J.D., Becker, T.M., Raut, U., Retherford, K.D., 2020. Ganymede’s Far-Ultraviolet Reflectance: Constraining Impurities in the Surface Ice. *Journal of Geophysical Research: Planets* 125, e2020JE006476. <https://doi.org/10.1029/2020JE006476>
- Moses, J.I., Fouchet, T., Bézard, B., Gladstone, G.R., Lellouch, E., Feuchtgruber, H., 2005. Photochemistry and diffusion in Jupiter’s stratosphere: Constraints from ISO observations

- and comparisons with other giant planets. *Journal of Geophysical Research* 110, 8001. <https://doi.org/10.1029/2005JE002411>
- Muinenen, K., Belskaya, I.N., Cellino, A., Delbò, M., Levasseur-Regourd, A.-C., Penttilä, A., Tedesco, E.F., 2010. A three-parameter magnitude phase function for asteroids. *Icarus* 209, 542–555. <https://doi.org/10.1016/j.icarus.2010.04.003>
- Mumma, M.J., Charnley, S.B., 2011. The Chemical Composition of Comets – Emerging Taxonomies & Natal Heritage. *Annual Review of Astronomy and Astrophysics* 49, 471–524.
- Mumma, M.J., Disanti, M.A., Dello Russo, N., Magee-Sauer, K., Gibb, E.L., Novak, R., 2003. Remote infrared observations of parent volatiles in comets: A window on the early solar system. *Advances in Space Research* 31, 2563–2575. [https://doi.org/10.1016/S0273-1177\(03\)00578-7](https://doi.org/10.1016/S0273-1177(03)00578-7)
- Mustard, J.F., Pieters, C.M., 1989. Photometric phase functions of common geologic minerals and applications to quantitative analysis of mineral mixture reflectance spectra. *Journal of Geophysical Research: Solid Earth* 94, 13619–13634. <https://doi.org/10.1029/JB094iB10p13619>
- Nakajima, T., Tanaka, M., 1988. Algorithms for radiative intensity calculations in moderately thick atmospheres using a truncation approximation. *Journal of Quantitative Spectroscopy and Radiative Transfer* 40, 51–69. [https://doi.org/10.1016/0022-4073\(88\)90031-3](https://doi.org/10.1016/0022-4073(88)90031-3)
- Nefedov, A.P., Sinel'shchikov, V.A., Usachev, A.D., 1999. Collisional Broadening of the Na-D Lines by Molecular Gases. *Phys. Scr.* 59, 432–442. <https://doi.org/10.1238/Physica.Regular.059a00432>
- Oklopčić, A., Hirata, C.M., Heng, K., 2017. How Does the Shape of the Stellar Spectrum Affect the Raman Scattering Features in the Albedo of Exoplanets? *ApJ* 846, 91. <https://doi.org/10.3847/1538-4357/aa8630>
- Parmentier, V., Guillot, T., 2014. A non-grey analytical model for irradiated atmospheres. I. Derivation. *Astronomy and Astrophysics* 562, A133. <https://doi.org/10.1051/0004-6361/201322342>
- Paynter, D.J., Ptashnik, I.V., Shine, K.P., Smith, K.M., McPheat, R., Williams, R.G., 2009. Laboratory measurements of the water vapor continuum in the 1200–8000 cm⁻¹ region between 293 K and 351 K. *Journal of Geophysical Research (Atmospheres)* 114, D21301. <https://doi.org/10.1029/2008JD011355>
- Penttilä, A., Shevchenko, V.G., Wilkman, O., Muinenen, K., 2016. H, G1, G2 photometric phase function extended to low-accuracy data. *Planetary and Space Science* 123, 117–125. <https://doi.org/10.1016/j.pss.2015.08.010>
- Petzold, L., 1983. Automatic Selection of Methods for Solving Stiff and Nonstiff Systems of Ordinary Differential Equations. *SIAM J. Sci. and Stat. Comput.* 4, 136–148. <https://doi.org/10.1137/0904010>

- Pollack, J.B., Rages, K., Baines, K.H., Bergstralh, J.T., Wenkert, D., Danielson, G.E., 1986. Estimates of the bolometric albedos and radiation balance of Uranus and Neptune. *Icarus* 65, 442–466. [https://doi.org/10.1016/0019-1035\(86\)90147-8](https://doi.org/10.1016/0019-1035(86)90147-8)
- Polyansky, O.L., Kyuberis, A.A., Zobov, N.F., Tennyson, J., Yurchenko, S.N., Lodi, L., 2018. ExoMol molecular line lists XXX: a complete high-accuracy line list for water. *Monthly Notices of the Royal Astronomical Society* 480, 2597–2608. <https://doi.org/10.1093/mnras/sty1877>
- Pommerol, A., Jost, B., Poch, O., Yoldi, Z., Brouet, Y., Gracia-Berná, A., Cerubini, R., Galli, A., Wurz, P., Gundlach, B., Blum, J., Carrasco, N., Szopa, C., Thomas, N., 2019. Experimenting with Mixtures of Water Ice and Dust as Analogues for Icy Planetary Material. *Space Sci Rev* 215, 37. <https://doi.org/10.1007/s11214-019-0603-0>
- Protopapa, S., Olkin, C.B., Grundy, W.M., Li, J.-Y., Verbiscer, A., Cruikshank, D.P., Gautier, T., Quirico, E., Cook, J.C., Reuter, D., Howett, C.J.A., Stern, A., Beyer, R.A., Porter, S., Young, L.A., Weaver, H.A., Ennico, K., Ore, C.M.D., Scipioni, F., Singer, K., 2020. Disk-resolved Photometric Properties of Pluto and the Coloring Materials across its Surface. *AJ* 159, 74. <https://doi.org/10.3847/1538-3881/ab5e82>
- Quémerais, E., Bertaux, J.-L., Korablev, O., Dimarellis, E., Cot, C., Sandel, B.R., Fussen, D., 2006. Stellar occultations observed by SPICAM on Mars Express. *Journal of Geophysical Research: Planets* 111. <https://doi.org/10.1029/2005JE002604>
- Régalia, L., Cousin, E., Gamache, R.R., Vispoel, B., Robert, S., Thomas, X., 2019. Laboratory measurements and calculations of line shape parameters of the H₂O–CO₂ collision system. *Journal of Quantitative Spectroscopy and Radiative Transfer* 231, 126–135. <https://doi.org/10.1016/j.jqsrt.2019.04.012>
- Robinson, T.D., Catling, D.C., 2014. Common 0.1 bar tropopause in thick atmospheres set by pressure-dependent infrared transparency. *Nature Geoscience* 7, 12–15. <https://doi.org/10.1038/ngeo2020>
- Robinson, T.D., Stapelfeldt, K.R., Marley, M.S., 2016. Characterizing Rocky and Gaseous Exoplanets with 2 m Class Space-based Coronagraphs. *PASP* 128, 025003. <https://doi.org/10.1088/1538-3873/128/960/025003>
- Rodgers, Clive D., 2000. Inverse Methods for Atmospheric Sounding | Series on Atmospheric, Oceanic and Planetary Physics [WWW Document]. URL <https://www.worldscientific.com/worldscibooks/10.1142/3171> (accessed 6.14.19).
- Rodgers, Clive D., 2000. Inverse Methods for Atmospheric Sounding: Theory and Practice. World Scientific. <https://doi.org/10.1142/3171>
- Rothman, L.S., Gordon, I.E., Barber, R.J., Dothe, H., Gamache, R.R., Goldman, A., Perevalov, V.I., Tashkun, S.A., Tennyson, J., 2010. HITEMP, the high-temperature molecular spectroscopic database. *Journal of Quantitative Spectroscopy and Radiative Transfer* 111, 2139–2150. <https://doi.org/10.1016/j.jqsrt.2010.05.001>
- Rubin, M., Altwegg, K., Balsiger, H., Berthelier, J.-J., Combi, M.R., De Keyser, J., Drozdovskaya, M., Fiethe, B., Fuselier, S.A., Gasc, S., Gombosi, T.I., Hänni, N., Hansen, K.C., Mall, U.,

- Rème, H., Schroeder, I.R.H.G., Schuhmann, M., Sémon, T., Waite, J.H., Wampfler, S.F., Wurz, P., 2019. Elemental and molecular abundances in comet 67P/Churyumov-Gerasimenko. *Monthly Notices of the Royal Astronomical Society* 489, 594–607. <https://doi.org/10.1093/mnras/stz2086>
- Sanchez, J.A., Reddy, V., Nathues, A., Cloutis, E.A., Mann, P., Hiesinger, H., 2012. Phase reddening on near-Earth asteroids: Implications for mineralogical analysis, space weathering and taxonomic classification. *Icarus* 220, 36–50. <https://doi.org/10.1016/j.icarus.2012.04.008>
- Sánchez-Lavega, A., Heimpel, M., 2017. Atmospheric Dynamics of Giants and Icy Planets, in: *Handbook of Exoplanets*. Springer, Cham, pp. 1–32. https://doi.org/10.1007/978-3-319-30648-3_51-1
- Sato, H., Robinson, M.S., Hapke, B., Denevi, B.W., Boyd, A.K., 2014. Resolved Hapke parameter maps of the Moon. *J. Geophys. Res. Planets* 119, 1775–1805. <https://doi.org/10.1002/2013JE004580>
- Saxena, P., Villanueva, G.L., Zimmerman, N.T., Mandell, A.M., Smith, A.J.R.W., 2021. Simulating Reflected Light Exoplanet Spectra of the Promising Direct Imaging Target, up Andromedae d, with a New, Fast Sampling Method Using the Planetary Spectrum Generator. *AJ* 162, 30. <https://doi.org/10.3847/1538-3881/abf657>
- Schleicher, D.G., 2010. The fluorescence efficiencies of the CN violet band in comets. *The Astronomical Journal* 140, 973–984. <https://doi.org/10.1088/0004-6256/140/4/973>
- Schleicher, D.G., A’Hearn, M.F., 1988. The fluorescence of cometary OH. *ApJ* 331, 1058. <https://doi.org/10.1086/166622>
- Schleicher, D.G., A’Hearn, M.F., 1982. OH fluorescence in comets - Fluorescence efficiency of the ultraviolet bands. *The Astrophysical Journal* 258, 864. <https://doi.org/10.1086/160133>
- Schleicher, D.G., Bair, A.N., 2011. The Composition of the Interior of Comet 73P/Schwassmann-Wachmann 3: Results from Narrowband Photometry of Multiple Components 141, 177. <https://doi.org/10.1088/0004-6256/141/6/177>
- Schöier, F.L., van der Tak, F.F.S., van Dishoeck, E.F., Black, J.H., 2005. An atomic and molecular database for analysis of submillimetre line observations. *Astronomy and Astrophysics* 432, 369–379. <https://doi.org/10.1051/0004-6361:20041729>
- Seleznev, N.V., 2005. Theoretical and Laboratory Investigation of Dielectric Properties of Partially Saturated Carbonate Rocks. St. Petersburg State Technical University, Russia.
- Serdyuchenko, A., Gorshelev, V., Weber, M., Chehade, W., Burrows, J.P., 2014. High spectral resolution ozone absorption cross-sections – Part 2: Temperature dependence. *Atmos. Meas. Tech.* 7, 625–636. <https://doi.org/10.5194/amt-7-625-2014>
- Serio, C., Masiello, G., Camy-Peyret, C., Liuzzi, G., 2019. CO₂ spectroscopy and forward/inverse radiative transfer modelling in the thermal band using IASI spectra. *Journal of Quantitative Spectroscopy and Radiative Transfer* 222–223, 65–83. <https://doi.org/10.1016/j.jqsrt.2018.10.020>

- Serio, C., Masiello, G., Liuzzi, G., 2016. Demonstration of random projections applied to the retrieval problem of geophysical parameters from hyper-spectral infrared observations. *Appl. Opt.*, AO 55, 6576–6587. <https://doi.org/10.1364/AO.55.006576>
- Shaw, J.R., Bridges, M., Hobson, M.P., 2007. Efficient Bayesian inference for multimodal problems in cosmology. *Monthly Notices of the Royal Astronomical Society* 378, 1365–1370. <https://doi.org/10.1111/j.1365-2966.2007.11871.x>
- Shepard, M.K., 2017. *Introduction to Planetary Photometry*. Cambridge University Press, Cambridge. <https://doi.org/10.1017/9781316443545>
- Shine, K.P., Campargue, A., Mondelain, D., McPheat, R.A., Ptashnik, I.V., Weidmann, D., 2016. The water vapour continuum in near-infrared windows - Current understanding and prospects for its inclusion in spectroscopic databases. *Journal of Molecular Spectroscopy* 327, 193–208. <https://doi.org/10.1016/j.jms.2016.04.011>
- Shine, K.P., Ptashnik, I.V., Rädcl, G., 2012. The Water Vapour Continuum: Brief History and Recent Developments. *Surveys in Geophysics* 33, 535–555. <https://doi.org/10.1007/s10712-011-9170-y>
- Sihvola, A., 2000. Mixing Rules with Complex Dielectric Coefficients. *Subsurface Sensing Technologies and Applications* 1, 393–415. <https://doi.org/10.1023/A:1026511515005>
- Skilling, J., 2006. Nested sampling for general Bayesian computation. *Bayesian Analysis* 1, 833–859. <https://doi.org/10.1214/06-BA127>
- Smith, D.E., Zuber, M.T., Frey, H.V., Garvin, J.B., Head, J.W., Muhleman, D.O., Pettengill, G.H., Phillips, R.J., Solomon, S.C., Zwally, H.J., Banerdt, W.B., Duxbury, T.C., Golombek, M.P., Lemoine, F.G., Neumann, G.A., Rowlands, D.D., Aharonson, O., Ford, P.G., Ivanov, A.B., Johnson, C.L., McGovern, P.J., Abshire, J.B., Afzal, R.S., Sun, X., 2001. Mars Orbiter Laser Altimeter: Experiment summary after the first year of global mapping of Mars. *Journal of Geophysical Research* 106, 23689. <https://doi.org/10.1029/2000JE001364>
- Smith, D.E., Zuber, M.T., Jackson, G.B., Cavanaugh, J.F., Neumann, G.A., Riris, H., Sun, X., Zellar, R.S., Coltharp, C., Connelly, J., Katz, R.B., Kleyner, I., Liiva, P., Matuszeski, A., Mazarico, E.M., McGarry, J.F., Novo-Gradac, A.-M., Ott, M.N., Peters, C., Ramos-Izquierdo, L.A., Ramsey, L., Rowlands, D.D., Schmidt, S., Scott, V.S., Shaw, G.B., Smith, J.C., Swinski, J.-P., Torrence, M.H., Unger, G., Yu, A.W., Zagwodzki, T.W., 2010. The Lunar Orbiter Laser Altimeter Investigation on the Lunar Reconnaissance Orbiter Mission. *Space Sci Rev* 150, 209–241. <https://doi.org/10.1007/s11214-009-9512-y>
- Smith, M.D., 2004. Interannual variability in TES atmospheric observations of Mars during 1999–2003. *Icarus* 167, 148–165. <https://doi.org/10.1016/j.icarus.2003.09.010>
- Sneep, M., Ubachs, W., 2005. Direct measurement of the Rayleigh scattering cross section in various gases. *Journal of Quantitative Spectroscopy and Radiative Transfer* 92, 293–310. <https://doi.org/10.1016/j.jqsrt.2004.07.025>
- Spurr, R., 2002. Simultaneous derivation of intensities and weighting functions in a general pseudo-spherical discrete ordinate radiative transfer treatment. *Journal of Quantitative Spectroscopy and Radiative Transfer* 75, 129–175. [https://doi.org/10.1016/S0022-4073\(01\)00245-X](https://doi.org/10.1016/S0022-4073(01)00245-X)

- Stamnes, K., Conklin, P., 1984. A new multi-layer discrete ordinate approach to radiative transfer in vertically inhomogeneous atmospheres. *Journal of Quantitative Spectroscopy and Radiative Transfer* 31, 273–282. [https://doi.org/10.1016/0022-4073\(84\)90031-1](https://doi.org/10.1016/0022-4073(84)90031-1)
- Stamnes, K., Tsay, S.C., Jayaweera, K., Wiscombe, W., 1988. Numerically stable algorithm for discrete-ordinate-method radiative transfer in multiple scattering and emitting layered media. *Applied Optics* 27, 2502–2509. <https://doi.org/10.1364/AO.27.002502>
- Stamnes, K., Tsay, S.-C., Laszlo, I., 2000. DISORT, a General-Purpose Fortran Program for Discrete-Ordinate-Method Radiative Transfer in Scattering and Emitting Layered Media: Documentation of Methodology (No. DISORT Report v1.1).
- Syme, A.-M., McKemmish, L.K., 2021. Full spectroscopic model and trihybrid experimental-perturbative-variational line list for CN. *Monthly Notices of the Royal Astronomical Society* 505, 4383–4395. <https://doi.org/10.1093/mnras/stab1551>
- Takir, D., Clark, B.E., Drouet d'Aubigny, C., Hergenrother, C.W., Li, J.-Y., Lauretta, D.S., Binzel, R.P., 2015. Photometric models of disk-integrated observations of the OSIRIS-REx target Asteroid (101955) Bennu. *Icarus* 252, 393–399. <https://doi.org/10.1016/j.icarus.2015.02.006>
- Tedesco, F., Veeder, J., Fowler, W., Chillemi, R., 1992. The IRAS Minor Planet Survey 456.
- Tennyson, J., Yurchenko, S.N., 2012. ExoMol: molecular line lists for exoplanet and other atmospheres. *Monthly Notices of the Royal Astronomical Society* 425, 21–33. <https://doi.org/10.1111/j.1365-2966.2012.21440.x>
- Toon, O.B., McKay, C.P., Ackerman, T.P., Santhanam, K., 1989. Rapid calculation of radiative heating rates and photodissociation rates in inhomogeneous multiple scattering atmospheres. *Journal of Geophysical Research: Atmospheres* 94, 16287–16301. <https://doi.org/10.1029/JD094iD13p16287>
- Turbet, M., Boulet, C., Karman, T., 2020. Measurements and semi-empirical calculations of CO₂ + CH₄ and CO₂ + H₂ collision-induced absorption across a wide range of wavelengths and temperatures. Application for the prediction of early Mars surface temperature. *Icarus* 346, 113762. <https://doi.org/10.1016/j.icarus.2020.113762>
- van Ravenzwaaij, D., Cassey, P., Brown, S.D., 2018. A simple introduction to Markov Chain Monte-Carlo sampling. *Psychon Bull Rev* 25, 143–154. <https://doi.org/10.3758/s13423-016-1015-8>
- Venot, O., Bénilan, Y., Fray, N., Gazeau, M.-C., Lefèvre, F., Es-sebbar, E., Hébrard, E., Schwell, M., Bahrini, C., Montmessin, F., Lefèvre, M., Waldmann, I.P., 2018. VUV-absorption cross section of carbon dioxide from 150 to 800 K and applications to warm exoplanetary atmospheres. *A&A* 609, A34. <https://doi.org/10.1051/0004-6361/201731295>
- Vereš, P., Jedicke, R., Fitzsimmons, A., Denneau, L., Granvik, M., Bolin, B., Chastel, S., Wainscoat, R.J., Burgett, W.S., Chambers, K.C., Flewelling, H., Kaiser, N., Magnier, E.A., Morgan, J.S., Price, P.A., Tonry, J.L., Waters, C., 2015. Absolute magnitudes and slope parameters for 250,000 asteroids observed by Pan-STARRS PS1 – Preliminary results. *Icarus* 261, 34–47. <https://doi.org/10.1016/j.icarus.2015.08.007>

- Villanueva, G.L., Bonev, B.P., Mumma, M.J., Magee-Sauer, K., Disanti, M.A., Salyk, C., Blake, G.A., 2006. The Volatile Composition of the Split Ecliptic comet 73P/Schwassmann-Wachmann 3: A Comparison of Fragments C and B. *The Astrophysical Journal* 650, L87–L90. <https://doi.org/10.1086/508806>
- Villanueva, G.L., Disanti, M.A., Mumma, M.J., Xu, L.-H., 2012a. A Quantum Band Model of the ν_3 Fundamental of Methanol (CH_3OH) and its Application to Fluorescence Spectra of Comets. *The Astrophysical Journal* 747, 1–11. <https://doi.org/10.1088/0004-637X/747/1/37>
- Villanueva, G.L., Liuzzi, G., Crismani, M.M.J., Aoki, S., Vandaele, A.C., Daerden, F., Smith, M.D., Mumma, M.J., Knutsen, E.W., Neary, L., Viscardy, S., Thomas, I.R., Lopez-Valverde, M.A., Ristic, B., Patel, M.R., Holmes, J.A., Bellucci, G., Lopez-Moreno, J.J., NOMAD team, 2021. Water heavily fractionated as it ascends on Mars as revealed by ExoMars/NOMAD. *Sci. Adv.* 7, eabc8843. <https://doi.org/10.1126/sciadv.abc8843>
- Villanueva, Geronimo L, Magee-Sauer, K., Mumma, M.J., 2013. Modeling of nitrogen compounds in cometary atmospheres: Fluorescence models of ammonia (NH_3), hydrogen cyanide (HCN), hydrogen isocyanide (HNC) and cyanoacetylene (HC_3N). *Journal of Quantitative Spectroscopy and Radiative Transfer* 129, 158–168. <https://doi.org/10.1016/j.jqsrt.2013.06.010>
- Villanueva, G.L., Mumma, M.J., Bonev, B.P., Novak, R.E., Barber, R.J., Disanti, M.A., 2012b. Water in planetary and cometary atmospheres: $\text{H}_2\text{O}/\text{HDO}$ transmittance and fluorescence models. *Journal of Quantitative Spectroscopy and Radiative Transfer* 113, 202–220. <https://doi.org/10.1016/j.jqsrt.2011.11.001>
- Villanueva, G.L., Mumma, M.J., Disanti, M.A., Bonev, B.P., Gibb, E.L., Magee-Sauer, K., Blake, G.A., Salyk, C., 2011a. The Molecular Composition of Comet C/2007 W1 (Boattini): Evidence of a Peculiar Outgassing and a Rich Chemistry. *Icarus* 216, 227–240. <https://doi.org/10.1016/j.icarus.2011.08.024>
- Villanueva, G.L., Mumma, M.J., Magee-Sauer, K., 2011b. Ethane in planetary and cometary atmospheres: Transmittance and fluorescence models of the ν_7 band at $3.3\ \mu\text{m}$. *Journal of Geophysical Research* 116, 1–23. <https://doi.org/10.1029/2010JE003794>
- Villanueva, G.L., Mumma, M.J., Novak, R.E., Radeva, Y.L., Käufel, H.U., Smette, A., Tokunaga, A., Khayat, A., Encrenaz, T., Hartogh, P., 2013. A sensitive search for organics (CH_4 , CH_3OH , H_2CO , C_2H_6 , C_2H_2 , C_2H_4), hydroperoxyl (HO_2), nitrogen compounds (N_2O , NH_3 , HCN) and chlorine species (HCl, CH_3Cl) on Mars using ground-based high-resolution infrared spectroscopy. *Icarus* 223, 11–27. <https://doi.org/10.1016/j.icarus.2012.11.013>
- Villanueva, G.L., Smith, M.D., Protopapa, S., Faggi, S., Mandell, A.M., 2018. Planetary Spectrum Generator: An accurate online radiative transfer suite for atmospheres, comets, small bodies and exoplanets. *Journal of Quantitative Spectroscopy and Radiative Transfer* 217, 86–104. <https://doi.org/10.1016/j.jqsrt.2018.05.023>
- Weaver, H.A., Mumma, M.J., 1984. Infrared molecular emissions from comets. *The Astrophysical Journal* 276, 782–797. <https://doi.org/10.1086/161664>

- Weiler, M., Rauer, H., Knollenberg, J., Jorda, L., Helbert, J., 2003. The dust activity of comet C/1995 O1 (Hale-Bopp) between 3 AU and 13 AU from the Sun. *A&A* 403, 313–322. <https://doi.org/10.1051/0004-6361:20030289>
- Wells, R.J., 1999. Rapid approximation to the Voigt/Faddeeva function and its derivatives. *Journal of Quantitative Spectroscopy and Radiative Transfer* 62, 29–48. [https://doi.org/10.1016/S0022-4073\(97\)00231-8](https://doi.org/10.1016/S0022-4073(97)00231-8)
- Williams, J.-P., Paige, D.A., Greenhagen, B.T., Sefton-Nash, E., 2017. The global surface temperatures of the Moon as measured by the Diviner Lunar Radiometer Experiment. *Icarus, Lunar Reconnaissance Orbiter - Part II* 283, 300–325. <https://doi.org/10.1016/j.icarus.2016.08.012>
- Wiscombe, W.J., 1977. The Delta–M Method: Rapid Yet Accurate Radiative Flux Calculations for Strongly Asymmetric Phase Functions. *Journal of the Atmospheric Sciences* 34, 1408–1422. [https://doi.org/10.1175/1520-0469\(1977\)034<1408:TDMRYA>2.0.CO;2](https://doi.org/10.1175/1520-0469(1977)034<1408:TDMRYA>2.0.CO;2)
- Wolff, M.J., Smith, M.D., Clancy, R.T., Arvidson, R., Kahre, M., Seelos, F., Murchie, S., Savijarvi, H., 2009. Wavelength dependence of dust aerosol single scattering albedo as observed by the Compact Reconnaissance Imaging Spectrometer. *Journal of Geophysical Research* 114, E00D04. <https://doi.org/10.1029/2009JE003350>
- Xie, X., Mumma, M.J., 1992. The Effect of Electron Collisions on Rotational Populations of Cometary Water. *The Astrophysical Journal* 386, 720. <https://doi.org/10.1086/171053>
- Yamamoto, T., 1981. On the photochemical formation of CN, C2, and C3 radicals in cometary comae. *Moon and the Planets* 24, 453.
- Yang, K., Liu, X., 2019. Ozone profile climatology for remote sensing retrieval algorithms. *Atmos. Meas. Tech.* 12, 4745–4778. <https://doi.org/10.5194/amt-12-4745-2019>
- Yule, J.A.C., Nielsen, W.J., 1951. The penetration of light into paper and its effect on halftone reproduction (Kodak Research Laboratories No. Communications No. 1416).
- Yurchenko, S.N., Mellor, T.M., Freedman, R.S., Tennyson, J., 2020. ExoMol line lists – XXXIX. Ro-vibrational molecular line list for CO₂. *Monthly Notices of the Royal Astronomical Society* 496, 5282–5291. <https://doi.org/10.1093/mnras/staa1874>
- Yurchenko, S.N., Owens, A., Kefala, K., Tennyson, J., 2024. ExoMol line lists – LVII. High accuracy ro-vibrational line list for methane (CH₄). *Monthly Notices of the Royal Astronomical Society* 528, 3719–3729. <https://doi.org/10.1093/mnras/stae148>
- Zakharov, V., Bockelée-Morvan, D., Biver, N., Crovisier, J., Lecacheux, A., 2007. Radiative transfer simulation of water rotational excitation in comets. Comparison of the Monte Carlo and escape probability methods. *Astronomy and Astrophysics* 473, 303–310. <https://doi.org/10.1051/0004-6361:20066715>
- Zuber, M.T., Smith, D.E., Solomon, S.C., Muhleman, D.O., Head, J.W., Garvin, J.B., Abshire, J.B., Bufton, J.L., 1992. The Mars Observer laser altimeter investigation. *Journal of Geophysical Research: Planets* 97, 7781–7797. <https://doi.org/10.1029/92JE00341>